

The
University
Of
Sheffield.

**Shape dependant properties of
Catalytic micro-swimmers**

By Alice Elizabeth Kirvin

The department of Chemical and Biological Engineering

The University of Sheffield

June 2021

Abstract

This thesis explores catalyst driven micro-swimmers which propel via phoretic mechanisms. This is achieved with a Janus structure of active and inert sides, which when exposed to chemical fuel causes asymmetric forces across the swimmer, leading to propulsion. Catalytic micro-swimmers have proposed applications such as microfluidic transport, cargo delivery, micro-stirring, and environmental remediation. These active swimmers, whilst popular in the literature, have yet to be optimised for their intended practical applications. The randomised motion at long time scales is a problem for transport applications and synthesis methods are complicated and produce a low yield of swimmers.

This thesis focusses on platinum coated insulator swimmers, which when exposed to hydrogen peroxide propel via a mechanism, which is proposed to be self-electrophoretic, in the literature. The bulk of the thesis explores the relationship between the geometry of the starting colloid, and the resulting motion and swimmer dynamics. For ellipsoidal swimmers, this was found to have a significant impact on the swimmer's angular velocity and interactions with the fluid and bounding surfaces. Whilst investigating the motion of ellipsoidal colloids, a self-imposed flow alignment effect was observed and thoroughly investigated. The findings revealed a strong preference for motion across the flow field rather than along the streamlines.

Bowl and Dumpling shaped colloids were also investigated to see if they would self-shadow and induce enough asymmetry in the catalyst cap to produce driven rotations. In certain colloid orientations, before coating, this was successful producing much higher angular velocities than spherical swimmers whilst other orientations produced negligible spin.

In an effort to further investigate how geometry impacts the motion of active swimmers, the symmetry of the catalytic patch was intentionally broken by glancing angle deposition to induce beneficial rotations. This had previously been achieved with close packed spherical swimmers, but the work here aims to reduce the steps

required to achieve this in the hopes of improving scalability of synthesis. The data shows that introducing even a slight glancing angle during coating provides enough shadowing of well-spaced ellipsoidal colloids to produce swimmers with angular velocities 16x the magnitude of ellipsoidal colloids coated at a direct angle.

Acknowledgements

I would like to thank my supervisor Dr Stephen Ebbens for his support throughout my PhD, and Dr Andrew Campbell for his assistance with ray tracing analysis.

I would also like to thank my husband, Jack Kirvin for his endless support, patience, and impeccable proof reading.

Publications

- “Rotating Ellipsoidal Catalytic Micro-Swimmers via Glancing Angle Evaporation”.

Alice Kirvin, David Gregory, Andrew Parnell, Andrew Campbell, Stephen Ebbens – published September 2021 RSC Materials advances¹.

Conference Posters

- ChemEng Day, Heriot Watt University Edinburgh, April 2019.

Autonomous motion of ellipsoidal micro-swimmers in a self-generated flow regime

2nd prize in poster competition

- International Colloids conference, Sitges, June 2019

Flow phenomena in ellipsoidal micro-swimmers”

Table of Contents

Chapter 1:	1
1 Introduction	2
1.1 Forces on the nanoscale	2
1.2 Janus Colloids	4
1.3 Overview of experimental literature	6
1.3.1 Popular Experimentally tested systems	6
1.4 Mechanism of propulsion	9
1.4.1 Phoresis	9
1.5 Motion control of active colloids	12
1.5.1 Motion control by changing catalyst geometry.	12
1.5.2 Asymmetrical swimmers	16
1.5.3 Theoretical predictions of asymmetric shapes	19
1.6 Flow	29
1.6.1 Micro-pumping	31
1.6.2 Orientation phenomena of active colloids in flow fields	34
1.7 Thesis Aims and Structure	37
2 Methods	41
2.1 Synthesis	41
2.1.1 Colloid stretching	41
2.1.2 Spin Coating	43

2.1.3	Catalyst deposition.....	44
2.2	Characterization	48
2.2.1	Scanning Electron Microscopy	48
2.2.2	Optical Microscopy	50
2.2.3	Fluorescence Microscopy.....	51
2.3	Particle Tracking	52
2.3.1	Labview software and MSD analysis	52
3	Ellipsoidal Micro-swimmers.....	60
3.1	Introduction	60
3.2	Experimental.....	62
3.2.1	Synthesis.....	62
3.2.2	Tracking.....	62
3.3	Results	64
3.3.1	SEM and size analysis.....	64
3.3.2	Motion.....	65
3.3.3	Self-generated flow.....	81
3.4	Discussion	82
3.4.1	Translational and Angular velocity	82
3.4.2	Bulk vs. surface following motion	82
3.4.3	Previous work.....	83
3.4.4	Mechanism	85

3.5	Conclusions.....	86
4	Flow phenomena in ellipsoidal micro-swimmers	88
4.1	Introduction	88
4.2	Experimental.....	90
4.2.1	Convective Flow	90
4.2.2	Induced Flow.....	90
4.3	Results	92
4.3.1	External imposed flow (Control)	92
4.3.2	Self-generated convective flow	106
4.3.3	A comparison of Active and Passive ellipsoids in a flow	123
4.3.4	High Spin Ellipsoids.....	125
4.4	Discussion	129
4.4.1	Flow field	129
4.5	Conclusions.....	135
5	Ellipsoidal Janus swimmers with enhanced rotational motion	138
5.1	Introduction	138
5.2	Methods	140
5.3	Results.....	142
5.3.1	Theoretical Prediction of the Catalyst shapes	142
5.3.2	Experimental Results	145
5.4	Discussion	153

5.5	Conclusions.....	157
6	Dumpling and Bowl-shaped swimmers	159
6.1	Introduction	159
6.2	Methods	160
6.3	Results	161
6.3.1	'Dumpling' shaped PDMS colloids.....	161
6.3.2	Bowl shaped PDMS Colloids	174
6.4	Discussion	186
6.5	Conclusions.....	188
7	Conclusions and Future Work.....	190
7.1	Ellipsoidal Micro-swimmers	191
7.1.1	Conclusions	191
7.1.2	Future work.....	192
7.2	Flow phenomena in ellipsoidal micro-swimmers.....	192
7.2.1	Conclusions	192
7.2.2	Future work.....	193
7.3	Ellipsoidal micro-swimmers with enhanced rotational motion.....	194
7.3.1	Conclusions	194
7.3.2	Future work.....	195
7.4	Dumpling and Bowl-shaped swimmers.....	198
7.4.1	Conclusions	198

7.4.2	Future work	199
8	References	201

Table of Figures

Figure 1-1: Schematic of a Janus sphere.....	5
Figure 1-2: Examples of experimentally tested micron scale motors. a) spherical Pt-PS Janus swimmers ^{21,22} b) Si-Au photothermal micro swimmers ²³ c) Pt-Au Janus nano rods ²⁴	7
Figure 1-3: Schematic of the reaction leading to self-electrophoretic motion in Pt-peroxide systems.	10
Figure 1-4:a) schematic showing shadowing or a lack of, for colloids in a closely packed colloidal crystal(left) and well-spaced colloids (right) during Pt deposition. b) predicted cap shapes for closely packed colloids with varying θ , c) trajectories of resulting spinning swimmers with corresponding MSD data in d) from Archer et al. ²¹	13
Figure 1-5: Trajectories of bubble propelled spherical swimmers with decreasing catalytic patch size, left to right. From Gregory et al. ⁴²	15
Figure 1-6: a) Experimental trajectories measured at the same angle. Increasing number corresponds to greater illumination. b) Diagram of L-shaped swimmer ⁴⁴ ...	16
Figure 1-7: Time series images of Janus ellipsoids translating ballistically and rotationally. (from Shemi et al. ⁴⁷).....	17
Figure 1-8: a) Experimental data for P^* vs ϕ , the blue curve shows the theoretical data from equation 5. b) State diagrams for each type of motion with illustrations of theoretical data for swimmer trajectories given by equation 4 ⁴⁴	21
Figure 1-9: Schematic of rods disks and spheres modelled by the Lugli group ⁵⁰	22
Figure 1-10: a) Propulsive velocity (v) as a function of reactant concentration, for long rod (black), short rod (red), sphere (green), and disk (blue); v is in dimensionless DPD units. b) Rotational time (τ_R) as a function of reactant	

concentration, for long rod (black), short rod (red), sphere (green), and disk (blue). T_R is in dimensionless DPD units.	24
Figure 1-11: Comparison of swimmer propulsion speeds of different shaped colloids depending on their slenderness ratio ⁵²	26
Figure 1-12: a) Schematic of a spherical swimmer at low speed ($U^{sd}/U_0 = 0.1$) following the step on a chemically patterned wall. b) Schematic of a spherical swimmer at high speed ($U^{sd}/U_0 = 0.4$) passing over the step on a chemically patterned wall.....	27
Figure 1-13: Schematic of ellipsoidal swimmer following a chemically patterned step. From Uspal et al. ⁵³	28
Figure 1-14: Schematic of a cyclical density driven flow produced by the decomposition of hydrogen peroxide by catalytic swimmers. From Balasz et al. ⁵⁴ .	30
Figure 1-15: Model of the fluid flows (arrows) generated by chemical decomposition of peroxide around a mobile (red) particle which drags a (blue) tracer particle blue from left to right. ⁵⁴	31
Figure 1-16: Images showing the organisation of tracer colloids into an organised crystal. an electric field pointing from gold to platinum drives a fluid flow in this direction ⁵⁵	32
Figure 1-17: Enzyme powered micro-pumps designed by Sengupta et al. ⁵⁶	33
Figure 1-18: Schematic of rheotaxing gold-platinum nano-rods produced by Baker et al. ⁶²	35
Figure 1-19: Trajectories of rheotaxing nanorods designed by Ren et al. ⁵⁸	36
Figure 2-1: Custom built stretching equipment for ellipsoid preparation.....	42
Figure 2-2: Schematic showing the spin coating process.....	43

<i>Figure 2-3: A basic representation of the sample chamber of an Electron beam evaporator.....</i>	<i>45</i>
<i>Figure 2-4: A basic representation of the sample chamber of ion sputtering equipment.</i>	<i>46</i>
<i>Figure 2-5: Schematic illustrating the directionality of electron beam evaporation and sputter coating.....</i>	<i>47</i>
<i>Figure 2-6: A simplified representation of the inner components of a Scanning Electron Microscope.....</i>	<i>49</i>
<i>Figure 2-7: Basic schematic of a fluorescence microscope.....</i>	<i>51</i>
<i>Figure 2-8: Schematic showing a simple 6 position MSD calculation.....</i>	<i>53</i>
<i>Figure 2-9: A typical MSD plot for a propulsive micro swimmer without any rotational propulsion.....</i>	<i>55</i>
<i>Figure 2-10: Screen capture from originpro graphing software of an MSD fitting curve.</i>	<i>57</i>
<i>Figure 3-1: Schematic of a PS-Pt ellipsoidal micro swimmer, coated along its major axis, in hydrogen peroxide fuel.....</i>	<i>60</i>
<i>Figure 3-2: Representative SEM image of ellipsoidal polystyrene colloids.....</i>	<i>64</i>
<i>Figure 3-3: Schematic illustrating the calculation to derive the angle between the field of vision and the ellipsoid, from the results provided by LabVIEW.</i>	<i>66</i>
<i>Figure 3-4: a) A trajectory of an ellipsoidal Micro swimmer translating in the bulk fluid, this type of swimmer represents <20% of the total swimmer population. b) A schematic showing the allowed rotations around each axis for an ellipsoid in the bulk fluid. c) a plot to show the fluctuation over time of the angle between the plane of vision and the ellipsoid's major axis for 30 seconds.</i>	<i>68</i>

Figure 3-5: a) A trajectory of an ellipsoidal swimmer translating near the cuvette boundary, this type of swimmer represents >80% of the total swimmer population. b) A schematic showing the allowed rotations around each axis for an ellipsoid near the cuvette boundary. c) a plot to show the fluctuation over time of the angle between the plane of vision and major axis for 30 seconds..... 69

Figure 3-6: Trajectory and corresponding MSD plot with angular velocity fitting ($\omega=8.88 \times 10^{-7} \text{ rads}^{-1}$) for a representative ballistic Janus ellipsoid. 71

Figure 3-7: Trajectory and corresponding MSD plot with angular velocity fitting ($\omega=0.245 \text{ rads}^{-1}$) for a representative slowly rotating Janus ellipsoid. 72

Figure 3-8: Trajectory and corresponding ensemble average MSD plot for a population of 10 Janus ellipsoids undergoing Brownian motion in the absence of hydrogen peroxide fuel. Error bars indicate the standard deviation for each timestep. 75

Figure 3-9: a) Diagram showing axis assignment and angles of interest b) Difference between orientation of ellipsoid body long axis and direction of travel for a representative ellipsoidal micro-swimmer..... 78

Figure 3-10: Average angle between orientation and direction for a series of swimmers. 79

Figure 4-1: Schematic of the experimental set up leading to a convective flow (red arrow)..... 88

Figure 4-2: Diagram showing the formation of cyclical flow due to density differences of products and reactants within a closed cuvette. 89

Figure 4-3: Diagram showing the effect of orientation of ellipsoidal colloids in a density driven flow field. Red arrows indicate the direction of the flow. 89

<i>Figure 4-4: Photographs of the pump and sample chamber used to create the externally imposed flow.</i>	91
<i>Figure 4-5: Schematic showing relevant dimensions of the sample holder for Reynold's number calculation.</i>	94
<i>Figure 4-6: Schematic showing coordinates as assigned for these calculations.</i>	94
<i>Figure 4-7: The predicted flow profile for a laminar shear flow in the z direction.</i>	96
<i>Figure 4-8: Z-shear profile within 10μm of the lower boundary. The expected range of heights and their corresponding experienced flow velocities are indicated within the dashed red lines.</i>	97
<i>Figure 4-9: Prediction of the flow profile across the width of the sample holder at a height of 2.5 μm.</i>	98
<i>Figure 4-10: X- shearing in the region of interest near the centre of the sample chamber at our experimental height (black) and $\pm 1\mu$m from the experimental height red is 1μm below the experimental height whilst blue is 1μm above.</i>	99
<i>Figure 4-11: Trajectories of tracer particles in a pressure pump induced flow for 10 seconds. Tracers have been numbered from left to right.</i>	100
<i>Figure 4-12: Velocities of tracers shown in Figure 4-11, the tracer position corresponds to the number assigned in Figure 4-11. The predicted flow profile at this height is overlaid in red squares.</i>	101
<i>Figure 4-13: a) Trajectory of a passive ellipsoid travelling in a 10 μm/s externally induced flow; overlaid with a time lapse image. b) MSD analysis of trajectory a).c) A 30s time lapse image of an ellipsoid translating in a 10 μm/s⁻¹ externally induced flow</i>	102

<i>Figure 4-14: Binned wind rose diagrams showing alignment with the direction of flow for passive ellipsoidal colloids in a $10 \mu\text{ms}^{-1}$ imposed flow: a) distribution of direction angles. b) distribution of orientation angles.</i>	<i>105</i>
<i>Figure 4-15: A representative trajectory of an ellipsoidal micro swimmer, overlaid with a time lapse image (30s). Tracer particles illustrating the self-induced convective flow field are shown in colour whilst the propulsive ellipsoid is shown in black.</i>	<i>106</i>
<i>Figure 4-16: MSD graph for the swimmer shown in Figure 4-15.</i>	<i>107</i>
<i>Figure 4-17: Predicted thin ($H < L$) channel velocity profiles for a flow due to convection from Williams et al⁸⁵.</i>	<i>109</i>
<i>Figure 4-18: Diagram depicting the measurements used to fit the flow profile to experimental parameters.</i>	<i>110</i>
<i>Figure 4-19: Approximate z-shear profile for the self-convective flow in a cuvette of defined geometry.</i>	<i>111</i>
<i>Figure 4-20: Approximate z-shear profile for the self-convective flow in the experimental region of interest (height$<10\mu\text{m}$.)</i>	<i>112</i>
<i>Figure 4-21: Trajectories of tracer particles in a self-generated convective flow. Tracers have been numbered from left to right.</i>	<i>114</i>
<i>Figure 4-22: Tracer velocities from Figure 4-22.</i>	<i>115</i>
<i>Figure 4-23: A representative trajectory showing the raw data in black, with the data after advective drift subtraction highlighted in blue. The flow direction and speed are shown by the (to scale) red arrow.</i>	<i>117</i>
<i>Figure 4-24: Corrected trajectories with the average flow field depicted by red arrows (angle and arrow length to scale with direction and velocity)</i>	<i>118</i>

<i>Figure 4-25: Binned wind rose diagrams showing alignment with or perpendicular to the direction of flow: a) distribution of direction angles from perpendicular alignment</i>	
<i>b) distribution of orientation angles from parallel alignment.</i>	<i>122</i>
<i>Figure 4-26: A comparison of data from passive and active ellipsoids; a) Distribution of direction angles. b) Distribution of orientation angles. Flow directions are defined as seen in the schematics in Figure 4-14 and Figure 4-26 for passive and active swimmers respectively.</i>	<i>123</i>
<i>Figure 4-27: A comparison of data from passive and active ellipsoids; a) Distribution of direction angles. b) Distribution of orientation angles.</i>	<i>124</i>
<i>Figure 4-28: MSD plot with angular velocity fitting (originPro) for a low angular velocity ellipsoidal swimmer.</i>	<i>125</i>
<i>Figure 4-29: MSD plot with angular velocity fitting (originPro) for a high angular velocity ellipsoidal swimmer.</i>	<i>126</i>
<i>Figure 4-30: A bar chart comparing the distribution of direction angles relative to the flow. Low angular velocity ellipsoids ($\omega < 0.15 \text{ rads}^{-1}$) are represented in black whilst high spin ellipsoids are represented in red ($\omega > 0.15 \text{ rads}^{-1}$).....</i>	<i>127</i>
<i>Figure 4-31: A bar chart comparing the reduction in alignment relative to the flow. $\Delta[(\text{Flow} + \text{Activity}) - (\text{Flow})]$ is represented in blue whilst $\Delta[(\text{High spin}) - (\text{Low spin})]$ is represented in red.</i>	<i>128</i>
<i>Figure 4-32: Schematic showing assigned lengths for surface area calculation. ...</i>	<i>130</i>
<i>Figure 4-33: Figures from Katuri et al. Trajectories and Optical microscopy images of Janus spheres exposed to a flow with velocity $14 \mu\text{ms}^{-1}$.⁵⁷</i>	<i>131</i>
<i>Figure 4-34: Figure from Katuri et al. Angular probability distributions at different flow velocities⁵⁷.....</i>	<i>133</i>

<i>Figure 4-35: Schematic by Katuri et al. showing how a flow with shearing in the z-direction leads to alignment of spherical Janus Swimmers⁵⁷.....</i>	<i>133</i>
<i>Figure 4-36: Close up SEM image of an ellipsoidal colloid prior to catalyst coating.</i>	<i>135</i>
<i>Figure 5-1: Schematic from Archer et al. showing how a closely packed crystal of spheres induces shadowing when coated at an angle, θ^{21}.....</i>	<i>139</i>
<i>Figure 5-2: Schematic showing how ellipsoidal colloids induce shadowing at a glancing angle, θ, without the need for a closely packed crystal.</i>	<i>139</i>
<i>Figure 5-3: Custom built angle changing slide holder (by Richard Archer former CBE student, University of Sheffield), the right side is turned to $\theta=60^\circ$ to achieve a glancing angle deposition.....</i>	<i>140</i>
<i>Figure 5-4:Diagram showing the experimental setup used for deposition a) standard perpendicular coating b) sample rotated by 60°.....</i>	<i>141</i>
<i>Figure 5-5: Schematic showing the coating conditions which would lead to a symmetrical hemispheroidal coating.</i>	<i>142</i>
<i>Figure 5-6: Schematic showing how a glancing angle deposition leads to shadowing over the long body and a build of catalytic material and the tip closest to the metal source.</i>	<i>144</i>
<i>Figure 5-7: A scatter plot of translational velocity (v) vs. angular velocity (ω) for a population of high spin swimmers (red) and swimmers coated with standard deposition conditions (black).....</i>	<i>145</i>
<i>Figure 5-8: Part of a trajectory for a spinning ellipsoid overlaid with a time-lapse image of the video recording.....</i>	<i>146</i>
<i>Figure 5-9: Representative trajectories of Ellipsoidal swimmers with enhanced rotational motion.....</i>	<i>147</i>

<i>Figure 5-10: MSD data and angular velocity fitting for trajectory shown in red in Figure 5-9 $\omega=0.884 \text{ rads}^{-1}$.</i>	148
<i>Figure 5-12: MSD data and angular velocity fitting for the trajectory shown in Figure 5-9 in black $\omega=1.25 \text{ rads}^{-1}$.</i>	149
<i>Figure 5-11: MSD data and angular velocity fitting for the trajectory shown in Figure 5-9 in blue $\omega=2.43 \text{ rads}^{-1}$.</i>	150
<i>Figure 5-13: Scatter plot of raw angular velocities for a population of ellipsoidal swimmers coated under standard conditions (black) vs. a glancing angle deposition (red). Error bars are included but are too small to see in most cases.</i>	151
<i>Figure 5-14: A bar chart showing the normalised frequency of ellipsoids in 0.5 rads^{-1} bins. Standard deposition is shown in black whilst Glancing angle deposition is shown in red.</i>	152
<i>Figure 5-15: Schematic showing a high spin swimmer in the top-down configuration on a substrate (grey), showing how the differences in Pt thickness leads to rotational motion, whilst swimming close to the cuvette boundary.</i>	154
<i>Figure 5-16: Figure from Archer et al. Trajectories of spherical Janus swimmers coated at 50° and 70° glancing angles²¹.</i>	155
<i>Figure 6-1: Scanning electron microscope images of dumpling shaped PDMS colloids; a) air dried from solution b) spin coated at 2000rpm.</i>	161
<i>Figure 6-2: Schematic of assigned colloid orientations; a) single concave surface facing up b) plural concave surfaces facing up c) convex surface facing up.</i>	162
<i>Figure 6-3: Ensemble average MSD plot for 20 dumpling shaped colloids in deionised water.</i>	164
<i>Figure 6-4: Representative trajectories of dumpling shaped colloids with $\omega < 0.01 \text{ rads}^{-1}$ in 10% wt. H_2O_2.</i>	165

<i>Figure 6-6: Representative trajectories of dumpling shaped colloids with $w = 0.01-0.099 \text{ rads}^{-1}$ in 10% wt. H_2O_2.....</i>	<i>167</i>
<i>Figure 6-5: Representative trajectories of dumpling shaped colloids with $w > 0.1 \text{ rads}^{-1}$ in 10% wt. H_2O_2.....</i>	<i>166</i>
<i>Figure 6-7: MSD curve fitted to Equation 4 to determine angular velocity using Originpro software.....</i>	<i>168</i>
<i>Figure 6-8: Angular velocities for a set of swimmers. Error bars (calculated by Originpro fitting software) are provided for all data points but are too small to be seen in most cases.</i>	<i>169</i>
<i>Figure 6-9: Bar chart showing the distribution of angular velocities of a set of swimmers at 0.05 rads^{-1} intervals.....</i>	<i>170</i>
<i>Figure 6-10: Bar chart showing angular velocities grouped as high ($>0.1 \text{ rads}^{-1}$), medium ($0.01-0.099 \text{ rads}^{-1}$) and low ($>0.01 \text{ rads}^{-1}$).....</i>	<i>171</i>
<i>Figure 6-11: Scatter plot of translational velocity vs. angular velocity.</i>	<i>172</i>
<i>Figure 6-12: A bar chart showing the average velocity of a set of swimmers within defined bands for angular velocity.....</i>	<i>173</i>
<i>Figure 6-13: Scanning electron microscope images of bowl shaped PDMS colloids a) air dried from solution b) spin coated at 2000rpm</i>	<i>174</i>
<i>Figure 6-14: Schematic of assigned orientations; a) cavity facing up b) cavity facing to the side c) cavity facing down.</i>	<i>175</i>
<i>Figure 6-15: Ensemble average MSD plot for bowl shaped colloids in deionised water.</i>	<i>177</i>
<i>Figure 6-16: Representative trajectories of bowl-shaped colloids with $\omega > 0.1 \text{ rads}^{-1}$ in 10% wt. H_2O_2.</i>	<i>178</i>

<i>Figure 6-17: Representative trajectories of bowl-shaped colloids with $\omega=0.01-0.099$ rads^{-1} in 10% wt. H_2O_2.</i>	179
<i>Figure 6-18: Representative trajectories of bowl shaped colloids with $\omega < 0.01$ rads^{-1} in 10% wt. H_2O_2.</i>	180
<i>Figure 6-19: Angular velocities for a set of swimmers. Error bars (calculated by Originpro fitting software are provided for all data points but are too small to be seen in most cases.</i>	181
<i>Figure 6-20: Bar chart showing the distribution of angular velocities for a set of swimmers at 0.05 rads^{-1} intervals.</i>	182
<i>Figure 6-21: A bar chart showing angular velocities grouped as high ($>0.1\text{rads}^{-1}$), medium ($0.01-0.099\text{rads}^{-1}$) and low ($>0.01\text{rads}^{-1}$) for a set of swimmers.</i>	183
<i>Figure 6-22: Scatter plot of translational velocity vs. angular velocity</i>	184
<i>Figure 6-23: A bar chart showing the average velocity of a set of swimmers within defined bands for angular velocity.</i>	185
<i>Figure 6-24: A comparison bar chart showing the distribution of angular velocities for all samples at 0.05 rads^{-1} intervals.</i>	186
<i>Figure 7-1: Epoxy replica of the surface of a petal. Scale bar 10μm from Wilts. et al.⁹²</i>	195
<i>Figure 7-2: Schematic showing predictions for how the reducing glancing angle results in increased symmetry breaking in the catalyst. a) $\theta=90^\circ$, b) $\theta=80^\circ$, c) $\theta=70^\circ$, d) $\theta=60^\circ$, e) $\theta=50^\circ$, f) $\theta=40^\circ$, g) $\theta=30^\circ$, h) $\theta=20^\circ$, i) $\theta=10^\circ$.</i>	197
<i>Figure 7-3: Diatomic frustules in various geometries imaged by SEM, by Hildebrand et al.⁹³</i>	199

Chapter 1:

Introduction

1 Introduction

The desire to artificially mimic biological processes such as chemotaxis and rheotaxis has driven a significant effort over recent decades, to produce simple active colloids that can reproduce the behaviours seen in micro-organisms, in response to a change in their environment.

Micro-scale particles have been shown to be capable of active propulsion when exposed to a gradient such as temperature, concentration, electrostatic potential, or light. These gradients can be externally imposed on a population of colloids to achieve heteronomous motion, or the colloid can be modified in such a way that it generates its own gradient of stimuli. The use of surface catalysts, which are able to utilise a chemical “fuel”, creates an asymmetric distribution of reactants and products which yields autonomous self-propulsion.

This was discovered in the early 2000's and inspired extensive research into various catalyst/fuel systems, the mechanisms by which they propel, and the dynamics of these systems. These micro-swimmers are of continued interest in the field of nanomaterials due to their applications in drug delivery systems^{2,3}, in-vitro diagnostics, ‘micro-stirring’⁴, environmental remediation⁵, sensing and sorting⁶, and repair of conductive surfaces⁷.

1.1 Forces on the nanoscale

Nano and micro-scale particles face several challenges in achieving directed propulsion due to their small size, such as Brownian motion and a low Reynold's number regime.

Brownian motion refers to the pattern of random fluctuations in position of a particle suspended in a medium (liquid or gas). The medium is composed of solvent molecules

which are in constant motion due to thermal energy; these solvent molecules collide with the particles, transferring kinetic energy to them⁸. This transfer of kinetic energy is experienced to differing degrees depending on the mass of the particle. Larger objects require more energy to accelerate than smaller objects as described by Newton's second law of motion.

In macro-scale systems, motion is often produced by a reciprocal deformation mechanism consisting of repetitive cyclical motions. In these large systems, inertia works to keep the swimmer in motion once propulsion has been initiated. During this time the swimmers moving parts return to their origin to repeat the cycle. Conversely, on the nanoscale the size of the swimmer dictates that the viscous forces acting on the particle dominate over inertial forces. This effect is quantified by its Reynolds number; the ratio of inertial forces to viscous forces acting on a swimmer⁹.

Equation 1-1:
$$Re = \frac{\rho v L}{\mu}$$

ρ = Fluid density

v = Fluid velocity

L = Swimmer length

μ = Dynamic viscosity of the fluid, = $\tau / \dot{\gamma}$ where τ is shear stress rate of the fluid and $\dot{\gamma}$ is shear strain rate.

At sufficiently low Reynold's numbers, inertia does not keep the particle in motion whilst the propulsion mechanism returns to its origin. This means that the reciprocal motion results in a zero-net force and motion does not occur. This is often visualised by

Purcell's scallop theorem which describes motion of swimmers at low Reynold's number in Newtonian fluids. Purcell states that in a low Reynolds number regime the swimmer must deform in a way that is not invariant under time reversal¹⁰. Essentially, the return to origin must not be the same as the initial deformation or the equal and opposite forces balance out, resulting in no net translational motion.

Non-reciprocal motion on the micro-scale has been perfected in nature by micro-organisms which use cilia and flagella to perform "run and tumble" style swimming¹¹. The flagella are twisted into a single filament and rotated in one direction. The body of the bacteria rotates in the opposite direction and the flagella are rapidly unbundled to change direction. Similar deformable systems have been experimentally realised, such as the William's group synthetic flagellum¹². At 2 mm in length, these flagella are far from the ideal size for micro-scale applications and factoring the time and economic cost of manufacturing such swimmers renders them incompatible for industrial or commercial production.

1.2 Janus Colloids

To avoid lengthy and complicated synthesis, a scheme to achieve propulsion in non-deformable colloids was devised based on catalytic reactions. In order to achieve non-reciprocal motion, swimmers were designed so that a chemical reaction would occur on one side only. This produces constant asymmetrical forces on the particle, avoiding the need for inertia as the driving force is non-reciprocal and resulting in net motion. This is achieved by having a Janus structure with two distinct sides with different chemical functionalities¹³, as seen in *Figure 1-1*. An example would be having two different materials or functional groups on the surface of the colloid. One of these sides should

be a catalytic material that can react with a fuel in the surrounding media whilst the other side should be inert. Micro-swimmers with a platinum catalytic patch able to decompose hydrogen peroxide as fuel have proved to be the most popular system due to their straightforward production, speed and efficiency.

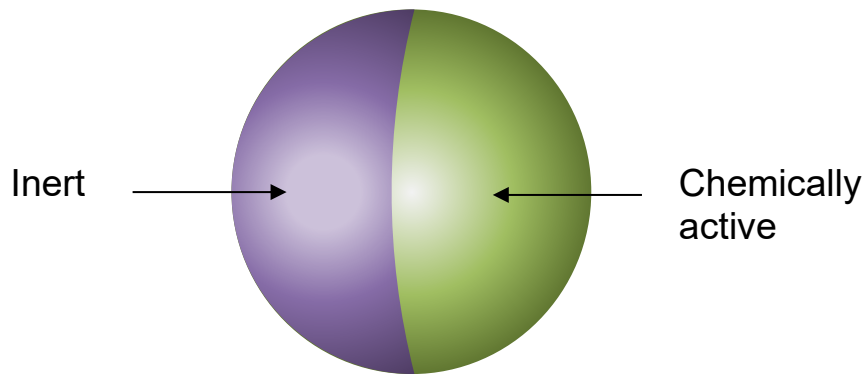


Figure 1-1: Schematic of a Janus sphere.

1.3 Overview of experimental literature

In the ever-growing field of autonomous nano-propulsion, many approaches have been successful. Bio-hybrids based on rotating flagella¹², helical corkscrew type motors¹⁴ and trapped bacteria¹⁵ have been used to mimic naturally occurring micro-swimmers. These intricate motors require complicated synthesis and are difficult to reproduce at a size that would be appropriate for their applications.

To simplify synthesis and analysis of results, inorganic motors of simple shapes were designed which rely on a gradient across the particle such as heat¹⁶, light¹⁷ or a chemical fuel for propulsion.

Platinum is a popular catalyst for motion as it is generally non-reactive until certain fuels such as hydrogen peroxide are introduced. For this reason, and the ability to derive high speeds, swimmers consisting of an inert base material such as gold or polystyrene with a platinum coating have proved the most popular. Groups have attempted basic shapes such as spheres, rods and nano-tubes, an overview of which is available in section 1.3.1^{18–20}. Differences between these basic shapes have been noted with rods and tubes usually producing highest speeds.

1.3.1 Popular Experimentally tested systems

Many experimental systems have been tested with similar desirable qualities in mind. The aim is predominantly to produce high speed, directional swimmers that have no requirement for external guidance such as magnetic fields.

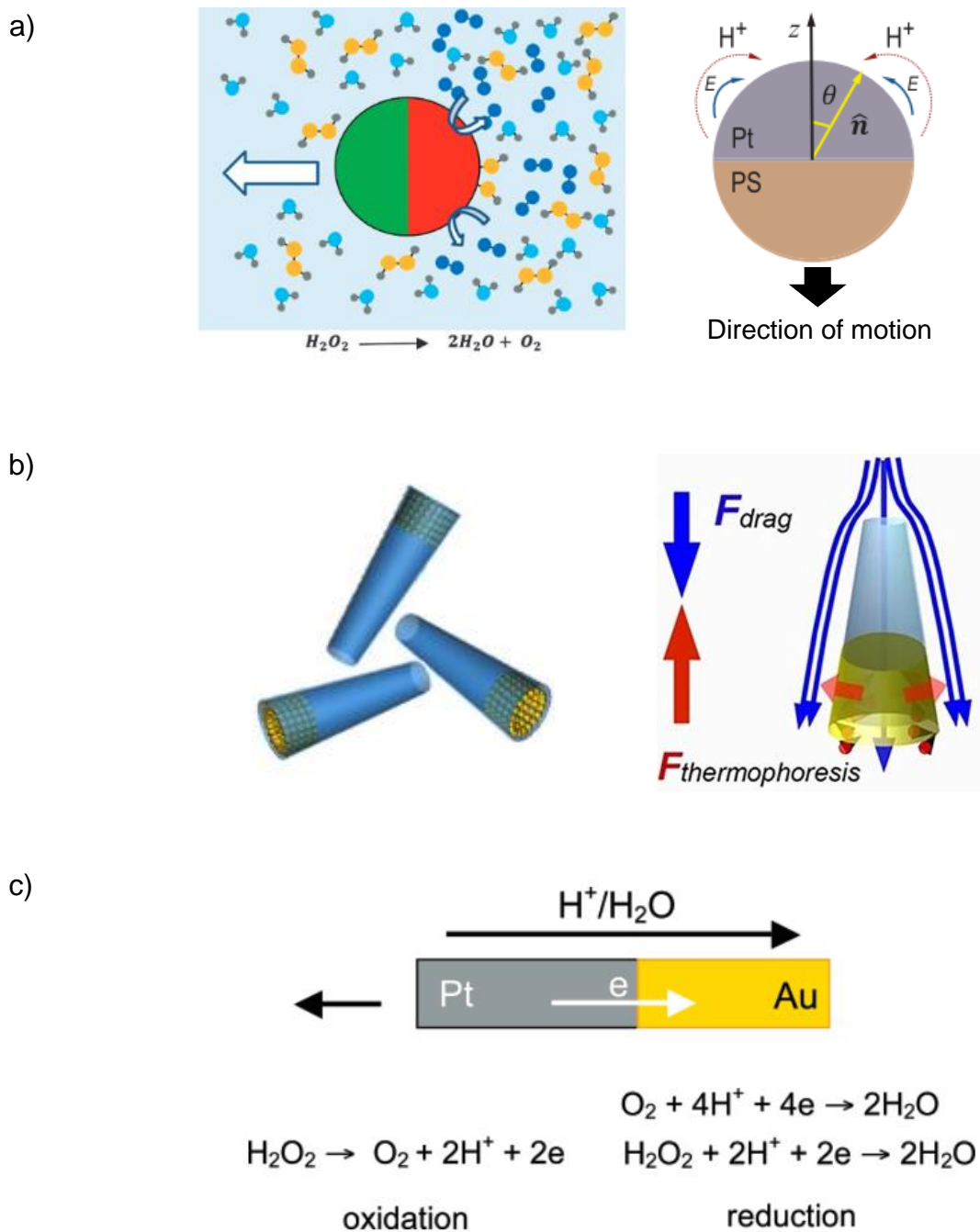


Figure 1-2: Examples of experimentally tested micron scale motors. a) spherical Pt-PS Janus swimmers^{21,22} b) Si-Au photothermal micro swimmers²³ c) Pt-Au Janus nano rods²⁴.

The Ebbens group synthesised 1.9 μm fluorescent Pt-PS spherical swimmers (Figure 1-2a) which achieved high ballistic velocities of up to 15-16.5 $\mu\text{m}\text{s}^{-1}$. Motion is directed towards the PS side, via a self-electrophoretic mechanism relying on hydrogen peroxide as fuel. Spheres were synthesised using a physical vapour deposition technique to

achieve defined hemispheres of platinum²¹. A gradient in platinum thickness, and therefore reaction rate, from the pole to the hemisphere of the sphere generates a flow of electrons across the colloid. The resulting electric field generates self-electrophoretic motion in the direction opposite to the electric field as seen in *Figure 1-2a*²².

8 ± 2 μm silica tubes functionalised with Au Np's (*Figure 1-2b*)²³ were tested by Rao et al. This fuel free system relies on the photothermal effect of gold nanoparticles to achieve nano-propulsion. A laser is used to heat the gold nanoparticles creating a thermal gradient inside the tube, this results in thermophoretic motion directed away from the gold end of the tube. Speeds range from 0.8–20 μms^{-1} , depending on the intensity of the laser used. Whilst a fuel free system is desirable, the requirement of an external source to keep the swimmers in motion would result in limited applications of use.

Wang et al. devised striped nano-rods (*Figure 1-2c*) consisting of approximately equal parts of gold and platinum. The rods move autonomously towards the direction of the platinum end via a self-electrophoretic mechanism. When the platinum end of the rod is exposed to peroxide fuel, the peroxide is oxidised producing protons and electrons. These protons and electrons are then consumed at the gold end causing an electron flow from platinum to gold (*see Figure 1-2c*). Motion is then directed in the opposite direction of this electric field; with the platinum end forward. It is worth noting that the flow of protons and electrons in this system is in the opposite direction than the Pt-PS system and thus the motion is directed towards the platinum end rather than away from it. Speeds were reported up to 20 μms^{-1} in 2-3% H_2O_2 fuel. Mean squared displacement data has not been provided for this or similar papers by the group, making it difficult to definitively assume that nano-propulsion is taking place²⁴.

These mechanisms will be discussed in more detail in *section 1.4*.

1.4 Mechanism of propulsion

There have been many mechanisms proposed for the self-propulsion of active colloids such as osmotic pressure, self-diffusiophoresis, bubble production, interfacial tension gradients and self-electrophoresis²⁵. It is now widely accepted that the dominant mechanism is self-electrophoresis^{18,26,19,27} in low micron – nanometre sized systems which rely on platinum as a catalyst. Note that bubble propulsion becomes a significant mechanism for larger, more reactive devices and tubular micromotors^{28,29}.

1.4.1 Phoresis

Phoresis is a broad term describing the migration of particles in a fluid or gel in a gradient. Common types of phoresis include diffusiophoresis, thermophoresis and electrophoresis. In diffusiophoresis the driving force for motion comes from a concentration gradient of a reactant or product in solution³⁰. Thermophoresis describes the “migration of colloidal particles in solution in response to a macroscopic temperature gradient”³¹, often produced locally by an exothermic reaction taking place^{16,32,33}. Movement of charged particles in response to a uniform imposed electric field is known as electrophoresis. A negative charge is applied, and anionic particles move towards a positive charge whilst cationic particles move towards a negative charge³⁴. This phenomenon is most commonly exploited for separation of suspended particles based on their size, charge or binding affinity³⁵. More recently it has been discovered that the electric field can be produced locally by an electrochemical reaction in order to drive the self-propulsion of active colloids, this is called self-electrophoresis³⁶.

1.4.1.1 Self-electrophoresis

In bi-metallic systems, like the example discussed in *Figure 1-2c*, the decomposition reaction of H_2O_2 by platinum becomes an electrochemical reaction when coupled with an appropriate cathode, gold.

The oxidation of H_2O_2 at platinum generates protons in solution and electrons on the platinum surface (*Figure 1-3*). The reduction of H_2O_2 at the gold electrode consumes these protons and electrons. This creates an ion flux from platinum to gold, generating a local electric field which drives the motion of the negatively charged particles³⁷.

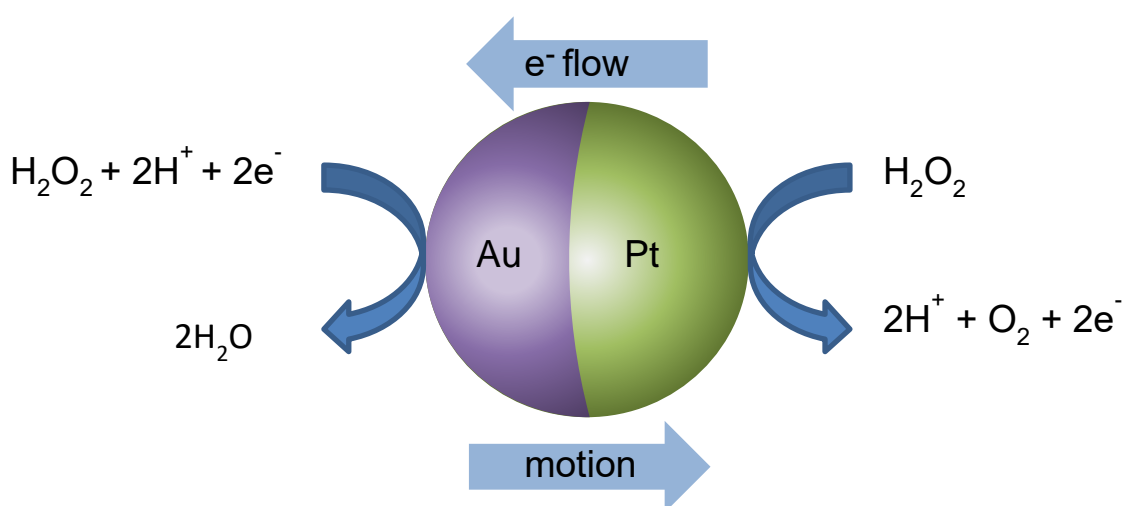


Figure 1-3: Schematic of the reaction leading to self-electrophoretic motion in Pt-peroxide systems.

In metal-insulator systems, like the example discussed in *Figure 1-2a*, the self-electrophoretic mechanism is dependent upon a systematic variation of the reaction rate of Pt with H_2O_2 . This arises due to a non-uniform covering of the colloid with the catalytic metal. As the platinum is deposited by a “line of sight” method there is a thicker coating of the metal at the pole than the equator²².

This mechanism of motion significantly reduces the practical applications of active colloids as it has been found that the presence of salt, even at very low concentrations, can interfere with motion in both bimetallic and metal-insulator systems. Salt masks the charges of the colloids and they no longer move in the generated electric field³⁷. As blood and the majority of biofluids contain salt ions³⁸, they would not be propulsion supporting mediums. This, along with their relatively large size rules out most in-vivo applications and so the focus is predominantly applications in in-vitro testing, microfluidics, and lab on chip style devices³⁹.

The remainder of the introduction now reviews in detail, three key themes that are relevant to this thesis, focusing on examples that mainly feature catalytic Janus propulsion. Firstly, a review of attempts to control the motion of propulsive colloids of any shape, with emphasis on catalyst patterning (chapter 5). Secondly, the existing knowledge around asymmetrically propulsive colloids (chapters 3 and 6), in particular ellipsoids the focus of much of this work. And finally, an overview of the ways in which fluid flow can influence the behaviour of motile colloids, another strong focus of this work (chapter 4).

1.5 Motion control of active colloids

Whilst there are many published instances of successfully propelling spherical and rod-shaped micro-swimmers, due to their vulnerability to Brownian fluctuations, the motion achieved is often somewhat random. The motion can be directed externally using external fields such as a magnetic field^{40,41}. Use of these fields removes the autonomy of the individual swimmers and is rarely practical for real life applications. Further investigations have begun into controlling the direction and increasing persistence length by changing either the colloid geometry or the geometry of the catalytic patch⁴². Use of chemically patterned substrates also show promising results for directing the motion of autonomous catalytic micro-swimmers⁴³.

1.5.1 Motion control by changing catalyst geometry.

During initial investigations into catalytic active colloids, it was assumed that a perfect hemispherical (or other symmetrical half coating) coating was needed to achieve directed motion. More recently it has been shown that non symmetrical catalyst cap shapes can be used to produce a variety of desirable types of motion in spherical swimmers.

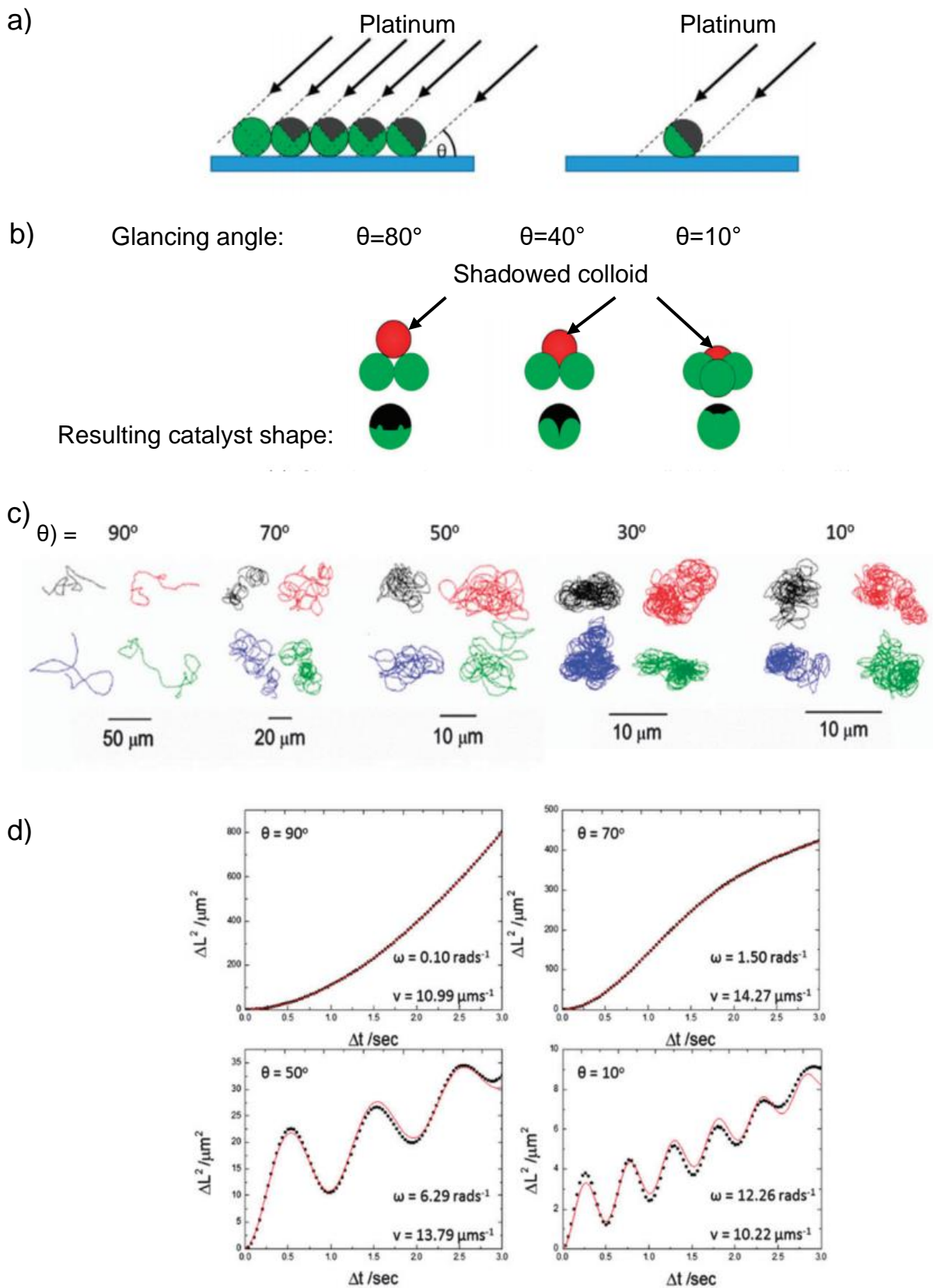


Figure 1-4:a) schematic showing shadowing or a lack of, for colloids in a closely packed colloidal crystal(left) and well-spaced colloids (right) during Pt deposition. b) predicted cap shapes for closely packed colloids with varying θ , c) trajectories of resulting spinning swimmers with corresponding MSD data in d) from Archer et al. ²¹

Investigations into varying the size and shape of the catalytic patch proved successful in controlling the angular velocity of spherical electrophoretic swimmers.²¹ The platinum coating was systematically varied by depositing the platinum from different angles onto a closely packed colloidal crystal, illustrated in *Figure 1-4a*. This creates shadowing in the line-of-sight deposition leading to well defined non-hemispherical coatings. It was found that decreasing angles of deposition produced smaller platinum patches and these swimmers produced the highest angular velocities, up to 16.46 rads^{-1} .

The electrophoretic model for spherical Pt-PS swimmers relies on a variation in Pt thickness from the pole to the equator of the colloid. In a hemispherical coating this leads to rotationally symmetrical pole-equator reaction rate gradients and generates ballistic electrophoretic motion with little to no rotational component. When the glancing angle is employed, the platinum coating is no longer distributed in a hemisphere and the reaction rate gradients across the swimmer are no longer rotationally symmetrical. It is suggested that this asymmetry in reaction rate gradients introduces a rotational component to the phoretic propulsion and produces swimmers with comparatively high angular velocities.

For much larger ($30\mu\text{m}$) bubble propelled catalytic swimmers, similar investigations have been conducted regarding catalytic patch size. The colloids were fully coated in platinum and then masked with chromium to reveal a range of catalytic patch sizes. This revealed an opposing effect to the glancing angle deposition of smaller phoretic swimmers, where smaller catalytic patches produced more directional ballistic motion, see *Figure 1-5*, than the standard Janus configuration, at a great cost to their velocity. When fully coated with catalyst, the group found that their bubble-propelled swimmers produced very high instantaneous velocities of up to 1.8mms^{-1} however the trajectories produced were random and lacked directionality⁴².

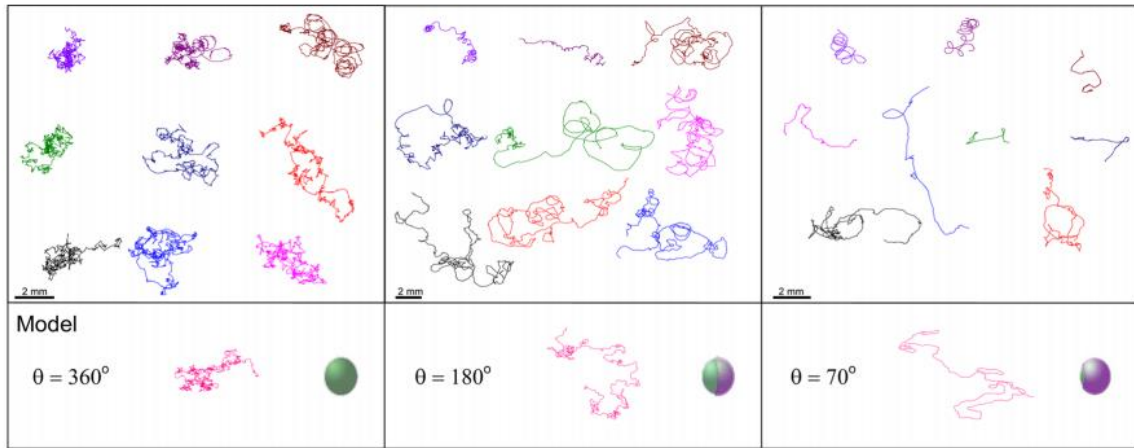


Figure 1-5: Trajectories of bubble propelled spherical swimmers with decreasing catalytic patch size, left to right. From Gregory et al.⁴²

1.5.2 Asymmetrical swimmers

Due to the difficulty in synthesising colloids of a specific non-spherical shape, most of the literature investigating non-spherical swimmers is theoretical. This will be discussed in section 1.5.3, whilst experimental literature covers only simple, rotationally symmetrical non-spherical shapes such as rods. Some more complicated geometries have been attempted in recent years with promising results.

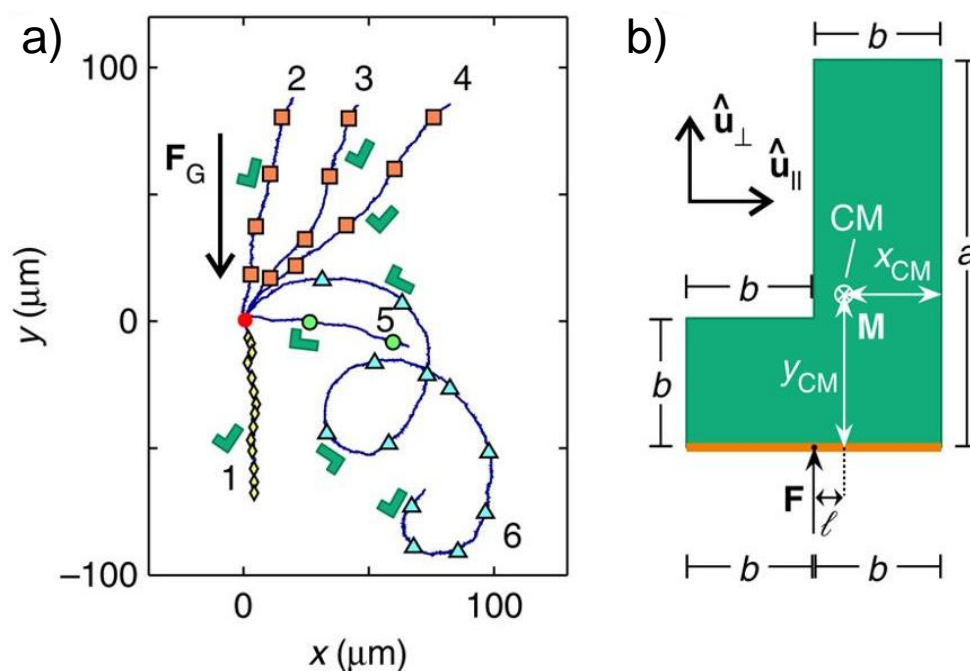


Figure 1-6: a) Experimental trajectories measured at the same angle. Increasing number corresponds to greater illumination. b) Diagram of L-shaped swimmer⁴⁴.

The Hagen group experimentally tested L-shaped swimmers produced by soft lithography with arms 6 and 9 μm respectively and a thickness of 3 μm (Figure 1-6). A gold cap on the front face of the short arm is illuminated to cause a local heating gradient. This allows the swimmers to propel self diffusiophoretically in the direction perpendicular to the plane of the metal cap⁴⁴.

During testing the sample cell was tilted by a known angle to achieve control of the gravitational force. Experimental trajectories can be seen in *Figure 1-6a*. The study provides valuable information about the motion seen in non-standard shape swimmers, however the reliance on an external light source to achieve propulsion is not ideal for the proposed applications of active swimmers.

1.5.2.1 Ellipsoidal Micro-swimmers

There has been an interest in recent years which focusses on the dynamics of ellipsoidal micro-swimmers as they can be synthesised in monodisperse populations relatively easily by stretching spherical polystyrene colloids. The effect of the colloids aspect ratio⁴⁵ and their behaviours, specifically near an interface⁴⁶, are of great interest. As of yet few of these predictions have been experimentally tested, likely due to the difficulty in applying the catalyst to the ellipsoid in the preferred orientation, along the short axis.

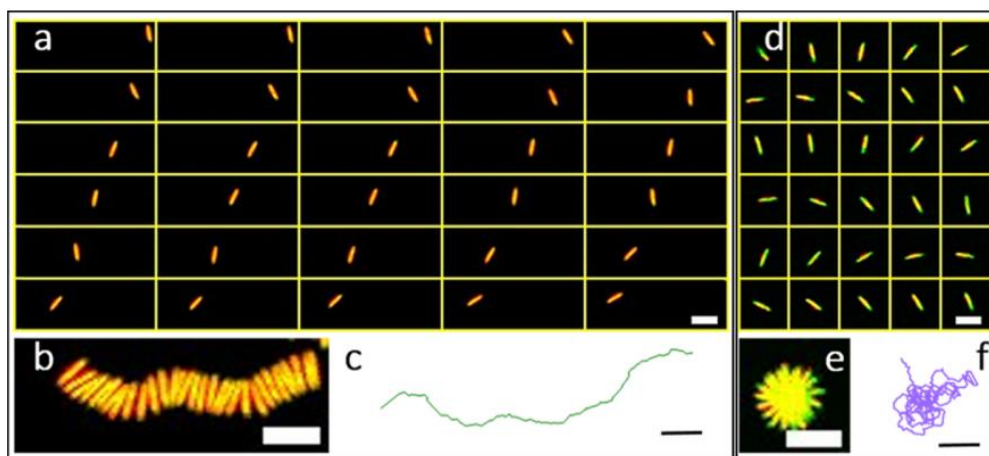


Figure 1-7: Time series images of Janus ellipsoids translating ballistically and rotationally. (from Shemi et al.⁴⁷)

Recently, Solomon and Shemi published a study on prolate Janus ellipsoids, half coated along their major axis. The study maps the effect of the aspect ratio on translational and angular velocity⁴⁷, the first work of its kind to date.

The group discovered a range of motion from purely ballistic to rotational motion, directed perpendicular to the major axis, illustrated in *Figure 1-7*. It was also reported that both angular and translational velocity increases as the aspect ratio of the ellipsoid increases.

The ellipsoidal micro-swimmers swim in a way that is analogous to their spherical counterparts, and it is likely that they share the self-phoretic mechanism of motion. It is not yet known for ellipsoidal micro-swimmers whether motion is directed away from or towards the catalytic cap, which is indicative of certain propulsion mechanisms, meaning that assignment of a mechanism of motion is currently speculative.

If the direction of motion generated is away the platinum cap, this would be highly suggestive of an electrophoretic or bubble propelled mechanism, as other popular mechanisms like diffusiophoresis tend to generate motion towards from the platinum side. The absence of bubbles occurring on the swimmer surface, presence of rotational quenching of a swimmer's orientation when near a substrate⁴⁸ and a sensitivity to salt²² would help to distinguish a self-electrophoretic mechanism from a bubble propelled one, with the former being highly sensitive to salt contamination.

The shape asymmetry of ellipsoids gives the potential for different applications than the more commonly seen spherical swimmers. Ellipsoids have more fluid interaction and disturb a larger local fluid field which, when spinning about their major axis, allows for better stirring on the micro level. The increased surface area of this geometry also gives them a natural ability to convey more cargo in transport applications.

1.5.3 Theoretical predictions of asymmetric shapes

Theoretical simulations are useful to guide experimental procedures and give a general idea of what to expect when testing what has been proposed.

The results from a variety of theoretical techniques used to simulate active swimmers and their interactions will be used as a guide in the design of experiments and the analysis of results.

Whilst there are geometries available in the theoretical literature that have yet to be tested experimentally, the complexity of mathematics required to run such simulations limits the range of shapes that have been modelled. This includes predominantly rotationally symmetrical geometries such as rods, discs, ellipsoids, and spindles.

There have been attempts in recent years to investigate more complicated geometries, such as the L shaped swimmers produced by the Hagen group.

Prior to experimental testing, the Hagen group⁴⁴ used Langevin equations to predict the centre of mass (position) and orientation of their micro swimmers. Langevin equations are stochastic differential equations used in statistical physics to describe the time-dependant evolution of the 'degrees of freedom' of a system. The degrees of freedom are usually a group of macroscopic variables moving slowly compared with microscopic variables of the system which are responsible for the stochastic nature of the equations. They were originally used to model Brownian motion of microscopic particles in a fluid⁴⁹, where the position of the particle is the degree of freedom desired. The particle position varies quickly compared to the mass and energy of the system. The division of the degrees of freedom into fast and slow-moving variables is an essential condition of Langevin equations.

The group used *Equation 1-2* and *Equation 1-3* in order to demonstrate that shape anisotropy can induce gravitaxis⁴⁴.

$$\text{Equation 1-2: } \dot{\mathbf{r}} = \frac{P^*}{b} (\underline{\mathbf{D}}_T \hat{\mathbf{u}}_{\perp} + l \mathbf{D}_c) = \beta \underline{\mathbf{D}}_T \mathbf{F}_G + \zeta_r$$

$$\text{Equation 1-3: } \dot{\varphi} = \frac{P^*}{b} (l D_R + \mathbf{D}_c \hat{\mathbf{u}}_{\perp}) + \beta \mathbf{D}_c \mathbf{F}_G + \zeta_{\varphi}$$

$\dot{\mathbf{r}}$ = Centre of mass (position)

$\hat{\mathbf{u}}_{\perp}$ = Direction

β = Inverse effective thermal energy $\beta=1/(k_B T)$

$\dot{\varphi}$ = Orientation

D_R = Rotational diffusion coefficient

P^* = Strength of propulsion (dimensionless)

$\underline{\mathbf{D}}_T$ = Translational short-time diffusion tensor

l = Effective lever arm

\mathbf{D}_c = translational-rotational coupling vector

\mathbf{F}_G = Gravitational force

$\zeta_{\varphi} + \zeta_r$ = Brownian noise terms

b = Characteristic length of L-shaped particle

Using the experimentally obtained diffusion coefficients, coupling coefficients and propulsion strength, *Equation 1-2* and *Equation 1-3* were used to produce theoretical data which is illustrated in *Figure 1-8*. Noise free theoretical example trajectories are as expected based on the experimental trajectories seen in *Figure 1-6*, as are the predictions for orientation at a given propulsive strength.

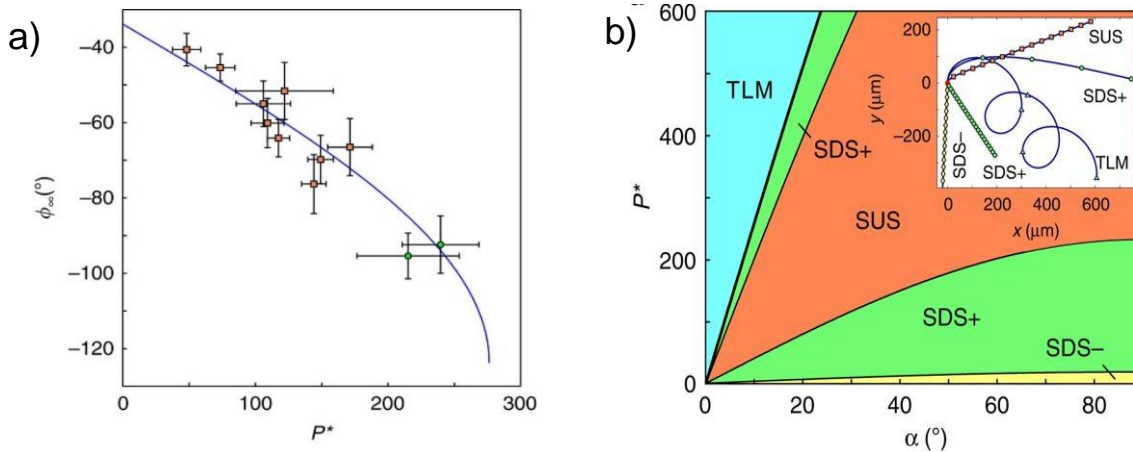


Figure 1-8: a) Experimental data for P^ vs ϕ , the blue curve shows the theoretical data from equation 5. b) State diagrams for each type of motion with illustrations of theoretical data for swimmer trajectories given by equation 4⁴⁴.*

The Lugli group⁵⁰ used Dissipative particle dynamics (DPD) to predict the behaviours of catalytically active micro-rods, disks and spheres (*Figure 1-9*)

Dissipative particle dynamics (DPD) is a mesoscopic stochastic simulation technique initially devised by Hoogerbrugge and Koelman⁵¹ to improve upon the hydrodynamic time and space scales available with molecular dynamics (MD). MD uses interatomic potentials or molecular mechanics force fields to predict forces between particles and their potential energies of systems containing high densities of particles, which are too time consuming to be modelled analytically.

DPD involves a set of particles, modelled as “soft beads” which represent either a portion of a particle or a fluid element, moving in continuous space and discrete time. The evolution of the positions and momenta of all interacting beads over time are governed by Newton’s equation of motion for the particle, i . (*Equation 1-4*)

$$\text{Equation 1-4: } m_i \frac{dv_i}{dt} = f_i = \sum_{j \neq i} F_{ij}^C + \sum_{j \neq i} F_{ij}^D + \sum_{j \neq i} F_{ij}^R$$

F_{ij}^C = Conservative force

F_{ij}^D = Dissipative force

F_{ij}^R = Random force

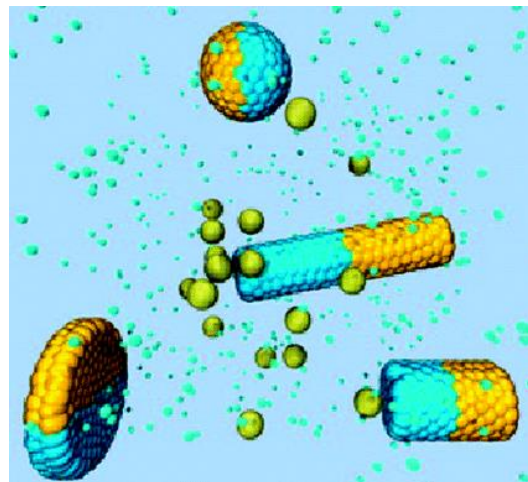


Figure 1-9: Schematic of rods disks and spheres modelled by the Lugli group⁵⁰.

The Lugli simulation addresses effective propulsion in mesoscopic swimming systems based on ‘good’ and ‘poor’ solvent interactions arising from a chemical reaction across a Janus particle. These ‘poor’ and ‘good’ solvent interactions are quantified based off the Flory-Huggins mixing parameter (χ_{ij}) where a compatible system has a Flory-Huggins parameter of 25, whereas an oil-water system would have a Flory-Huggins

parameter of 80. The group use $X_{ij} = 25$ for the interaction between fluid particles and $X_{ij} = 12.5$ for the interactions between fluid and the swimmer. The products, P, interact with the other fluid particles with $X_{ij} = 25$ and with a highly repulsive value, $X_{ij} = 100$, with the swimmer.

The chemically active side converts a reactant fuel with 'good' interactions into a product with 'poor' interactions. This product rapidly leaves the particle surface which is consequently propelled in a non-Brownian manner. This system addresses, theoretically, the shape dependent properties of catalytic swimmers by predicting their effective diffusion coefficient (*Equation 1-5*) as a function of reactant concentration. D_{eff} increases with increasing fuel concentration. The centres of mass were recorded during the simulation, and the displacement, velocity and orientation were calculated and averaged.

Equation 1-5:
$$D_{eff} = D_0 + \left(\frac{1}{6}v^2\tau_R\right)$$

D_{eff} = effective diffusion coefficient

D_0 = diffusion coefficient in pure solvent

v = velocity

τ_R = rotational diffusion time

The group found that the rod has the biggest increase in velocity with fuel concentration due to their increased catalytic surface area compared with disks and spheres, as seen in *Figure 1-10a*. This is consistent with experimental findings.

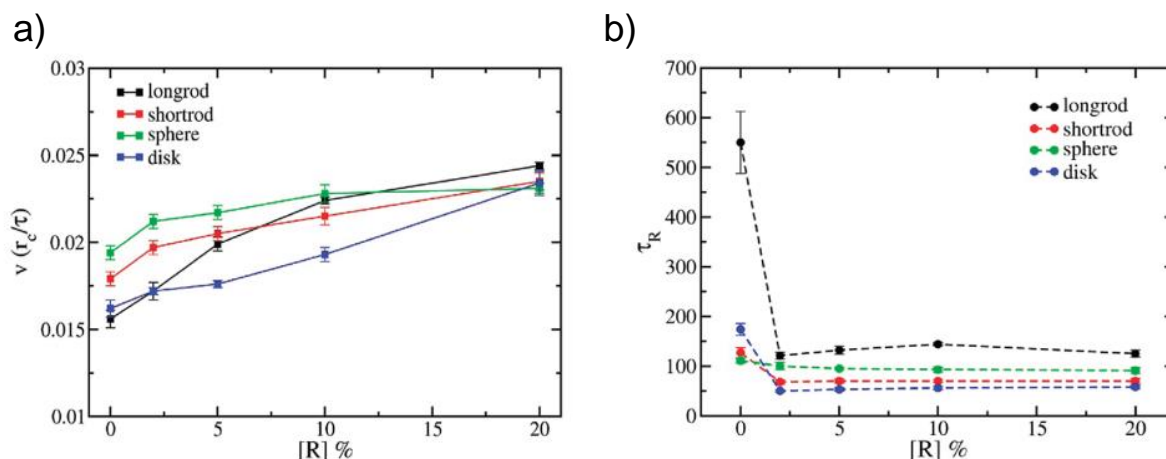


Figure 1-10: a) Propulsive velocity (v) as a function of reactant concentration, for long rod (black), short rod (red), sphere (green), and disk (blue); v is in dimensionless DPD units. b) Rotational time (τ_R) as a function of reactant concentration, for long rod (black), short rod (red), sphere (green), and disk (blue). τ_R is in dimensionless DPD units.

Most importantly, the group reported that the diffusion coefficient and rotational time are functions of the colloid shape and have a large impact on the angular velocity and direction of the particle motion⁵⁰. All swimmers showed a reduction in rotational time with increasing fuel concentration during the reaction as compared to in pure solvent indicating that the reaction induces rotational motion.

As seen in *Figure 1-10b*, the long rod had the largest reduction in rotational time, but even after this reduction had the highest rotational time. This indicates that the propulsive ballistic motion of the rod persists for longer and has less rotational component. The reductions in τ_R for the short rod and disk are similar in magnitude and

much less significant than for the long rod, whilst the reduction in τ_R for spheres starts and remains low. These findings can be very useful to groups looking to produce catalytic swimmers with tailored velocities and rotational times by altering the geometry of the swimmer.

1.5.3.1 Theoretical predictions for ellipsoidal swimmers

The Golestanian group⁴⁵ have used analytical theory, which is a fine-grained technique used to predict physical outputs such as velocity of a system over a period of time, using a purely mathematical approach to calculate the propulsion speeds of self-phoretic ellipsoids as a “function of their slenderness ratio, ϵ ”⁴⁵ (*Equation 1-6*).

Equation 1-6:
$$\epsilon = \frac{\text{Cross sectional diameter}}{\text{Length of major axis}}$$

Calculation of propulsion speeds is accomplished by considering a colloid with heterogeneous catalytic surface. The colloid produces or consumes a chemical fuel on its surface in a varied manner. This generates a local concentration gradient of the fuel near the colloid.

The steady-state velocity of the colloid, generated by the concentration gradient, is calculated by solving the coupled equations of motion of the concentrations of products and reactants and local conservation of momentum. Boundary conditions on the colloid surface are accounted for⁵².

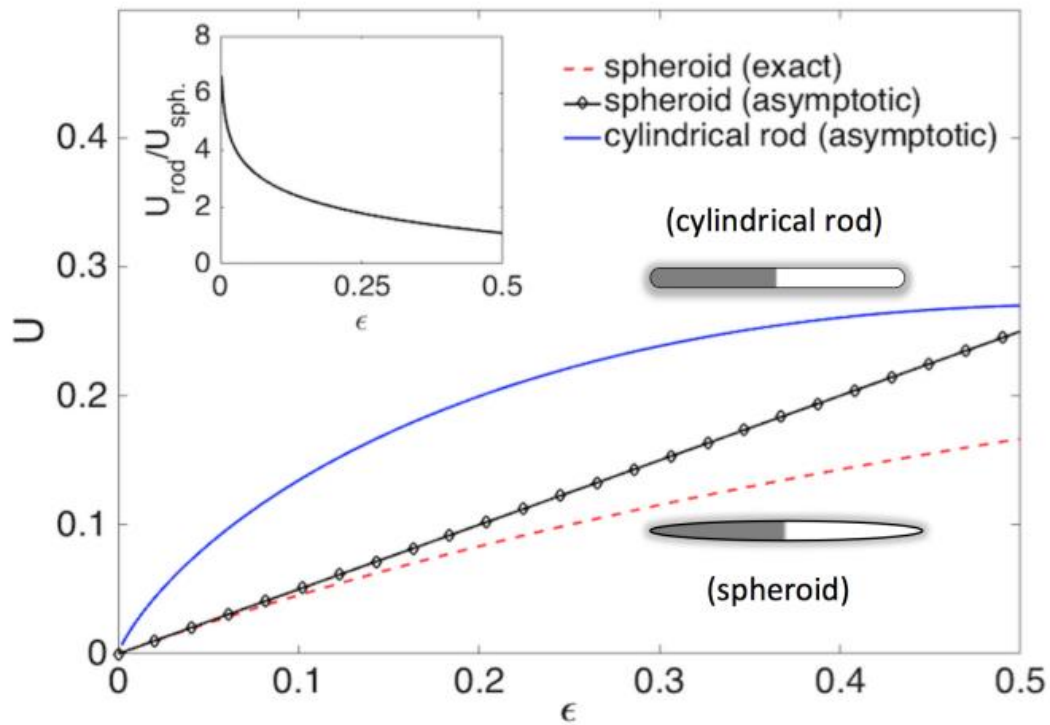


Figure 1-11: Comparison of swimmer propulsion speeds of different shaped colloids depending on their slenderness ratio⁵².

The group found that the finer details of the swimmer shape have a significant impact on the propulsive speed with variances caused by both the slenderness ratio and the bluntness of the ends of the ellipsoid. In Figure 1-11 it is shown that the greatest speeds will be achieved with blunt ended rod-like swimmers with larger slenderness ratios.

Uspal et al. modelled similar swimmers to the Golestanian groups blunt-ended-spheroids. The group used “analytical theory based on the point-particle approximation”⁵³ to quasi-quantitatively describe the dynamics of the system. They use this method to predict the interactions of spheres and blunt ended ellipsoidal swimmer interactions with a chemically patterned wall, where both regions of the substrate have a repulsive effective interaction with the solute molecules. The region to the right of the step (grey) has a stronger repulsive interaction.

For spherical colloids at sufficiently low velocities ($U^{sd}/U_0 = 0.1$), the swimmer docks close to the boundary seen in *Figure 1-12a*, on the less repulsive side and then follows this edge. At higher velocities ($U^{sd}/U_0 = 0.4$) the swimmer passes over the step, as seen in *Figure 1-12b*.

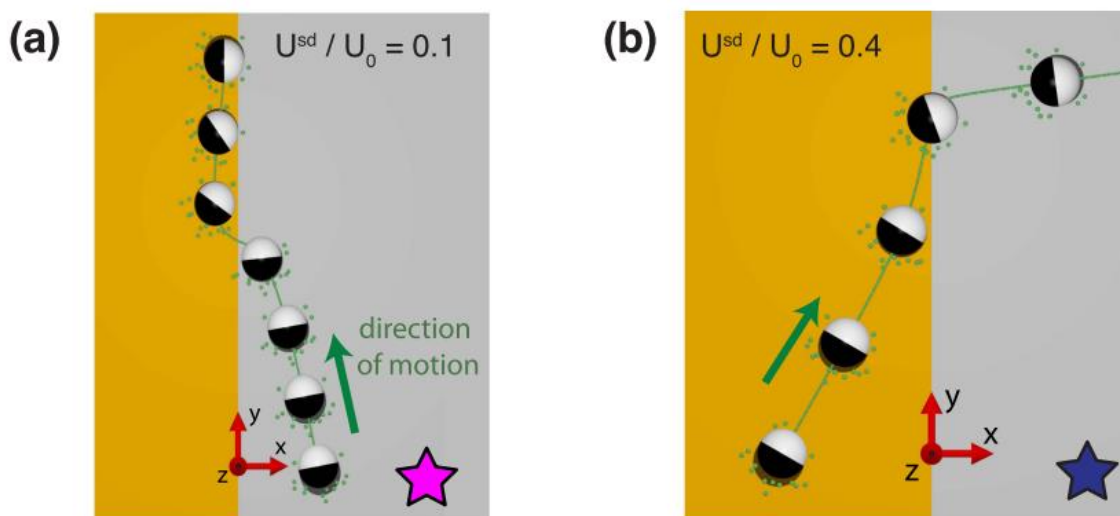


Figure 1-12: a) Schematic of a spherical swimmer at low speed ($U^{sd}/U_0 = 0.1$) following the step on a chemically patterned wall. b) Schematic of a spherical swimmer at high speed ($U^{sd}/U_0 = 0.4$) passing over the step on a chemically patterned wall.

For ellipsoidal swimmers the alignment effects are more pronounced. At low speeds ($U^{sd}/U_0 = 0.12$) there is a stable ‘edge-following’ state in which the particle remains at a fixed distance and angle, almost parallel to the step edge, but tilted slightly towards the more repulsive region, this is illustrated in *Figure 1-13a*.

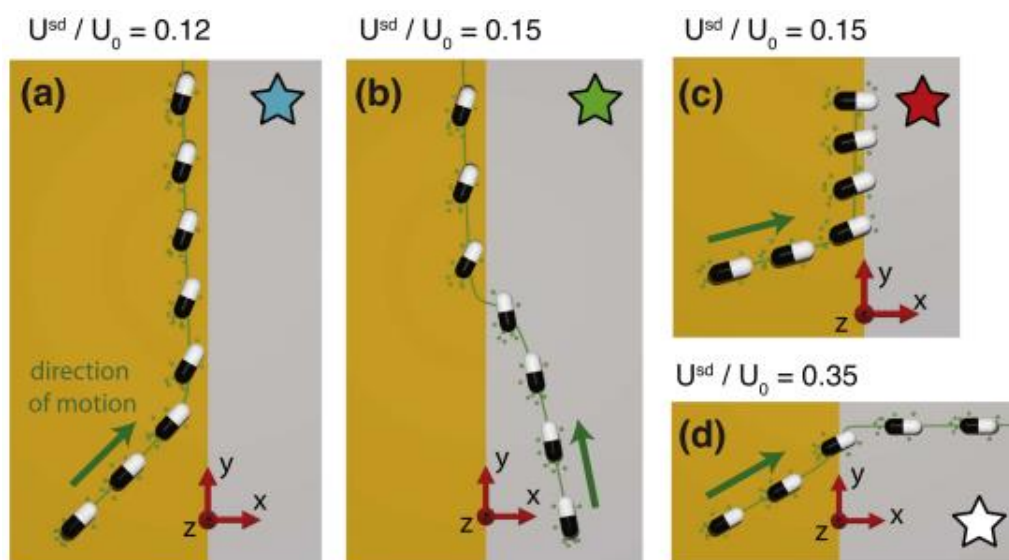


Figure 1-13: Schematic of ellipsoidal swimmer following a chemically patterned step.

*From Uspal et al.*⁵³

At a slightly higher speed ($U^{sd}/U_0 = 0.15$) the edge-following state co-exists with a stable docking state depending on the side and angle of approach to the chemical step. When approaching from the more repulsive side, the swimmer passes over to the less repulsive side and then follows the edge in the same way as the slower swimmer (*Figure 1-13b*). When the swimmer approaches the edge from the less repulsive side, it docks almost perpendicular with the edge and motion continues at this orientation (*Figure 1-13c*).

As with the spherical simulation, at high speeds ($U^{sd}/U_0 = 0.35$) the swimmer passes over the step in any situation where the direction is pointing towards the chemical step (*Figure 1-13d*).

The study demonstrates the possibility for 'edge-following' ellipsoidal swimmers. The swimmer propels along a chemically patterned wall at a consistent distance and orientation. If these phenomena could be recreated experimentally in a controlled manner it would open up the practical applications of micron scale swimmers.

1.6 Flow

When working with micron scale catalytic systems in fluid, a regularly occurring issue is that of fluid convection, either as a by-product of the chemical reaction driving the motion, or as a consequence of the application they are being used for. In fact, fluid is almost never fully static and micron scale swimmers are disproportionately affected by even small currents. It is important to understand how swimmers respond to different flow fields in order to optimise them for real life applications. The use of active swimmers in vivo would be subject to blood flow around the body, as swimmers used for environmental remediation may be subject to river currents, and in systems with large numbers of swimmers they would be subject to forces generated by other nearby swimmers.

Fluid convection that is induced by chemical activity can be driven by heat evolution, electron flow or differences in density of the chemical reactants and products in a catalytic reaction. Due to the small size of the swimmers in question, these fluid convection effects can override the autonomous motion desired for these devices. In laboratory situations, the number of swimmers in a sample can be controlled to reduce

or eliminate flow effects, however this hinders research into how the swimmers behave collectively and for most applications it is likely that many swimmers would be needed.

In Pt/peroxide systems, the motion is driven by the decomposition of H_2O_2 by platinum into water and oxygen. As the products (H_2O and O_2 ; densities 0.998 gcm^{-3} and 0.00143 gcm^{-3} respectively) of this reaction are less dense than the reagents (H_2O_2 ; density 1.45 gcm^{-3}), density differences are generated around the colloids which causes a rising convective flow. Due to the imposed boundary of the sample cuvette walls the convective flow circulates back around forming a flow field that follows the cuvette geometry, illustrated in *Figure 1-14*. As the colloids are significantly more dense than the reactants/products, once coated they localize at the bottom plane of the cuvette and the flow moves upward⁵⁴.

The flows generated by swimmers can be harnessed and used as micro-pumping devices, or even used to direct the swimmers via artificial Rheotaxis.

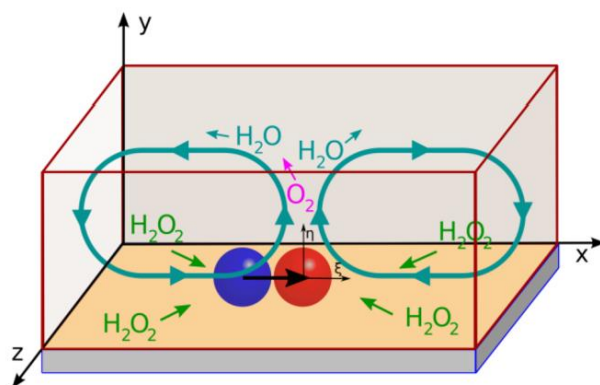


Figure 1-14: Schematic of a cyclical density driven flow produced by the decomposition of hydrogen peroxide by catalytic swimmers. From Balasz et al. ⁵⁴

1.6.1 Micro-pumping

The use of catalytic swimmers or substrate patches can produce well defined flow fields that can be harnesses to transport or pump inactive tracer particles around microfluidic devices.

The Balasz group modelled a system where active colloids which were able to generate a density driven flow field were mixed with passive colloids. The active and passive particles form organised clusters which can be driven along the bottom of a micro-channel by the flow. In this situation the active colloids act as chemical pumps and motion of the passive tracer particles is driven by the resulting flow field⁵⁴.

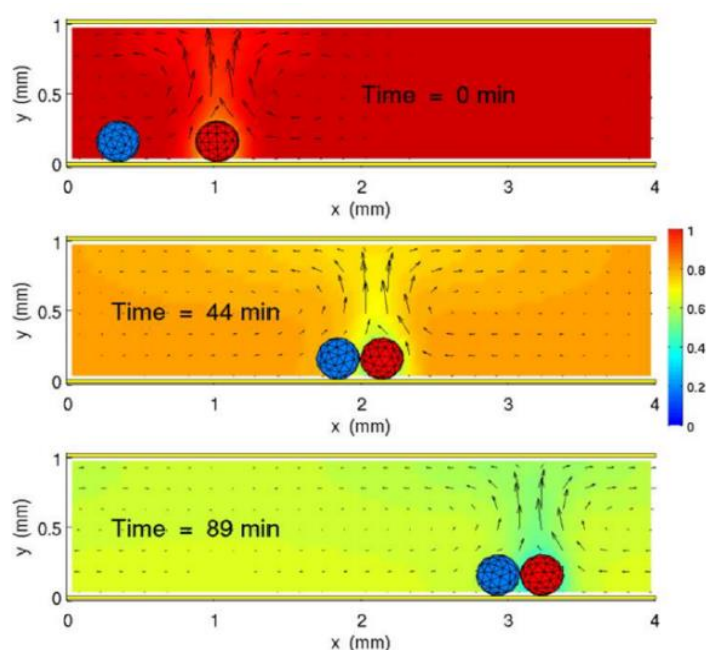


Figure 1-15: Model of the fluid flows (arrows) generated by chemical decomposition of peroxide around a mobile (red) particle which drags a (blue) tracer particle blue from left to right. ⁵⁴

The model is based on the decomposition of hydrogen peroxide and the system relies upon the catalyst coated particle having a higher density than the surrounding fluid and

sedimenting to the lower boundary of the sample holder. Whilst the less dense products and uncoated tracer particles rise to the upper boundary driving a cyclical flow field in a confined sample holder.

Farniya et al. demonstrated that in addition to the 'pumping' effect of Pt/peroxide systems, the introduction of gold turns the reaction into an electrochemical cell. The group used circular patches of platinum 20-50 μm in diameter patterned onto gold films to manipulate negatively charged silica colloids into well packed colloidal crystals⁵⁵.

This effect occurs in sequential steps. Initially, after the pump is 'turned on', an excess of protons are generated at the anode (gold) and then consumed at the cathode (platinum). As a result, an electric field pointing inwards towards the platinum disk is generated which drives fluid flows in the same direction. Negatively charged silica

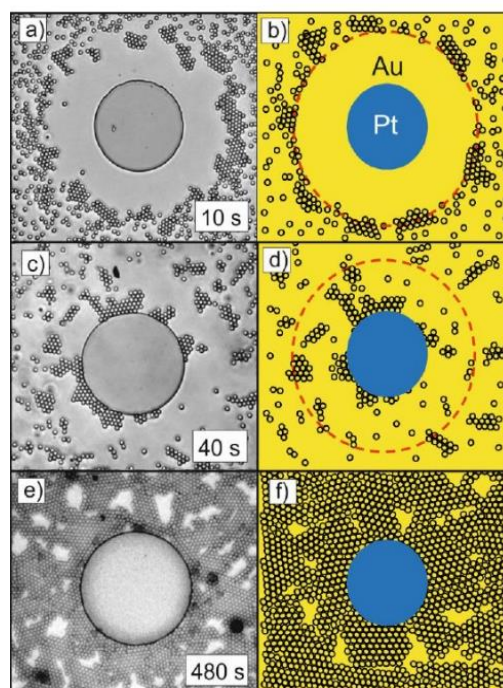
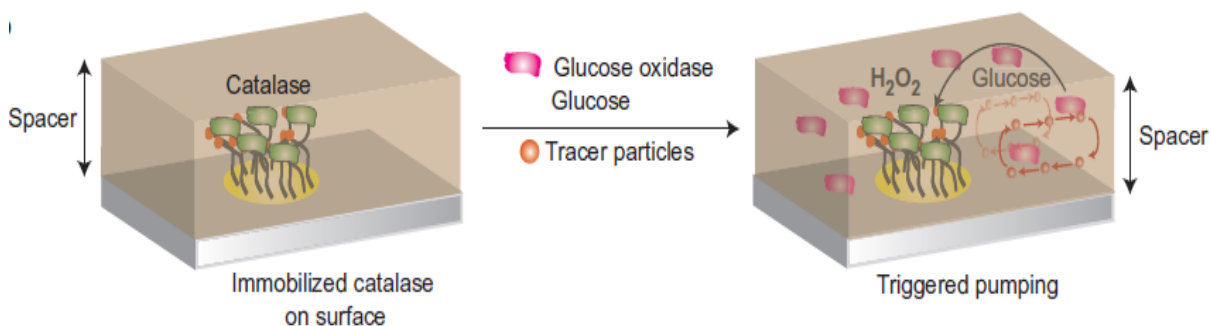


Figure 1-16: Images showing the organisation of tracer colloids into an organised crystal. an electric field pointing from gold to platinum drives a fluid flow in this direction⁵⁵.

colloid are initially repelled by this electric field leaving a band around the Pt patch which is free of colloids.

Over time the excess production of protons leads to a decrease in the pH of the fluid around the colloids and protonation of the colloids alters their zeta potential. The reduced charge of the colloids promotes colloid interactions and clusters begin to form. As these clusters form and the pH decreases further, the repulsion between the clusters decreases and they arrange into well packed crystals around the Pt disk, see *Figure 1-16*.

In 2014 the Sen group showed that enzymes anchored to substrates can be used to produce catalysis induced density driven flows. The group attached various enzymes to glass substrates by patterning gold patches onto PEG covered slides and then using thiol chemistry to anchor the chosen enzyme to the gold patch⁵⁶.



*Figure 1-17: Enzyme powered micro-pumps designed by Sengupta et al.*⁵⁶

Catalase decomposes hydrogen peroxide into water and oxygen. When the fuel is added with tracer particles, the tracer particles move towards the functionalised surface indicating that fluid is pumped inwards. This effect is also seen for lipase and glucose oxidase catalysts. The products of these catalytic reactions are less dense than the reactants, so they rise to the upper surface of the container resulting in a cyclical flow.

1.6.2 Orientation phenomena of active colloids in flow fields

Alongside investigations into pumping colloids, groups have started to investigate the dynamics of non-pumping colloids in externally imposed flows which result from mechanical rather than chemical sources^{57–62}. These imposed flow fields must be non-pulsatile, extremely stable, and very low speeds. Few methods of producing flow are able to meet these criteria:

Pressure pump: controls the flow rate by applying pressure to a sealed fluid reservoir. The pressure applied by the air above the liquid surface pushes the liquid out of the reservoir through microfluidic tubing at a constant rate.

Syringe pump: Syringe Pumps are widely used in microfluidic applications. Once a syringe is filled with the liquid of interest, it is placed on the syringe pump, based on a moving piston which is pushed (or pulled) by a motor. The force applied on the syringe piston by the motor's rotation of a screw corresponds to the flow rate. Syringe pumps generally give less control over the flow rate than a pressure pump and are limited in volume by the syringe capacity.

1.6.2.1 Artificial Rheotaxis

There have been several cases of confirmed rheotaxis in gold/platinum nanorods. Baker et al. devised tuneable rheotaxing gold-platinum nanorods which orient parallel or antiparallel to the direction of a flow field⁶². In the absence of chemical fuel, the rods travel along the streamlines. Hydrogen peroxide fuel is added via the externally imposed flow to 'activate' the nanorods. The electrochemical decomposition reaction of H_2O_2 across the anodic platinum and cathodic gold segments generates an ion flux

along the nanorod which gives rise to a local dipole. The rod has an overall negative zeta potential with a permanent separation of charges between the two metal halves.

When combined with a substrate such as polydimethylsiloxane (PDMS) or glass which also has a negative zeta potential, the rods adopt an equilibrium position with respect to the surface with the less negatively charged platinum end closer to the surface (*Figure 1-18*).

A. Reorienting for Rheotaxis

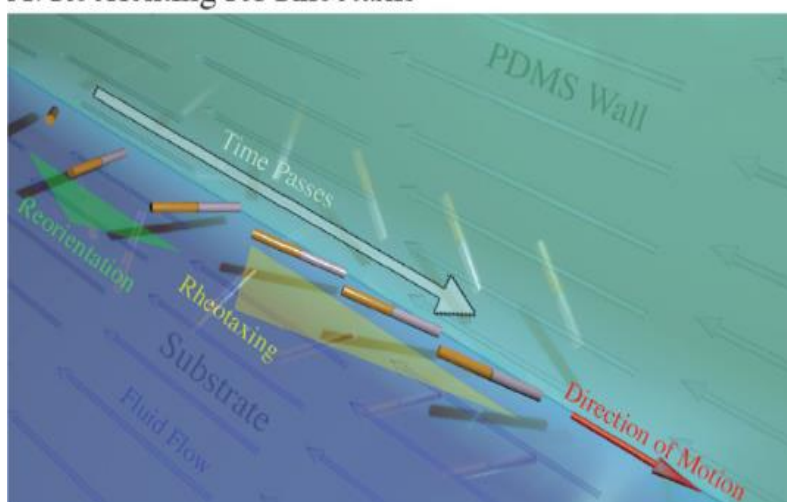


*Figure 1-18: Schematic of rheotaxing gold-platinum nano-rods produced by Baker et al.*⁶²

The imposed fluid flow has a shear gradient along the length of the tilted rods, which respond to the dynamic environment by reorienting anti-parallel to the flow whilst maintaining its equilibrium position from the surface. The fluid shearing gives rise to two modes of artificial rheotaxis:

High shear flows with fast flow rates, which can be found in the bulk of the fluid, cause negative rheotaxis. The active nanorods follow the flow streamlines much like the passive rods.

Low shear flows, with slow flow rates, are found near to the surface of the sample container and especially in the corners. These slower flows allow positive rheotaxis, where the nano rods migrate upstream in the anti-parallel position.

As rods migrate from high to low shear regimes their swimming direction flips from negative to positive.

In 2017 Ren et al. combined the phenomena of artificial rheotaxis produced by a chemically propulsive system with an acousto-fluidic device to achieve tuneable negative and positive rheotaxis with efficient upstream migration⁵⁸. Bimetallic rods, 2-3 μm in length and 300nm in diameter were produced by template assisted electrochemical deposition of rhodium/ ruidium and gold. The rods were tested in a square glass capillary modified as an acousto-fluidic device.

The bimetallic micromotors in peroxide fuel exhibit propulsion via a self-electrophoretic mechanism. In the absence of a shear flow this motion is directed towards the Rh end in random directions. When a shear flow is introduced via the siphon effect, the rods align axially with the flow with their Rh end against the flow and migration upstream occurs, this illustrated in *Figure 1-19*.

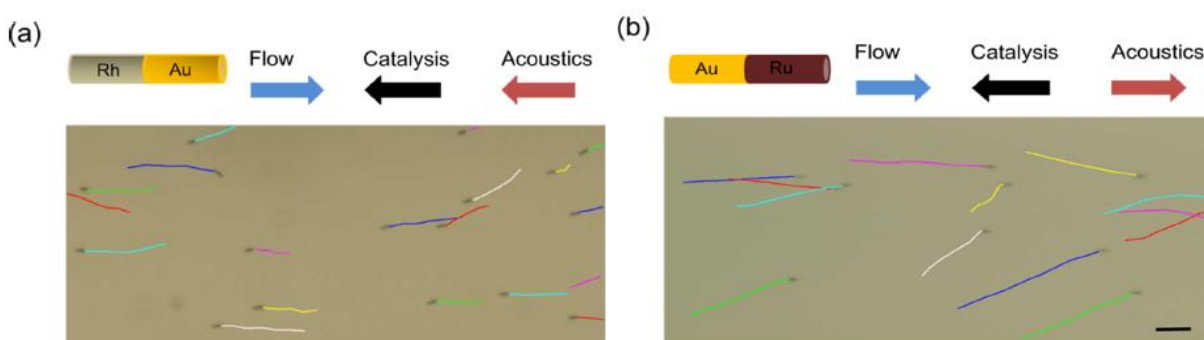


Figure 1-19: Trajectories of rheotaxing nanorods designed by Ren et al.⁵⁸

When tested in an acousto-fluidic device, the rods align axially with the flow and acoustic field. In the absence of fuel, which drives the electrophoretic component of alignment, the rods show no preference for which metal end faces against the flow. As such, when swimming commences the motion is directed towards the Rh end either up or downstream.

Whilst the chemically powered bimetallic motors exhibit unidirectional positive rheotaxis, their upstream migration velocity is limited by the magnitude of the shear flow. A fast shear flow gives better orientation control, but the process compromises the actual velocity of the micromotor.

Acoustically powered micromotors achieve much higher velocities with more direction control than their chemically powered counterparts but cannot achieve unidirectional motion. When these two processes are combined, fast unidirectional rheotaxis can be achieved in either the positive or negative direction.

1.7 Thesis Aims and Structure

The work presented in this thesis aims to further the understanding of how and to what extent variances in the geometry of active swimmers (colloid shape and catalytic patch shape) affect the behaviour and dynamics of the resulting active swimmers. It can be seen in sections 1.5.1 and 1.5.2 that geometrical changes can be used to induce desirable types of motion in many different catalytic systems but there is still a gap in the literature for more complex, rotationally asymmetrical swimmer shapes.

Theoretical simulations of ellipsoidal swimmers, in particular, predict rich dynamics depending on aspect ratio and proximity to bounding surfaces. Alignment phenomena

are expected in response to flow fields and chemically patterned surfaces. The majority of these predictions are as yet untested experimentally. Many of these predictions will be explored as the bulk of the experimental work in this thesis.

This work focusses on Pt-insulator swimmers in hydrogen peroxide fuel which are autonomously propelled at room temperature and require no external actuation. This simplifies the experimental set up considerably and enables applications outside of the lab to be considered, such as portable lab on chip devices, environmental remediation, and micro-stirring. Peroxide as a fuel is readily available and inexpensive and as such there is an interest in the literature to optimise such swimmers. The system is extensively studied for spherical swimmers, which will allow for direct comparisons of the behaviours of the swimmers in this work, with previously published data and predictions.

Chapter 2 will address the methods of synthesis, characterization and data analysis used in this study.

The majority of the work presented will focus on the swimming dynamics of ellipsoidal Janus ellipsoids coated in platinum along their long axis. The basics of motion, such as the direction of motion with respect to the coating and the differing behaviours of ellipsoids traveling in the bulk solution as opposed to those which follow the cuvette surface, will be covered in chapter 3.

Chapter 4 combines two key concepts from the literature; shape and flow, in order to direct the motion of ellipsoidal Janus swimmers in response to a self-generated density driven flow field. To date this has only been achieved in metallic rods, and spheres in response to an external flow stimuli. This chapter has also been prepared as a manuscript ready for submission.

Chapter 5 will focus on the catalyst geometry, to enhance the rotational velocity of the resulting swimmers in one simple step. Catalytically propelled colloidal rotation has been previously achieved in spherical swimming devices by means of neighbour shadowing during catalyst deposition leading to non-symmetrical coatings. However, in this work shadowing effects arise due to the ellipsoid's inherent anisotropy, removing the requirement for a closely packed colloidal crystal monolayer. This chapter has been prepared as a manuscript titled "Rotating Ellipsoidal Catalytic Micro-Swimmers via Glancing Angle Evaporation" and submitted to The Royal Society of Chemistry - Materials Advances for review.

The final experimental chapter 6, presents some much more complex shaped colloids which will be used as a base for catalytic swimmers. As discussed in the literature, experimentally tested swimmers have so far been restricted to basic, well-defined shapes. This chapter will investigate rotationally asymmetrical 'bowl' and 'dumpling' colloids. These geometries introduce a further degree of asymmetry with more possible orientations and potential for shadowing prior to coating. This chapter will explore the link between colloid shape and the quantity of rotational motion generated by catalyst shape asymmetries under standard coating conditions. It is expected that a wider range on angular velocities will be sampled than for spheres and ellipsoids as concave catalytic surfaces induce uneven propulsion across the swimmer.

Chapter 2:

Methods

2 Methods

This chapter will provide an overview of the methods of synthesis, characterization and mathematical analysis for the swimmers studied in this thesis. Details of chapter specific experimental procedures are covered in the experimental sections of the chapter.

2.1 Synthesis

When preparing micron-scale active colloids, precise and reproducible synthesis methods are key to ensure each colloid is of the same size and geometry, and that there are no unwanted variances between batches.

As such, spherical swimmers were produced using purchased samples of monodisperse spheres, and ellipsoidal colloids were produced by stretching these already monodisperse colloids. This results in samples of ellipsoidal colloids that are consistent in both geometry and size.

Methods for applying the catalyst were chosen similarly for precision and reproducibility in the catalyst shape and thickness, which have been shown to have significant effects on the motion achieved by swimmers^{21,22,42}.

2.1.1 Colloid stretching

Ellipsoidal colloids, studied in chapters 3-5, were produced by stretching spherical polystyrene colloids with a diameter of 2.16 μm (Sigma Aldrich)⁶³. The spherical

colloids were thoroughly mixed in a 25% wt. PVA (Mowiol 4-88 Sigma Aldrich) water solution. This mixture was spread thinly in a petri dish and allowed to dry for 3 days. The resulting film contained an even distribution of embedded isolated spherical colloids.

This film was mounted in custom-built stretching equipment seen in *Figure 2-1* (provided by Dr. Andrew Parnell, department of Physics and Astronomy, University of Sheffield), that could apply a well-defined uni-axial displacement to the film and dipped into an oil bath at 135 °C. This temperature was chosen as it is above the glass transition temperature (T_g) of the polystyrene colloids (105 °C) and the PVA film matrix (~38 °C). The process involved immersion followed by a rapid stretch and removal which provides a rapid quench below T_g . The film was stretched to 4.5x its original length, and after cooling the apparatus the film was released from the clamp.



Figure 2-1: Custom built stretching equipment for ellipsoid preparation.

To remove the colloids from the PVA matrix, the films were dissolved in a 70:30 ratio of isopropyl alcohol and deionised water. The mixture was then centrifuged to localise the colloids at the bottom of the tube and the supernatant was replaced with deionised water. This process was repeated 3 times to ensure all of the PVA was removed.

2.1.2 Spin Coating

Spherical, bowl and dumpling shaped colloids, studied in chapter 6 were deposited onto plasma cleaned glass slides via spin coating. This method allows for evenly spaced monolayers of colloids in a short time frame. The removal of solvent during the deposition process also reduces any solvent residue on the slides, caused by air drying, which can contaminate samples. Bowl and dumpling shaped colloids were produced by Prof. Syuji Fujii at Osaka Institute of Technology and spherical colloids were purchased from Sigma-Aldrich.

The slide is secured in place on the stage by a low vacuum and the stage spins at 2000 rpm. Colloids are suspended in a solvent and then pipetted onto the rotating stage from above, illustrated in *Figure 2-2*. As the stage spins and the solvent is subjected to the vacuum it is evaporated off very quickly whilst the insoluble colloids remain on the slide.

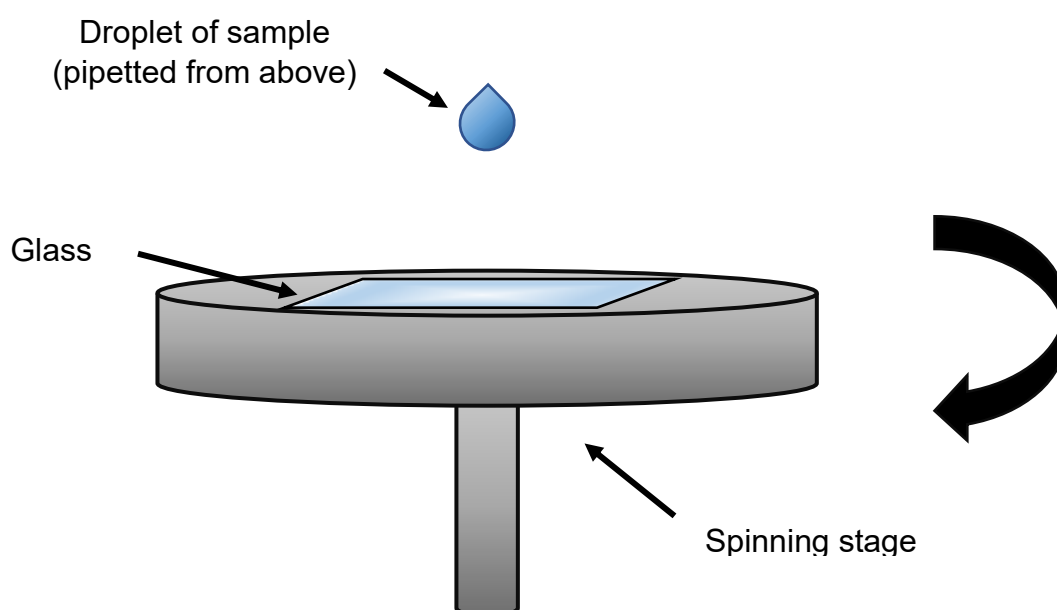


Figure 2-2: Schematic showing the spin coating process.

2.1.3 Catalyst deposition

As previously discussed, the catalyst shape and thickness are extremely important when preparing active swimmers, especially if the aim is a perfect Janus structure. This work uses physical vapour deposition of platinum to apply the catalyst. There are many methods for depositing platinum from solid however the coatings achieved are not all of comparable quality. For a Janus structure the most precise method is electron beam evaporation which is highly directional and via shadowing of the underside of the colloid an almost perfect hemisphere can be achieved.

2.1.3.1 Electron beam evaporation

Electron beam evaporation is a physical vapour deposition technique which allows for direct line of sight deposition (*Figure 2-3*) A target metal (in this case platinum) is bombarded by an electron beam given off by a charged tungsten filament in a high vacuum ($\approx 10^{-7}$ bar). The electron beam causes atoms from the target metal to transform into the gaseous phase. Providing the system is under high vacuum and there are no contaminants, these gaseous atoms have nothing to interact with between the target and the sample to be coated so they precipitate onto the sample directly above the target. This gives the metal deposition a high degree of directionality and is the most effective way to achieve a hemispherical coating, the underside of the colloid is almost completely shadowed and no metal is deposited⁶⁴.

Electron beam evaporation also allows for control over the thickness of the catalyst coating using a quartz crystal monitor. The QCM uses the piezoelectric effect of a thin quartz crystal between two electrodes to determine the mass of metal deposited.

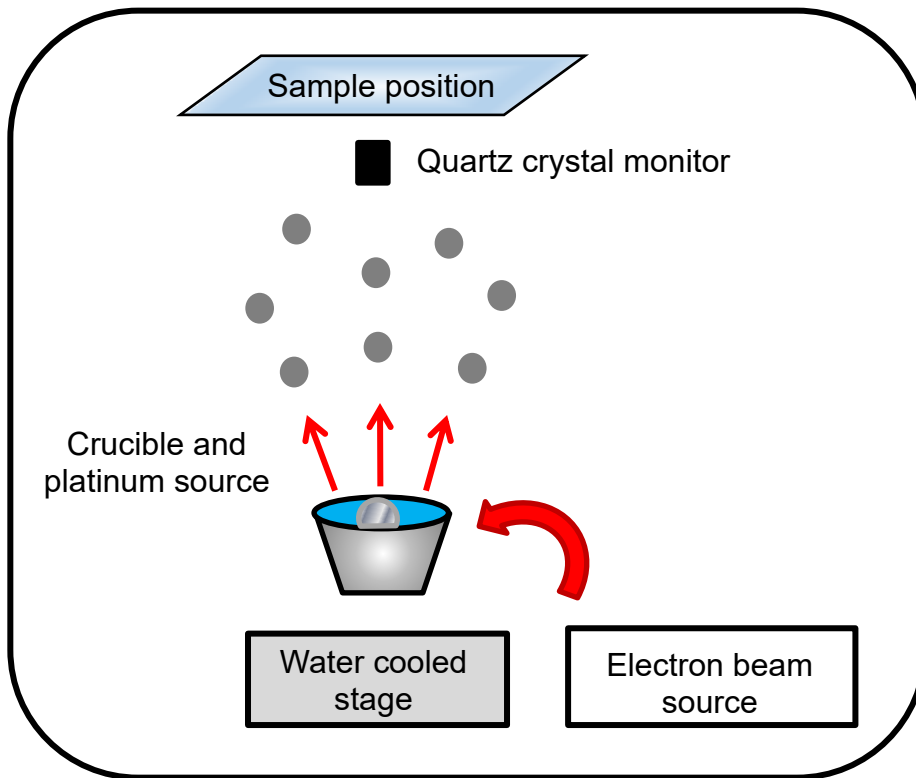


Figure 2-3: A basic representation of the sample chamber of an Electron beam evaporator.

During the coating process an electric field is applied to the monitor which causes it to oscillate at a certain resonance which is very sensitive to thickness changes. As the metal is deposited onto the sample it is also deposited onto the QCM which results in a change of resonance of the crystal, decreasing as the thickness increases. This change in resonance frequency is converted into a mass change using the Sauerbrey equation (Equation 2-1)^{65,66}:

Equation 2-1:
$$\Delta f = \frac{2f_0^2}{A\sqrt{\rho_q\mu_\rho}} \Delta m$$

2.1.3.2 Ion Sputtering

Ion sputtering is another physical vapour deposition technique where metal atoms are ejected from a solid target by energetic argon plasma (*Figure 2-4*). This process is performed under low vacuum ($\approx 10^{-3}$ mBar) which dramatically decreases the time taken to achieve the right pressure, but this increase in coating speed comes at the cost of precision and vapour directionality.

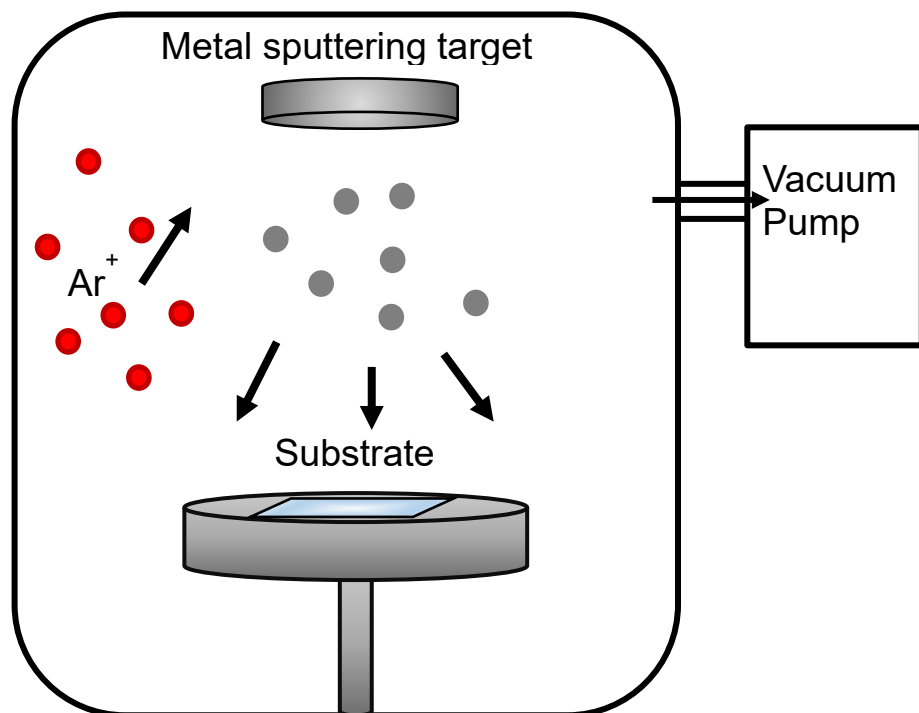


Figure 2-4: A basic representation of the sample chamber of ion sputtering equipment.

The target metal is bombarded with Argon ions and collisions between gaseous Argon ions and the atoms in the target occur, leading to a transfer of momentum which sets the target atoms in motion. If enough energy is transferred the binding energy can be overcome and an atom ejected. Higher ion energies cause collision

cascades. When the cascades recoil with sufficient energy, atoms can be ejected from the target.

Coating occurs via diffusion of these ejected atoms in any direction. This lack of directionality removes the shadowing effect observed during electron beam evaporation, so that all of the surface that is not covered will be coated, illustrated in *Figure 2-5*. Control of coating thickness is also more difficult to achieve as there is no quartz crystal monitor. Ideally, colloid coatings to produce micro-swimmers would more precise and for this reason (where possible) electron beam evaporation will be used to produce micro-swimmers, and sputter coating will only be used when faster preparation times are required.

Electron beam evaporation

Sputter Coating

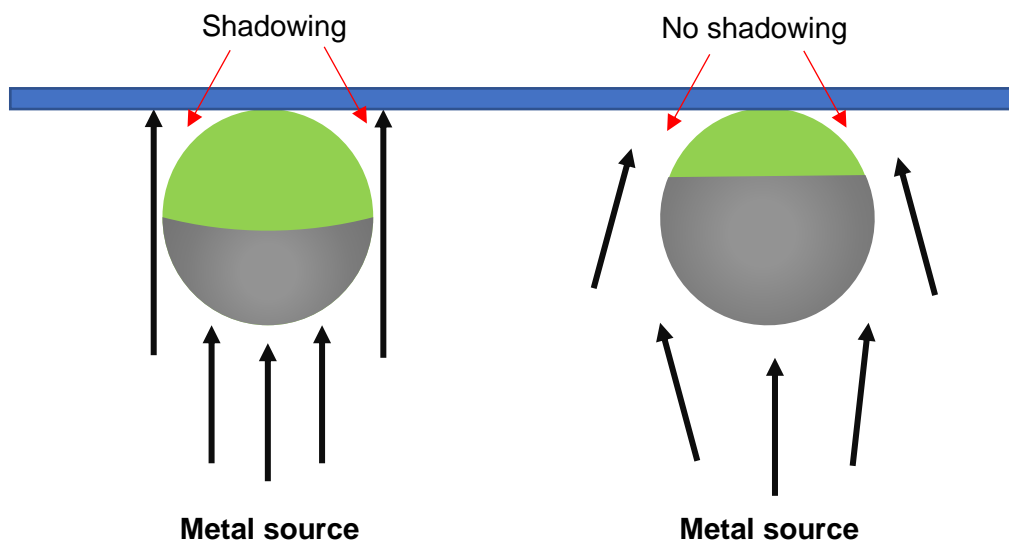


Figure 2-5: Schematic illustrating the directionality of electron beam evaporation and sputter coating.

2.2 Characterization

The techniques in this section were used to characterize the swimmers to ensure that they are the desired size and shape and record high quality videos of their motion for analysis.

2.2.1 Scanning Electron Microscopy

Scanning electron microscopy (SEM) was used to produce high resolution images of all colloids. The images were used to calculate the sizes of the colloids, investigate any surface morphological features, and determine the orientation of asymmetrical colloids after deposition on the slides. In some cases, where sufficient contrast could be achieved, SEM was used to visualise the shape of the Pt cap.

SEM produces high resolution images of nano and micro-scale samples by scanning the surface with a focussed beam of electrons⁶⁷, illustrated in *Figure 2-6*. These electrons are emitted from an electron gun containing a tungsten filament cathode. The electrons are accelerated towards the sample by an anode which is placed near the gun and allows changes in voltage potential between the anode and electron gun between 1 and 20 KeV. This allows tuning of the energy of the electron beam which dictates signal intensity and the depth at which the electron penetrates the sample.

The electrons produced interact with atoms in the sample resulting in the emission of Back Scattered Electrons (BSE), secondary electrons, X-rays and cathodoluminescence in certain samples⁶⁸.

High energy BSEs are beam electrons which are reflected from deep in the sample by elastic scattering. BSEs are most useful for providing contrast in samples containing more than one material as heavy elements backscatter electrons more strongly than light elements. Lower energy secondary electrons are emitted very close to the sample surface and give detailed topographical and morphological information. These electron signals are displayed as variations in brightness on a computer monitor where each pixel is synchronised with the corresponding position of the beam on the sample.

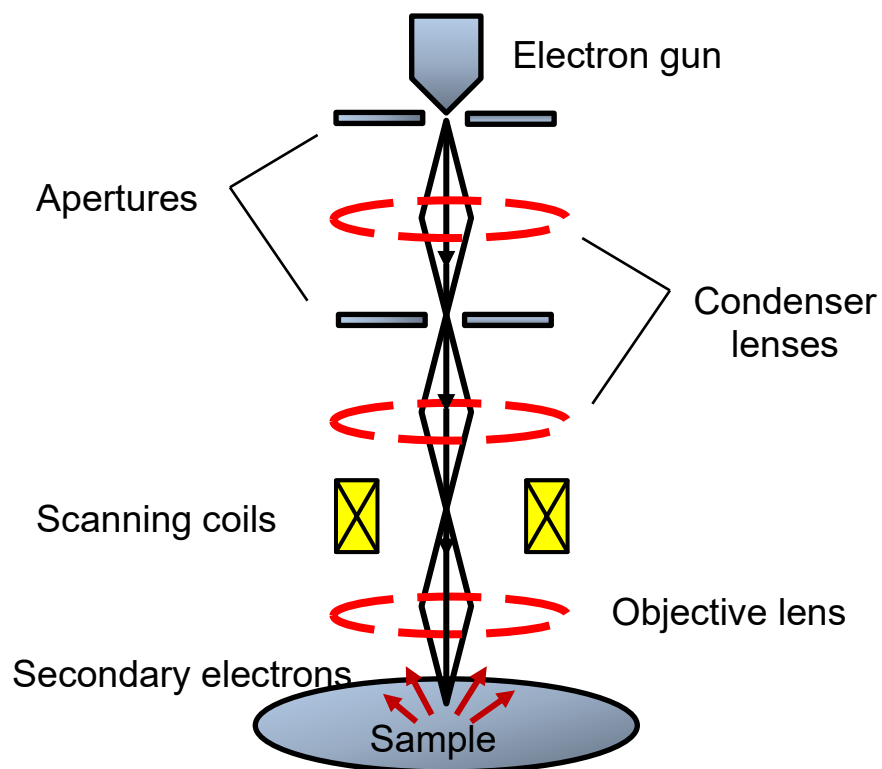


Figure 2-6: A simplified representation of the inner components of a Scanning Electron Microscope.

The resulting image is a distribution map of signal intensity with objects showing as white on a black background. In order to prevent damage to samples or equipment, the sample must be conductive and able to withstand a high vacuum. If the sample is

non-conductive the electron beam causes a charge build-up in the sample, resulting in machine faults and image artefacts. Samples are usually made conductive by depositing a thin layer (5-10nm) of Gold onto the surface via ion sputtering (section 2.1.3.2). SEM images produced for this thesis were recorded using BSE signals at 15KeV for images requiring contrast and secondary electron signals at 10KeV to visualise the finer details of colloid surfaces.

2.2.2 Optical Microscopy

Brightfield optical microscopy in transmission mode was used to view and record the swimmers in fuel solution for tracking analysis. In brightfield microscopy, conventionally, the sample is lit from below and light passes through the sample; the contrast seen is from light transmitted through the sample. The microscope used in this research is inverted, meaning that the light source and condenser are above the sample, whilst the objectives and turret are below the sample. Inverted microscopes are more suitable for observing samples in fluid in their natural state, particularly the swimmers discussed in this work which tend to sediment to the lower surface of the cuvette. Having the objective lens below the sample holder allows for better resolution as the colloids are closer to the lower surface.

Optical microscopy uses visible light from an incandescent source and a system of lenses to magnify samples on the micron-mm scale. The resolution of optical microscopy is limited to the wavelength of visible light, theoretically between 390 and 700nm⁶⁹, however in practice 800 nm is the smallest object that could be resolved successfully in most experimental set ups. As the colloids studied in this thesis are

all of greater size than this limit, transmission mode microscopy is the most appropriate characterization method.

The light source is incandescent, meaning it creates both heat and light, therefore care must be taken to ensure that observed particles are not propelling due to heating effects. The use of mean square displacement analysis (2.3.1) will help to rule out heating effects and convection and confirm propulsive motion.

2.2.3 Fluorescence Microscopy

Fluorescence microscopy is very useful in the characterization of metal/insulator swimmers. If a fluorescent base colloid is used, the metal coating masks the fluorescence and when observed by a fluorescence microscope only the uncoated section can be seen.

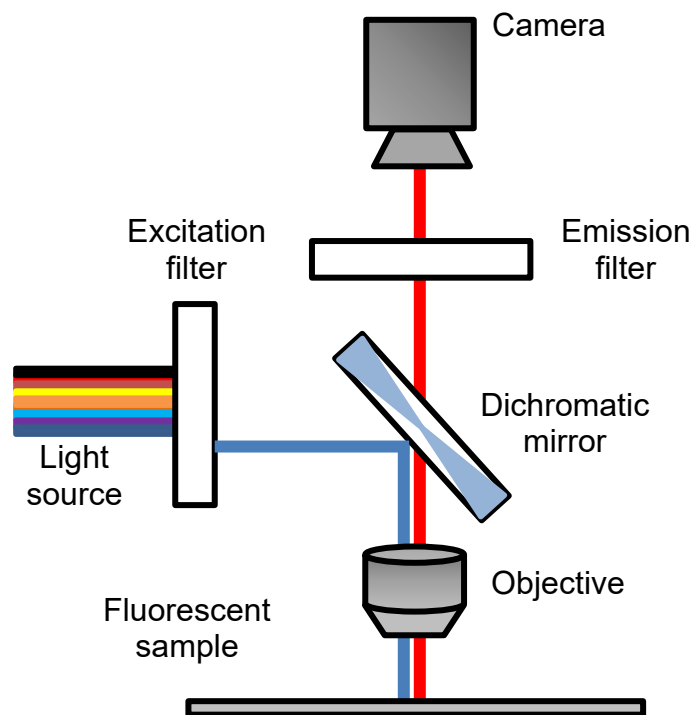


Figure 2-7: Basic schematic of a fluorescence microscope

This allows visualisation of both the size and shape of the catalyst patch and also the direction of motion away from / towards the catalyst which is important information when assigning a mechanism of motion. In fluorescence microscopy the specimen is illuminated by light of a specific wavelength which corresponds to the wavelength absorbed by fluorophores on the colloid surface. The light is absorbed by the fluorophores causing the emission of light of a defined longer wavelength. A dichromatic beam splitter (shown in *Figure 2-7*) is required to separate the excitation and emitted light. The emitted light is transmitted through an eyepiece or camera whilst the excitation light is reflected back towards the source.

2.3 Particle Tracking

The active swimmers in this thesis undergo enhanced motion when exposed to hydrogen peroxide fuel as discussed in chapter 1. In order to confirm that the enhanced motion is due to propulsion rather than convection effects, the motion observed must be characterised.

This analysis allows the quantification of velocity, MSD and x-y coordinates of the colloid to produce the trajectories displayed throughout this thesis.

2.3.1 Labview software and MSD analysis

A custom LabVIEW programme created by Dr. Stephen Ebbens and Dr. Jonathan Howse was used to analyse the recorded videos and calculate the colloid's centre of

mass and location to give x-y coordinates. The x-y coordinates allow the calculation of the mean square displacement, velocity and diffusion coefficient.

Mean square displacement (MSD) is a measure of the deviation of the position of a particle over time with respect to a reference position, usually the starting position⁷⁰. It is calculated by averaging the square of the distance between 2 points over incremental time intervals (Δt) see *Equation 2-2* to *Equation 2-4*. The overall MSD is then an average of the data for each time step⁷¹.

Equation 2-2: $\Delta T = 1:$ $\langle \Delta L \rangle^2 = \frac{(L_{1,2} + L_{2,3} + L_{3,4} + L_{4,5} + L_{5,6})^2}{5}$

Equation 2-3: $\Delta T = 2:$ $\langle \Delta L \rangle^2 = \frac{(L_{1,3} + L_{2,4} + L_{3,5} + L_{4,6})^2}{4}$

Equation 2-4: $\Delta T = 3:$ $\langle \Delta L \rangle^2 = \frac{(L_{1,4} + L_{2,5} + L_{3,6})^2}{3}$

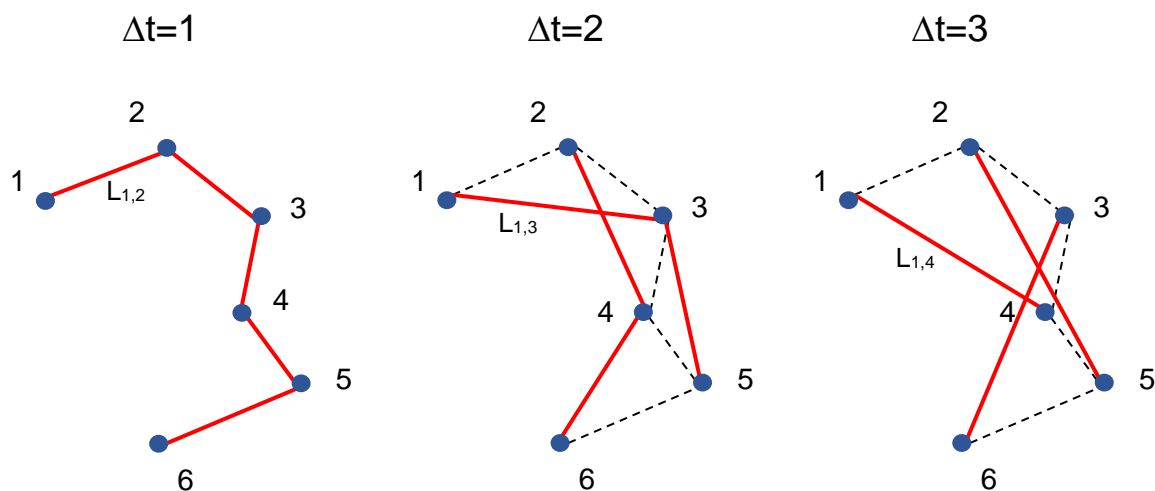


Figure 2-8: Schematic showing a simple 6 position MSD calculation.

MSD analysis is especially useful in the field of active colloids as it allows the distinction between expected Brownian diffusion and propulsion caused by chemical gradients e.g. via electro-kinetic effects. The 2 dimensional MSD variation as a function of time for a propulsive particle without any angular rotation is given by *Equation 2-5*.

$$\text{Equation 2-5: } \langle \Delta L \rangle^2 = 4D\Delta t + \frac{v^2 \tau_R^2}{2} \left[\frac{2\Delta t}{\tau_R} e^{\frac{2\Delta t}{\tau_R}} - 1 \right]$$

Where:

D = Diffusion coefficient

Δt = Time interval

v = Velocity

τ_R = Inverse rotational diffusion coefficient

Over short periods of time Δt is significantly smaller than τ_R meaning the colloid has not had time to rotate. At this timescale, propulsion is in one direction with a ballistic trajectory. MSD data at short time scales fits the simplified form, *Equation 2-6*.

$$\text{Equation 2-6: } \langle \Delta L \rangle^2 = 4D\Delta t + v^2 \Delta t^2$$

Over these short time scales, propulsion cannot not be distinguished from other effects such as convection and sedimentation as the MSD vs. time plots appear the same⁷².

Over longer time periods where $\Delta t \gg \tau_R$, the direction of motion changes due to rotation of the colloid. Propulsive motion changes from ballistic to diffusive behaviour with an enhanced diffusion coefficient fitting from *Equation 2-7*.

$$\text{Equation 2-7:} \quad \langle \Delta L \rangle^2 = (4D + v^2 \tau_R) \Delta t - \frac{v^2 \tau_R^2}{2}$$

This transition from ballistic to diffusive behaviour is what separates propulsion from convective motion, in which rotation of the colloid does not occur and ballistic motion persists. A quadratic curve plot, seen in the red section of *Figure 2-9*, is indicative of propulsive behaviour. Whereas enhanced diffusion such as Brownian motion produces a straight-line plot⁷⁰. This is shown in blue on *Figure 2-9*.

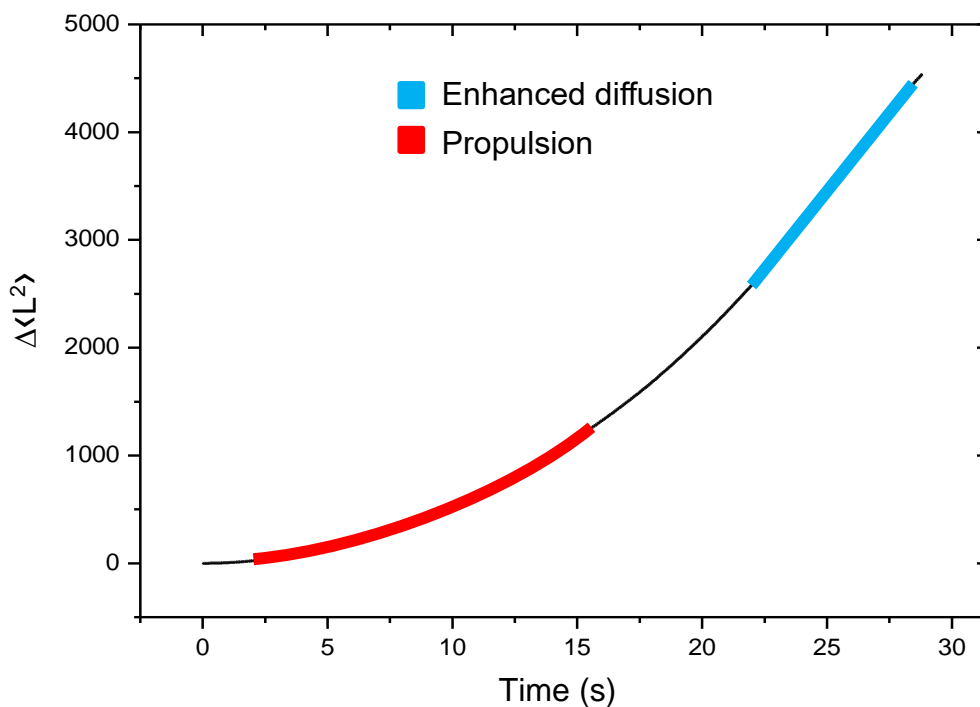


Figure 2-9: A typical MSD plot for a propulsive micro swimmer without any rotational propulsion.

2.3.1.1 Derivation of Angular velocity, ω

It has previously been confirmed for spherical swimmers that the size and shape of the catalytic patch has a significant effect on the angular velocity, or rotational speed, of a swimmer⁷³. This results in trajectories that range from linear motion with a large deviation from the origin, to circular motion around a central point. The orientation of asymmetrical colloids on the slide before deposition of platinum will affect the line-of-sight deposition of the catalyst. The result is that of a variation in the size and shape of the catalytic patch within a sample of swimmers. In order to investigate the effect of catalyst deposition onto asymmetrical colloids, the angular velocity must be derived from the MSD data.

The angular velocity is calculated by fitting the MSD curve for each swimmer with *Equation 2-8* using OriginPro graphing software using an iterative approach (*Figure 2-10*).

$$\text{Equation 2-8: } \langle \Delta L \rangle^2 = 4D_t t + \frac{2v^2 D_r t}{D_r^2 + \omega^2} + \frac{2v^2 (\omega^2 - D_r^2)}{(D_r^2 + \omega^2)^2} + \frac{2v^2 e^{-D_r t}}{(D_r^2 + \omega^2)^2} [(D_r^2 - \omega^2) \cos \omega t - 2\omega D_r \sin \omega t]$$

Where:

D_t = Translational diffusion coefficient

D_r = Rotational diffusion coefficient

Δt = Time interval

v = Translational velocity

ω = Angular velocity

T_R = Inverse rotational diffusion coefficient

K_B = Boltzmann constant

R = Colloid radius

The fitting process requires the input of sensible values for v , D_r and D_t . The velocity is provided by the LabVIEW software and D_r and D_t are estimated using the Stokes Einstein equations for spherical colloids:

Equation 2-9:
$$D_t = \frac{k_B T}{6\pi\eta R}$$

Equation 2-10:
$$D_r = \frac{k_B T}{8\pi\eta R^3}$$

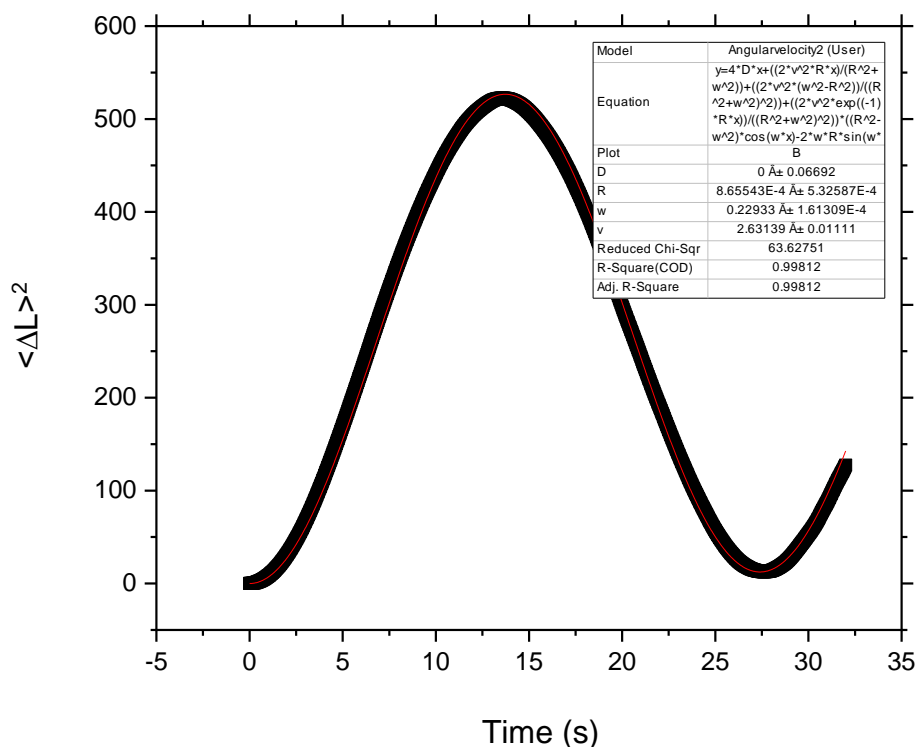


Figure 2-10: Screen capture from originpro graphing software of an MSD fitting curve.

The diffusion coefficients of ellipsoidal colloids were calculated by applying a Perrin factor⁷⁴ to the diffusion coefficient of a sphere of the same volume. These calculations are displayed in detail in chapter 3.

The bowl and dumpling shaped colloids under investigation do not have equations to give accurate calculations, so these values have been estimated using the Stokes-Einstein equation for spherical colloids (*Equation 2-9 and Equation 2-10*).

Chapter 3:

Ellipsoidal Micro-swimmers

3 Ellipsoidal Micro-swimmers

3.1 Introduction

This chapter will act as an introduction to the main experimental theme in the thesis: ellipsoidal swimmers. The work in this chapter was done concurrently with a similar publication by Shemi et al. and as such much of the results confirm the findings in this publication⁴⁷. This chapter characterizes the more basic aspects of the motion of ellipsoidal micro-swimmers in order to fully understand the complex dynamics at play in chapters 4 and 5, which move beyond the concurrent work by demonstrating novel findings for the behaviour of catalytic ellipsoids in self-induced flow, and the ability to impart controllable rotation to their trajectories.

The ellipsoids studied in this work were prepared using a simple stretching process, starting with monodisperse polystyrene spheres which reduced the variation within the resulting ellipsoidal colloids⁶³.

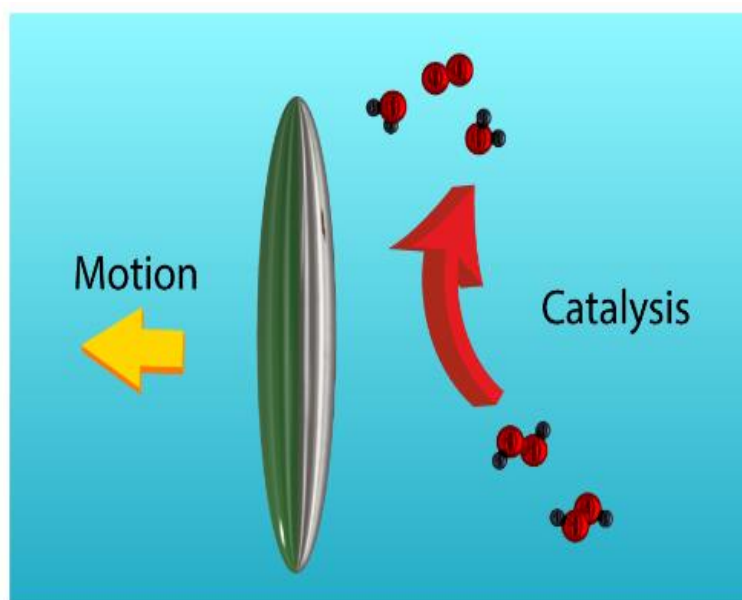


Figure 3-1: Schematic of a PS-Pt ellipsoidal micro swimmer, coated along its major axis, in hydrogen peroxide fuel.

The dynamics of ellipsoidal micro swimmers has been previously investigated, both theoretically and experimentally as discussed in detail in chapter 1. Shemi et al. recently experimentally tested ellipsoidal micro swimmers, coated along their major axis. They found that propulsion occurs in a direction perpendicular to their major axis and that their velocity is dependent upon their aspect ratio⁴⁷.

Theoretical simulation of similar colloids have focussed on ellipsoids coated along their short axis, which at present has not been achieved experimentally due to the difficulty of orienting the colloids for such a coating via a physical vapour deposition technique.

Uspal et al. modelled ellipsoids (spheroids) near chemically patterned surfaces and concluded that the colloids will align (dock) with and follow a surface when favourable chemical interactions are present⁵³.

The work in this chapter aims to expand upon previously established dynamics of ellipsoidal micro-swimmers, with interest especially regarding the behaviours of the swimmers near to boundaries, as compared to those in the bulk fluid and the direction of motion from the catalytic patch. This additional data will facilitate a deeper understanding of the mechanism by which ellipsoidal swimmers propel. It is predicted that, like spherical swimmers, there is an electrophoretic component to the mechanism. If this is the case, ellipsoidal swimmers are expected to experience alignment with the chamber surface (lower) where rotations about the long axis are quenched and the swimmer follows the surface at a stable distance. This effect is discussed in detail by Nas et al⁴⁸.

3.2 Experimental

3.2.1 Synthesis

Colloid synthesis

Ellipsoidal colloids were produced by stretching spherical polystyrene colloids with a starting diameter of 2.16 μm (Sigma Aldrich)⁶³ as described in detail in section 2.1.1. The cleaned colloids were deposited onto pre-cleaned glass by pipetting the suspension into hydrogel wells to concentrate the colloids at the centre of the slide.

Catalyst coating

The ellipsoidal colloids were then coated with 10nm of chromium followed by 20 nm of platinum (Kurt J Lesker 99.99% purity) while localised near the centre of the slide. platinum was deposited via electron beam evaporation (Moorfield minilab) at $\approx 1 \times 10^{-7}$ atm.

3.2.2 Tracking

Ellipsoidal colloids were transferred to solution by rubbing wetted lens tissue onto the colloid deposited glass slides. The lens tissue was then shaken in a small volume of deionised water which is then separated from the tissue to produce a low concentration volume of the desired colloids in deionised water. In order to assess the fuelled catalytic motion of the Janus ellipsoids, hydrogen peroxide was added to these suspensions to produce a 10% wt aqueous solution. The ellipsoids were

observed at 20x magnification once sedimented at the bottom surface of a quartz cuvette with an inverted microscope (Nikon eclipse T-100 microscope) equipped with a Pixelink PL-B742F camera.

Tracking videos were recorded for 30 seconds at a time, at a framerate of 33 fps and a resolution of 640x480 pixels. These were taken of the colloids suspended in solution to capture their diffusive/propulsive motion. Negative control experiments without the addition of hydrogen peroxide were also performed as described. The x,y coordinates of ellipsoids and tracer particles were determined as a function of time using custom image analysis algorithms written using LabVIEW by Dr. Stephen Ebbens and Dr. Jon Howse. The orientation of the asymmetrical ellipsoids ($\Theta_{\text{orientation}}$) were determined as a function of time using an algorithm to determine the major axis angle.

Angular Velocity analysis

As described in chapter 2 in detail, the angular velocity of the colloids can be determined by fitting the mean-square displacement (MSD) data as a function of time ($\Delta L^2 \langle t \rangle$) to the following expression⁷⁰: As these equations were derived for spherical colloids, this is an estimation of angular velocity, using the diffusion coefficient for an ellipsoid given by the Perrin friction factor.

$$\text{Equation 3-1 : } \Delta L^2 \langle t \rangle = 4D_t t + \frac{2v^2 D_r t}{D_r^2 + \omega^2} + \frac{2v^2(\omega^2 - D_r^2)}{(D_r^2 + \omega^2)^2} + \frac{2v^2 e^{-D_r t}}{(D_r^2 + \omega^2)^2} [(D_r^2 - \omega^2) \text{Cos} \omega t - 2\omega D_r \text{Sin} \omega t]$$

This analysis was applied to the raw x,y coordinates for the ellipsoidal colloids via fitting with suitable physical constraints (all returned values >0 , and physically sensible constraints applied to D_t and D_r) performed using OriginPro.

3.3 Results

3.3.1 SEM and size analysis

Qualitatively it is apparent that reasonably uniform ellipsoids have been successfully produced (*Figure 3-2*). Quantitative analysis of ≈ 100 ellipsoids reveals that the mean major axis is $8.05 \mu\text{m} \pm 0.98$ and the mean minor axis is $2.33 \mu\text{m} \pm 0.34$, giving a mean aspect ratio of 3.55 ± 0.78 . The mean minor axis is slightly larger than that of the starting colloid suggesting that the polystyrene expands during the stretching process, resulting in decreased density of ellipsoids compared to spherical colloids.

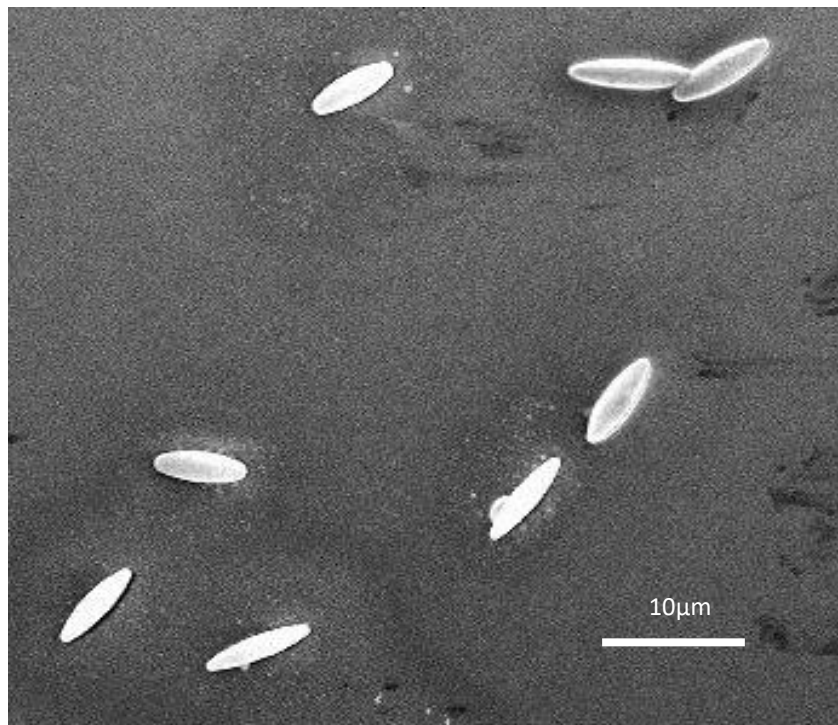


Figure 3-2: Representative SEM image of ellipsoidal polystyrene colloids.

3.3.2 Motion

Once the particle geometry was confirmed, the ellipsoids were coated with Pt while localised on a planar substrate. This exploited the previously demonstrated directionality of metal evaporation to produce a half-coated structure: a Janus ellipsoid (*Figure 3-1*).

The ellipsoids were removed from the substrate and then suspended in an aqueous Hydrogen Peroxide solution (10 wt. %), where the Pt catalyses the decomposition of the fuel (H_2O_2), and was expected to produce motion in analogy to the much studied conventional Janus spheres²².

Bulk vs. Surface restricted motion

Propulsive ellipsoids in hydrogen peroxide fuel are predominantly found to sediment to the lower boundary of the cuvette. A small number of ellipsoids however can be found in the bulk solution (<20% of the population). Analysis on both populations revealed that sedimenting ellipsoids remain on the surface and translate in this restricted plane (*Figure 3-5b*). Ellipsoids propelling in the bulk fluid have more degrees of freedom, they can rotate freely around each of their axes (see *Figure 3-4b*) and swim in and out of the field of vision. As motion in the z-direction cannot be resolved with an optical microscope this results in inconsistent data acquisition.

This is quantified by the angle between the field of vision (x,y plane) and the ellipsoid given by *Equation 3-2*.

Equation 3-2:
$$\text{Cos}\theta = \frac{\text{Measured length}}{\text{Known length}}$$

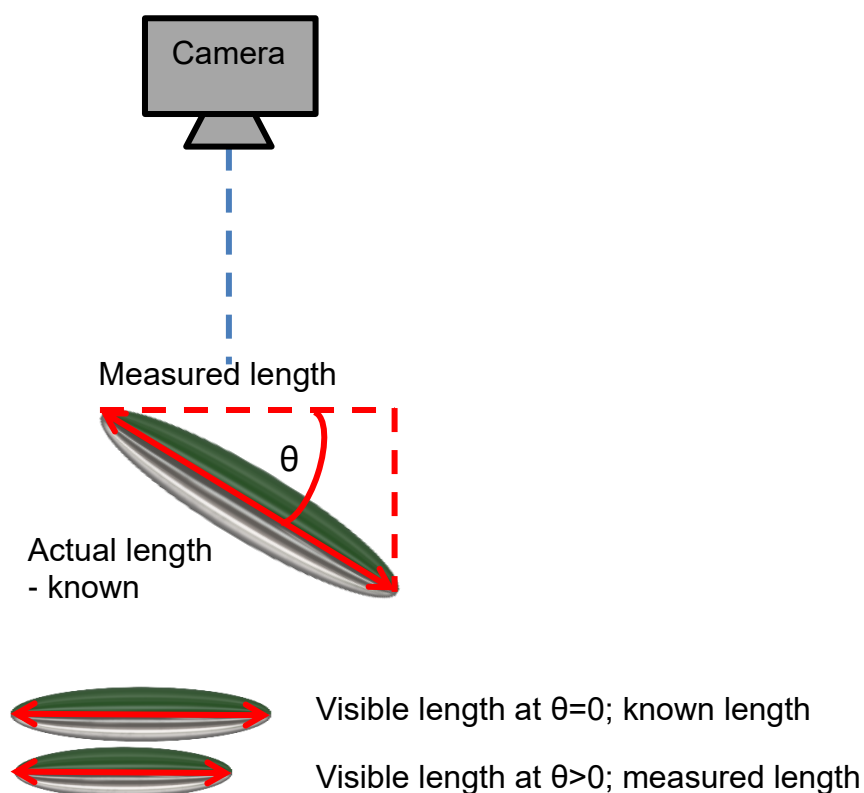


Figure 3-3: Schematic illustrating the calculation to derive the angle between the field of vision and the ellipsoid, from the results provided by LabVIEW.

Custom LabVIEW software recorded the length of the major axis throughout the tracking process. The length of the ellipsoid was used to calculate the fluctuating angle between the colloid and the field of vision using the calculation illustrated in *Figure 3-3*. The evolution of this angle was plotted for both ellipsoids translating in the bulk solution, and those which had sedimented to the lower cuvette surface (*Figure 3-4c* and *Figure 3-5c*). For ellipsoids in the bulk solution, the angle plot shows no restriction of motion in the z-plane. In the example shown, the ellipsoid rotates away from the field of vision causing Θ to steadily increase.

In all cases where sedimentation occurs, the proximity of the ellipsoids to the boundary resulted in them lying relatively flat against the cuvette wall. The angle plot for a surface restricted ellipsoid shows that the major axis remains $\approx 20^\circ$ away from the field of vision and out of plane rotations were not observed, i.e. the ellipsoids remain orientated as shown in *Figure 3-5c*.

In order to maintain as much experimental control of the ellipsoidal micro swimmers as possible, further observations will be taken exclusively near the cuvette surface and analysis will focus on the dynamics of the ellipsoidal micro swimmers near this surface.

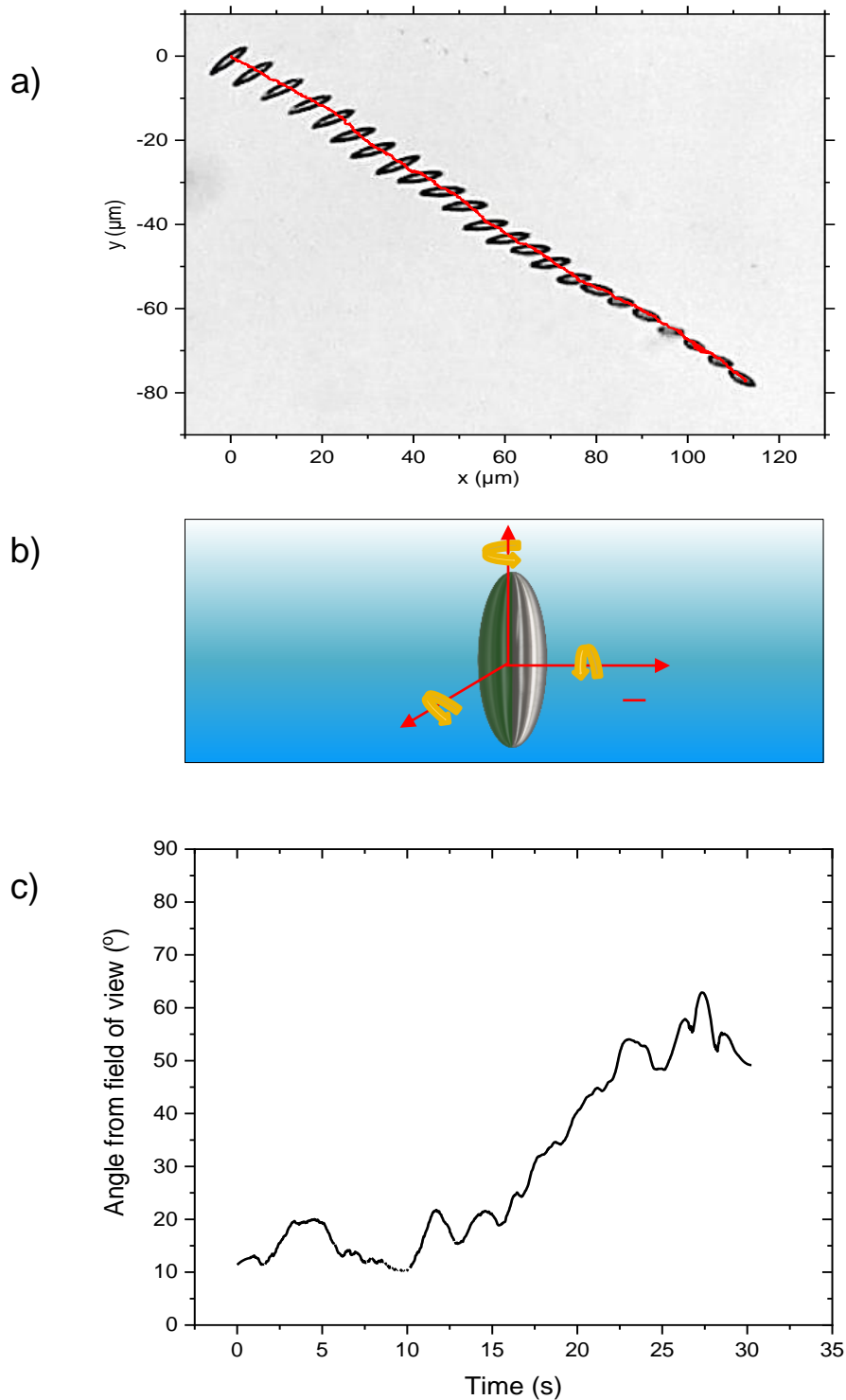


Figure 3-4: a) A trajectory of an ellipsoidal Micro swimmer translating in the bulk fluid, this type of swimmer represents <20% of the total swimmer population. b) A schematic showing the allowed rotations around each axis for an ellipsoid in the bulk fluid. c) a plot to show the fluctuation over time of the angle between the plane of vision and the ellipsoid's major axis for 30 seconds.

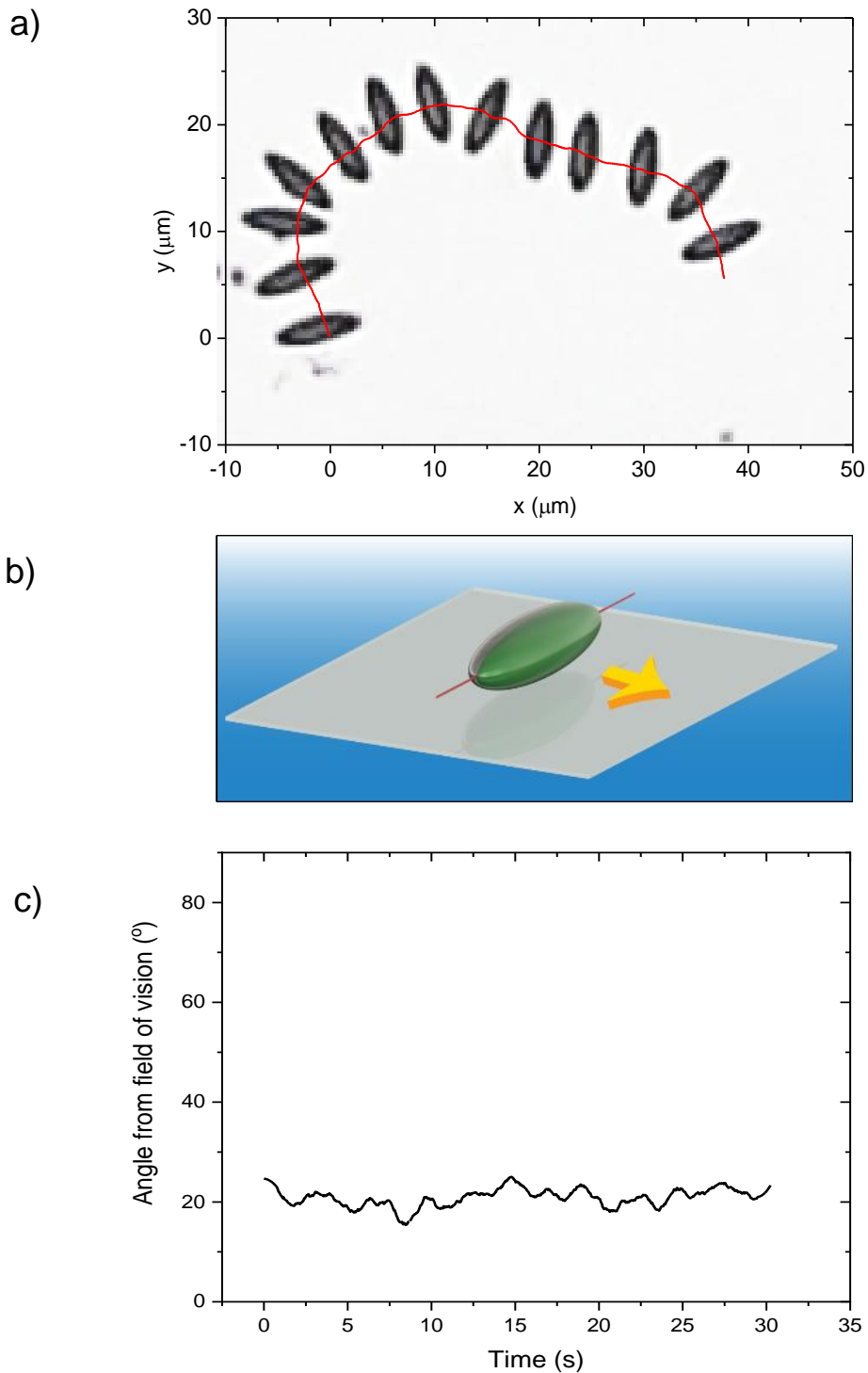


Figure 3-5: a) A trajectory of an ellipsoidal swimmer translating near the cuvette boundary, this type of swimmer represents >80% of the total swimmer population. b) A schematic showing the allowed rotations around each axis for an ellipsoid near the cuvette boundary. c) a plot to show the fluctuation over time of the angle between the plane of vision and major axis for 30 seconds.

Observations of motion

The mean translational velocity of the ellipsoidal micro-swimmers was $4.00 \pm 1.21 \mu\text{ms}^{-1}$ and a range of behaviours was qualitatively observed.

Some ellipsoidal swimmers had almost purely ballistic behaviour resulting in long smooth trajectories with few turns, like the one displayed in *Figure 3-6*. MSD plots for this data show initially a quadratic curve which indicates propulsive behaviour, after a short propulsive period the behaviour becomes diffusive, and the plot becomes more linear.

This transition from propulsive to diffusive behaviour is indicative of an autonomously propelling swimmer, if the curve were to persist without transitioning to diffusive behaviour it is likely that the propulsion is caused by some external factor, e.g. flow field⁷².

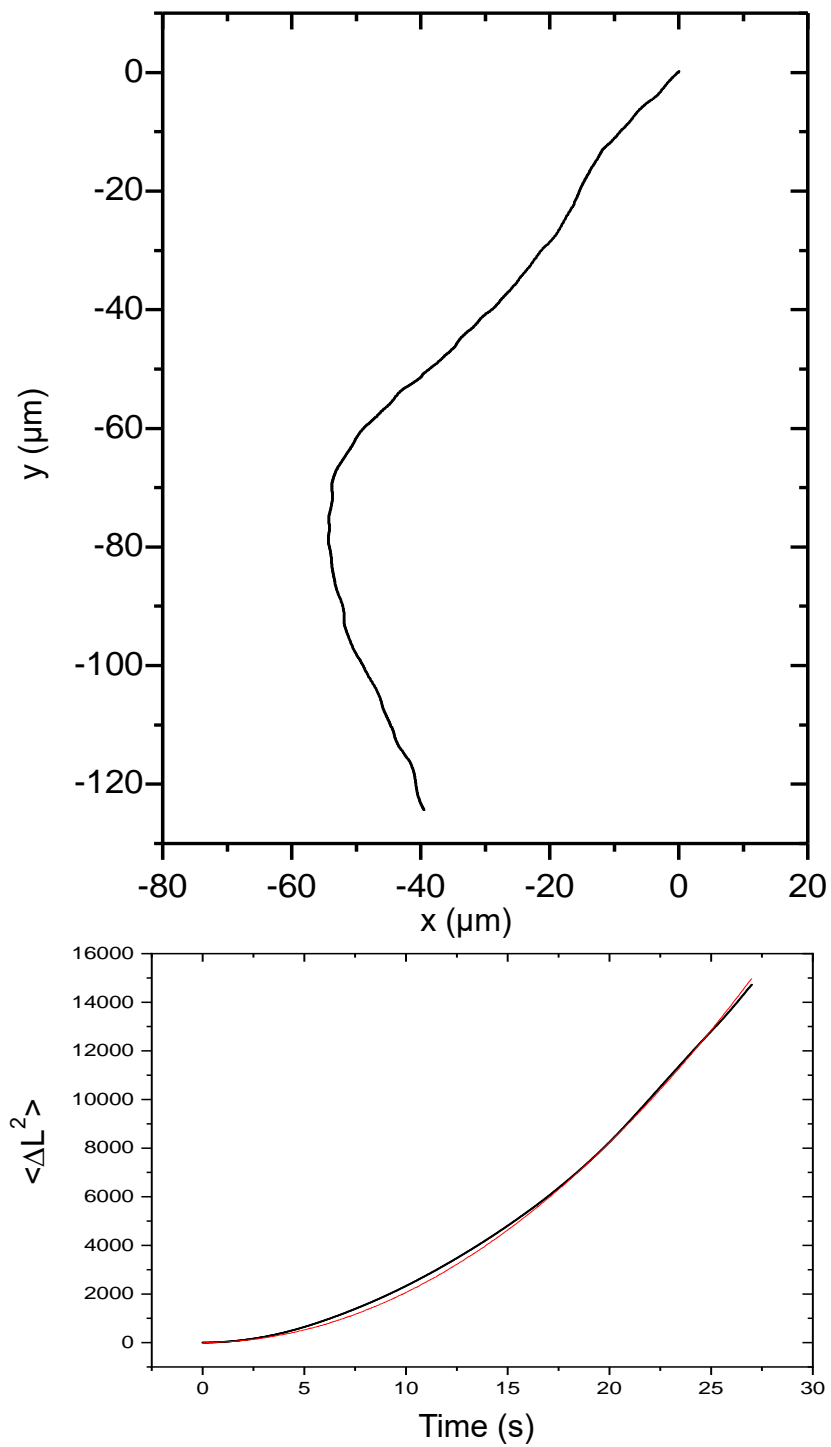


Figure 3-6: Trajectory and corresponding MSD plot with angular velocity fitting ($\omega=8.88 \times 10^{-7} \text{ rads}^{-1}$) for a representative ballistic Janus ellipsoid.

Other trajectories showed circling behaviour, usually around a fixed point, which persisted for the duration of the experiment. An example of this circling behaviour can be seen in *Figure 3-7*. The MSD data for these ellipsoids showed a similar quadratic curve initially, but as the swimmer turns and rotates, the direction of motion is back towards the origin and so the gradient of distanced travelled becomes negative and returns to zero. As the colloid turns, the distance travelled will go up and down leading to oscillatory MSD plots.

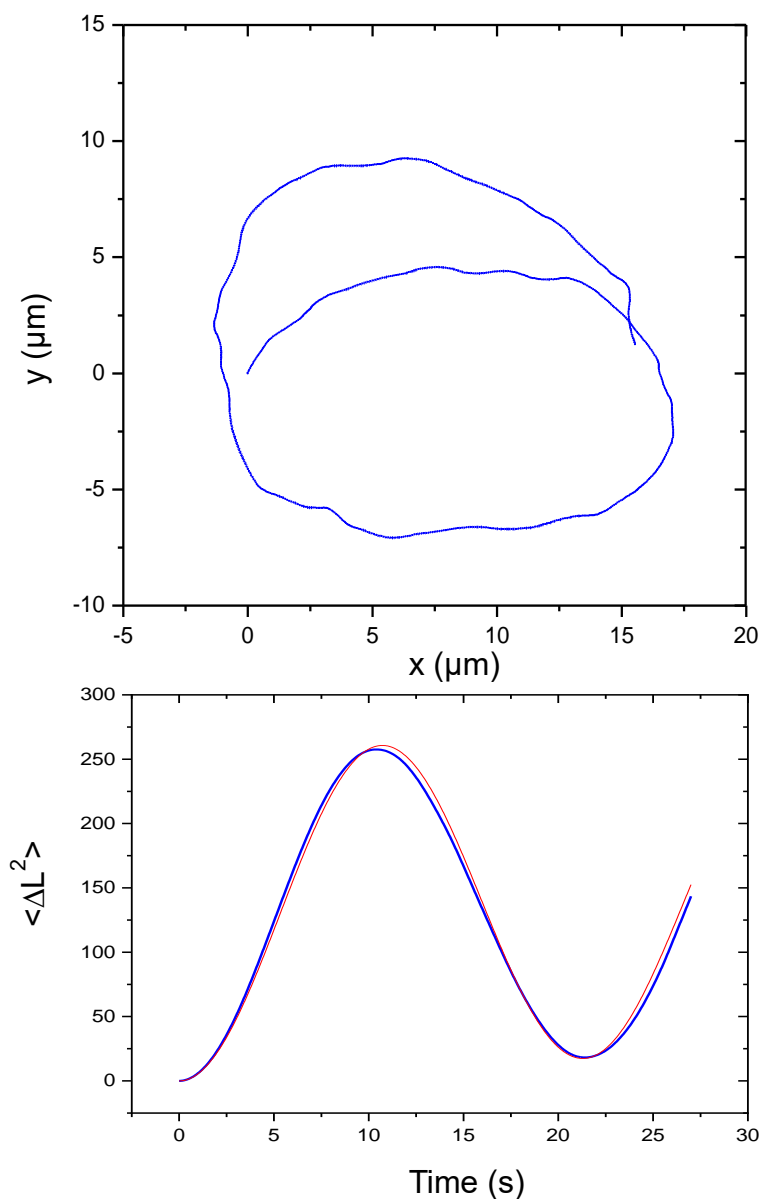


Figure 3-7: Trajectory and corresponding MSD plot with angular velocity fitting ($\omega=0.245$ rads $^{-1}$) for a representative slowly rotating Janus ellipsoid.

These behaviours were analysed quantitatively by calculating the angular velocity for each ellipsoid using the fitting procedure outlined in the methods section of this chapter. Angular velocity analysis revealed a large spread of rotational speeds spanning from 8.88×10^{-7} to 0.295 rads^{-1} with an average value of $0.112 \pm 0.0880 \text{ rads}^{-1}$. These values are much smaller than the reported average angular velocities of well-spaced, hemispherical coated spheres of a similar volume ($1.32 \pm 0.28 \text{ rads}^{-1}$). However, the much larger standard deviation of ellipsoidal data vs. spherical data when compared to the mean value indicates a much larger range of angular velocities than would be expected for a population of spherical Janus swimmers coated using a line-of-sight deposition technique.

This increased deviation from the mean angular velocity is most likely caused by shadowing effects during the coating, levels of adventitious angular propulsion has also been observed for Janus spheres, and was assigned to asymmetries in the coating⁷³. As the ellipsoid has anisotropy and an orientation with respect to the metal source which spheres do not, areas will be blocked from platinum deposition whilst others will have an excessive build-up of platinum. This would cause an imbalance of forces across the catalytic surface and could explain the spinning behaviour seen. This theory will be tested in more detail in chapter 5.

Spheres achieve higher velocities generally $\approx 16 \mu\text{ms}^{-1}$ vs $\approx 5 \mu\text{ms}^{-1}$ for ellipsoidal swimmers. This is consistent with the spheres much higher diffusion coefficient which is approximately double that of the ellipsoid. This is presented in detail later in this section using *Equation 3-3*. Whilst spherical swimmer motion is faster it is much more erratic than ellipsoidal swimmer motion, the ellipsoids larger effective radius acts to reduce random reorientations of swimmers leading to less noisy trajectories

with increased directionality. These differences are important when considering geometries of swimmers for specific applications. Spheres would be more appropriate for applications where high speeds are more important than persistent directionality of a swimmer. Applications such as cargo delivery would be more suited to ellipsoids which have more directional motion and more surface area for cargo carrying.

Currently our observations cannot discern if ellipsoids are translating away from or towards the Pt cap. For this study we depict motion as occurring away from the Pt cap, in analogy to previous observations for Janus spheres and assume analogous mechanisms of motion, although this is not confirmed. A lack of bubble nucleation at the surface of the swimmers is strongly suggestive of a diffusiophoretic or self-electrophoretic mechanism.

In the absence of fuel, ellipsoids displayed only small displacement and random rotations. These were quantitatively confirmed to be consistent with Brownian motion alone (*Figure 3-8*) as the ensemble average MSD plot for 10 Brownian ellipsoids shows no quadratic curve, only linear diffusive behaviour. This confirms that the observed motion is due to the catalytic reaction.

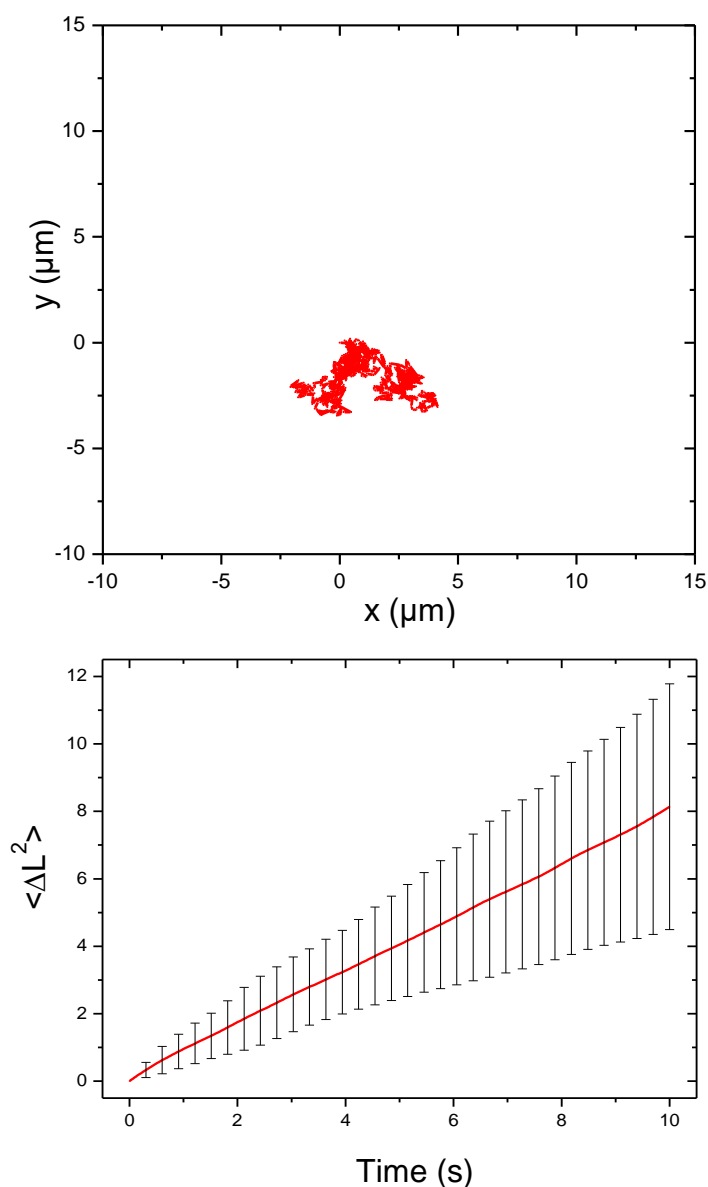


Figure 3-8: Trajectory and corresponding ensemble average MSD plot for a population of 10 Janus ellipsoids undergoing Brownian motion in the absence of hydrogen peroxide fuel. Error bars indicate the standard deviation for each timestep.

These control experiments were also used to determine the diffusion coefficient of ellipsoidal colloids. The experimentally measured diffusion coefficient was on average $0.0730 \pm 0.0107 \mu\text{ms}^{-2}$. This is consistent with the theoretically calculated diffusion coefficient for a prolate spheroid (ellipsoid with 2 short and one long axis) which was calculated to be $0.0761 \mu\text{ms}^{-2}$ using a Perrin friction factor⁷⁴ and the following equations (*Equation 3-3 to Equation 3-5*) derived from the Stokes-Einstein equation⁷⁵:

Equation 3-3:
$$D = \frac{k_B T}{f_{tot}}$$

Where:

D = diffusion coefficient

k_B = Boltzmann constant

T = temperature

$$f_{tot} = f_{sphere} f_P$$

Where f_P is the Perrin friction factor (*Equation 3-4*) for the ellipsoid and f_{sphere} (*Equation 3-5*) is the friction coefficient of a sphere of equivalent volume.

Equation 3-4:
$$f_P \stackrel{\text{def}}{=} \frac{2p^{\frac{2}{3}}}{s}$$

Equation 3-5:
$$f_{sphere} = 6\pi\eta R_{eff} = 6\pi\eta \left(\frac{3V}{4\pi}\right)^{\frac{1}{3}}$$

Where:

η = dynamic viscosity

R_{eff} = effective radius

p = axial ratio, major/minor axis

$$S \stackrel{\text{def}}{=} 2 \frac{\text{atanh } \xi}{\xi} \quad \text{and} \quad \xi \stackrel{\text{def}}{=} \frac{\sqrt{|p^2-1|}}{p}$$

Direction of motion

Ellipsoids in the surface-restricted configuration were qualitatively observed to produce enhanced translation perpendicular to their major axis, with some ellipsoids showing almost linear paths like the example in *Figure 3-6*, and others showing persistent circling behaviour, see *Figure 3-7*.

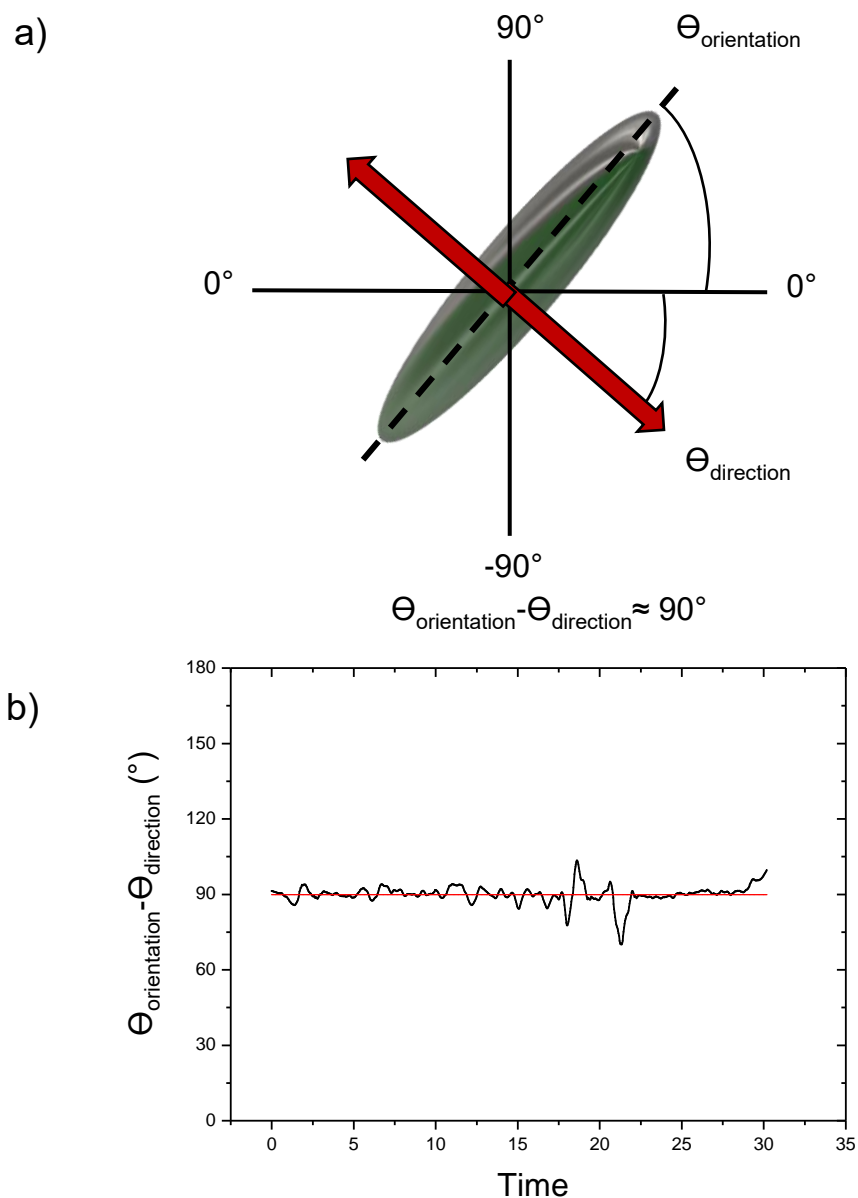


Figure 3-9: a) Diagram showing axis assignment and angles of interest b) Difference between orientation of ellipsoid body long axis and direction of travel for a representative ellipsoidal micro-swimmer.

For the linear trajectories, plots of the angle of translation relative to the angle of orientation of the major axis (See *Figure 3-9b*) confirm the translational motion is almost perpendicular to the major axis. Analysis of the average angle between orientation and direction for a larger population (*Figure 3-10*) revealed that this is consistent for all ellipsoidal swimmers studied, however ballistic swimmers have smaller standard deviations.

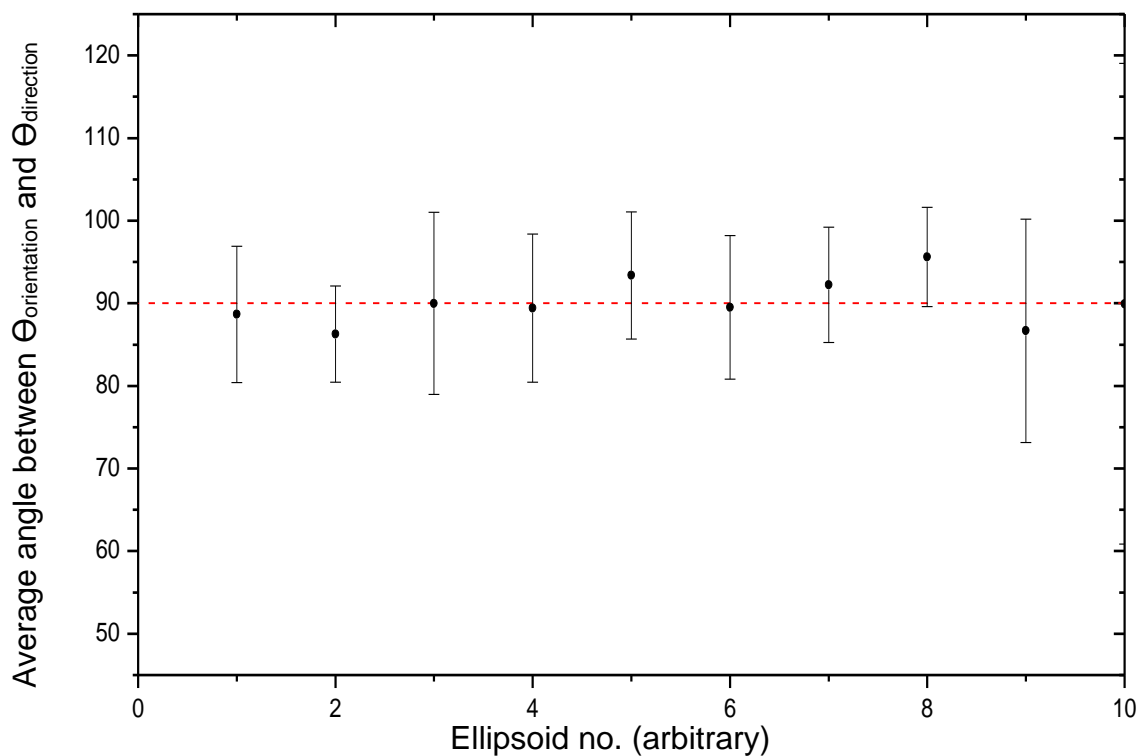


Figure 3-10: Average angle between orientation and direction for a series of swimmers.

These qualitative observations strongly suggest i) the propulsive motion direction is perpendicular to the orientation of the cap/major axis. ii) the platinum coated half adopts a constant perpendicular alignment relative to the boundary as shown in *Figure 3-5b*, with Brownian rotation about the axis shown in red is quenched. This

later point follows from the first: if rotation about this axis was unrestricted, the ellipsoid could not make translations in a persistent direction. This effect is observed in *Figure 3-4a&c* where the motion is initially directed perpendicular to the major axis, but rotations about this axis disrupt the motion and the ellipsoid leaves the plane of vision. The origin of this boundary alignment effect was thoroughly investigated for Janus spheres, and attributed to specific mechanistic details^{48,57}, it is likely that a similar mechanism exists for the ellipsoids, which only differ in geometry.

3.3.3 Self-generated flow

While making these observations to document the motion of the Janus ellipsoids, the motion of occasional non-propulsive small-scale debris particles within the cuvettes revealed that a fluid flow phenomenon, driven by the density differences between the products and reactants of the catalytic reaction, was also occurring in the fuelled ellipsoid suspensions.

As it is well known that such fluid flows can complicate the quantitative analysis of propulsive systems, tracer particles without any catalytic activity were deliberately introduced into the cuvette to aid measurement of the magnitude and direction/stability of the flow. These tracers revealed that the flow was circulatory and well defined relative to the macroscopic geometry of the cuvette, such that circulation occurred along the long axis of the rectangular cuvette. The tracers revealed that the flow velocity in the near surface region ranged from $0.372 \mu\text{ms}^{-1}$ to $1.33 \mu\text{ms}^{-1}$ with an average of $0.682 \pm 0.330 \mu\text{ms}^{-1}$. In addition, the flow uniquely occurred in the presence of fuelled ellipsoidal Janus colloids: control experiments with the same concentration of tracers and ellipsoidal Janus colloids in absence of hydrogen peroxide did not produce any detectable flow. This suggests that the flow is not induced simply by sedimenting tracer colloids/ellipsoids, but instead is likely to indicate density driven convective flow due to the production of less dense product molecules by the catalytically active Janus colloids. The details of this self-generated flow and the dynamics of the ellipsoidal swimmers that are exposed to it will be investigated in detail in chapter 4.

3.4 Discussion

3.4.1 Translational and Angular velocity

Initial experiments with ellipsoidal Janus swimmers revealed an average translational velocity of $4.00 \pm 1.21 \mu\text{m s}^{-1}$ which is in the range of spherical swimmers velocities under similar conditions ⁷⁶. The reduction of speed is likely due to the significantly reduced diffusion coefficient of $0.0761 \mu\text{m s}^{-2}$ compared to a sphere of the same volume which has a diffusion coefficient of $0.139 \mu\text{m s}^{-2}$, this reduction occurs because the ellipsoidal colloid has a much larger effective radius than a sphere.

Ellipsoidal swimmers were also found to have a large range of angular velocities within a single sample coated at standard operating conditions. This “undesigned” or adventitious spin has been also observed for spheres, the ability to enhance and control the level of spin is the subject of detailed investigation in chapter 5

3.4.2 Bulk vs. surface following motion

Most ellipsoidal swimmers were predominantly found to sediment to the lower surface of the cuvette and adopt a relatively stable orientation 20° from the surface. These ellipsoids were restricted to surface following motion in the x-y plane. The direction of this motion was confirmed to be perpendicular to the ellipsoids major axis which is to be expected for coatings along this long axis. Few ellipsoids were found translating in the bulk fluid, but the few that were, were able to translate in the z direction as well as the x-y plane and rotations about the major axis were not quenched. This increase in degrees of freedom adds unwanted complexity to analysis of results with low yields in terms of advantageous behaviour for practical

applications. As such all future investigations of ellipsoidal micro-swimmers in chapters 4 and 5 will focus on surface following ellipsoid at the lower boundary of the cuvette.

3.4.3 Previous work

Whilst related to the concurrent work,⁴⁷, the findings in this chapter do differ in two key aspects: In the publication, there was no mention of a self-generated flow field which this thesis considers in detail in chapter 4 as it introduces additional complexity and alignment effects. Previous work on spherical Pt swimmers in H₂O₂, which produced a flow field, found that the sample holder geometry, colloid size and volume fraction significantly affected the magnitude of the resulting flow⁷⁷. Flow velocities for larger swimmers above the volume fraction threshold produced much faster flows.

The flows generated by ellipsoids in this study are likely a consequence of the sample cuvette geometry which was initially chosen as the sealed system allows for more experimental flexibility once fuel is added. The sample can be easily transported between microscopes or even laboratories. The flow was found to cause an alignment effect and so experiments (chapter 4) were continued using the cuvette to investigate this. Shemi et al. opted for an open chambered cover glass which given its 2d nature and lack of an upper bounding surface would not result in the cyclical flow found in this work.

Despite many experimental similarities, the results of this chapter and that of Shemi's study differ quite dramatically. The range of angular velocities reported by

them was transient, meaning ellipsoids could transition between ballistic and rotational behaviour, often after interacting with another swimmer. This is not consistent with the majority of published work on active colloids, where the motion observed is generally fixed in nature. However, the majority of work focusses on low volume fractions of swimmers where interactions between individual swimmers are unlikely. The dynamics of active swimmers are both complex and easily influenced. Small changes such as the surface chemistry of the boundary where the ellipsoids translate could affect the motion seen and potentially cause this transient behaviour. Whilst interesting, these results suggest that the rotations seen were not caused by catalytic asymmetries which would result in persistent rotations, like the rotating ellipsoids in this chapter.

The persistent rotations seen here are very likely caused by catalytic asymmetries which then allow tuning of the angular velocity which would be ineffective in a transient system. This will be confirmed in chapter 5 where further asymmetries are introduced to increase the rotational velocity.

The comparison here between two similar investigations highlights how sensitive these active swimmer systems are towards seemingly small changes such as chamber geometry or colloid size. This is an issue that effects the whole field of active colloids in that reproducibility of these colloids to guarantee certain behaviours each time still needs much more work. An effort to standardise coating method, thickness and also sample chambers across the field would likely lead to higher reproducibility of swimming devices but would come at large upfront equipment costs for research groups attempting to do so.

3.4.4 Mechanism

The direction of motion, towards or away from the catalyst, could not be discerned for ellipsoidal swimmers. Attempts to observe the direction of motion directly using fluorescence microscopy were unsuccessful due to the unprecedented amount of fluorescence bleaching that occurs when ellipsoids are exposed to the electron source during coating. As spherical swimmers do not experience this level of fluorescence bleaching, it is likely that changes in the distribution and stability of fluorophore occurred during the stretching process which made the colloids more vulnerable to bleaching. Without confirmation of this direction, it is impossible to assign a definite mechanism of motion for ellipsoidal swimmers, however it is extremely likely that the mechanism is the same as for Pt/PS spherical swimmers which are analogous in all ways except for geometry. Lack of evidence of any bubble nucleation on the surface of the colloids and an extreme sensitivity to contamination are strongly indicative of a self-electrophoretic mechanism like the spherical swimmers²².

The stable orientation of ellipsoids on the lower boundary, with rotational quenching about the major axis also lends credibility to an electrophoretic mechanism. Das et al. modelled spherical Pt-PS Janus swimmers near a bounding surface and found that rotational quenching and orientational stability of active swimmers on a surface is dependent on a self-electrophoretic mechanism where the motion is away from the Pt cap⁴⁸.

3.5 Conclusions

Observation of the motion of $\sim 9 \times 4 \mu\text{m}$ Janus ellipsoidal micro-swimmers in hydrogen peroxide fuel revealed that when coated along their major axis the ellipsoids travel in a direction perpendicular to this, as predicted in theoretical literature. A range of angular velocities from 8.88×10^{-7} to 0.295 rads^{-1} over a sample of 20 separate ellipsoids is observed within a single sample of swimmers produced under standard conditions. Swimmers which are considered high spin in this sample ($>0.15 \text{ rads}^{-1}$) account for 27.27% of the total population and are attributed to defects in the catalytic coating based on previous literature²¹. The fixed, non-varying rotational velocities observed in ellipsoidal swimmers suggest a strong link between the cap shape, including defects, and the resulting motion. This link between cap shape and angular velocity will be exploited in chapter 5, where the symmetry of the cap will be intentionally broken, producing ellipsoidal swimmers with significantly higher angular velocity.

In addition to the typical motion, it was found that even at very low volume fractions, the decomposition of hydrogen peroxide by ellipsoidal swimmers generates a significant cylindrical density driven convective flow within the sample cuvette. This is likely due to the significantly increased catalyst surface area when compared to an analogous sphere. The flow characteristics and the dynamics of ellipsoidal swimmers in response to this flow will be explored in detail in the following chapter.

Chapter 4:

Flow phenomena in ellipsoidal micro-swimmers

4 Flow phenomena in ellipsoidal micro-swimmers

4.1 Introduction

Chapter 3 noted that under ‘normal’ testing conditions, ellipsoidal micro-swimmers generate an appreciable convective flow within the sample cuvette, which was absent in a related study. This convective flow is significantly more persistent compared with their spherical counterparts. A schematic of the cuvette and resulting flow field, as qualitatively observed during these initial experiments, is shown in *Figure 4-1*.

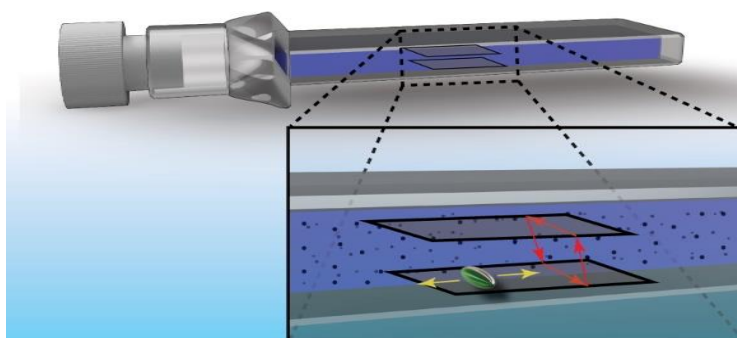


Figure 4-1: Schematic of the experimental set up leading to a convective flow (red arrow)

Our system for motion relies upon a catalytic decomposition of platinum by hydrogen peroxide into gaseous oxygen and water. As the products (H_2O and O_2 ; densities 0.998 gcm^{-3} and 0.00143 gcm^{-3} respectively) of this reaction are less dense than the reagents (H_2O_2 ; density 1.45 gcm^{-3}), density differences are generated around the colloids which causes a rising convective flow. Due to the imposed boundary of the sample cuvette walls the convective flow circulates back around forming a flow field that follows the cuvette geometry⁷⁷, see *Figure 4-2* for diagram.

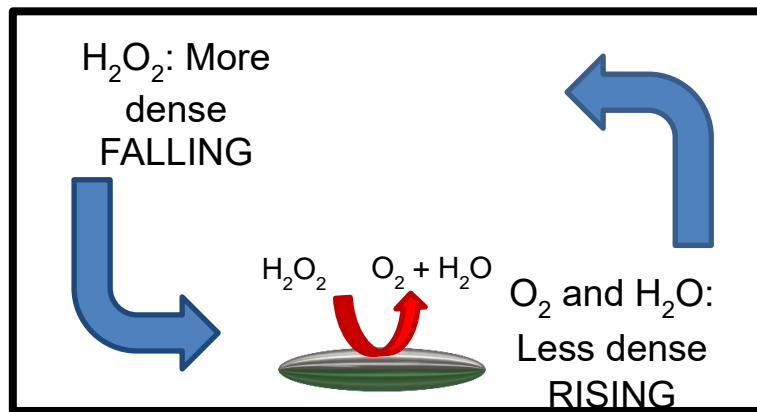


Figure 4-2: Diagram showing the formation of cyclical flow due to density differences of products and reactants within a closed cuvette.

In order to understand this unusual observation, investigation of the origin of the flow and its implications on the autonomous motion of ellipsoidal micro-swimmers was conducted.

Initial qualitative observations also suggested that the inbuilt asymmetry of the ellipsoidal swimmers introduces a preference to align with the major axis almost parallel to the direction of the driven flow field, Figure 4-3. This chapter describes how this leads to the ellipsoids performing motion that is biased by the self-generated flow, which in turn can be related to the macroscopic shape of the container they are in.

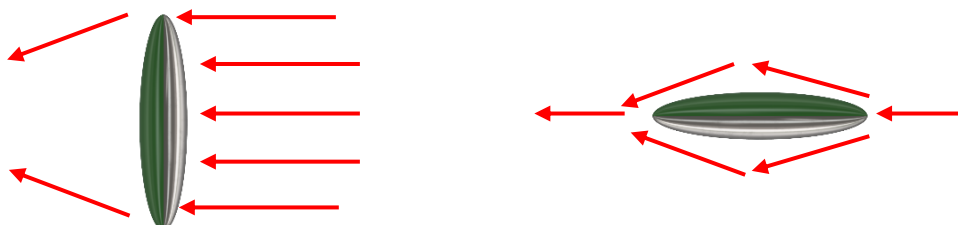


Figure 4-3: Diagram showing the effect of orientation of ellipsoidal colloids in a density driven flow field. Red arrows indicate the direction of the flow.

4.2 Experimental

4.2.1 Convective Flow

Ellipsoidal colloids were coated and tested using the procedure outlined in chapter 3. In these experiments 0.1% wt. solids of (1 μm diameter) polystyrene tracer particles (Sigma-Aldrich) were added to allow any convective flow to be visualised. The motion of each tracer particle that remained within the field of view during a given video was averaged in order to obtain an estimate of the flow velocity (magnitude and orientation). This was performed by averaging the vectors indicating the start and end position of each useful tracer particle. This average flow vector was then used to correct the x,y trajectories for the influence of flow, by subtracting the average x and y flow displacement contribution from the observed x and y displacements as a function of time.

An estimate of the angle of the direction of travel, $\Theta_{\text{direction}}$, for the ellipsoidal colloids was obtained from these flow corrected trajectories; this was after smoothing with the Savitzky-Golay algorithm set at 30 pts to reduce noise in the direction angle data due to Brownian motion.

4.2.2 Induced Flow

To investigate the self-generated flow phenomena, it was necessary to also conduct experiments in a well-defined externally induced flow. A Dolomite P-Pump (*Figure 4-4*) was used, at 500 mBar, to produce a flow of approximately $10 \mu\text{m s}^{-1}$ through a PDMS sample chamber. Uncoated polystyrene ellipsoids ($2 \times 9 \mu\text{m}$) and spheres ($2.16 \mu\text{m}$ diameter) were introduced to the flow and observed near the lower surface,

close to the centre of the sample chamber. The colloids were tracked using a (Nikon eclipse T-100 microscope) equipped with a Pixelink PL-B742F camera.

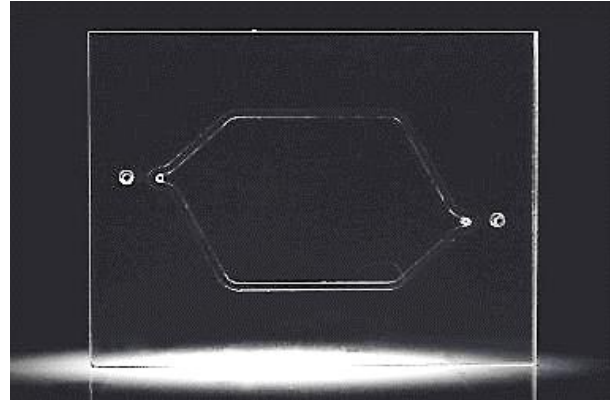


Figure 4-4: Photographs of the pump and sample chamber used to create the externally imposed flow.

4.3 Results

In this work observations focused solely on Janus ellipsoids moving near the lower surface of the sample holder, in order to avoid the complexities of considering the rotational freedom in the bulk solution discussed in chapter 3.

An externally imposed flow field analogous to the flow produced by the Janus ellipsoids was used to run control experiments in the absence of the catalytic reaction after the discovery that active ellipsoids show some degree of alignment. These experiments were conducted in order to determine whether inactive ellipsoids align in a flow field. An inherent alignment effect for ellipsoidal shaped colloids reinforces the conclusion that active ellipsoids in a flow also align, thus enabling crossflow motion.

This well-defined flow was also used to help understand the dynamics of the self-convective flow and allow further fitting of the flow profile experienced by the active ellipsoids in the presence of the catalytic reaction. For this reason, the results of the control experiments and flow profile predictions are presented before the self-generated flow.

4.3.1 External imposed flow (Control)

A Dolomite P-pump was used to produce a relatively stable flow with an average mass flow rate of $4.078 \times 10^{-8} \text{ kgs}^{-1}$. This gives an average tracer velocity of $\approx 7 \text{ } \mu\text{ms}^{-1}$ (measured by LABView software). This was used as a control experiment to investigate the dynamics of passive ellipsoids in a low-speed flow.

4.3.1.1 Prediction of the velocity profile in the chamber

To determine the characteristics of the flow regime created by the pump, the Reynolds number of the fluid was calculated using experimentally determined measurements. V_{avg} was calculated from the experimental mass flow rate of $4.078 \times 10^{-8} \text{ kgs}^{-1}$ to be $37.18 \text{ } \mu\text{ms}^{-1}$ using *Equation 4-1*.

Equation 4-1:
$$\dot{m} = \frac{\Delta m}{\Delta t} = \rho A \vec{V}$$

Where:

\dot{m} = mass flow rate (kgs^{-1})

m = mass (kg)

t = time (s)

A = flow area (m^2)

\vec{V} = average velocity (ms^{-1})

The experimentally determined velocity was then used to calculate the Reynold's number using *Equation 4-2* and *Figure 4-5*.

Equation 4-2:
$$Re = \frac{\rho V D_h}{\mu}$$

ρ = density of fluid (kgm^{-3})

V = velocity of fluid (ms^{-1})

D_h = hydraulic diameter (dimensionless) , $D_h = \frac{4(w.h)}{2(w+h)}$ 78

μ = dynamic viscosity (Pa s)

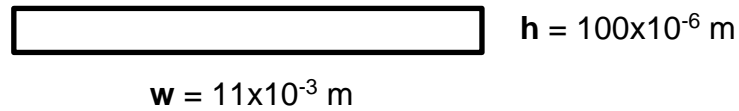


Figure 4-5: Schematic showing relevant dimensions of the sample holder for Reynold's number calculation.

The Reynolds number of the fluid in the chamber was determined to be ≈ 0.0825 , which is considered laminar flow (< 2000)⁷⁹.

The velocity profile of the flow chamber was approximated using the simplified equation for laminar flow in ducts with rectangular cross sections⁸⁰.

Equation 4-3:
$$V = (1 - |\hat{x}|^m) - (1 - |\hat{z}|^2)$$

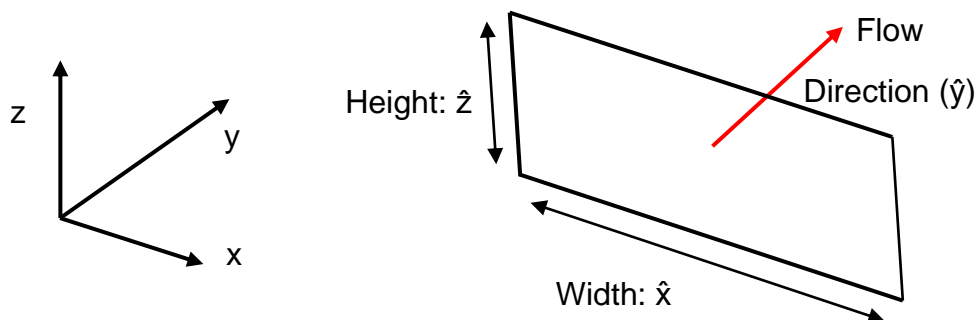


Figure 4-6: Schematic showing coordinates as assigned for these calculations.

Where:

V = reduced velocity, V/V_{\max}

\hat{x} = reduced width, $2x/w$

\hat{z} = reduced height, $2z/h$

$m = 1.54 \times w/h$

V_{\max} was calculated for the external flow pump from the calculated average velocity, where $V_{\max} = 2 \times V_{\text{avg}}$, which corresponds to a V_{\max} of $74.36 \mu\text{ms}^{-1}$.

Using the calculated V_{\max} , the z-profile of the flow was approximated across the entire z-axis and in the region of interest where experiments were performed (within $10 \mu\text{ms}^{-1}$).

Z-Shear profile over the whole sample chamber at $x=\text{width}/2$

The flow profile in the z direction over the whole sample chamber shows a dramatic increase from the centre of the chamber where the shearing is near zero, to a very high shear rate near the boundaries of the sample chamber.

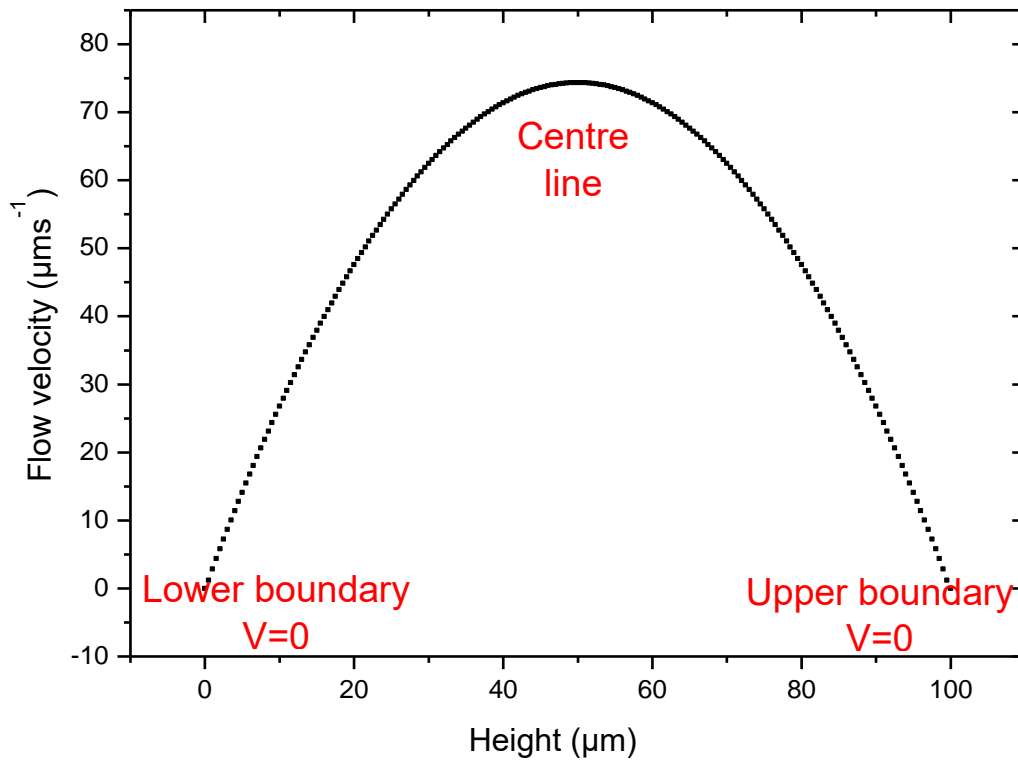


Figure 4-7: The predicted flow profile for a laminar shear flow in the z direction

Z- Shear profile in the region of interest (within 10 μm of the lower boundary)

As all the ellipsoid observations were performed within a few microns of the lower boundary, this region of interest was investigated further. It can be seen in *Figure 4-8* that the flow velocity in this region increases in an almost linear fashion with a gradient/shear strain rate of $\approx 2.25 \text{ s}^{-1}$. This is in dramatic contrast with the centre of the sample chamber where the shear strain rate is 0 and increases to just 0.4 s^{-1} at $10 \mu\text{m}$ from the centre.

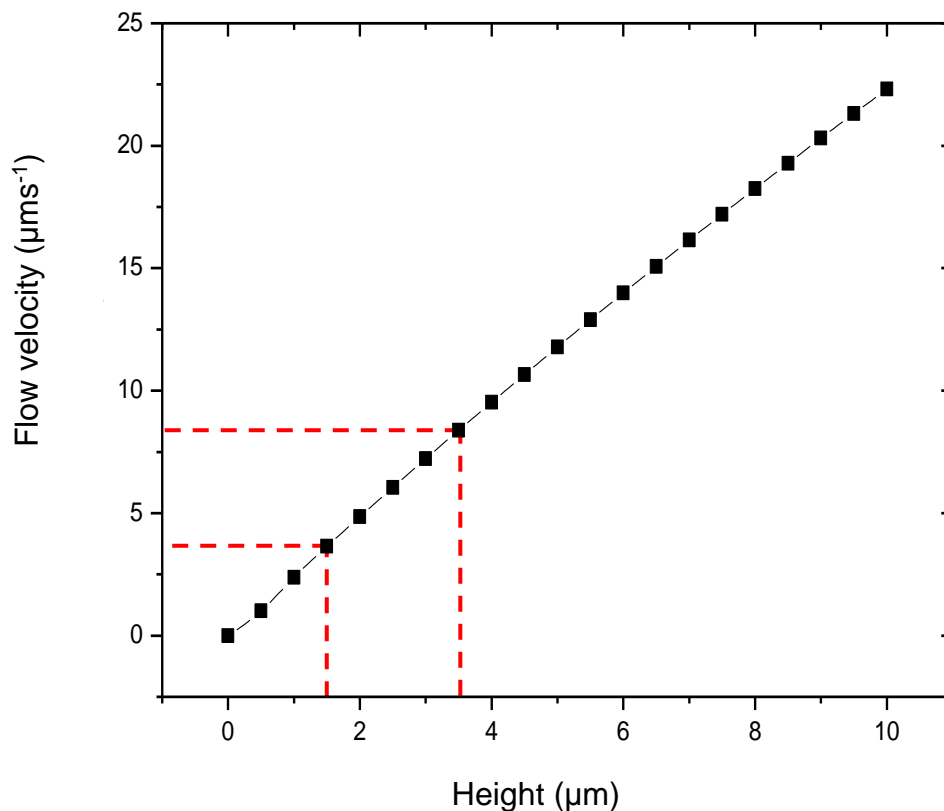


Figure 4-8: Z-shear profile within $10\mu\text{m}$ of the lower boundary. The expected range of heights and their corresponding experienced flow velocities are indicated within the dashed red lines.

X- shear profile at $z=2.5\mu\text{m}$ from the lower boundary

The height of the ellipsoids in the external flow was estimated using the predicted z shear profile and the experimentally measured passive ellipsoid velocities. An average velocity of $\approx 7 \mu\text{ms}^{-1}$ correspond to an estimated height of $2.5 \mu\text{m}$ from the lower surface of the sample chamber. These values were used to predict the profile of the x -shear experienced at the experimental height. As the chamber is very wide compared to it's height, the amount of shear experienced across the chamber is very low compared to the dramatic shearing in the z -direction seen in *Figure 4-9*

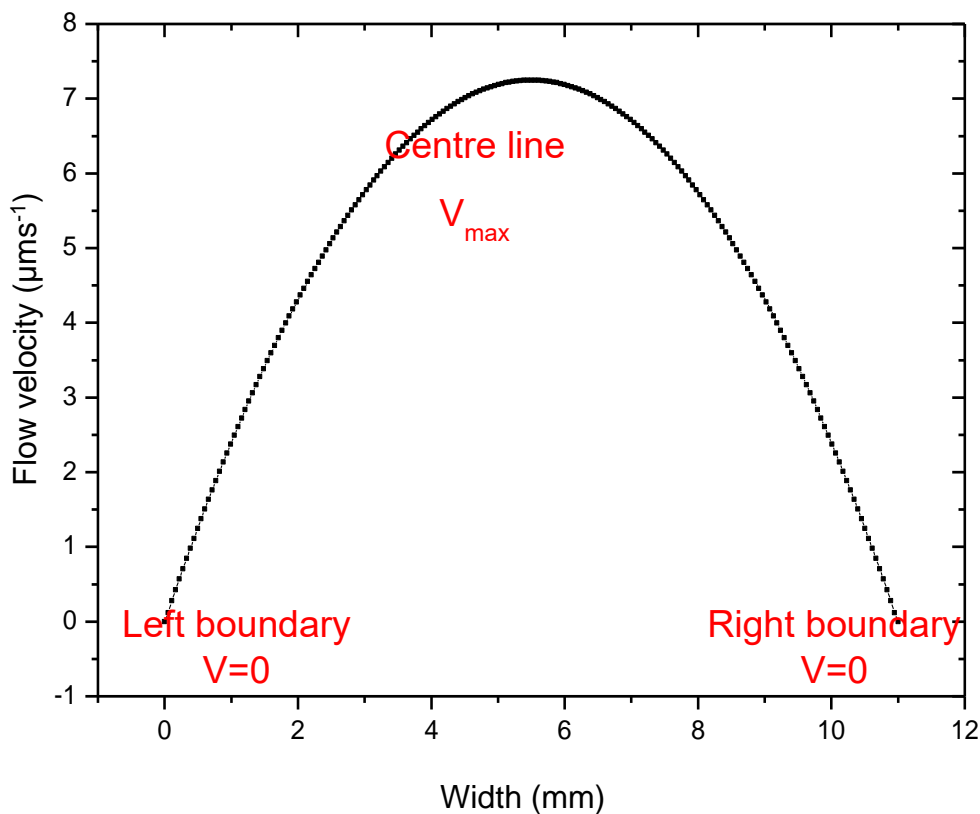


Figure 4-9: Prediction of the flow profile across the width of the sample holder at a height of $2.5 \mu\text{m}$.

X-shear profile in region of interest (within 500 μm of centre of chamber when $z=2.5\mu\text{m}$)

When the region of interest is considered, it becomes clear that the x- component of the fluid shearing is negligible and does not contribute to the alignment effect seen for ellipsoidal colloids. Note that this analysis of x shear is not sensitive to the details of the height selected. The magnitude of the flow velocity is affected by changes in height, but the amount of shear is unchanged in the region of interest when different heights are selected, this can be seen in *Figure 4-10* where the red line shows shearing 1 μm below the experimental height and the blue line shows shearing 1 μm above.

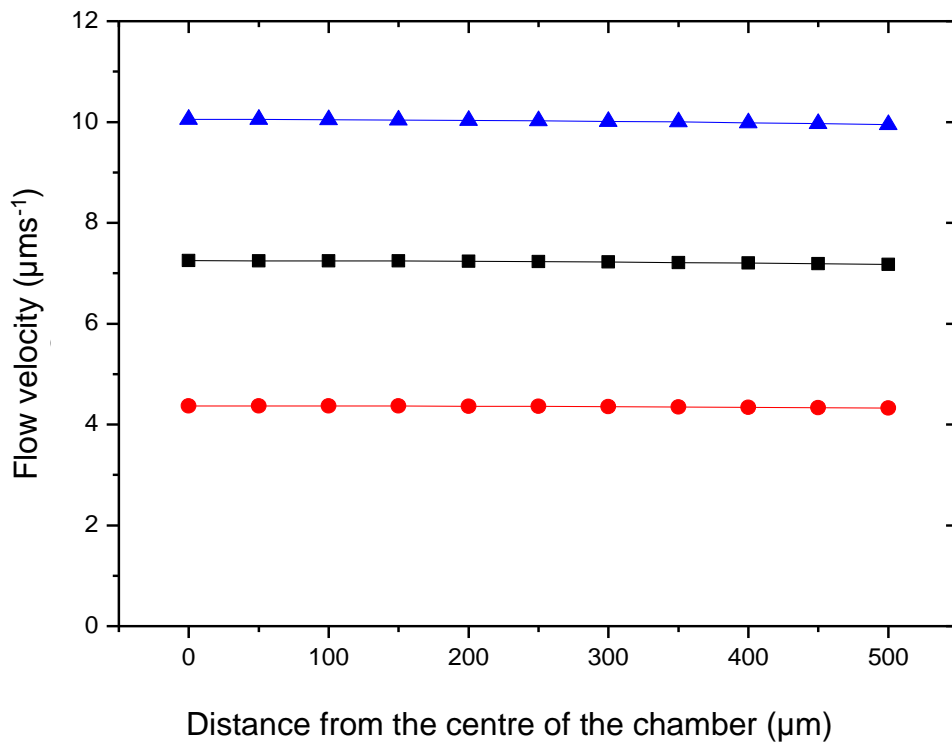


Figure 4-10: X- shearing in the region of interest near the centre of the sample chamber at our experimental height (black) and $\pm 1\mu\text{m}$ from the experimental height red is 1 μm below the experimental height whilst blue is 1 μm above.

4.3.1.2 Experimental analysis of velocity profile in induced flow

2.16 μm diameter spherical tracer particles were used to establish the direction and flow velocity; typical trajectories for these tracer particles in one representative field of view can be seen in *Figure 4-11*.

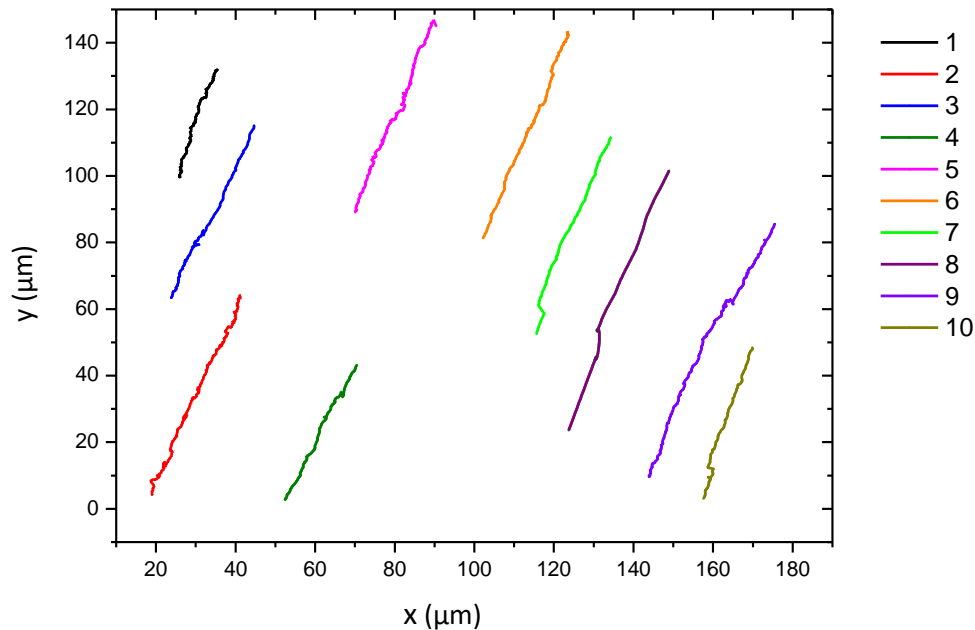


Figure 4-11: Trajectories of tracer particles in a pressure pump induced flow for 10 seconds. Tracers have been numbered from left to right.

The tracers were assigned a number corresponding to their position on the graph, from left to right. Analysis of the velocities of the tracers (*Figure 4-12*) show a trend of increasing velocity from left to right, which is inconsistent with the theoretical prediction that there is negligible x- shearing at constant height. Considering that these experiments were recorded near the centre of the cuvette where x-shearing is expected to be even lower, this is likely to be explained by the large amount of z shearing. A height change of just 0.5 μm can cause a change in velocity of $>1 \mu\text{ms}^{-1}$. Changes in height of up to $\approx 2 \mu\text{m}$ are not obvious in the recorded videos, due to the

focal depth of the objectives used. We expect this leads to the velocity variations in colloids that are recorded at nominally the same focal height, preventing us experimentally confirming the low x-y shear.

It is however also possible that these inconsistencies stem from deviation in our experimental conditions that are not considered in the theoretical predictions.

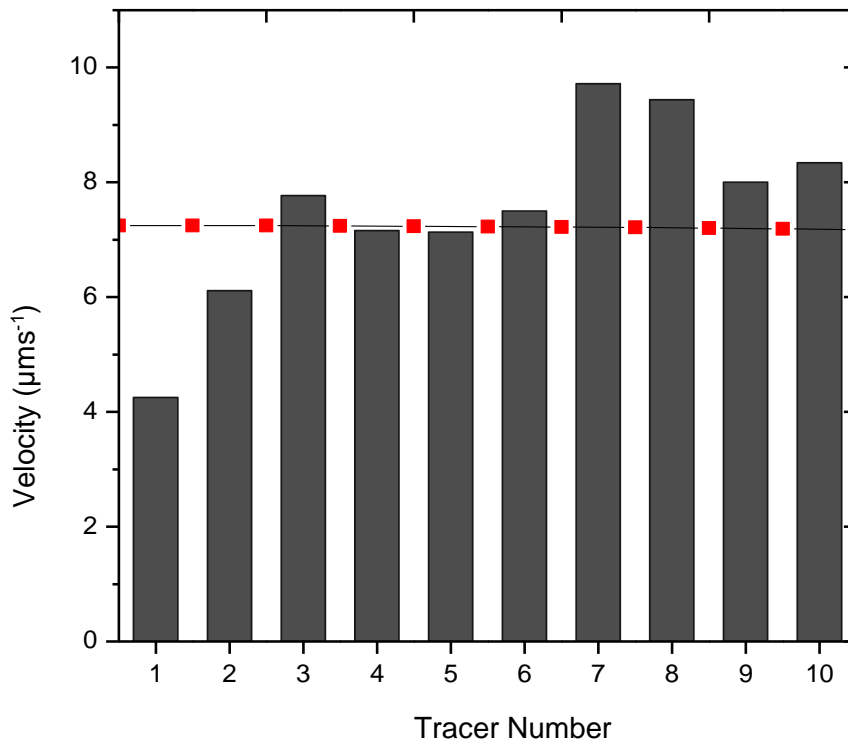


Figure 4-12: Velocities of tracers shown in Figure 4-11, the tracer position corresponds to the number assigned in Figure 4-11. The predicted flow profile at this height is overlaid in red squares.

4.3.1.3 Orientation and Direction of motion of passive ellipsoids

Figure 4-13a shows a representative trajectory from a non-active ellipsoid, overlaid with a time-lapse microscope image (20x magnification). Qualitatively it can be seen that in the absence of a catalytic system of motion, the colloid's major axis predominantly aligns close to the flow direction and travel is in this direction. Whilst the ellipsoids mostly prefer to align their long axis parallel to the flow direction, occasionally they will lose this alignment and spin out before quickly realigning as they were before. This is likely due to slight asymmetries in the shape of the colloids. This effect can be seen in the time lapse image presented in Figure 4-13c.

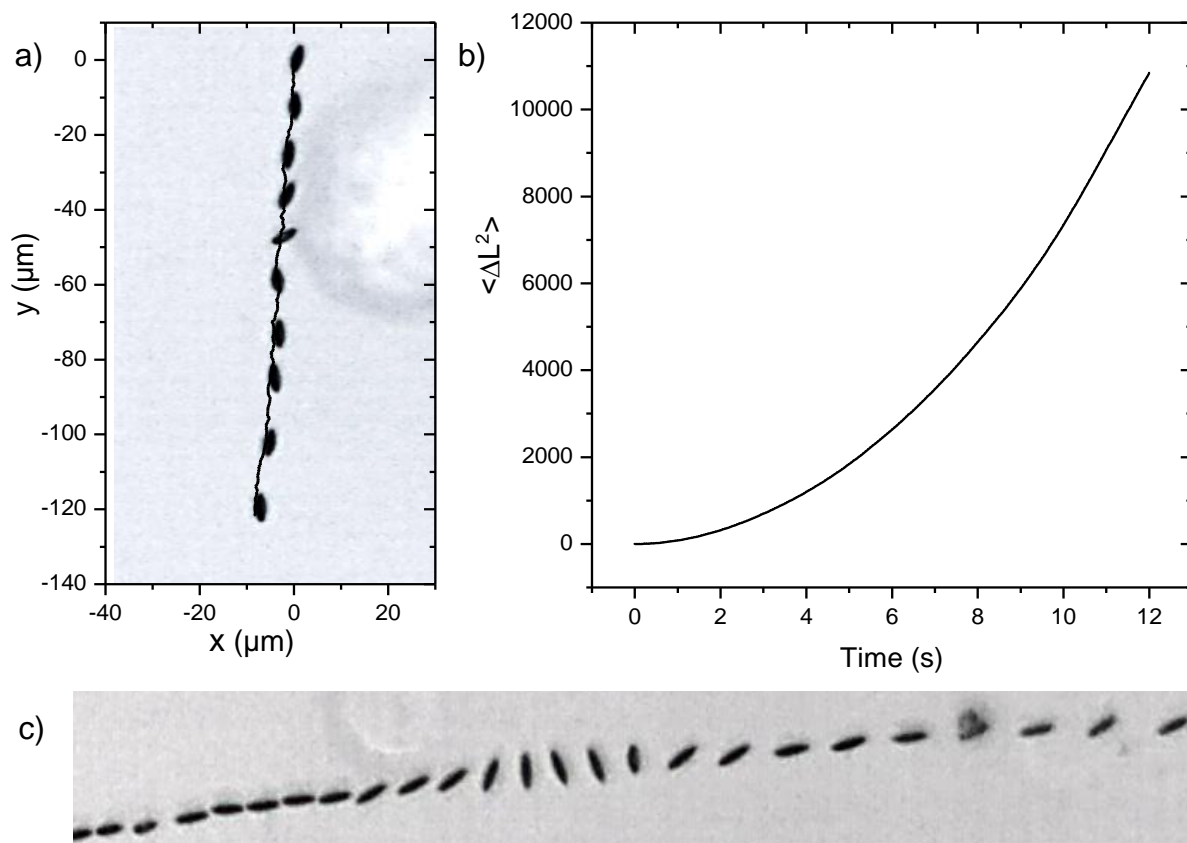


Figure 4-13: a) Trajectory of a passive ellipsoid travelling in a $10 \mu\text{ms}^{-1}$ externally induced flow; overlaid with a time lapse image. b) MSD analysis of trajectory a). c) A 30s time lapse image of an ellipsoid translating in a $10 \mu\text{ms}^{-1}$ externally induced flow

The MSD data for the colloid shows a continuing quadratic, not returning to linear – as is seen for catalytic colloids in still fluids, consistent with ballistic motion with a constant velocity indicative of particles which are translated by the steady state imposed fluid flow ⁷⁰. The quadratic is maintained throughout the entire video capture, with no change to diffusive behaviour which would appear as a straightening of the MSD curve.

For passive ellipsoids in a stable flow, perfect alignment was considered to be:

$$\theta_{Flow} = \theta_{Direction} = \theta_{Orientation}$$

The recorded orientation Θ_O and calculated direction of motion Θ_D for each frame of the videos were subtracted from the overall flow direction, Θ_F and binned to give a distribution of the frequency of a certain angle. This data was collated over a series of 15 separate colloids and is displayed as a time fraction in *Figure 4-14*. For example, the wind-rose diagram for direction of motion (*Figure 4-14a*) shows that, when all ellipsoidal colloids are considered the direction of motion is within $\pm 10^\circ$ of the flow direction for $\approx 37\%$ of the time that they are moving. Almost 65% of the total moving time is within $\pm 30^\circ$ of the flow direction. This is strongly indicative of an alignment effect, as in the absence of one, the wind-rose diagram should show an even distribution of angles for the direction of motion with time fractions $\approx 11\%$ each.

The data for the orientation (*Figure 4-14b*) shows a weak degree of parallel alignment with the flow direction, little time is spent within $\pm 10^\circ$ of the flow direction. Symmetrical peaks are instead seen between $\pm 10-30^\circ$, and the average angle

between the major axis and the flow direction was calculated to be 25.77° which suggests that alignment of the major axis is offset by around $\pm 20-30^\circ$. As with the direction data, this does indicate a degree of alignment as the distribution is not evenly spread. However, it is not the expected result of the major axis aligning parallel with the flow. The time-lapse image seen in *Figure 4-13c* shows an ellipsoid undergoing loss of orientational alignment and 'spinning out' of its initial path, whilst orientational alignment is lost the direction of motion is maintained. These periods of misalignment contribute to the offset seen for orientation data and may be due shape imperfections which affect hydrodynamic interactions of colloids.

Despite this misalignment of the orientation, the wind rose diagram for the direction of motion (*Figure 4-14a*) shows a significant preference towards moving directly parallel with the flow direction.

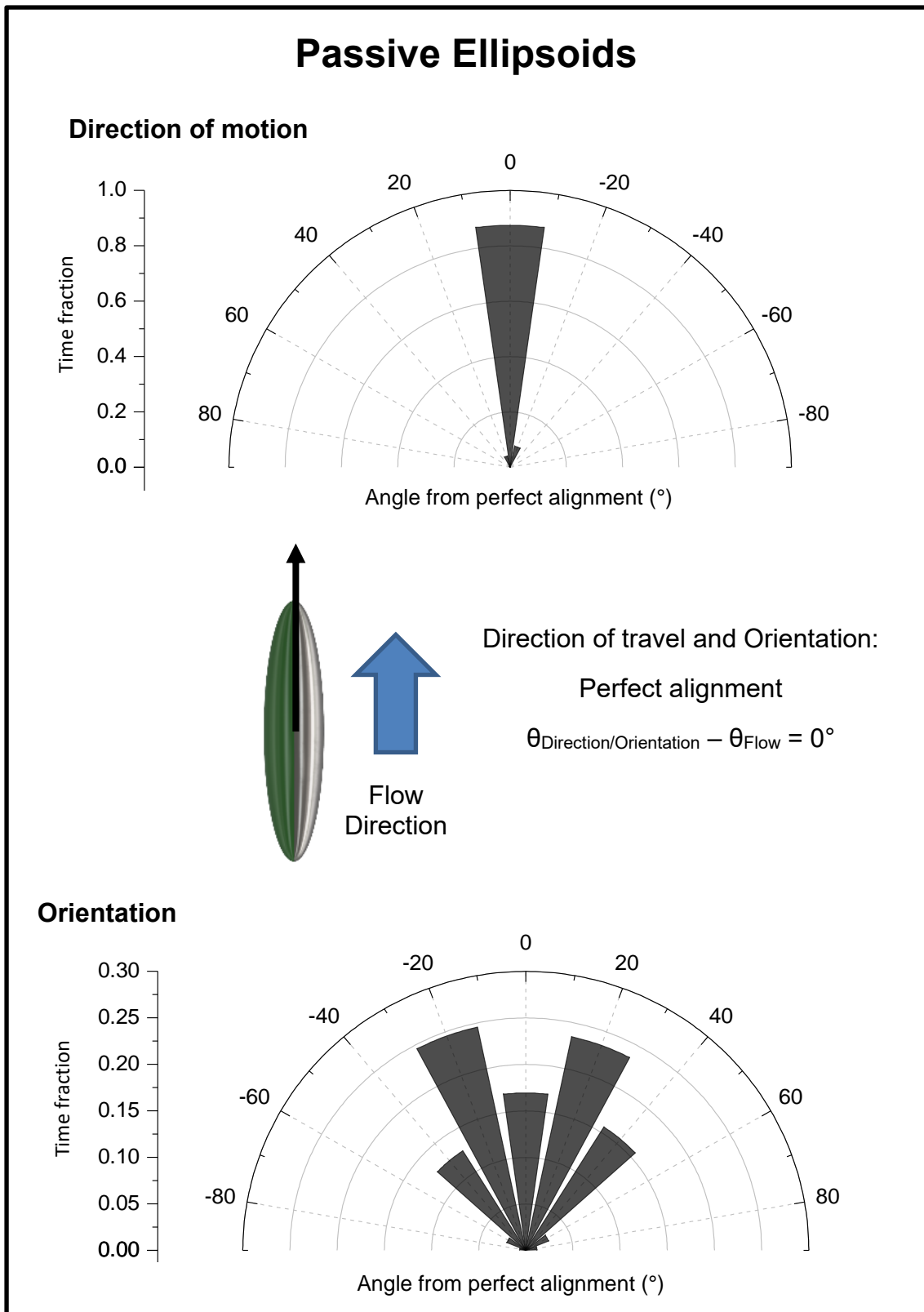


Figure 4-14: Binned wind rose diagrams showing alignment with the direction of flow for passive ellipsoidal colloids in a $10 \mu\text{ms}^{-1}$ imposed flow: a) distribution of direction angles. b) distribution of orientation angles.

4.3.2 Self-generated convective flow

Catalytically active ellipsoids were observed on the lower boundary of the cuvette in the presence of ($2.16\mu\text{m}$) spherical tracer colloids. Qualitatively it can be seen (*Figure 4-15*) that the ellipsoid translates across the flow field not down the streamlines. MSD analysis shown in *Figure 4-16* confirms that this motion is due to propulsion rather than convection. The quadratic curve seen up until $\approx 20\text{s}$ straightens out as a degree of Brownian rotations lead to linear diffusive behaviour which is not seen when convection is the sole cause of propulsion, as in *Figure 4-13b*. This long term return to diffusion also illustrates that the cross-flow migration is a statistical tendency rather than reflecting complete control of trajectory due to a

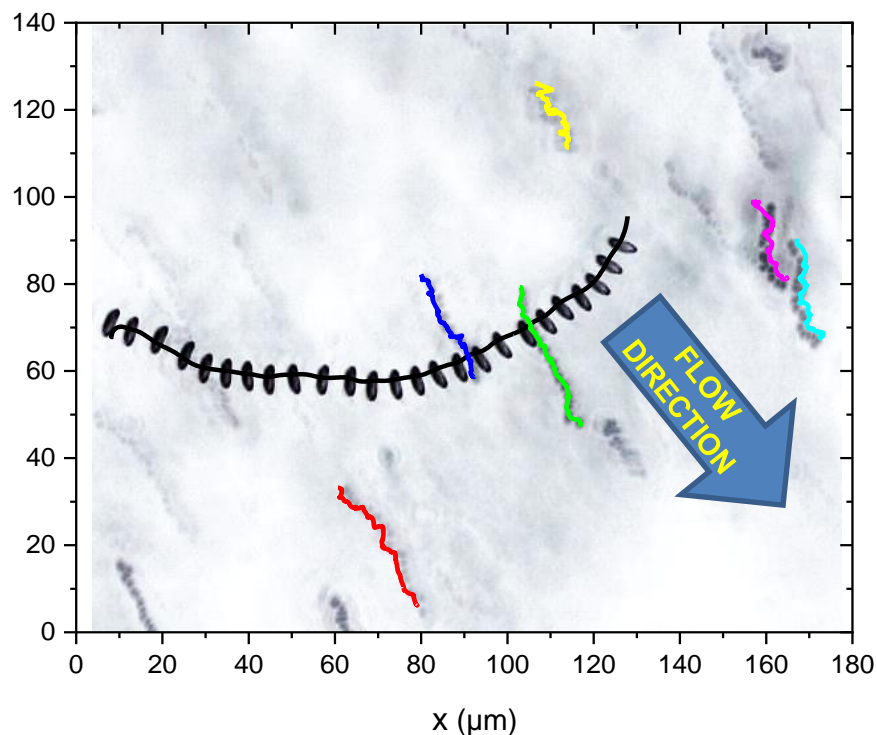


Figure 4-15: A representative trajectory of an ellipsoidal micro swimmer, overlaid with a time lapse image (30s). Tracer particles illustrating the self-induced convective flow field are shown in colour whilst the propulsive ellipsoid is shown in black.

fixed orientation, and the ellipsoid still undergoes a degree of stochastic rotation. This is reminiscent of the case of gravitational alignment of spherical Janus colloids where Brownian rotation and gravitational alignment compete to produce the observed trajectories.⁸¹

It is shown in the literature that objects with a long body axis, such as prolate ellipsoids studied here, have a preferential orientation with respect to different types of flow fields⁸²⁸³⁸⁴. The examples given are of turbulent or 'simple shear' flows and do not match the conditions of the flow that is tested in this chapter (laminar shear flow in a duct); however, it seems likely that the ellipsoidal colloids will adopt a preferred orientation with respect to any linear flow. This is supported by the results in the previous section where passive ellipsoids preferentially aligned in the direction of the flow.

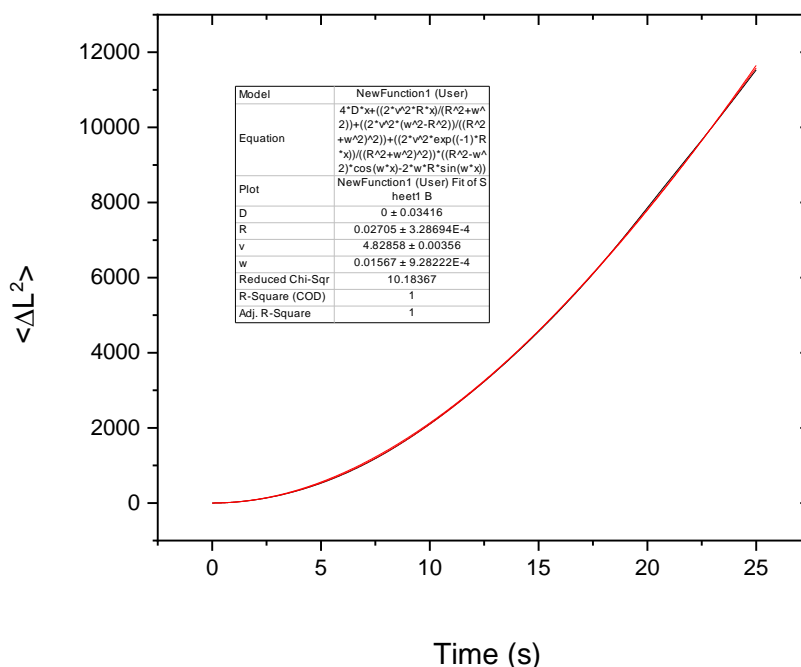


Figure 4-16: MSD graph for the swimmer shown in Figure 4-15.

Due to the lack of literature available on the specific conditions used during experiments, a prediction of the flow profile was used to understand the dynamics of the self-generated convective flow and investigate the cause of the alignment effects observed.

4.3.2.1 Fitting of the flow profile

The case of self-generated convective flow which is discussed in this section is significantly more complex than the externally imposed flow. The z-flow profile in the case of a convective flow in a channel, where $H < L$, has been described mathematically by Williams et al. using the equation⁸⁵:

Equation 4-4:
$$u_{x(z)} = u_b \left[\frac{1}{6} \left(\frac{z}{H} \right)^3 - \frac{1}{4} \left(\frac{z}{H} \right)^2 + \frac{1}{12} \left(\frac{z}{H} \right) \right]$$

Where:

$u_{x(z)}$ = flow velocity at a given height (z)

$u_b = \beta g H^3 / 96 \nu$, a characteristic velocity of the flow⁸⁶

Z = z position

H= total height

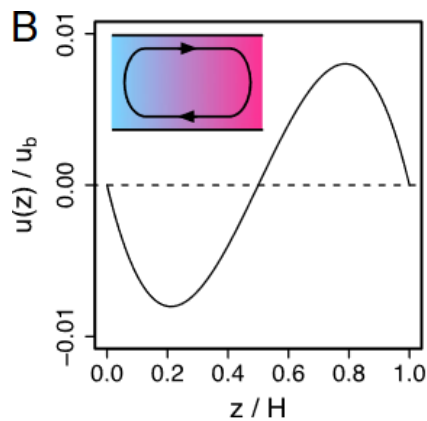


Figure 4-17: Predicted thin ($H < L$) channel velocity profiles for a flow due to convection from Williams et al⁸⁵.

When plotted over a range of z (height) values this gives the predicted flow profile seen in Figure 4-17.

In a self-imposed convective flow, the less dense products rise and the denser reactants fall generating a cyclical flow within the cuvette, the result of this is two cross sectional flows, one on top of each other, going in opposite directions. Where these directional flows meet at $H/2$, the velocity reduces to zero which can be seen in Figure 4-17.

This predicted flow profile is expected to resemble the flows experienced within the cuvette when active ellipsoidal swimmers are undergoing chemically driven propulsion. As such, Equation 4-4 has been fitted with the experimental parameters depicted in Figure 4-18 and experimentally measured variables to produce an estimated flow profile for the self-induced convective flow. X- shearing in this system has not been described but given that the flow velocity at the experimental height is very low and the width of the chamber is much larger than the height, it is assumed

that horizontal shearing would be negligible similar to the case for passive ellipsoids in section 4.3.1.1.

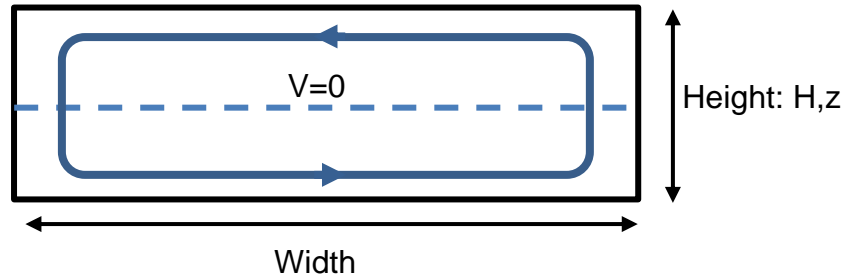


Figure 4-18: Diagram depicting the measurements used to fit the flow profile to experimental parameters.

The flow was confirmed to be laminar and have a Reynolds number of 0.0267 calculated using Equation 1-1:

$$R_e = \frac{\rho v L}{\mu}$$

with the experimentally measured parameters.

The measured average tracer velocity was substituted into the equation at the estimated height from the cuvette boundary that we conducted our observations (2.5 μm). This was then used to calculate u_b for these experiments and produce an extrapolated graph of actual velocity vs. height.

Shear profile over the whole sample chamber

It can be seen in *Figure 4-19* that the calculations predict a significant z-shear component in the near boundary region which decreases towards the cuvette centre.

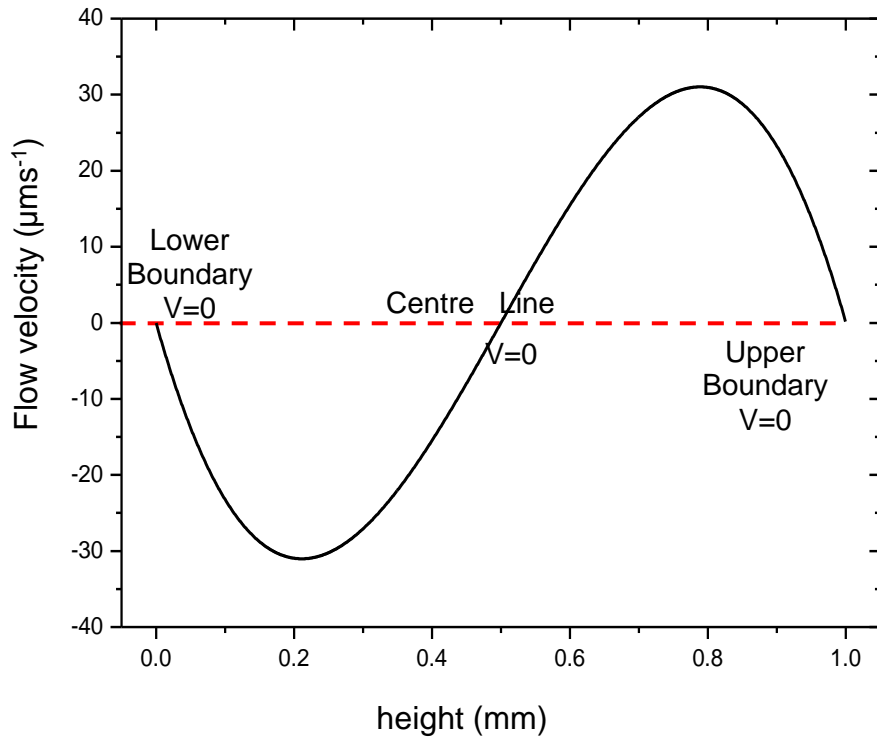


Figure 4-19: Approximate z-shear profile for the self-convective flow in a cuvette of defined geometry.

The negative gradient of flow velocity for the lower half of the cuvette depicts its direction with respect to the flow field above. For simplicity, the profile of the region of interest will be depicted as having a positive gradient.

Shear profile in the region of interest (within 10 μm of the lower boundary)

As these experiments were conducted near the bottom surface of the cuvette, within a few microns of the surface, a graph was produced in this region of interest to get a closer look at the shear rate. *Figure 4-20* shows the increase in flow velocity from zero at the lower boundary in the z direction. It can be seen that this is a very steep linear increase in velocity over just 10 microns. This dramatic z-shearing could be responsible for the alignment effect seen in ellipsoidal swimmers.

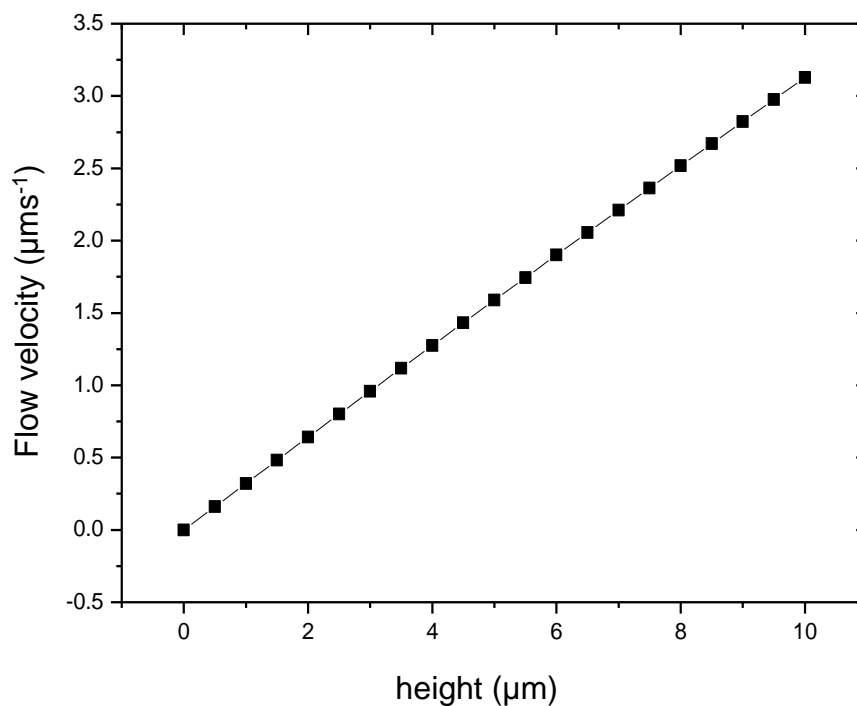


Figure 4-20: Approximate z-shear profile for the self-convective flow in the experimental region of interest (height < 10 μm .)

4.3.2.2 Experimental Analysis of Self-Convective flow

Tracking of the tracer colloids allowed us to quantify the average direction, Θ_{FLOW} , and magnitude of the generated flow in each video. For each tracer that remained in the field of view for a given video, a velocity vector \mathbf{v} , was defined with x component = $(x(\text{tracer})_2 - x(\text{tracer})_1)/t$ and y component = $(y(\text{tracer})_2 - y(\text{tracer})_1)/t$, where the subscripts 1 and 2 represent the initial and final coordinate of the tracer, and t is the duration of the video.

These vectors were averaged to arrive at the mean flow vector, \mathbf{v}_f for each video recorded. This procedure assumed the direction and magnitude of the flow velocity remained constant during the video, which appeared reasonable given the approximately constant overall translation rate and direction of each tracer, seen from the tracer trajectories (See *Figure 4-21*).

$$\text{Equation 4-5:} \quad \text{Direction} = \text{Tan}^{-1} \frac{(y_2 - y_1)}{(x_2 - x_1)}$$

$$\text{Equation 4-6:} \quad \text{Magnitude} = \sqrt{\frac{(x_2 - x_1)^2 + (y_2 - y_1)^2}{\text{time}}}$$

Figure 4-21 shows the trajectories of a set of tracers in the convective flow, and their corresponding velocities can be seen in Figure 4-22. The average tracer velocity was calculated to be $0.897 \mu\text{ms}^{-1}$ with a standard deviation of $\pm 0.239 \mu\text{ms}^{-1}$, a similar spread of velocities was observed for the same tracers in an externally imposed stable flow in section 4.3.1.2

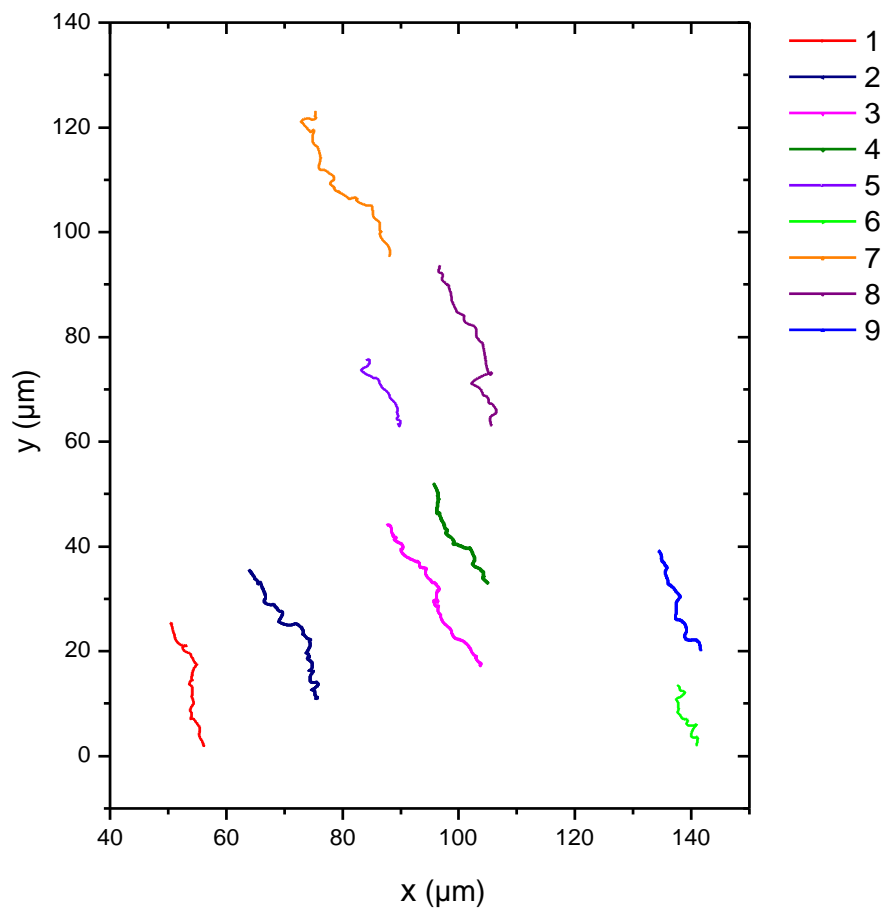


Figure 4-21: Trajectories of tracer particles in a self-generated convective flow. Tracers have been numbered from left to right.

These variations in the bulk fluid velocity are not indicative of the presence of any consistent x-plane shearing as they appear random with regards to their x-y position within the video. They are likely due to slight differences in tracer height relative to the cuvette boundary.

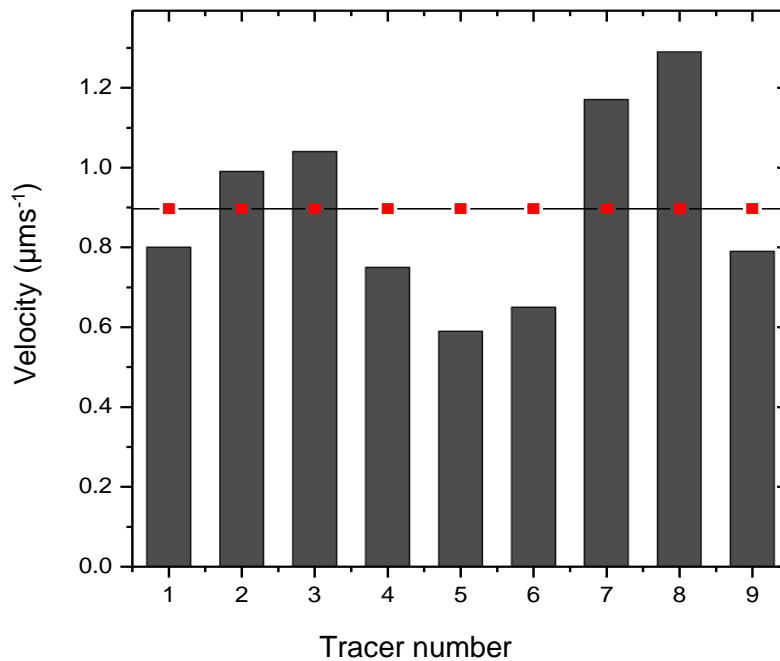


Figure 4-22: Tracer velocities from Figure 4-21.

Investigation, both experimentally and theoretically has been presented earlier in this chapter (Section 4.3.2.1) which confirms the assertions that x- shearing is negligible, but there is a dramatic z-shear profile in both sample chambers which could explain the alignment effect in catalytic ellipsoidal Janus swimmers subjected to low-speed flows.

4.3.2.3 Analysis of ellipsoid motion in a convective flow field

The average flow direction and velocity were used to subtract the advective drift to allow further analysis. (Figure 4-23).

Advective drift was subtracted from the raw x,y ellipsoid coordinates based on this flow vector, by subtracting the expected flow displacements contribution to each successive observed displacement of the ellipsoids.

$$\text{Equation 4-7: } x \text{ displacement} = \frac{\text{flow velocity} (\text{Cos}\theta_{\text{flow}})}{\text{frame rate}}$$

$$\text{Equation 4-8: } y \text{ displacement} = \frac{\text{flow velocity} (\text{Sin}\theta_{\text{flow}})}{\text{frame rate}}$$

Specifically, the following correction was made to each successive ellipsoid displacement (fps denotes the frames per second associated with the video):

$$\text{Equation 4-9 : } \Delta x_{\text{raw},t} = x(\text{ellipsoid, raw})_{t+(\frac{1}{\text{fps}})} - x(\text{ellipsoid, raw})_t$$

$$\text{Equation 4-10: } \Delta x_{\text{corrected},t} = \Delta x_{\text{raw},t} - x \text{ displacement}$$

$$\text{Equation 4-11 : } \Delta y_{\text{raw},t} = y(\text{ellipsoid, raw})_{t+(\frac{1}{\text{fps}})} - y(\text{ellipsoid, raw})_t$$

$$\text{Equation 4-12: } \Delta y_{\text{corrected},t} = \Delta y_{\text{raw},t} - y \text{ displacement}$$

The flow adjusted trajectory was then re-constructed by summing the corrected displacements. An example of the outcome of this procedure is displayed in Figure 4-23.

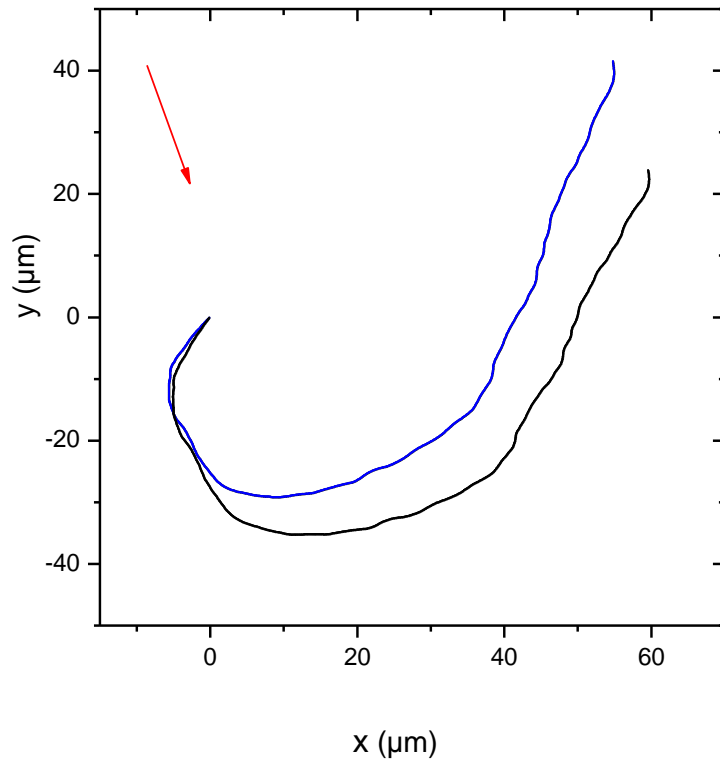


Figure 4-23: A representative trajectory showing the raw data in black, with the data after advective drift subtraction highlighted in blue. The flow direction and speed are shown by the (to scale) red arrow.

After advective drift subtraction, swimmer trajectories were smoothed using the Savitzky-Golay algorithm at 30 pts to reduce noise in the direction angle data caused by Brownian motion.

This process was performed on all active ellipsoid trajectories before orientation or direction analysis. Examples of smoothed, advection subtracted trajectories with their respective flow fields can be seen in *Figure 4-24*.

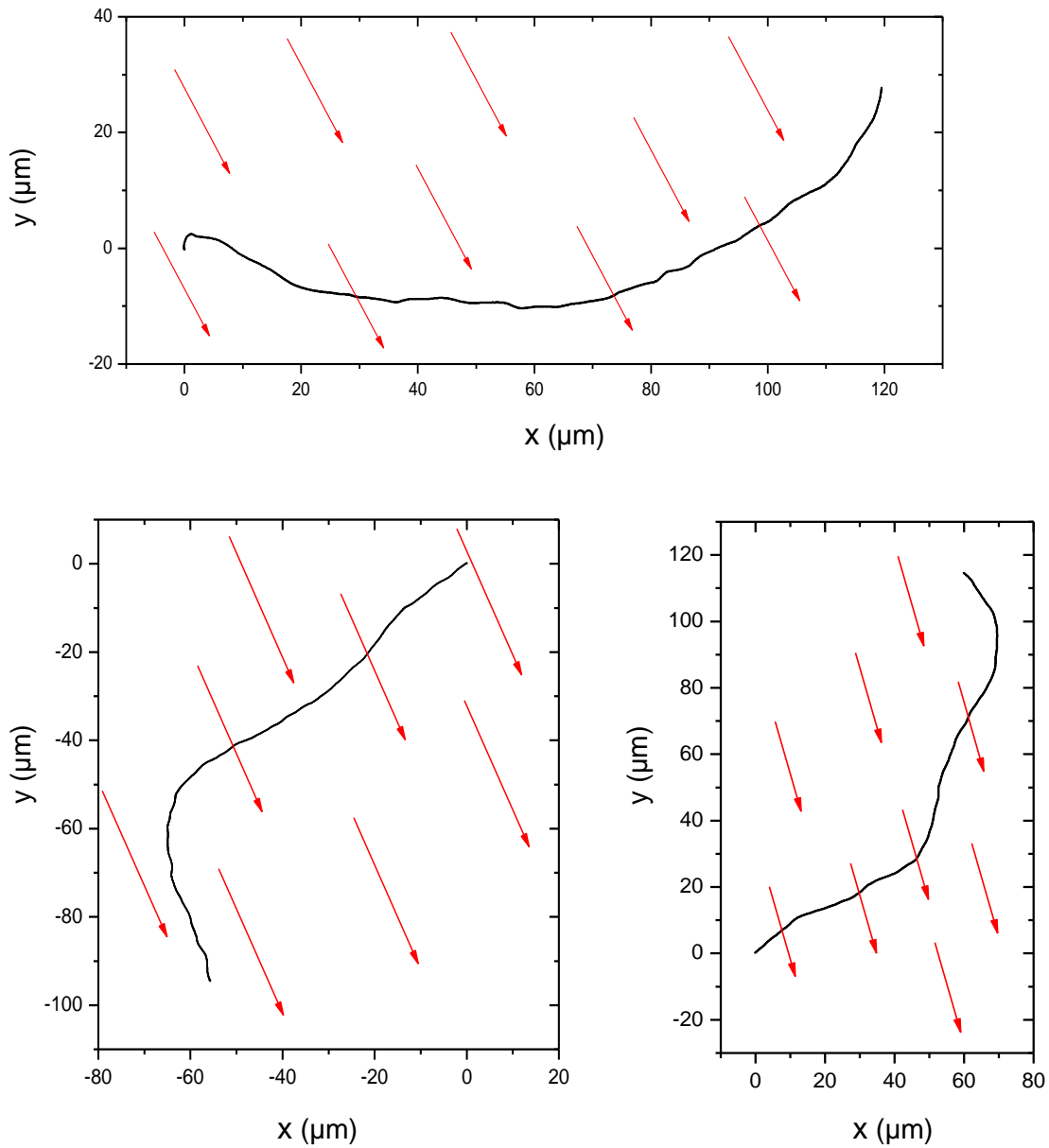


Figure 4-24: Corrected trajectories with the average flow field depicted by red arrows (angle and arrow length to scale with direction and velocity)

4.3.2.4 Flow Alignment

In order to measure the correlation between the direction of motion and the flow, $\Theta_{\text{direction}}$ was calculated for each frame of the video recordings. These values were subtracted from $\Theta_{\text{flow}} \pm 90^\circ$ to give the angle relative to the predicted perpendicular flow alignment for each frame.

Equation 4-13:
$$\theta_{\text{direction}} = \text{Tan}^{-1} \left(\frac{\delta y}{\delta x} \right)$$

The frequency of these angles was calculated in 10° increments between 90° and -90° and a distribution as a time fraction was generated.

Perfect major axis flow alignment, defined in *Equation 4-14*, for active ellipsoidal micro-swimmers was expected to result in correspondingly perfect cross-flow migration (*Equation 4-15*).

Equation 4-14:
$$\theta_{\text{Orientation}} = \theta_{\text{Flow}}$$

Equation 4-15:
$$\theta_{\text{Direction}} = \theta_{\text{Flow}} \pm 90^\circ$$

To statistically assess the alignment seen; the differences between Θ_D and perfect alignment for each video frame were calculated and sorted into 10° bins between $\pm 90^\circ$ using a frequency function. Where 0° is cross stream migration and $\pm 90^\circ$ suggests colloids are moving with/against the flow.

Data for all low spin ($< 0.15 \text{ rads}^{-1}$) colloids was combined and each bin was divided by the total number of frames to give a distribution of Θ_D as a time fraction.

This data is displayed as a binned wind rose diagram (*Figure 4-25a*) which shows a strong preference for active colloids to adopt a direction of motion that is within 10° of $\Theta_{\text{FLOW}} \pm 90^\circ$, each angle bracket after this becomes less populated indicating that further positions from alignment are less favoured. This suggests a preference for cross flow migration as is seen in spheres by Katuri et al.⁵⁷. Colloids with Θ_D within 30° of $\Theta_{\text{FLOW}} \pm 90^\circ$ account for $\approx 75\%$ of all frames collected.

It is not surprising, given the size of the active colloid, that Brownian fluctuations and unavoidable driven rotations disrupt ballistic paths leading to occasional loss of alignment. This is illustrated by the small populations of “misaligned” Θ_D angles seen in the data. This effect is also seen in the passive ellipsoids in a faster flow where fluctuations cause the ellipsoid to leave the path of the flow and spin in the horizontal plane before realigning.

The above analysis was repeated for the active ellipsoid’s orientation data which showed a much weaker degree of alignment than the direction of motion, shown in *Figure 4-25b*. The binned wind rose diagram shows no clear preference for the major axis to align parallel with the flow, with the population of angles between $\pm 0-30^\circ$ fairly evenly spaced. This suggests that alignment of the direction of motion can occur with quite a broad range of orientation angles, this is similar to the case of passive ellipsoids.

The average difference between Θ_{FLOW} and $\Theta_{\text{ORIENTATION}}$ was calculated to be $38.21^\circ \pm 20.67$. The data is consistent with that of the passive ellipsoids, but the alignment seen is somewhat weaker.

This decreased alignment could be due to the slower flow field in the self convective case, as Uspal et al. reported similar findings where their spherical janus swimmers showed higher degrees of alignment in faster externally imposed flows. Asymmetries in the shape of the ellipsoids could also play a part in the offset from perfect alignment for both active and inactive populations of ellipsoids.

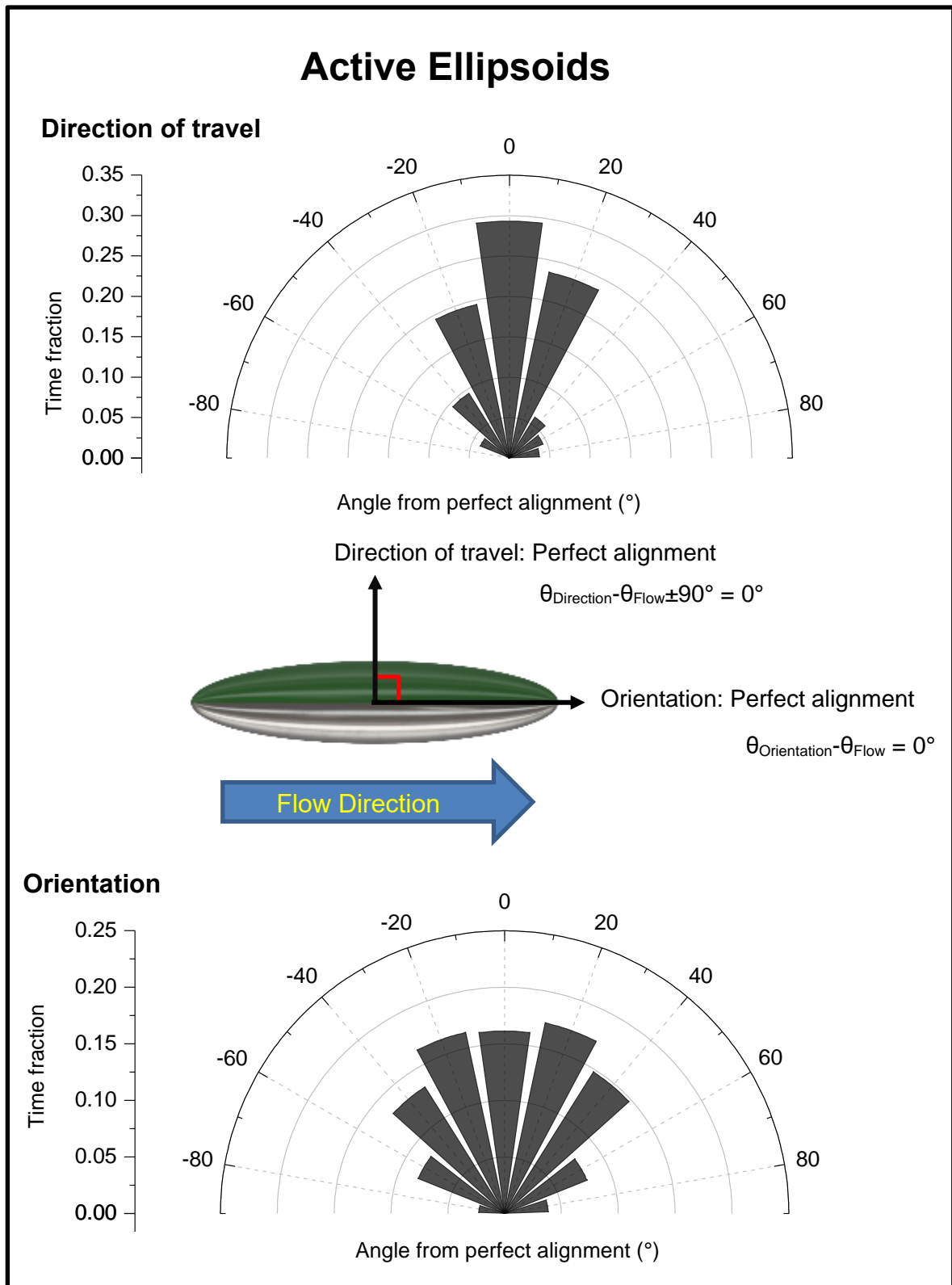


Figure 4-25: Binned wind rose diagrams showing alignment with or perpendicular to the direction of flow: a) distribution of direction angles from perpendicular alignment b) distribution of orientation angles from parallel alignment.

4.3.3 A comparison of Active and Passive ellipsoids in a flow

Figure 4-26 shows data for both active and passive ellipsoids where positive and negative angles of the same magnitude were combined e.g. -90° is binned with $+90^\circ$. The data for direction of motion shows a smooth distribution with significant peaks at $0-15^\circ$ showing a good degree of alignment for each case.

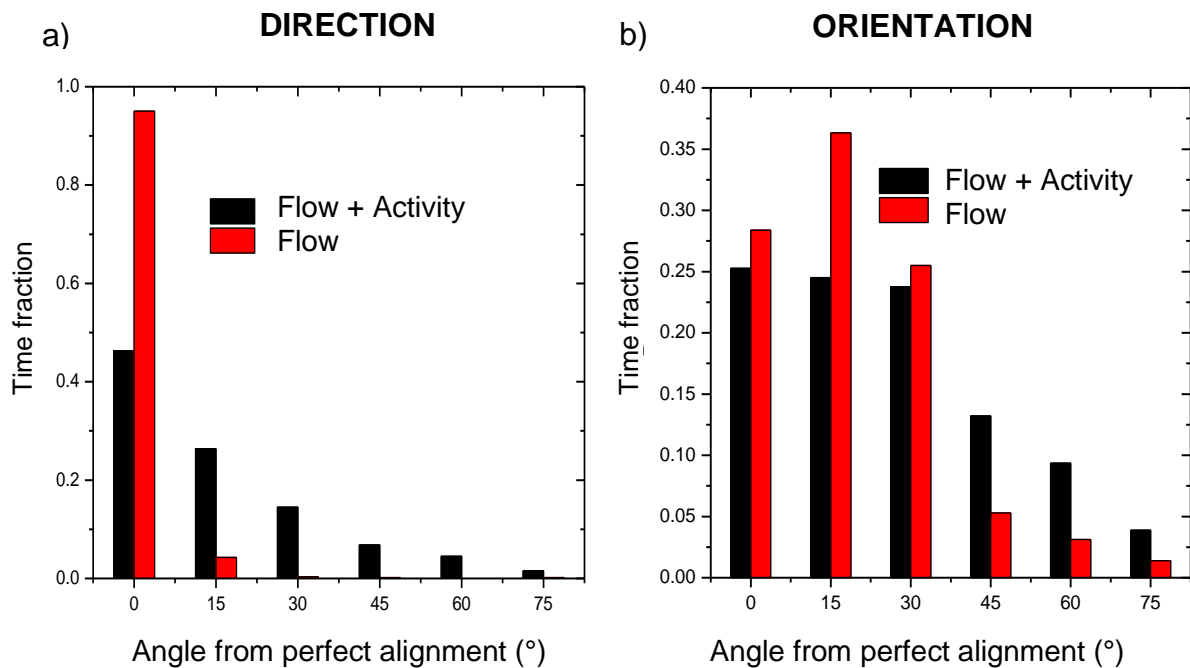


Figure 4-26: A comparison of data from passive and active ellipsoids; a) Distribution of direction angles. b) Distribution of orientation angles. Flow directions are defined as seen in the schematics in Figure 4-14 and Figure 4-25 for passive and active swimmers respectively.

A stronger degree of alignment is seen for the passive ellipsoids introduced into an externally driven flow. The reasons for this are likely due to the much larger fluid velocity seen in these experiments, combined with a more dramatic z-shear profile due to the significantly reduced height of the sample chamber, approximately 10x

that of the convective flow. Additionally, active ellipsoids have the competing effects of their chemical propulsion and small amounts of angular velocity, whilst passive ellipsoids are only exposed to convection driven propulsion. The orientation data for both sets of ellipsoids (*Figure 4-26b*) shows that the major axis does not align exactly with the flow direction as would be expected. passive and active ellipsoids show a ‘misalignment’ of $\approx 25^\circ$ and $\approx 38^\circ$ respectively.

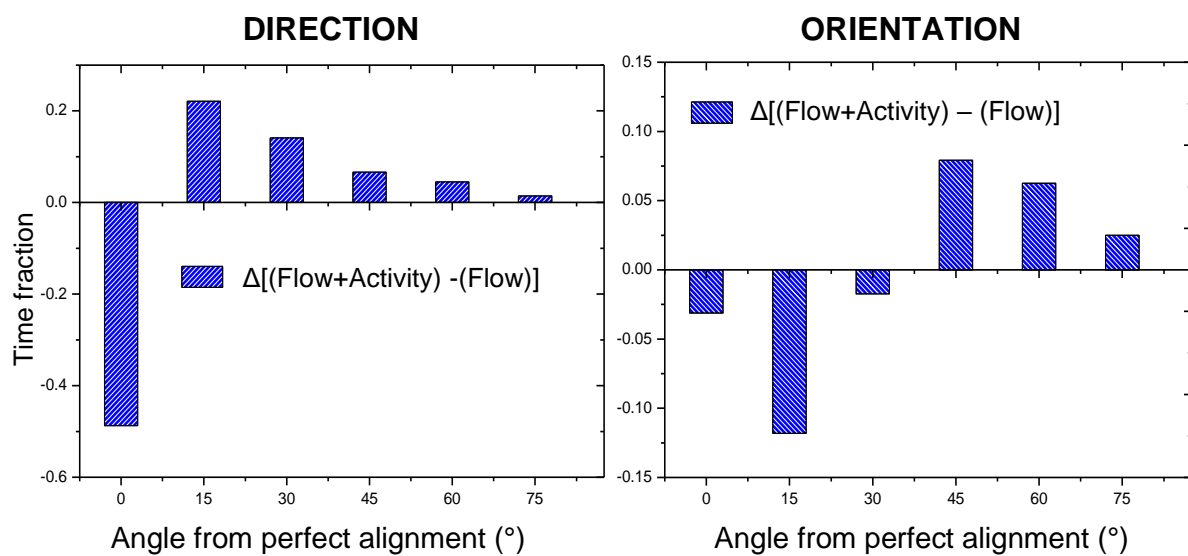


Figure 4-27: A comparison of data from passive and active ellipsoids; a) Distribution of direction angles. b) Distribution of orientation angles.

When the difference between these two sets of data are considered, it can be seen that when activity is introduced to the system, the greatest reduction in direction alignment effect occurs in the 0-15° bin (*Figure 4-27a*), further bins show higher populations of misaligned angles for active vs. passive swimmers. The populations of misaligned angles decrease steadily towards 75-90° where both sets of swimmers have negligible time spent parallel with the flow. This is consistent with the assertion that the higher flow velocity generates a stronger degree of alignment.

When orientation is considered, there is significantly less correlation between alignment and whether or not activity is present in the system (*Figure 4-27b*). Both active and inactive ellipsoids show similar degrees of alignment at 0-15° and 30-45°. The largest difference in alignment is seen at 15-30° where inactive ellipsoids show the greatest preference to orient. This reinforces the conclusion that directional alignment is not dependant on perfect orientational alignment.

4.3.4 High Spin Ellipsoids

The colloids discussed in this chapter so far were selected for their low angular velocity component ($\omega < 0.15 \text{ rads}^{-1}$), however MSD analysis of the total population of Janus ellipsoids revealed the angular velocity ranged from 8.8×10^{-7} - 0.295 rads^{-1} .

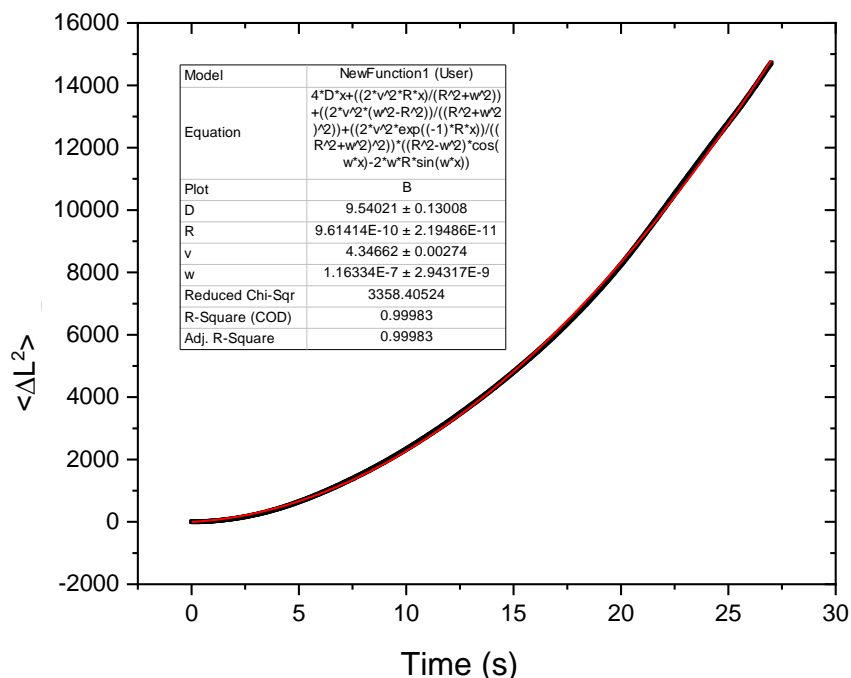


Figure 4-28: MSD plot with angular velocity fitting (originPro) for a low angular velocity ellipsoidal swimmer.

This is illustrated in *Figure 4-28*, a ‘low-spin’ example where angular velocity was calculated to be $1.16 \times 10^{-7} \text{ rads}^{-1}$ shows a smooth quadratic curve with a steady increase in distance from the origin. This is indicative of a ballistic swimmer that is not undergoing any driven rotations.

A high spin example ($\omega=0.295 \text{ rads}^{-1}$) is shown in *Figure 4-29*. This MSD plot shows a much smaller peak and then a trough where the colloid is undergoing a rotation and thus motion is directed back towards the origin with a negative gradient for $\langle \Delta L^2 \rangle$ Vs. time. To assess the prevalence of this self-induced alignment effect for a statistically significant number of ellipsoids with a range of angular velocities, colloids were produced with more controlled increases in spin, using a glancing angle deposition. This is explained fully in chapter 5.

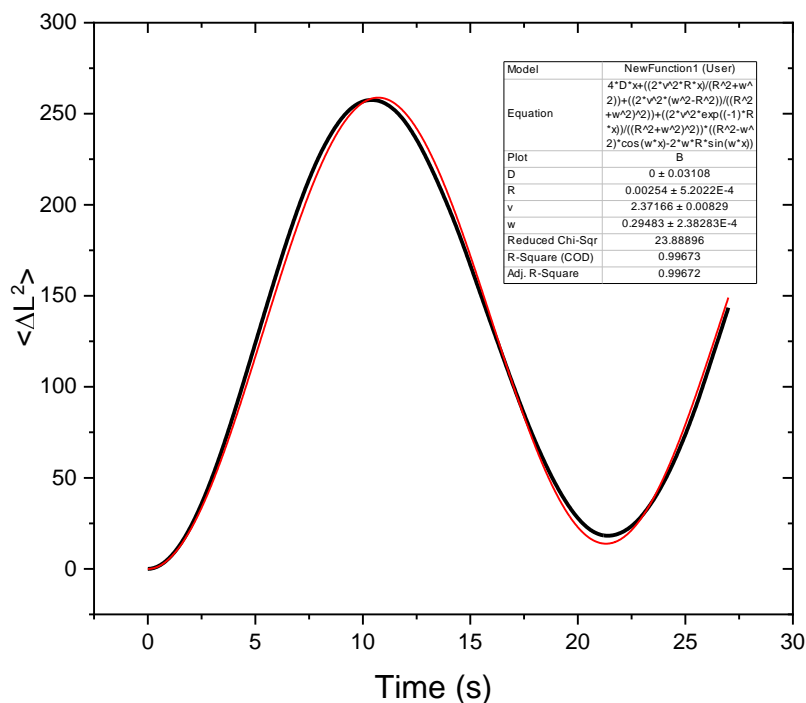


Figure 4-29: MSD plot with angular velocity fitting (originPro) for a high angular velocity ellipsoidal swimmer.

Data for high spin swimmers indicates that perpendicular alignment was not achieved; see *Figure 4-30*, where the distribution of angles relative to the flow is very evenly spread when compared to low angular velocity swimmers. Spinning swimmers account for 27.27% of the total population.

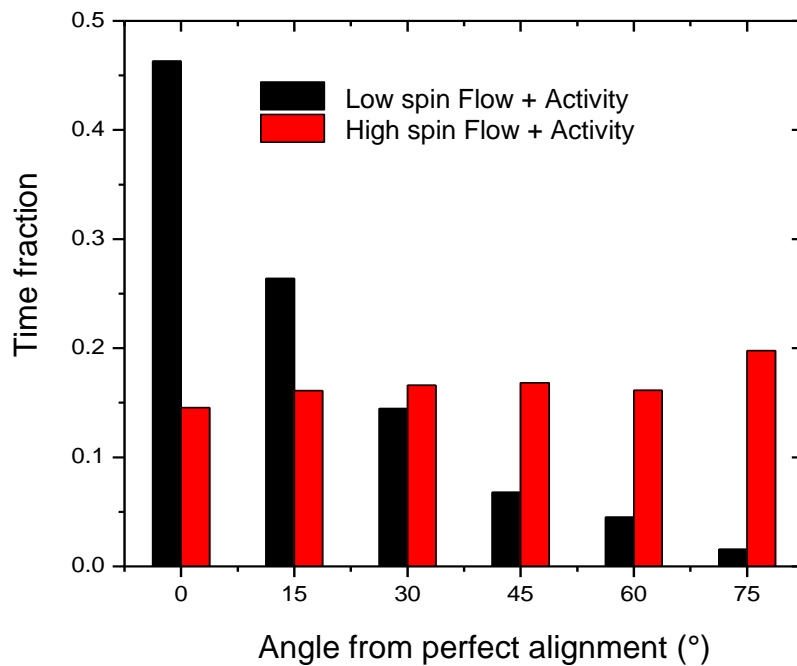


Figure 4-30: A bar chart comparing the distribution of direction angles relative to the flow. Low angular velocity ellipsoids ($\omega < 0.15 \text{ rads}^{-1}$) are represented in black whilst high spin ellipsoids are represented in red ($\omega > 0.15 \text{ rads}^{-1}$)

The reduction in alignment effect for high spin vs. low spin swimmers is illustrated in *Figure 4-31* (red). When compared to the reduction of alignment in active vs. passive swimmers (blue), a similar pattern of significant decrease in time spent well aligned (0-15°) is seen. Unlike low spin swimmers, the time spent in misaligned angle bins steadily increases towards being parallel with the flow. This increase is of the same magnitude, but the inverse of the pattern seen for active vs. passive ellipsoids.

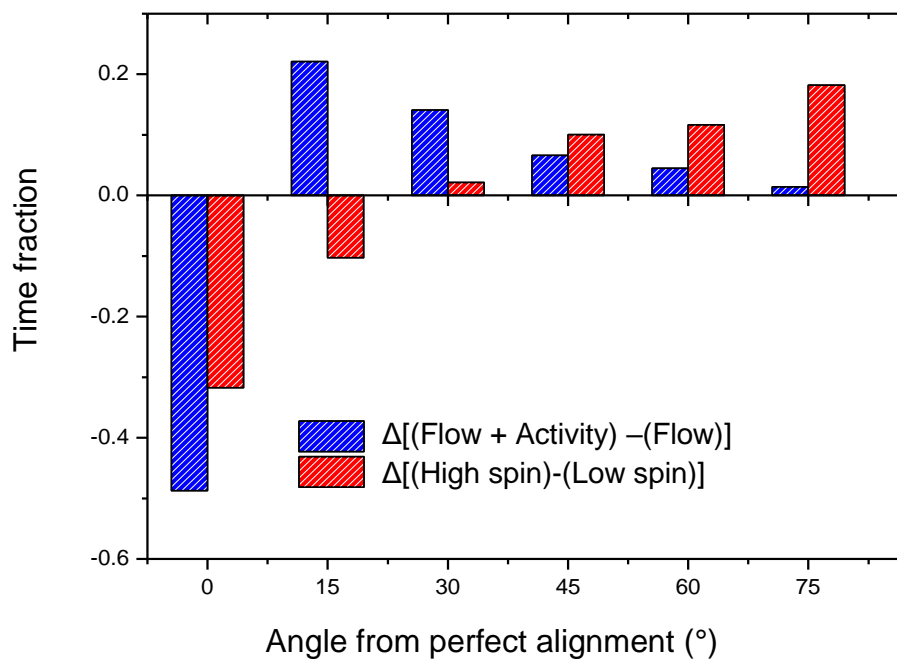


Figure 4-31: A bar chart comparing the reduction in alignment relative to the flow. $\Delta[(\text{Flow} + \text{Activity}) - (\text{Flow})]$ is represented in blue whilst $\Delta[(\text{High spin}) - (\text{Low spin})]$ is represented in red.

This data reinforces the assertion that flow alignment of ellipsoidal swimmers is strongly dependant on the angular velocity of the swimmer. Even small increases in driven rotations work in competition with the alignment effect and above a certain threshold the angular velocity dominates, resulting in full loss of alignment. It is possible that higher flow velocities may combat loss of alignment for high spin swimmers, and this should be considered for future work.

4.4 Discussion

4.4.1 Flow field

This chapter investigated the rich dynamics of ellipsoidal catalytic micro swimmers in a self-generated flow field, and also reported the behaviour of passive ellipsoids in an external flow.

The convective flow which was produced as a by-product of the catalytic reaction mimics the flow generation achieved by Gregory et al. and modelled by Shemi et al. The decomposition of H₂O₂ by platinum into less dense products which rise in the container produces a density driven convective flow⁷⁷. It is not entirely clear why ellipsoidal micro swimmers produce a convective flow at lower volume fractions than their spherical counterparts. An increase in catalytic surface area vs the sphere could lead to a higher production of less dense products, promoting a density driven convective flow. When the ellipsoids studied here were compared to a sphere of analogous volume using Equation 4-16 and Equation 4-17, the catalytic surface areas were approximated to be 23.85µm² and 19.46 µm² respectively; this is an increase of 18.4%.

Equation 4-16: *Catalytic surface area for a sphere* = $2\pi r^2$

Equation 4-17: *Catalytic surface area for ellipsoids* = $2\pi \left(\frac{(ab)^{1.6} + (ac)^{1.6} + (bc)^{1.6}}{3} \right)^{\frac{1}{1.6}}$

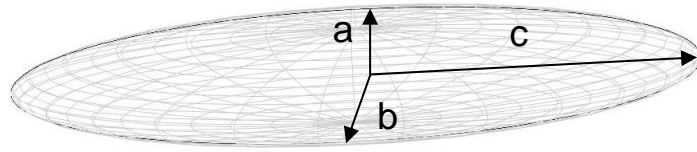


Figure 4-32: Schematic showing assigned lengths for surface area calculation.

Control experiments with passive ellipsoids were conducted using a pressure driven flow at around $10\mu\text{ms}^{-1}$. Ideally experiments would have been performed at the same velocity as the convective flow, but such low speeds proved to be unattainable with the pressure pump set up.

Both types of flow showed velocity profiles which had significant z shear whilst having negligible x - y shearing in the regions where experiments took place. It is possible that this would allow for the alignment of an axisymmetric object as was observed in both passive ellipsoid control experiments and to a slightly lesser degree, the active ellipsoids in the self-generated flow field.⁸²

4.4.1.1 Direction of motion

It is clear from the results in sections 4.3.1 and 4.3.2 that when exposed to a fluid flow, passive ellipsoids will translate parallel to the flow whilst (low spin) active ellipsoids translate across the flow.

This is consistent with results from similar experiments where Katuri et al. exposed spherical Pt-PS Janus particles to an external flow and found that cross stream migration occurred when activity was turned on⁵⁷. The paper (2018) introduces the concept of using a flow field to produce different dynamic responses to those usually observed in rheotactic systems. Their artificial spherical platinum/polystyrene Janus swimmers were able to align in a controlled channel flow so that their propulsive axis is parallel with the flow⁵⁷. Motion is then directed almost perpendicular to this (*Figure 4-33*).

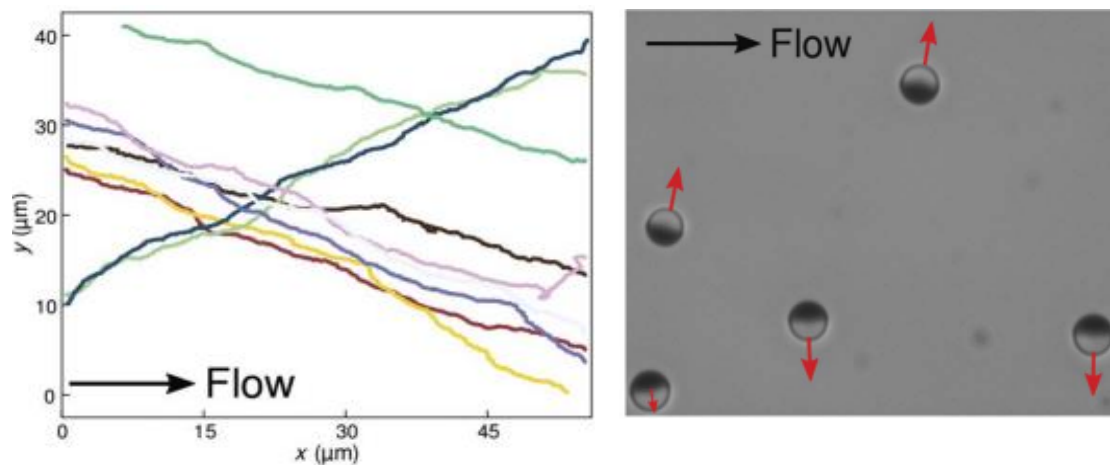


Figure 4-33: Figures from Katuri et al. Trajectories and Optical microscopy images of Janus spheres exposed to a flow with velocity $14\mu\text{m}\cdot\text{s}^{-1}$.⁵⁷

In the absence of an externally imposed flow they found that bottom heavy active Janus spheres accumulate on the lower boundary of the sample vessel and align with their Pt cap downwards, so their propulsion axis is parallel to the lower boundary. This restricts the spheres to a single plane of motion, and they translate along the lower surface with no preferred direction. As ellipsoidal colloids produced appreciable flow at very low volume fractions and fuel concentrations, these experiments could not be performed. However, the behaviours of the spherical and ellipsoidal swimmers in the flow were very similar.

When flow was introduced, they found that the orientation of the colloids on the bottom surface evolved such that the propulsion axis was almost perpendicular to the direction of the flow. The particles began to translate in response to the externally imposed flow whilst their self-propulsion velocity continued away from the Pt cap. These combined effects resulted in cross stream migration of the spherical colloids.

The stronger alignment seen in passive ellipsoids where the fluid velocity was higher is also consistent with the findings in this publication, where an increase in flow velocity from $14 \mu\text{ms}^{-1}$ to $24 \mu\text{ms}^{-1}$ significantly improved the alignment effect (*Figure 4-34*). It was also found that higher propulsion velocities damp orientation fluctuations.

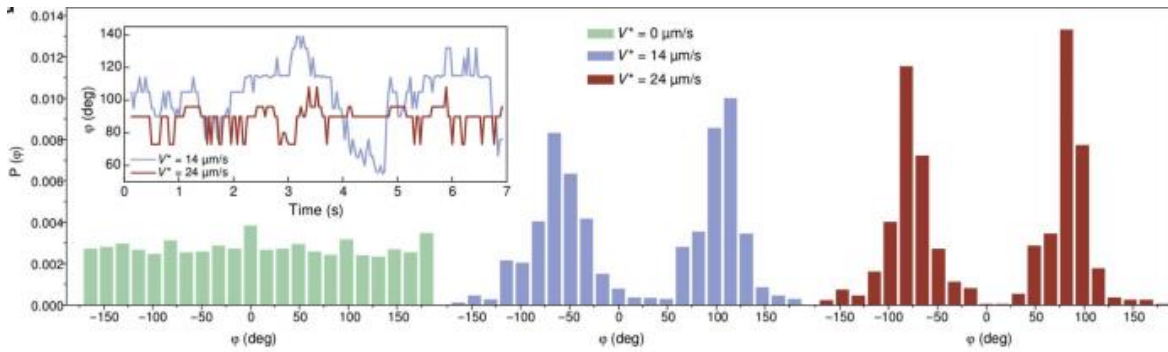


Figure 4-34: Figure from Katuri et al. Angular probability distributions at different flow velocities⁵⁷.

The group reported that the alignment was a result of shear forces and swimming in confinement, and it is likely that this is the case also with ellipsoidal swimmers. Near surface swimming introduces an effective friction opposing the rotation of the particle away from the preferred position, shown in Figure 4-35. Due to this alignment the particles migrate across the streamlines of the flow as they are carried downstream.

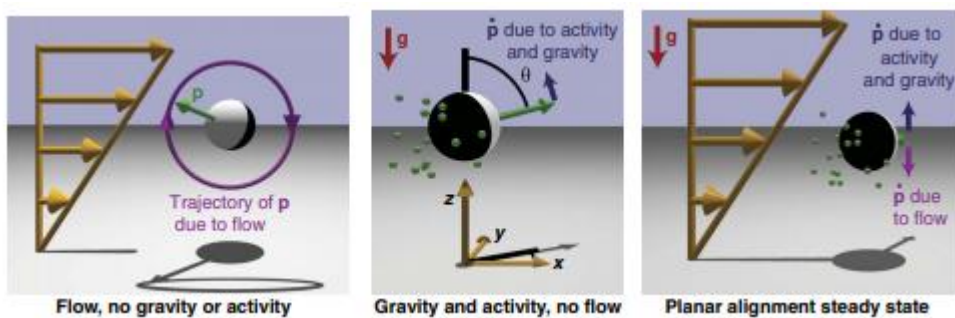


Figure 4-35: Schematic by Katuri et al. showing how a flow with shearing in the z -direction leads to alignment of spherical Janus Swimmers⁵⁷.

These experiments introduced the concept of cross stream migration in synthetic active colloids however the flow velocity required for alignment is extremely high ($14\mu\text{ms}^{-1}$). This is likely due to the symmetrical shape of the colloid which has no inherent preference to align. This phenomenon currently also relies upon external influence, with the use of expensive and complicated flow equipment both of which reduce the potential applications of these swimmers. The ellipsoidal swimmers reported here produce a flow significant enough to cause some alignment, during standard testing conditions (10% wt H_2O_2 fuel in a confined sample holder) which greatly reduces the time required, cost and chemical reagents needed to achieve similar results.

4.4.1.2 Orientation

Data for the orientation for both populations of ellipsoids show that the major axis does not align exactly with the flow, however there is an offset alignment at $\approx 30^\circ$ from the flow direction. This data was obtained directly from LabVIEW via a custom algorithm and given as an angle per frame.

It is not entirely clear where this offset in the orientation alignment comes from, as it does not translate to the direction of travel which is well aligned in both active and passive populations of ellipsoids. It is possible that this offset is caused by irregularities in the geometry and surface of the colloids which it can be seen in *Figure 4-36* are neither perfectly smooth nor symmetrical. This is a drawback of the synthesis methods for stretching the colloids and would be considered for any future experiments.

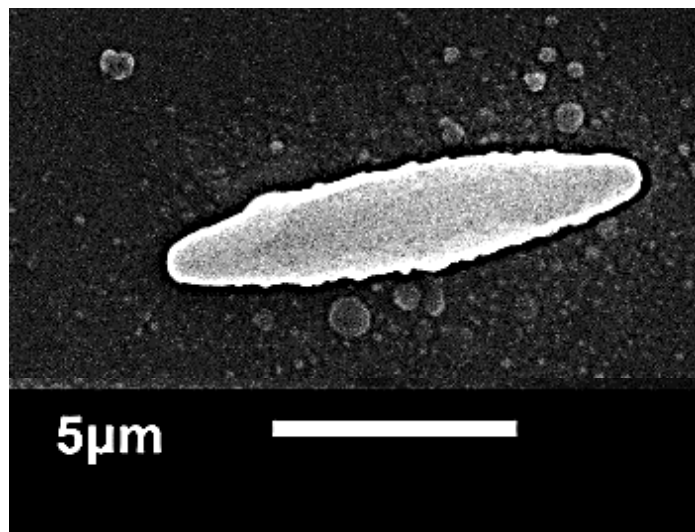


Figure 4-36: Close up SEM image of an ellipsoidal colloid prior to catalyst coating.

4.5 Conclusions

When platinum coated Janus ellipsoids are exposed to hydrogen peroxide fuel (10%wt) the Janus swimmers accumulate on the lower boundary of the cuvette where there is a relatively stable crossflow field, which is generated by density differences between the products and reactants of the catalytic reaction taking place. There is an observed preference to align so that their major axis is close to parallel with the flow direction and motion is directed perpendicular to this due to the placement of the catalyst coating.

Unusually this alignment effect is not seen in ellipsoids with a high angular velocity (spinning). Further experiments will be necessary to determine if the reason for this is an increased disturbance of the local fluid field, ie. stirring, or if these colloids are unaffected by the flow field.

In contrast to previous studies, the flow here is generated by the catalytic colloids, rather than externally imposed. As the flow direction is determined by the symmetry of the cuvette, the micron scale directed transport is dictated by the macroscopic confinement geometry.

The production of flow within the cuvette has many benefits over the use of an external flow, most significantly that the equipment needed for micro-fluidic pumping of this nature are both extremely costly and laborious to use. The closed system also reduces the amount of chemicals and micro-swimmers needed as they are not lost throughout the experiment.

Use of flow fields to direct the motion of active colloids provides a pathway towards enhanced cargo delivery⁸⁷, for which ellipsoids are especially beneficial due to their increased surface area which would allow for more 'cargo' to be collected. Such cargo collection and delivery behaviour could be used in in vitro testing devices.

There are further applications such as 'lab on chip' devices where a self-imposed flow field would allow for a closed system, isolated device for use outside of laboratory settings such as in the field testing of contaminants etc.

Chapter 5:

Ellipsoidal Janus swimmers with enhanced rotational motion

5 Ellipsoidal Janus swimmers with enhanced rotational motion

5.1 Introduction

Use of well-defined spinning and spiralling colloids has become a recent subject of interest in the biological field. Wu et al. used optically driven, rotating colloids to influence the direction of growth of neurons in vitro. The spinning colloids generate a microfluidic flow which cause shear forces on the surface of the growing axon cone⁸⁸. Zhang et al. used superparamagnetic nanoparticles rotated by a dynamic magnetic field generator to induce cell death⁸⁹. Introducing rotation has also been shown to increase the probability of binding of fluorescent nanoparticle targets to biochemically coated magnetic 'capture' particles⁹⁰.

However, each of these novel applications relies on external fields to generate rotations and with costly and complicated set up, this limits the potential applications. This limit has inspired research into colloids which, using a chemical fuel, can generate their own autonomous spinning motion.

Enhanced rotational velocity leading to spiralling behaviour has been achieved by spherical Janus swimmers²¹ by introducing asymmetry into the catalytic coating. Line of sight electron beam evaporation was used to deposit a platinum catalyst onto the spheres at a glancing angle to induce shadowing. As the spheres are symmetrical, when spaced out on the substrate, no shadowing occurs. To combat this, the spheres were closely packed in a crystal so that they shadowed one another (*Figure 5-1*), leading to different shapes of catalyst coated area at different glancing angles.

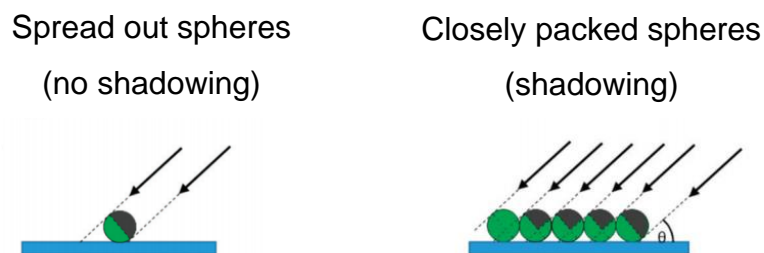


Figure 5-1: Schematic from Archer et al. showing how a closely packed crystal of spheres induces shadowing when coated at an angle, θ ²¹.

The ellipsoids studied in this chapter have a long body axis which induces shadowing and therefore catalytic patch asymmetries without the need for a closely packed crystal (*Figure 5-2*)

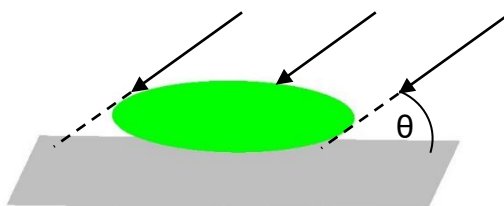


Figure 5-2: Schematic showing how ellipsoidal colloids induce shadowing at a glancing angle, θ , without the need for a closely packed crystal.

Following on from chapters 3 and 4, this chapter aims to influence the degree of angular velocity produced by ellipsoidal swimmers. Using a simple glancing angle deposition technique to reduce the symmetry of the catalyst coating we significantly enhance the rotational speeds. This opens up many applications such as micro-stirring and enhanced target capture which will both benefit greatly from the increased surface area of the ellipsoid vs. a sphere. In the case of micro-stirring, the long body axis of the ellipsoid should lead to much greater fluid perturbations vs a rotationally symmetrical sphere of the same volume.

5.2 Methods

Ellipsoidal colloids were prepared and cleaned as described in chapter 3. The cleaned colloids were then deposited onto pre-cleaned glass slides by pipetting the suspension into hydrogel wells to concentrate the colloids in certain locations of the slide. The slides were placed in custom built angle changing sample holder (*Figure 5-3*) which was set to $\theta=60^\circ$, as illustrated in *Figure 5-4*.

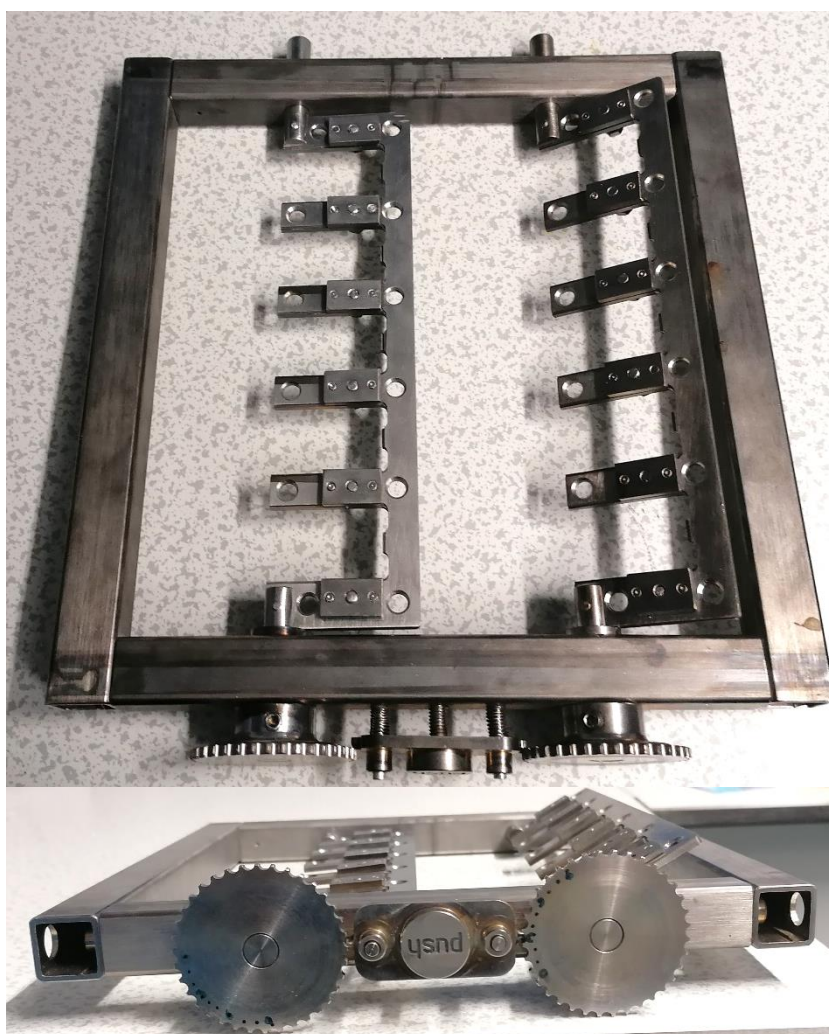


Figure 5-3: Custom built angle changing slide holder (by Richard Archer former CBE student, University of Sheffield), the right side is turned to $\theta=60^\circ$ to achieve a glancing angle deposition.

The ellipsoidal colloids were then coated with 20 nm of platinum (Kurt J Lesker 99.99% purity) while localised on the slide. Platinum was deposited via electron beam evaporation (Moorfield minilab) at $\approx 1 \times 10^{-7}$ atm.

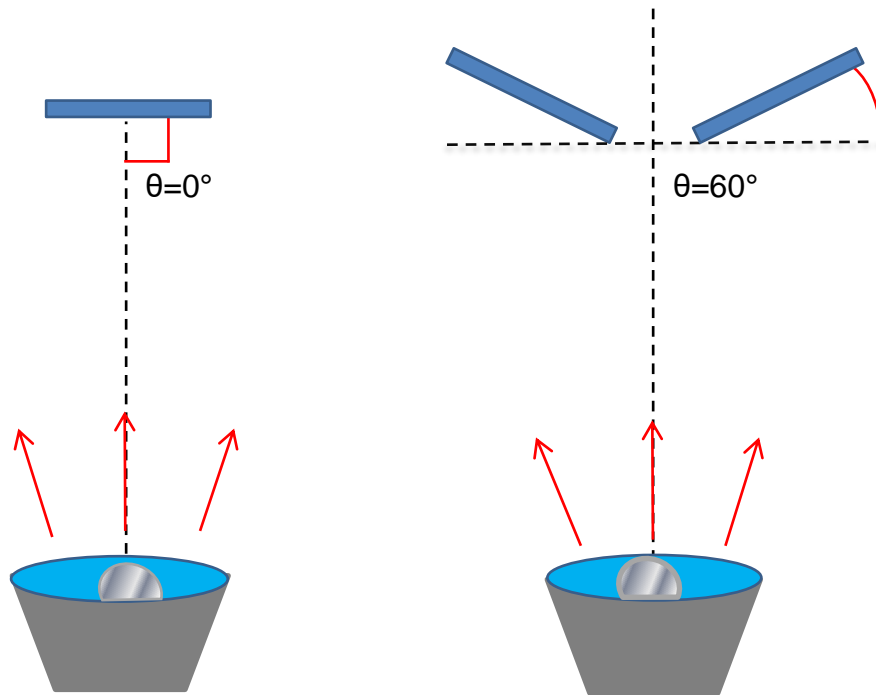


Figure 5-4: Diagram showing the experimental setup used for deposition a) standard perpendicular coating b) sample rotated by 60°.

The coated colloids were removed from the slides using slightly wetted lens tissues and submerged in 10% wt. H_2O_2 fuel containing 0.017% v/v of fluorescent polystyrene tracer colloids (Sigma-Aldrich 1 μm diameter). Swimmers which had sedimented to the lower surface of the cuvette were recorded at 86 fps for 23 seconds each and analysed using custom LABview software to calculate MSD data, translational velocities and angular velocities as described in chapter 2.

5.3 Results

5.3.1 Theoretical Prediction of the Catalyst shapes

As previously discussed, controlled asymmetries in the coating of spherical Janus swimmers have been shown to increase rotational speeds under very specific coating conditions using a closely packed colloidal crystal that is laborious to produce. When the spherical Janus swimmer has a rotationally symmetrical catalytic hemisphere, forces across the colloid surface result in purely translational thrust propulsion away from the catalytic hemisphere⁹¹. When the symmetry of the catalyst is broken, the introduction of an angular component to the thrust occurs, with smaller catalytic patches leading to enhanced rotational speeds²¹. The use of ellipsoidal colloids with rotational asymmetry allows for shadowing to be introduced during the coating procedure without the need for a colloidal crystal. Spinning ellipsoids would be especially advantageous as micro-stirrers due to their enhanced surface area and interactions with surrounding fluid when compared to spheres of the same volume.

Data suggesting that this is also the case for ellipsoidal swimmers was presented in chapter 3 where a broad range of angular velocities from, 8.88×10^{-7} to 0.295 rads^{-1} , were present in a single sample coated in the same way. This was attributed to

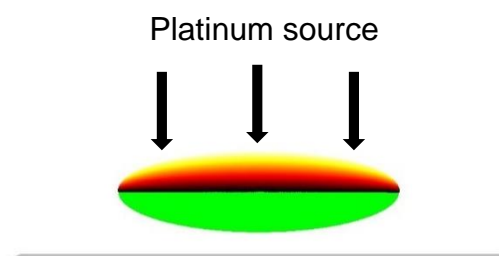


Figure 5-5: Schematic showing the coating conditions which would lead to a symmetrical hemispheroidal coating.

unintentional asymmetries in the coating perimeter, possibly caused by defects in the shape of the ellipsoidal colloids (*Figure 4-36*). The very low angular velocities observed were likely due almost perfectly symmetrical hemispheroidal catalyst with balanced forces across the entire ellipsoid (*Figure 5-5*).

A glancing angle deposition at $\theta=60^\circ$ was employed to induce further shadowing effects and more dramatic catalyst geometries with the aim of increasing the rotational speeds of ellipsoidal swimmers.

To understand how the catalyst shape may induce rotations, we must first look at the shape produced by the glancing angle. Due to the electron beam evaporation coating method used, the level of fluorescence bleaching from electron bombardment rendered fluorescence microscopy unusable, so it is difficult to directly optically visualise the shape of the catalyst patch during motion. Instead, predictions of the expected ellipsoid coating thicknesses were made for given glancing angles (θ), and long axis orientations (α), using a ray-tracing analysis. In reality, as we did not control alignment of the ellipsoidal colloids on the substrate, as seen in chapter 3 *Figure 3-2*, we expect to sample a random distribution of α during our experiments.

Figure 5-6 illustrates how, when ellipsoids are orientated parallel to the slide and metal, shadowing occurs over the length of the ellipsoid (long axis orientation angle, $\alpha=0^\circ$) leading to greater platinum thickness at the tip closest to the metal source which reduces to zero coverage at the tip farthest from the metal source.

However, if the ellipsoid had a perfect perpendicular orientation ($\alpha=90^\circ$), the glancing angle coating simply rotates about the major axis and the result is a standard

symmetrical Janus ellipsoid. This particular scenario, whilst unlikely, would not lead to any enhanced rotation, beyond that associated with unavoidable irregularities as reported in chapter 3.

Perfect alignment, either perpendicular or parallel, of the ellipsoids to the metal source are unlikely in this scenario where we have no control over the orientation before deposition.

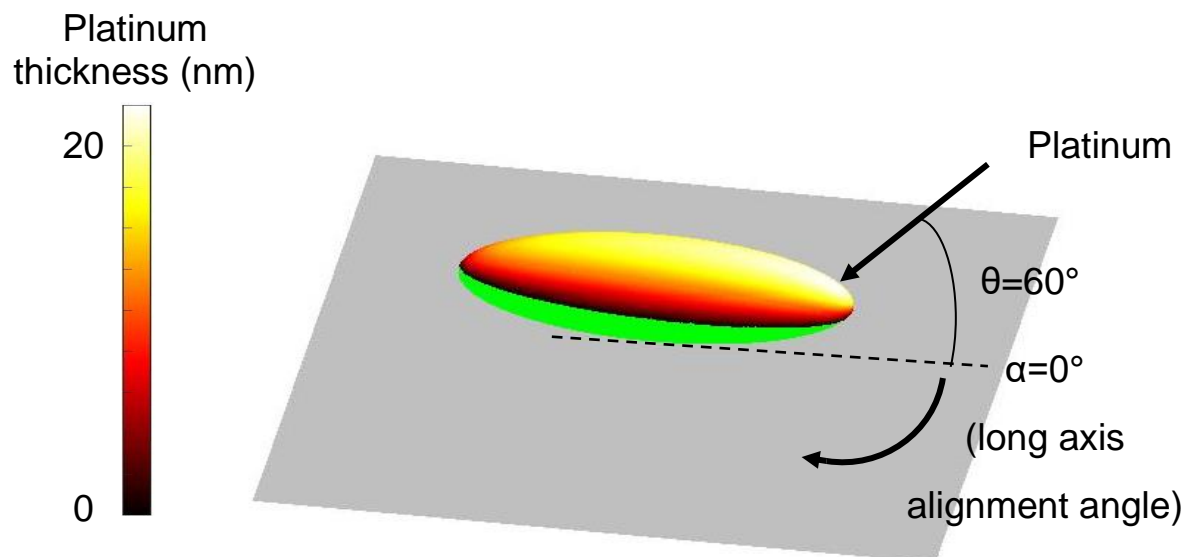


Figure 5-6: Schematic showing how a glancing angle deposition leads to shadowing over the long body and a build of catalytic material and the tip closest to the metal source.

5.3.2 Experimental Results

Ellipsoidal colloids coated at a 60° glancing angle were found to translate at an average velocity of $7.49 \mu\text{ms}^{-1} \pm 3.68$, an increase on the $4.35 \mu\text{ms}^{-1} \pm 1.05$ measured for colloids coated perpendicular to the source.

When the angular velocity is plotted against translational velocity, it can be seen in *Figure 5-7* that as the angular velocity increases the translational velocity decreases. Some glancing angle coated ellipsoids have a high translational velocity and low angular velocity. These anomalous values are likely caused by lack of control over α , when $\alpha = 90^\circ$, or the ellipsoid is oriented perpendicular to the platinum source, little to no shadowing is experienced. This leads to symmetrically shaped catalyst coating areas which produce low spin, fast ballistic motion.

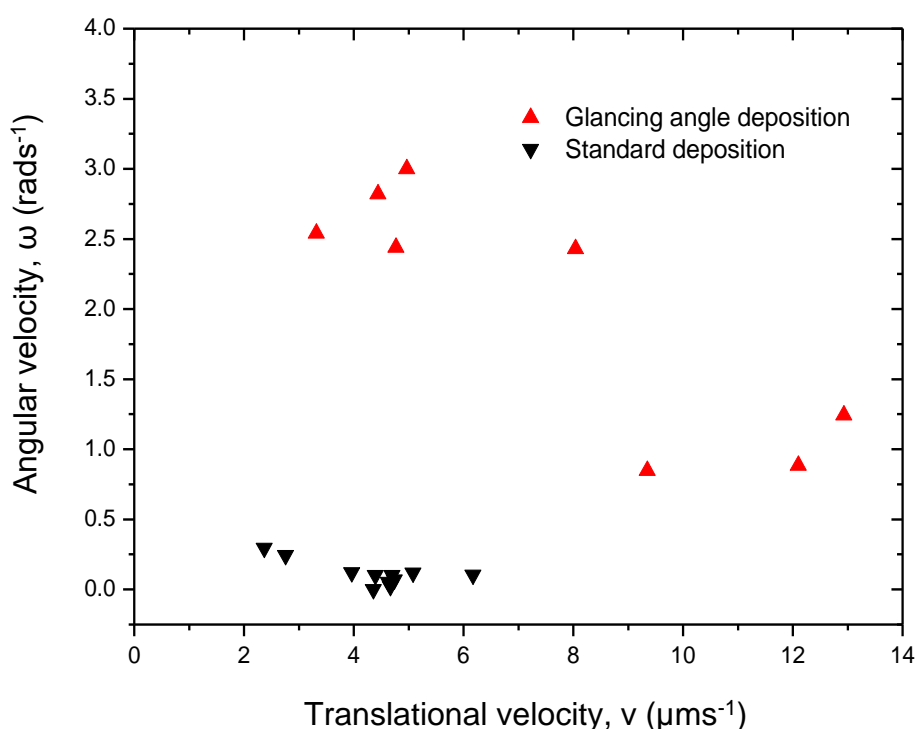


Figure 5-7: A scatter plot of translational velocity (v) vs. angular velocity (ω) for a population of high spin swimmers (red) and swimmers coated with standard deposition conditions (black).

This is in agreement with their spherical counterparts. The increase in translational velocity is most likely due to batch-to-batch variations in activity which are difficult to control even with the quartz crystal monitor to gauge the coating thickness.

Qualitatively it can be seen that ellipsoids coated in this way still travel in a direction approximately perpendicular to their major axis like their ballistic counterparts (*Figure 5-8*).

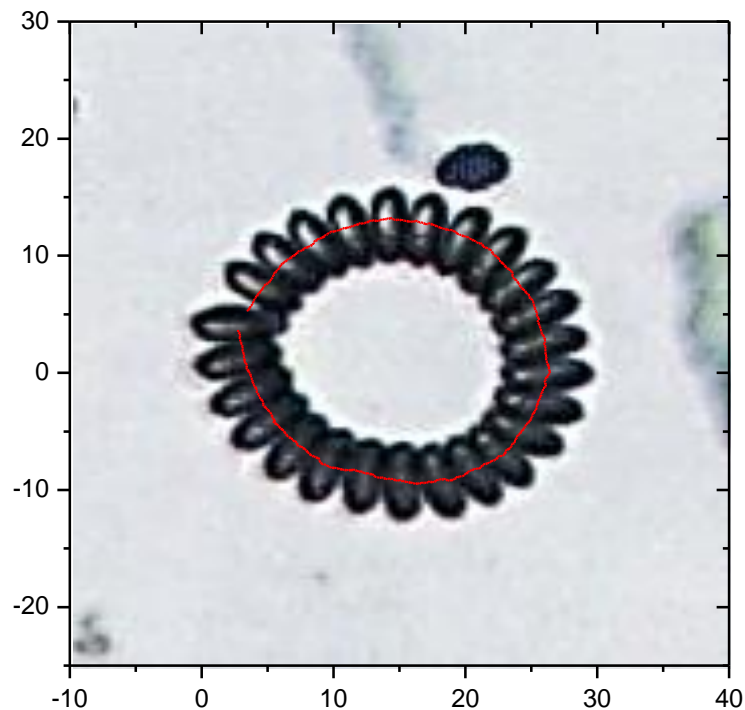


Figure 5-8: Part of a trajectory for a spinning ellipsoid overlaid with a time-lapse image of the video recording.

The trajectories produced by glancing angle deposition show smooth and persistent circling behaviour and only small translational distances are achieved as shown in *Figure 5-9*.

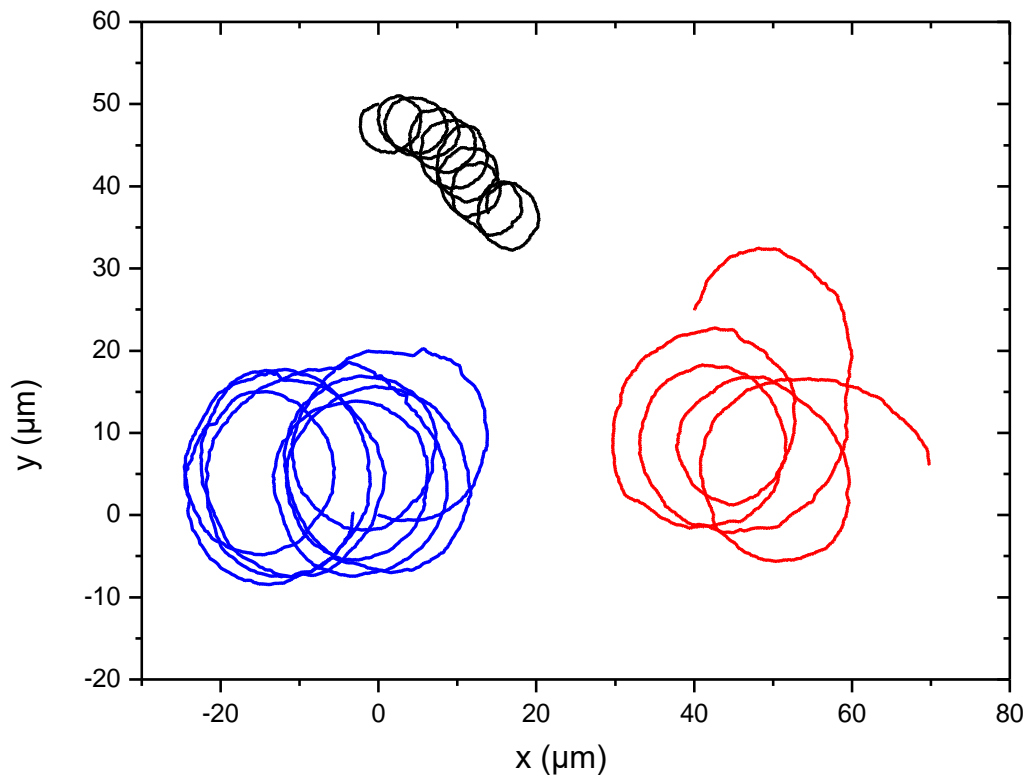


Figure 5-9: Representative trajectories of Ellipsoidal swimmers with enhanced rotational motion.

For spherical swimmers, the size of the circle in the trajectory is dependant on the size of the catalytic patch size, with smaller areas of catalyst producing tighter circling behaviour²¹.

The shapes of the catalytic area are not available during testing, however like spheres, the size of the circle seen for ellipsoidal swimmers in *Figure 5-9* likely corresponds with catalytic coating area. The tightest circle would theoretically be

produced by coating when the ellipsoids major axis is parallel with the platinum source ($\alpha=0^\circ$) and maximum shadowing occurs leading to a smaller catalytic area with a build up of platinum on one end of the ellipsoid.

MSD plots for these trajectories (*Figure 5-10 to Figure 5-12*) show several peaks and troughs where the distance travelled returns to zero as the colloid rotates. This is consistent with a swimmer propelling with high angular velocity.

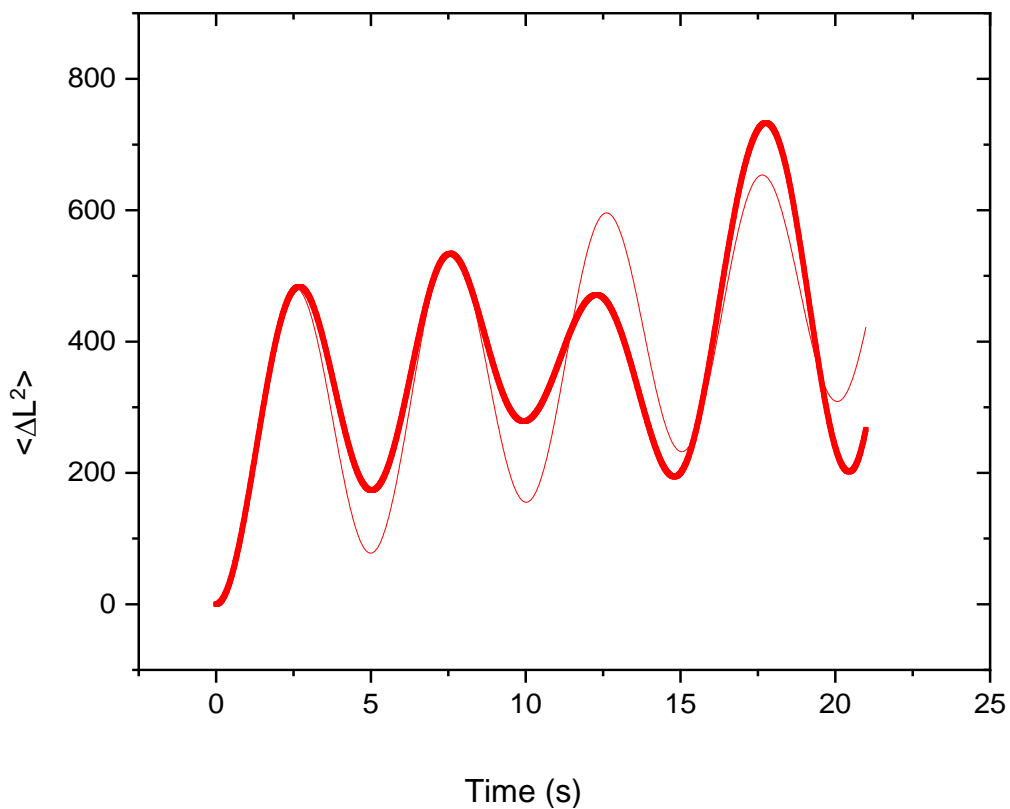


Figure 5-10: MSD data and angular velocity fitting for trajectory shown in red in Figure 5-9 $\omega=0.884 \text{ rads}^{-1}$.

Quantitative analysis of the angular velocities of each swimmer revealed an average angular velocity of $1.88 \pm 0.94 \mu\text{s}^{-1}$. An increase of 16x the naturally occurring average velocity of $0.11 \pm 0.088 \mu\text{s}^{-1}$. As expected, due to lack of control over the ellipsoid orientation before coating, there is still a range of angular velocities from $0.72 \mu\text{s}^{-1}$ to $3.00 \mu\text{s}^{-1}$. The lower limit of this range is still double that of the fastest spinning ellipsoid coated at standard sample positioning.

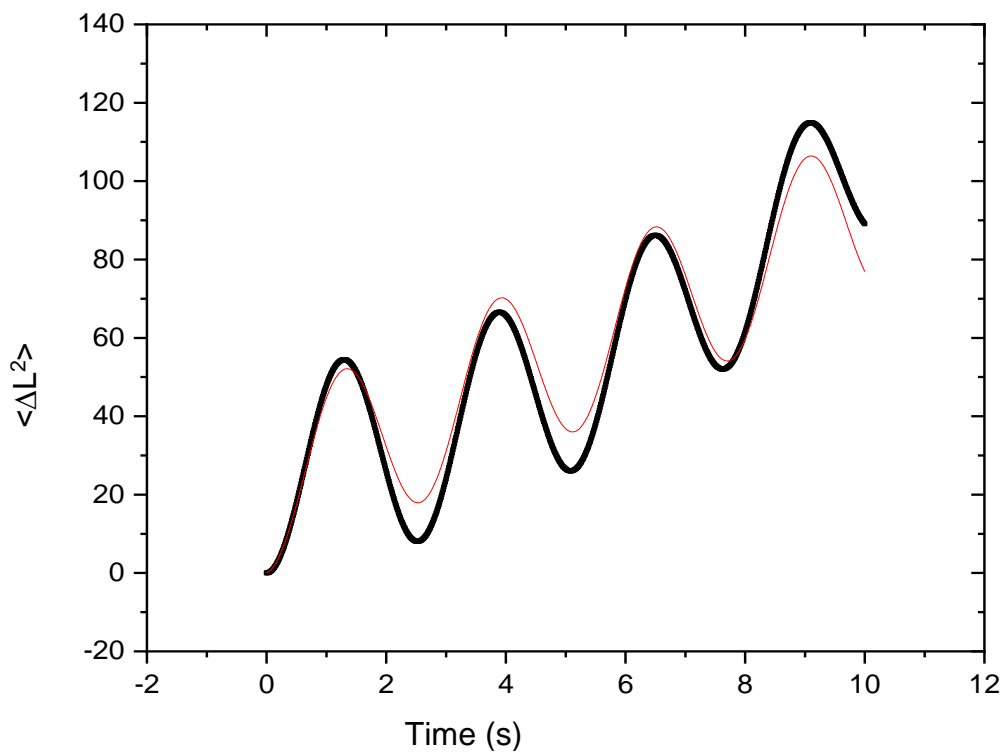


Figure 5-11: MSD data and angular velocity fitting for the trajectory shown in Figure 5-9 in black $\omega=1.25 \text{ rads}^{-1}$.

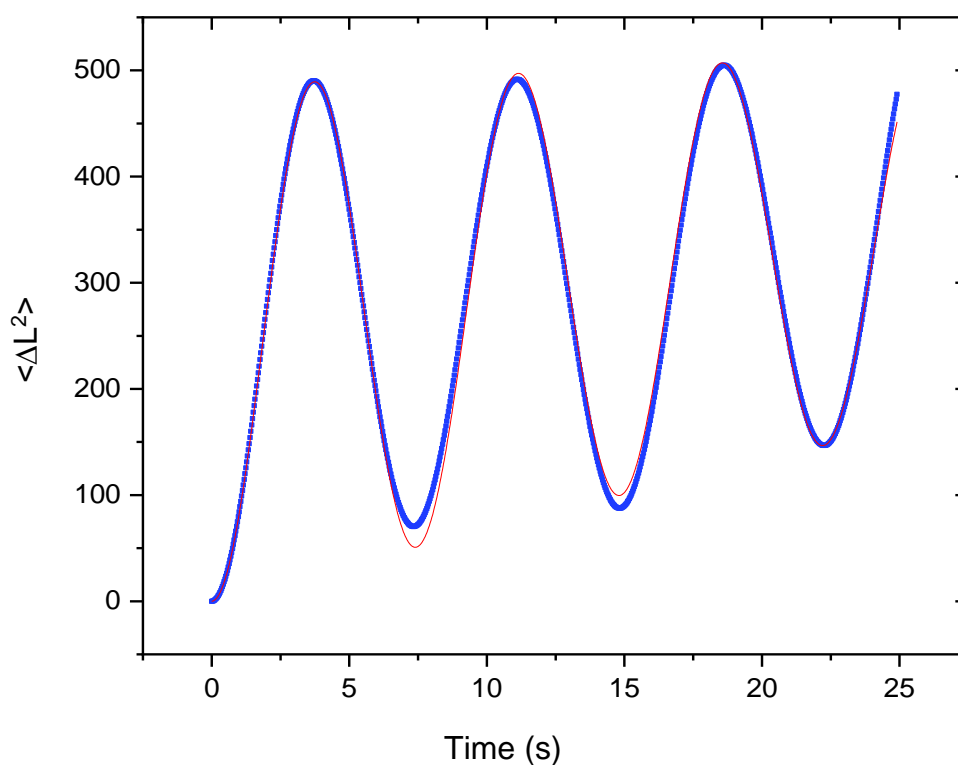


Figure 5-12: MSD data and angular velocity fitting for the trajectory shown in Figure 5-9 in blue $\omega=2.43 \text{ rads}^{-1}$.

Angular velocities of the two samples are shown in a scatter plot in Figure 5-13. As with the trajectories seen in Figure 5-9, the highest angular velocities seen here likely correspond to smaller catalytic patch sizes.

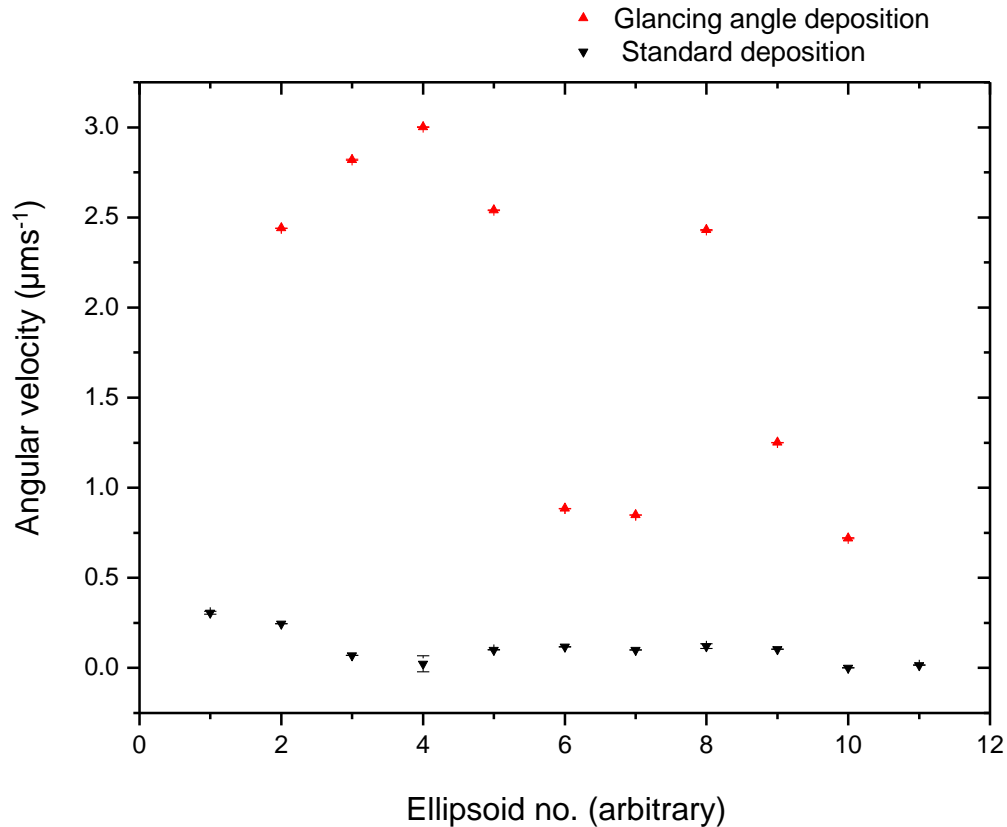


Figure 5-13: Scatter plot of raw angular velocities for a population of ellipsoidal swimmers coated under standard conditions (black) vs. a glancing angle deposition (red). Error bars are included but are too small to see in most cases.

Statistical assessment of the data was performed by sorting each set of data into 0.5 rads⁻¹ bins which was presented as a normalised bar chart. *Figure 5-14* shows that all of the ellipsoidal swimmers coated perpendicular to the source fall into the lowest angular velocity bin whilst none of the swimmers coated at a glancing angle do. This analysis highlights that, whilst there is a significant increase in angular velocity between the two populations, there is still a very broad range of rotational speeds.

Glancing angle ellipsoids populate 5 separate angular velocity bins. The ability to control the orientation of the ellipsoid would dramatically improve the results of such experiments and enable further control of the angular velocity to achieve the higher angular velocities seen in this chapter consistently across all swimmers coated at the same time. This will be further explored in chapter 7 which will cover suggested future work for this theme.

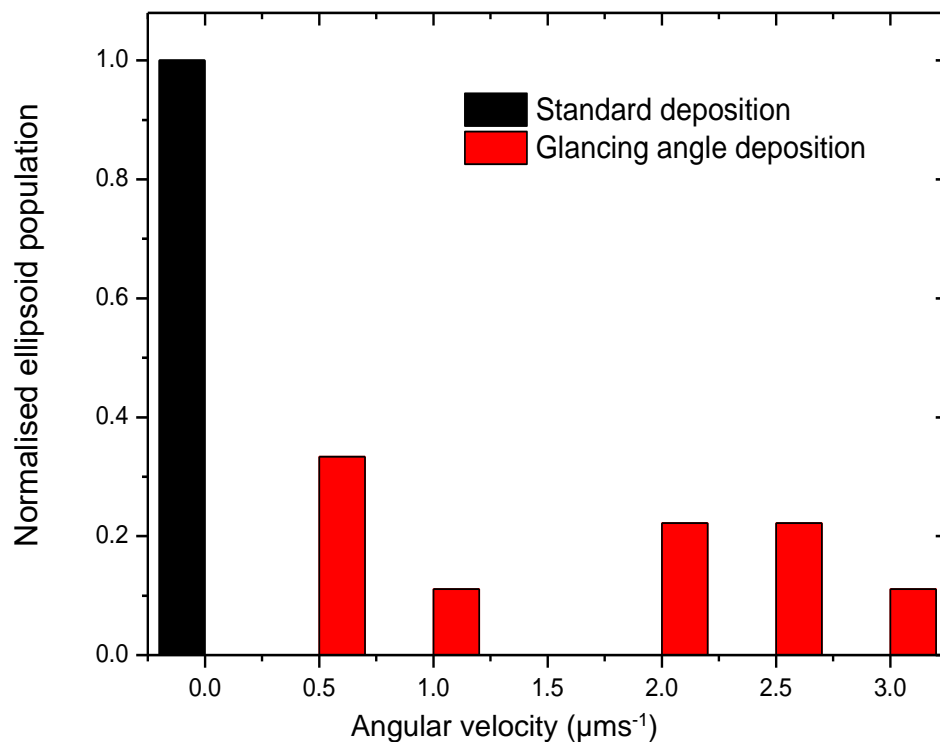


Figure 5-14: A bar chart showing the normalised frequency of ellipsoids in 0.5 rads^{-1} bins. Standard deposition is shown in black whilst Glancing angle deposition is shown in red.

5.4 Discussion

In order to understand why changes to the shape of the catalyst coating of evaporated Janus swimmers would lead to increased rotational motion, it is important to consider the mechanism by which motion is achieved in the first place.

The exact mechanism of ellipsoidal Janus swimmers has not been definitively proven to date. It was found that the process of stretching, washing, and coating of the colloids in a strong electron beam caused significant fluorescence bleaching of the colloids rendering fluorescence tracking of the direction of motion from the catalyst impossible. Experimental findings, such as a lack of bubble nucleation on the surface of the swimmers and an extreme sensitivity to contaminants such as salt strongly suggest that the mechanism is the self-electrophoretic in nature, consistent with their spherical counterparts.

The self-electrophoretic mechanism of motion in insulator/platinum swimmers has been previously proven to depend on a gradient in the thickness of the platinum coating which is thickest at the pole of a spherical swimmer and reduces to zero at the equator. This gradient in platinum thickness generates a gradient in the reaction rate across the particle causing an ion flux which drives motion. In the case of a perfect hemisphere or hemispheroid in this case, the propulsion would be rotationally symmetrical, theoretically producing no rotational component and purely translational motion²². This type of motion was presented in chapter 3.

When the symmetry of the catalytic patch is broken, as is the symmetry of the ion flux and resulting torque on the swimmer. This removes the rotational symmetry of the propulsion and as the symmetry is further reduced the rotational component of

the motion increases. Predictions of the catalytic patch at a 60° glancing angle deposition in *Figure 5-15* show the extent of this ‘symmetry breaking’ in ellipsoidal swimmers. Assuming areas with thicker platinum coatings produce a higher reaction rate and increased torque, it becomes easy to see why a glancing angle deposition would lead to the high angular velocities recorded in this chapter.

When compared to the spiralling spheres produced by Archer et al., the angular velocity achieved at similar glancing angles is comparable, with spheres achieving slightly higher for both velocities. Spheres coated at 50° and 70° glancing angles produced angular velocities of $\approx 4 \text{ rads}^{-1}$ and translational velocities $\approx 12 \text{ }\mu\text{ms}^{-1}$. The trajectories, however, are quite different.

Platinum thickness (nm)

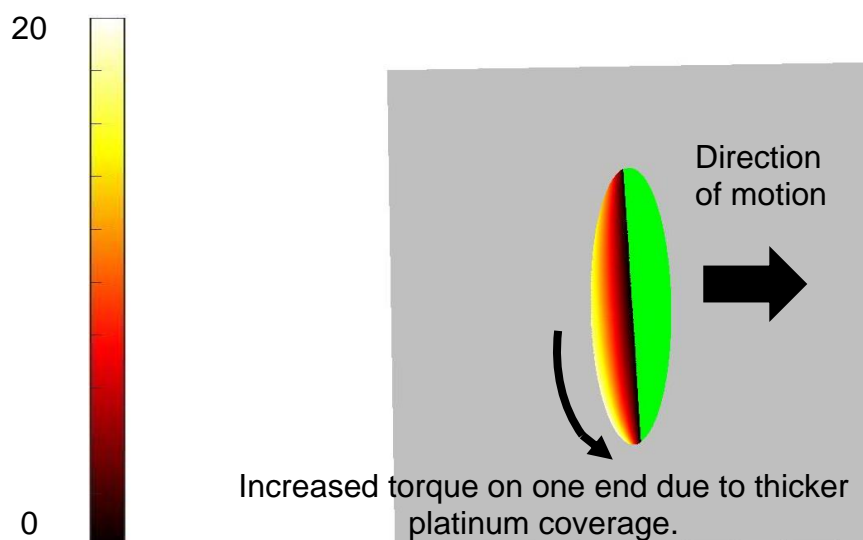


Figure 5-15: Schematic showing a high spin swimmer in the top-down configuration on a substrate (grey), showing how the differences in Pt thickness leads to rotational motion, whilst swimming close to the cuvette boundary.

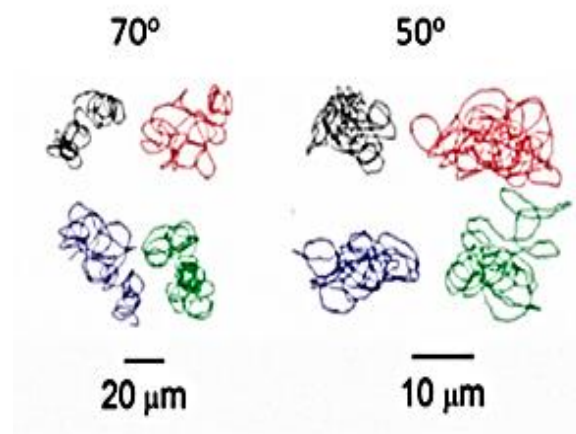


Figure 5-16: Figure from Archer et al. Trajectories of spherical Janus swimmers coated at 50° and 70° glancing angles²¹.

Figure 5-16 shows the trajectories of fast spinning spheres. Whilst there are many rotations, the trajectories appear somewhat random and disorganised, likely due to Brownian diffusion. This is in contrast to the ellipsoids presented in this work which produce very smooth circles, often around a fixed origin. Where the origin of the circle is not fixed, it gradually shifts in one direction, maintaining the spiralling behaviour. This is due to the convective flow effects produced by ellipsoidal swimmers.

The long axis of the ellipsoid is much larger than the diameter of the spheres tested and acts to reduce Brownian noise. It is also unclear if these experiments took place in the bulk fluid or if the spheres were near to a surface that they were not well coupled with.

The publication regarding spheres was able to test a broad range of glancing angles for deposition and recorded that at the shallowest glancing angles (10°-30°), very high angular velocities of $\approx 16-18 \text{ rads}^{-1}$ could be achieved²¹. Unfortunately this was

not possible in this work due to time constraints, but simulations of the catalyst coating shape of ellipsoids for a range of glancing angles will be available in chapter 7.

Whilst the introduction of controlled rotational motion in catalytic ellipsoids via glancing angle deposition was successful, it would be more useful for practical applications requiring a specific rotational speed, if the range of angular velocities could be reduced and controlled. As discussed in the results section, the use of ellipsoidal colloids as a substrate for coating platinum onto introduces an orientation with respect to the slide and metal source that is not present in spherical colloids. Depending on this orientation, the ellipsoid will experience varying degrees of shadowing, and the resulting angular velocity will reflect this.

Ideally, for more control over angular velocity, all of the ellipsoidal colloids would be aligned in a known configuration with respect to the slide. This would allow orientation relative to the metal source to be controlled, for example to result in the maximum shadowing shown in *Figure 5-15*, and investigate intermediate alignments. This type of alignment could be achieved using magnetic colloids or even a micro-ridged substrate which the colloids settle into. Similarly, the glancing angle could be reduced even further through to 10 degrees, which in theory would produce an even more pronounced 'nose of platinum' at one tip with almost no platinum reaching the rest of the colloid. This would potentially lead to translation in the direction of the long axis which is of great interest in theoretical literature but has yet to be realised experimentally. Ray tracing predictions of the catalyst coatings at further glancing angles has been provided in section 7.3.2.2

Such shallow glancing angles would dramatically increase the length of the shadow for each ellipsoid so care would have to be taken that the ellipsoids are well-spaced on the substrate, or they would shadow one another.

5.5 Conclusions

Further to the natural range of angular velocities in ellipsoidal micro-swimmers, here we demonstrate the ability to produce significantly enhanced rotational velocity by controlling the catalyst cap geometry. This was achieved by employing a glancing angle deposition which coupled with the anisotropy of the ellipsoidal colloids produces a shadowing effect during the coating. These asymmetrical catalyst distributions lead to asymmetrical forces on the colloid which induces rotating behaviour.

This enhanced rotation can be achieved in spherical colloids, but is a lengthy process relying on the use of colloidal crystals to induce the shadowing effect which occurs naturally with ellipsoidal colloids. The angular velocities of both spheres and ellipsoids are comparable at similar glancing angles, $\approx 4 \text{ rads}^{-1}$ and 1.88 rads^{-1} , respectively, but the trajectories produced by ellipsoids are much more organised and smoother (*Figure 5-9*).

The use of ellipsoids also improves the potential for applications as their increased surface area as compared to spheres allows for increased interactions with their environments or stimuli. In the case of these rotating ellipsoids, the increased interaction with the fluid has potential for more effective mixing devices on the micro-scale.

Chapter 6:

Dumpling and Bowl-shaped swimmers

6 Dumpling and Bowl-shaped swimmers

6.1 Introduction

Chapter 1 addressed the general lack of experimental data on Janus swimmers of differing geometries to the popular rods and spheres. Whilst chapter 3-5 investigated the rich dynamics of well-defined ellipsoidal Janus swimmers, this chapter will focus on a range of less well-defined geometries. ‘Bowl’ and ‘Dumpling’ shaped silica colloids are tested as a ‘one-pot’ approach to achieving a range of angular velocities.

As described in detail in chapter 5, the breaking of symmetry of the catalytic patch of a Janus swimmer can lead to an imbalance of torque across the swimmer and the introduction of an angular component to the velocity. This is usually achieved by coating the swimmers at a glancing angle, which requires a specific custom-built sample holder and the use of an electron beam evaporator for directionality. This method is costly in both time and equipment.

This chapter aims to provide a simple and fast approach to enhanced rotations in active swimmers using the colloid geometry, and sputter coating to break the symmetry of the catalytic coating. These colloids were provided by Prof Syuji Fujii of Osaka Institute of Technology and included in the study in an effort to foster collaborations with this university. The specific shapes were chosen as the uneven colloid surfaces with both convex and concave geometries will give rise to asymmetrical areas of catalytic coating. This is expected to induce rotational motion at a higher degree than either spheres or ellipsoids.

6.2 Methods

Bowl and Dumpling shaped colloids made from polydimethylsiloxane (PDMS) were provided as part of a collaboration with Osaka Institute of Technology. They were produced by Prof. Syuji Fujii.

The colloids were deposited onto cleaned glass slides from a suspension of 50:50 deionised water and ethanol either by spin coating or allowing a droplet of colloids to air dry on the slide. This was done to investigate if there are any differences in orientation between these two methods.

The slides were then sputter coated with platinum at $\approx 10^{-3}$ mBar for 30 seconds until a mirror finish was achieved. The swimmers were imaged using SEM and their orientations on the slides recorded.

Using a damp lens tissue and tweezers, the swimmers were gently wiped off the slides and suspended in 10% wt H_2O_2 and pipetted into a quartz sample cuvette and observed using an inverted transmission microscope. 30s videos at 33fps were recorded and the motion analysed by custom LabVIEW software.

6.3 Results

6.3.1 'Dumpling' shaped PDMS colloids

6.3.1.1 SEM Analysis

SEM analysis of Dumpling shaped colloids revealed a distinct lack of monodispersity which will hinder comparisons of velocity within the sample.

Due to the disparity in both size and general shape of these colloids (*Figure 6-1*) it is difficult to assign specific orientations. As such they were grouped as being either

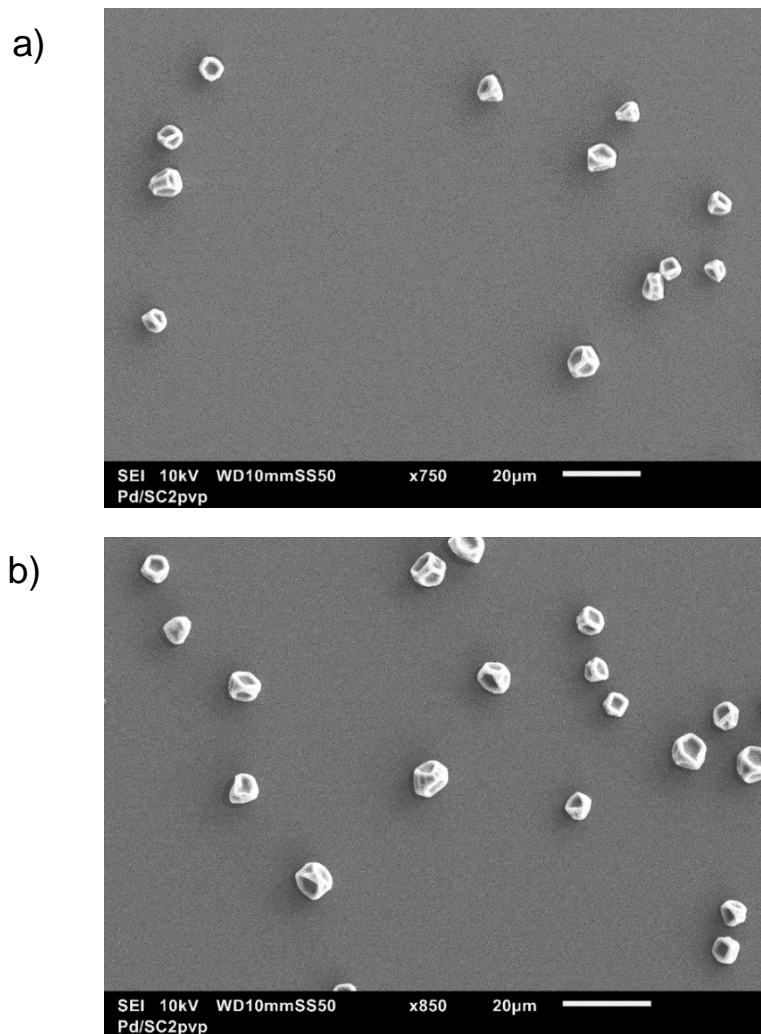


Figure 6-1: Scanning electron microscope images of dumpling shaped PDMS colloids; a) air dried from solution b) spin coated at 2000rpm.

convex surface facing up, single concave surface facing up, or plural concave surfaces facing up. A schematic for these assigned orientations is provided in *Figure 6-2*. The shape/size disparity will affect the validity of the results meaning systematic testing will not be possible, however it is worthwhile to investigate whether a correlation exists between shape and angular velocity in order to plan more rigorous experiments in future.

During SEM analysis it became apparent that there was no difference in the final orientation of colloids between the spin coated and air-dried samples. However due to contractions of the evaporating liquid in air dried samples, the colloids dimerised or were so close as to cause shadowing effects in the catalyst coating as seen in *Figure 6-1 (a)*.

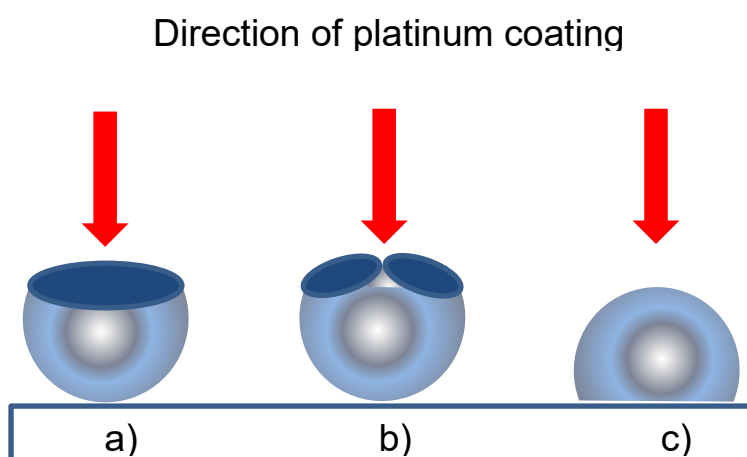


Figure 6-2: Schematic of assigned colloid orientations; a) single concave surface facing up b) plural concave surfaces facing up c) convex surface facing up.

As such only samples prepared by spin coating were analysed, the results of which can be seen in *Table 6-1*.

Orientation	% of population
Convex surface facing up	31
Single concave surface facing up	37
Plural concave surfaces facing up	32

Table 6-1:Relative population densities of each orientation

The weightings of orientations are evenly distributed with each orientation accounting for $\approx 1/3$ of the population. Colloids with concave surfaces facing up (one or multiple), which are expected to have more asymmetrical catalytic areas, account for 69% of the measured population. The angular velocity analysis is expected to reflect this with a higher weighting of higher angular velocity swimmers vs. low angular velocity swimmers. Colloids with convex surfaces facing up more resemble a sphere during coating and are expected to have symmetrical coatings which result in negligible angular velocity. Based on the populations seen in *Table 6-1*, swimmers with low angular velocity are expected to account for $\approx 1/3$ of swimmers during motion testing.

6.3.1.2 Motion Testing

The results from LabVIEW motion tracking software indicate that the coated colloids swim with an average velocity of $2.54 \pm 1.24 \mu\text{m s}^{-1}$ in 10%wt. H_2O_2 fuel.

Results were compared to control experiments completed in deionised water; in the absence of H_2O_2 fuel swimmers undergo Brownian motion as expected. Trajectories for control experiments can be seen in red in *Figure 6-5*, *Figure 6-6* and *Figure 6-4*. An ensemble average MSD plot for 20 dumpling shaped colloids seen in *Figure 6-3* shows almost linear behaviour which is consistent with pure Brownian diffusion, this confirms that the chemical reaction drives propulsion.

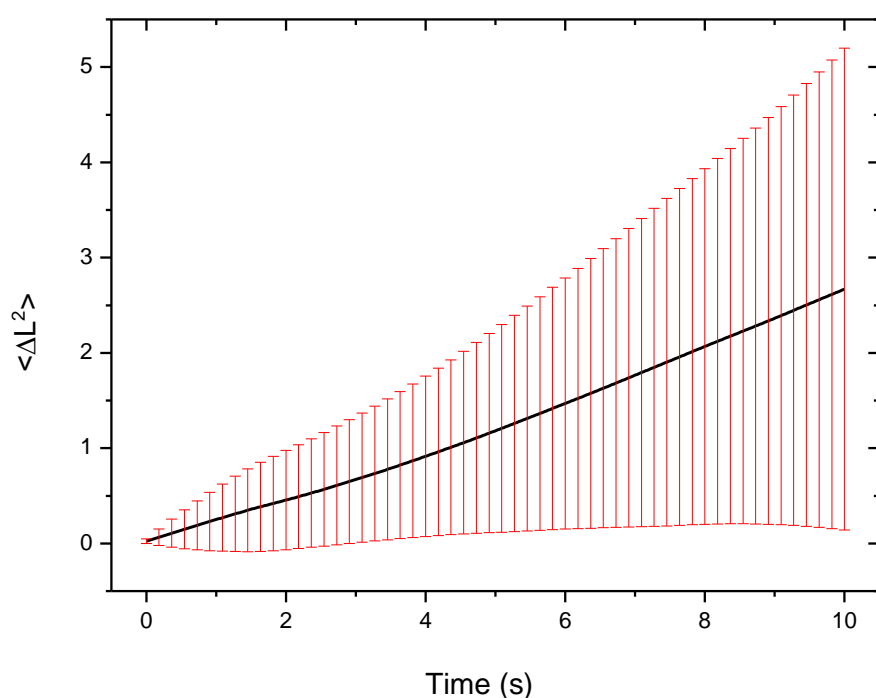


Figure 6-3: Ensemble average MSD plot for 20 dumpling shaped colloids in deionised water.

Measurements for the diffusion coefficients calculated in water gave an average value of $0.0376 \pm 0.0084 \mu\text{m}^2\text{s}^{-1}$. The measurements for diffusion coefficient in deionised water were used to estimate the size range of the swimmers using the Stokes-Einstein equation (*Equation 2-9*) for spherical colloids. The average diameter was measured as $11.90 \pm 2.26 \mu\text{m}$ with a 19% standard deviation. The sizes are reasonably consistent with the average diameter expected from the SEM ($\approx 9 \mu\text{m}$ diameter).

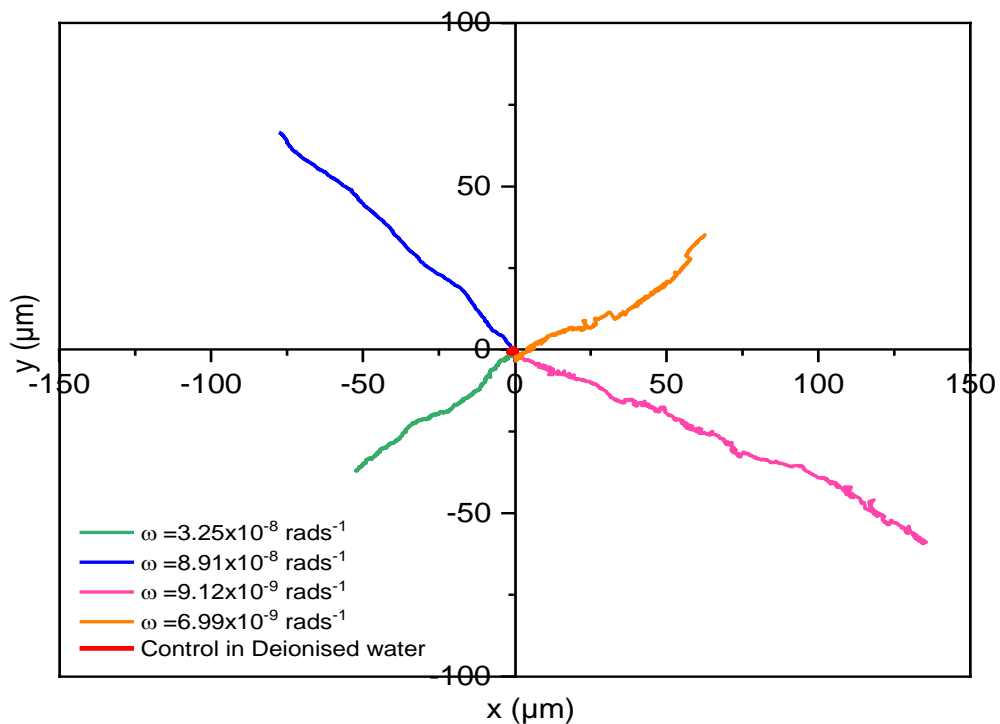


Figure 6-4: Representative trajectories of dumping shaped colloids with $\omega < 0.01 \text{ rads}^{-1}$ in 10% wt. H_2O_2 .

Qualitatively it can be seen that there are 3 basic types of swimmer behaviour. Some swimmers exhibit almost purely ballistic behaviour, travelling in straight lines with minor fluctuations caused by Brownian motion as seen in *Figure 6-4*, these ballistic swimmers account for 36% of the tested population.

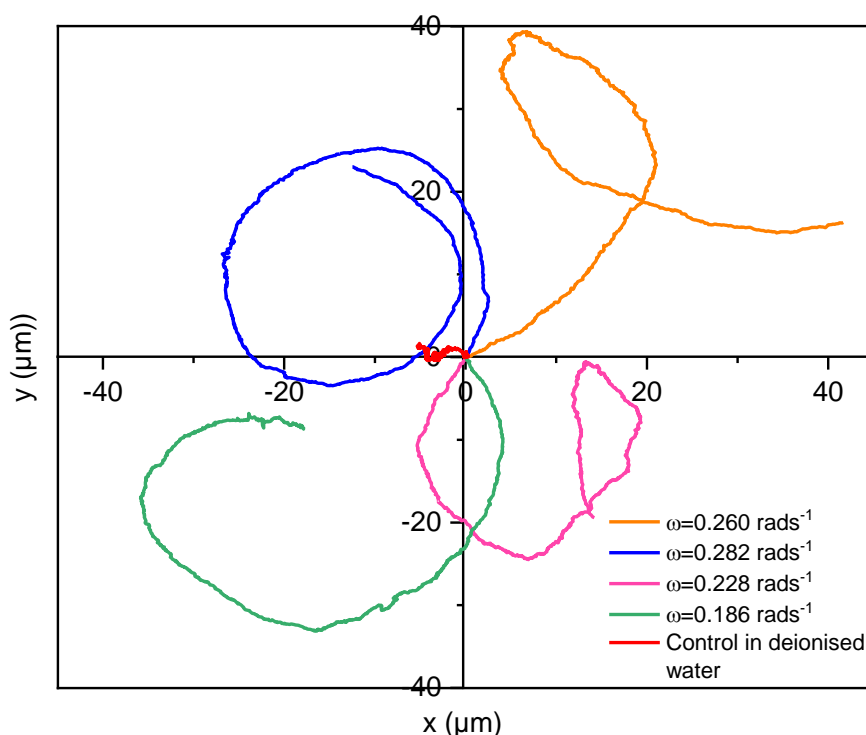


Figure 6-5: Representative trajectories of dumping shaped colloids with $w > 0.1 \text{ rads}^{-1}$ in 10% wt. H_2O_2 .

Others exhibit highly rotational behaviour, travelling in a circular motion around a centre point like those displayed in *Figure 6-5*, these swimmers account for 36% of the tested population. All other colloids exhibit behaviour that is somewhere in between these two extremes where curved but relatively translational motion is observed as in *Figure 6-6*, -these intermediate swimmers account for 28% of the tested population.

Swimmers with largely ballistic trajectories have a much larger displacement from their origin in the same timescale than swimmers travelling in a more rotational manner, suggesting that there may be a correlation between angular and translational velocity which will be investigated in section 6.3.1.3.

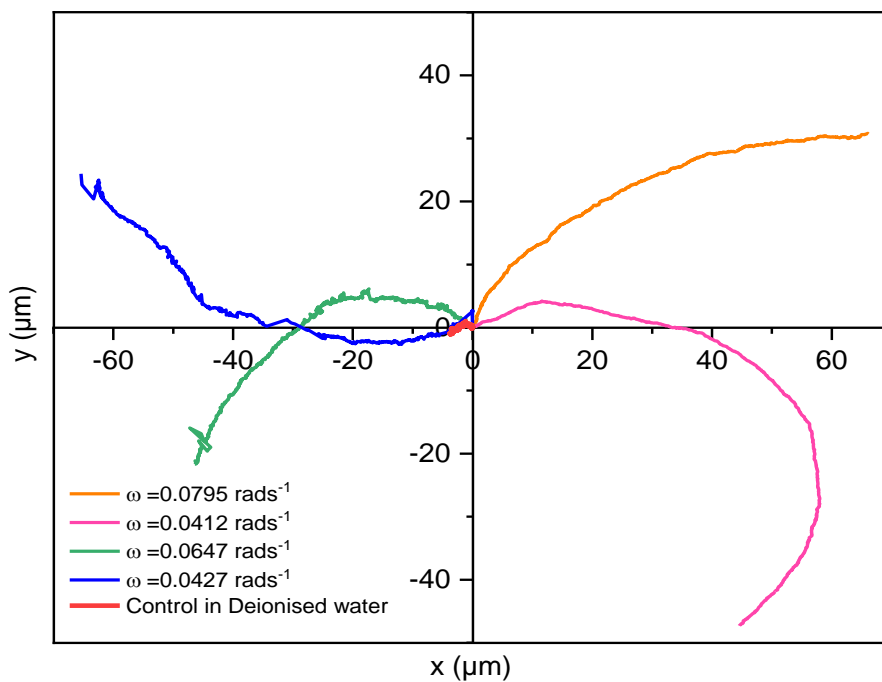


Figure 6-6: Representative trajectories of dumping shaped colloids with $w = 0.01$ - 0.099 rads^{-1} in 10% wt. H_2O_2 .

6.3.1.3 Angular velocity Analysis

Angular velocities were quantified using the procedure outlined in chapter 2, *Equation 2-8* was fitted to the experimental MSD data for each colloids using OriginPro software, an example of which can be seen in *Figure 6-7*. Raw data for angular velocity analysis is provided in *Figure 6-8*.

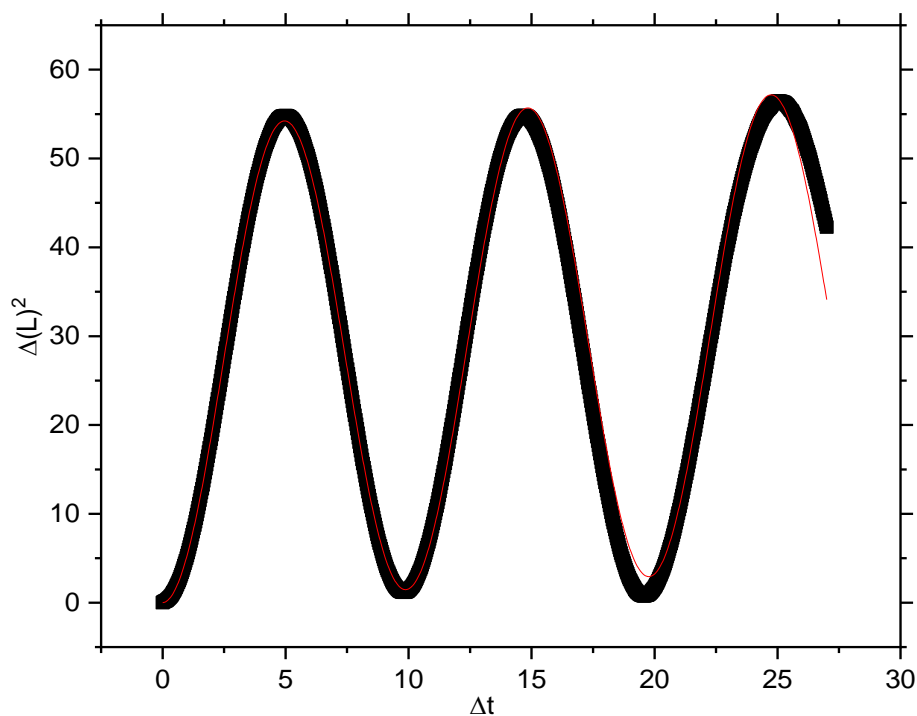


Figure 6-7: MSD curve fitted to Equation 4 to determine angular velocity using Originpro software.

The results of the angular velocity analysis were in good agreement with the 3 types of behaviour previously established. The raw results were binned every 0.05 rads^{-1} then normalised to give a distribution seen in *Figure 6-9*.

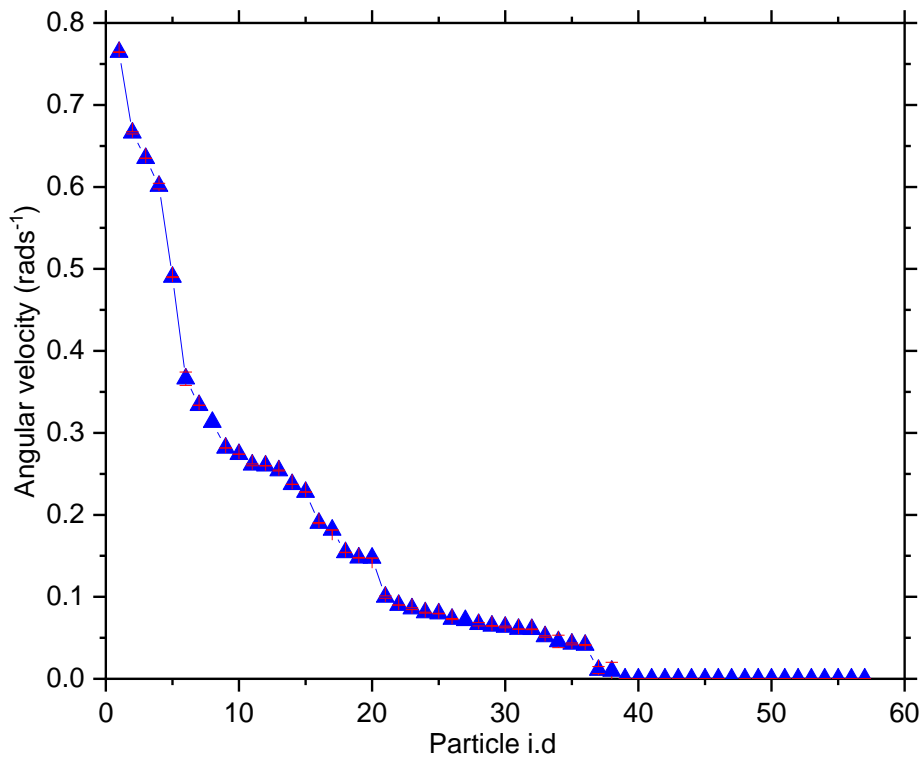


Figure 6-8: Angular velocities for a set of swimmers. Error bars (calculated by Originpro fitting software) are provided for all data points but are too small to be seen in most cases.

Figure 6-9 shows a wide distribution of angular velocities with almost all 0.05 rads^{-1} populated by at least one swimmer. The highest populated band is between 0 and 0.05 rads^{-1} which is expected as there were negligible variances between swimmers with very low angular velocity.

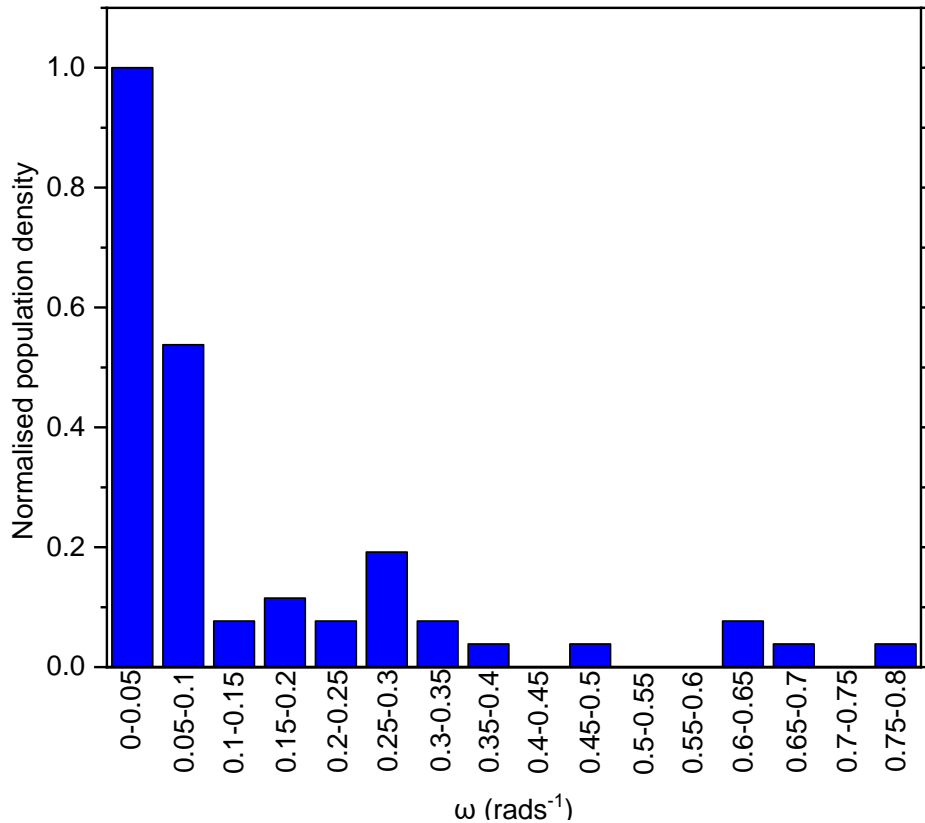


Figure 6-9: Bar chart showing the distribution of angular velocities of a set of swimmers at 0.05 rads⁻¹ intervals.

The angular velocities were then grouped into much larger angular velocity bins of $\omega < 0.01$ rads⁻¹, $\omega = 0.01-0.099$ rads⁻¹ and $\omega > 0.1$ rads⁻¹ and their % population compared to the % population of orientations from the SEM images.

Angular velocities are evenly distributed across the sample (Figure 6-10) with approximately the same number of swimmers in each assigned band for ω . This makes it difficult to observe a correlation between orientation and increased or decreased spin. The distributions, whilst not distinct, are in agreement with the orientation populations discussed in section 6.3.1.1 with very low spin swimmers (> 0.01 rads⁻¹) accounting for $\approx 1/3$ of the tested population and swimmers with a rotational component to their motion accounting for $\approx 2/3$ of the tested population.

In order to confirm which orientations are the cause of a particular behaviour it would be necessary to have control of the swimmer orientation before deposition of the catalyst. As previously mentioned, the sample was not monodisperse or of consistent shape which may also be causing some of the effects attributed to orientation.

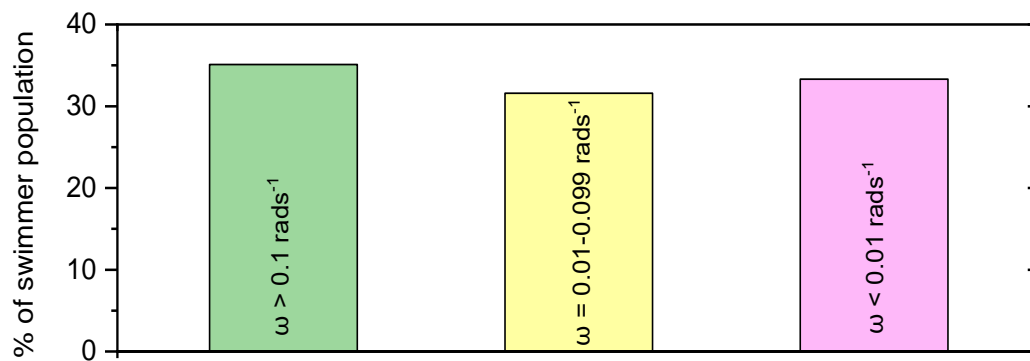


Figure 6-10: Bar chart showing angular velocities grouped as high ($>0.1\text{rads}^{-1}$), medium ($0.01-0.099\text{rads}^{-1}$) and low ($>0.01\text{rads}^{-1}$)

When the data for angular velocity and translational velocity was combined (Figure 6-11) it can be seen that the highest translational velocities were achieved by

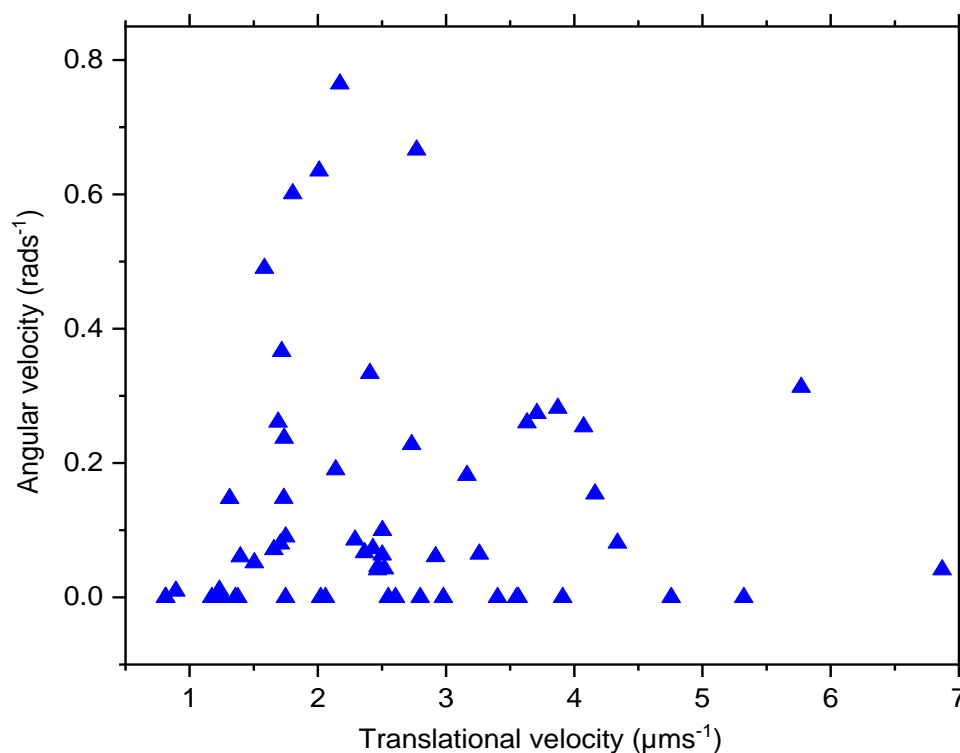


Figure 6-11: Scatter plot of translational velocity vs. angular velocity.

swimmers with very low angular velocity, whilst the swimmers with the highest angular velocities corresponded to a very low translational velocities. A low angular velocity swimmer with high translational velocity is indicative of a swimmer that has a catalytic coating area closely resembling a sphere, or in this case it was oriented with a convex surface facing upwards before coating. High angular velocities with low translational velocities is indicative of swimmers with non-hemispherical coatings, so these swimmers were likely oriented with concave surfaces facing up during coating.

The average translational velocities across the 3 assigned groups of angular velocity are extremely close and show that swimmers with the highest spin have also have

the highest translational velocity (*Figure 6-12*). This was unexpected based on a qualitative analysis of swimmer trajectories.

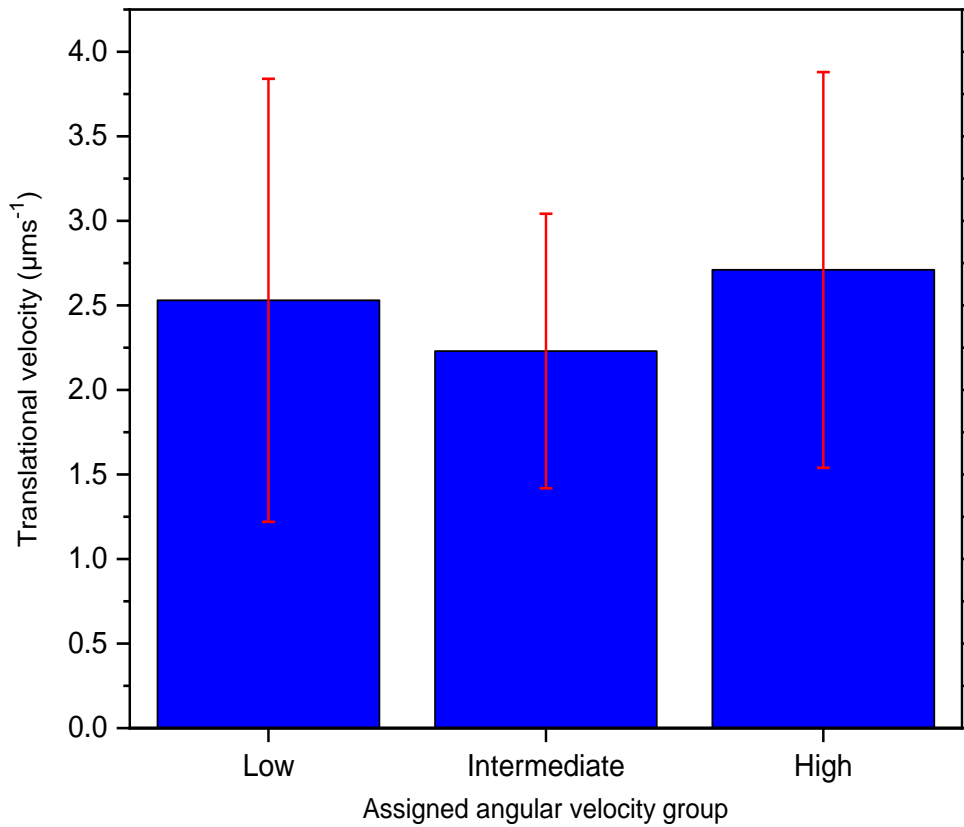


Figure 6-12: A bar chart showing the average velocity of a set of swimmers within defined bands for angular velocity.

6.3.2 Bowl shaped PDMS Colloids

6.3.2.1 SEM Analysis

It can be seen from the SEM images in *Figure 6-13* that the bowl shaped colloids have 3 general orientations; cavity facing up, cavity facing down and cavity facing to the side, a schematic for these orientations has been provided in *Figure 6-14*.

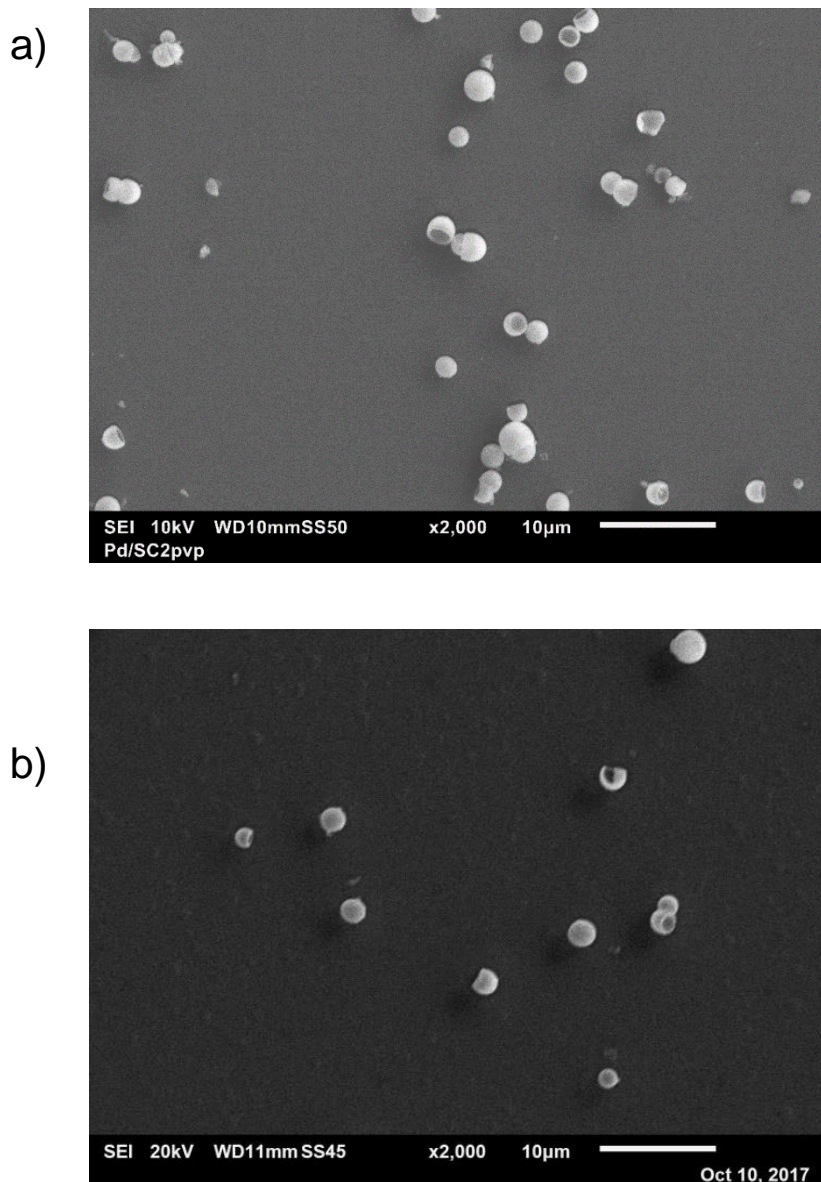


Figure 6-13: Scanning electron microscope images of bowl shaped PDMS colloids
a) air dried from solution b) spin coated at 2000rpm

As with the previous sample, drying effects caused colloids to stick together along with shadowing effects in air dried samples, so only spin coated swimmers were analysed. Statistical analysis was performed to determine the frequency of each orientation in a set of 100 colloids (*Table 6-2*)

It can also be seen from the images that the sample is not monodisperse in size and some have formed dimers which is likely to have an effect of both translational and angular velocity and will affect the validity of results derived from these samples. Results from coupled colloids differ dramatically from those of individual colloids and so were not included at this stage of the research.

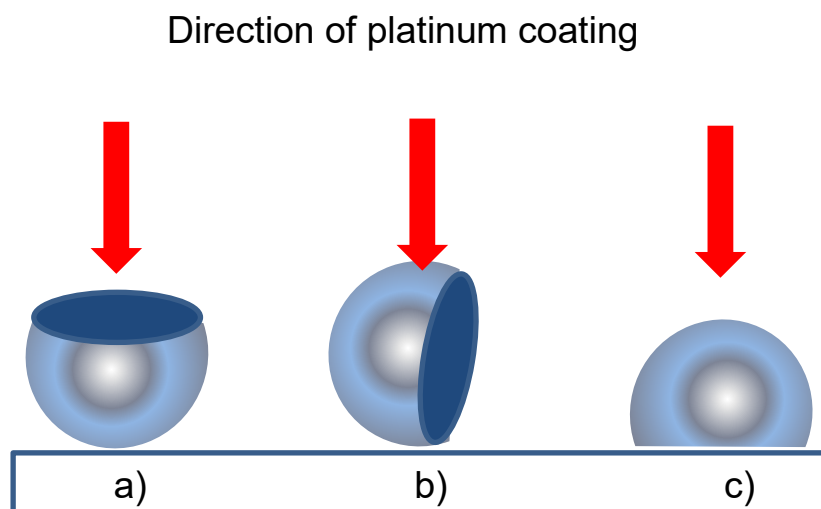


Figure 6-14: Schematic of assigned orientations; a) cavity facing up b) cavity facing to the side c) cavity facing down.

Orientation	% of population
Cavity facing to the side	38
Cavity facing up	42
Cavity facing down	20

Table 6-2: Relative population densities of each orientation.

The orientation population weightings for bowl shaped swimmers are more distinct than for dumping shaped colloids with only 20% appearing with their cavity facing down. In this orientation the colloids most resemble spheres and their catalytic coating area will be hemispherical. As with dumpling shaped swimmers this should be reflected in the angular velocity analysis where around 20% of the tested population are expected to have negligible angular velocity. The rest of the population ($\approx 80\%$) are expected to have a rotational component to their motion.

6.3.2.2 Motion Testing

The results from LabVIEW motion tracking software indicate that the coated colloids are swimming with an average velocity of $2.55 \pm 1.09 \mu\text{m s}^{-1}$.

These results were compared to control experiments completed in deionised water, in the absence of H_2O_2 fuel swimmers undergo Brownian motion as expected. Trajectories for control experiments can be seen in red in *Figure 6-16* to *Figure 6-17*.

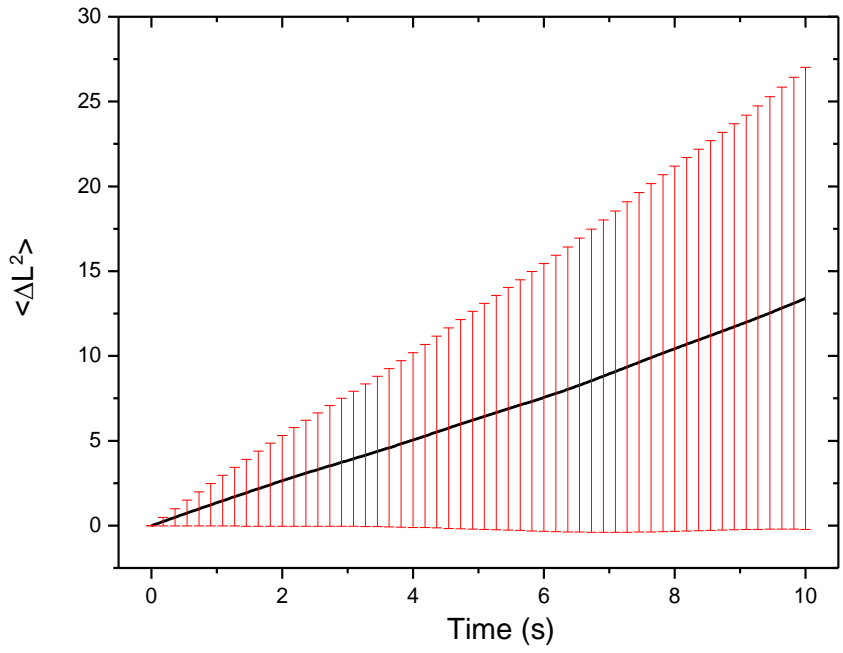


Figure 6-15: Ensemble average MSD plot for bowl shaped colloids in deionised water.

The ensemble average MSD plot for 20 bowl shaped colloids in deionised water (Figure 6-15) shows a linear plot which is consistent with pure Brownian diffusion, indicating that the chemical reaction is the origin of the propulsive mechanism.

Measurements for the diffusion coefficients calculated in water were used to estimate the size range of the swimmers using Equation 2-9, which assumes spherical colloids. The average diameter was measured as $2.94 \pm 1.27 \mu\text{m}$ with a 43% standard deviation. This is in agreement with SEM analysis and explains the large range of velocities measured.

Larger swimmers will have a smaller diffusion coefficient than smaller swimmers due to the dependency of D on swimmer radius. This leads to a decrease in velocity compared to smaller swimmers.

Trajectories of bowl shaped colloids with angular velocity greater than 0.01 rads^{-1} shown in *Figure 6-17* and *Figure 6-16* are as expected. The motion is similar to the larger dumping shaped colloids but with more Brownian fluctuations and a decreased persistence length due to their lower size.

Swimmers with a rotational component to their motion account for 82% of the tested population whilst ballistic swimmers with negligible angular velocity account for only 18% of the tested population. This is consistent with the orientation distributions discussed in 6.3.2.1.

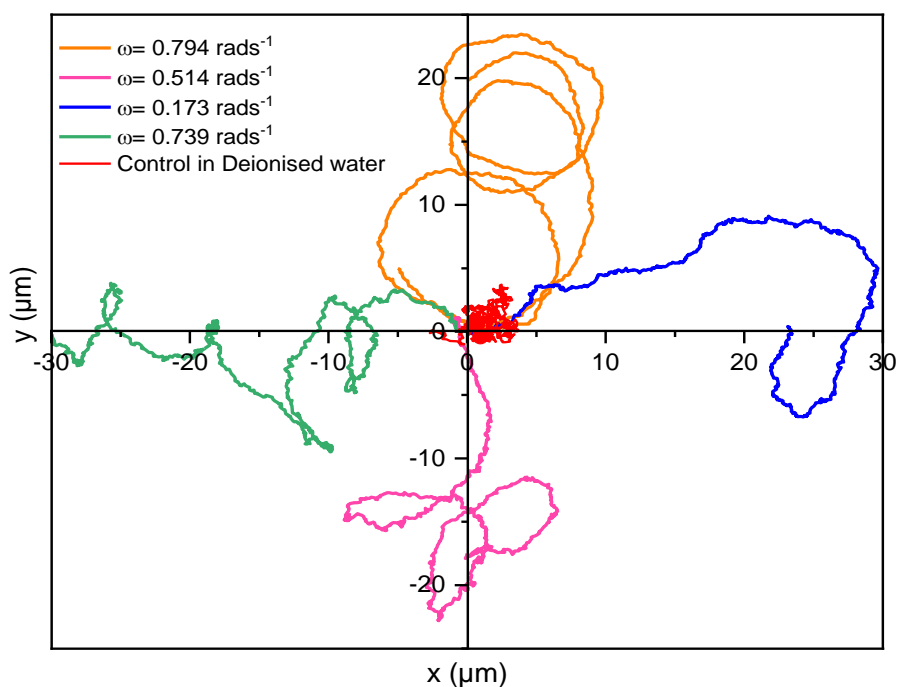


Figure 6-16: Representative trajectories of bowl-shaped colloids with $\omega > 0.1 \text{ rads}^{-1}$ in 10% wt. H_2O_2 .

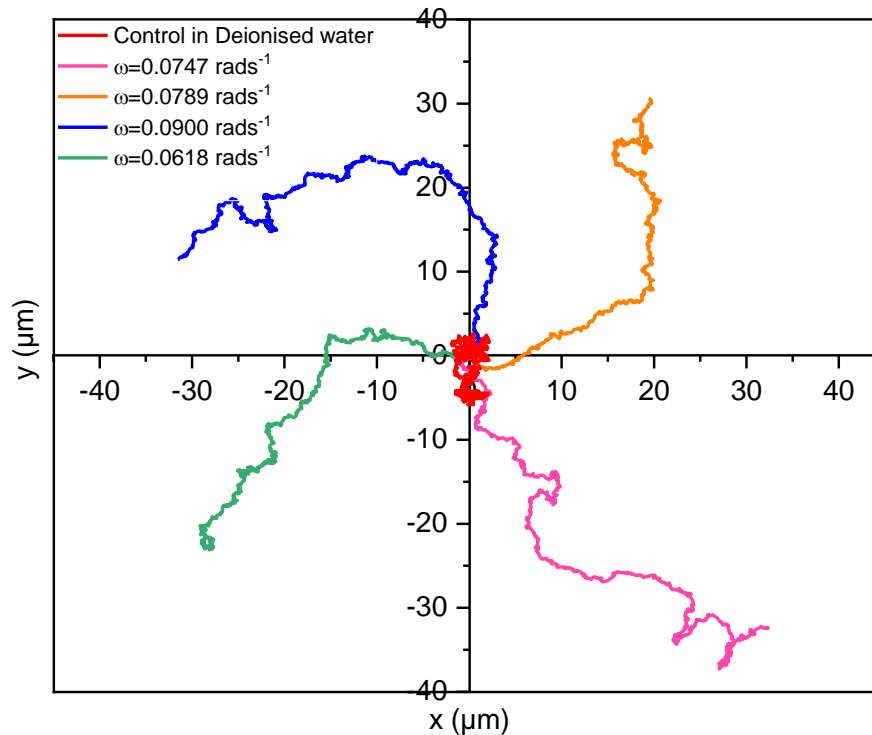


Figure 6-17: Representative trajectories of bowl-shaped colloids with $\omega=0.01-0.099$ rads^{-1} in 10% wt. H_2O_2 .

Whilst the trajectories in *Figure 6-18* show a relatively ballistic motion, they also appear to have an unexpected periodic part-rotation despite producing negligible results for angular velocity in OriginPro. It is possible this could be caused by Brownian fluctuations, however the periodic nature of the disturbance, which is also seen in *Figure 6-17* suggests a non-random effect. The unusual geometry of the starting colloid is likely to have an effect on the rotational time of the swimmers. A decreased rotational time when compared to the same size of sphere without a cavity could explain this periodic change of direction that does not appear to be caused by an increase in angular velocity.

Periodic rotations in the direction perpendicular to the field of vision, which cannot be seen due to the 2D limitations of the video capture and analysis software, could also potentially explain the disturbances in the trajectories. Difficulties encountered due to motion in the z-axis are a driving factor in why ellipsoids, which sediment and couple well with the lower boundary, were predominantly studied near a bounding surface (Chapter 3).

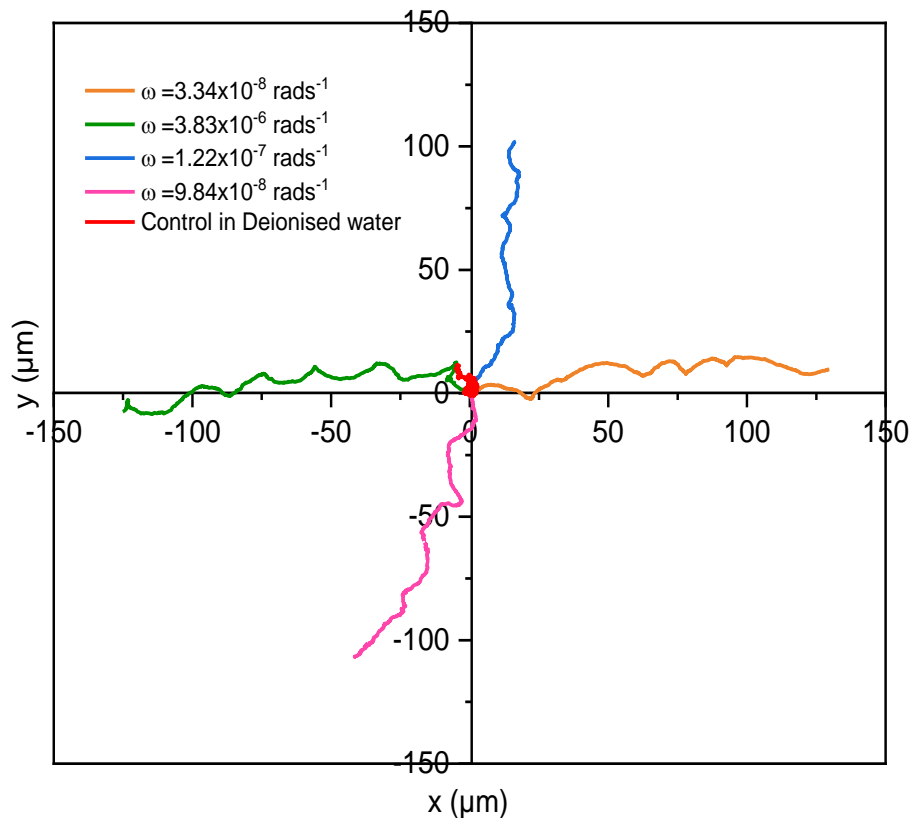


Figure 6-18: Representative trajectories of bowl shaped colloids with $\omega < 0.01 \text{ rads}^{-1}$ in 10% wt. H_2O_2 .

6.3.2.3 Angular velocity analysis

Angular velocities were calculated using *Equation 2-8* which are plotted with their errors in *Figure 6-19*.

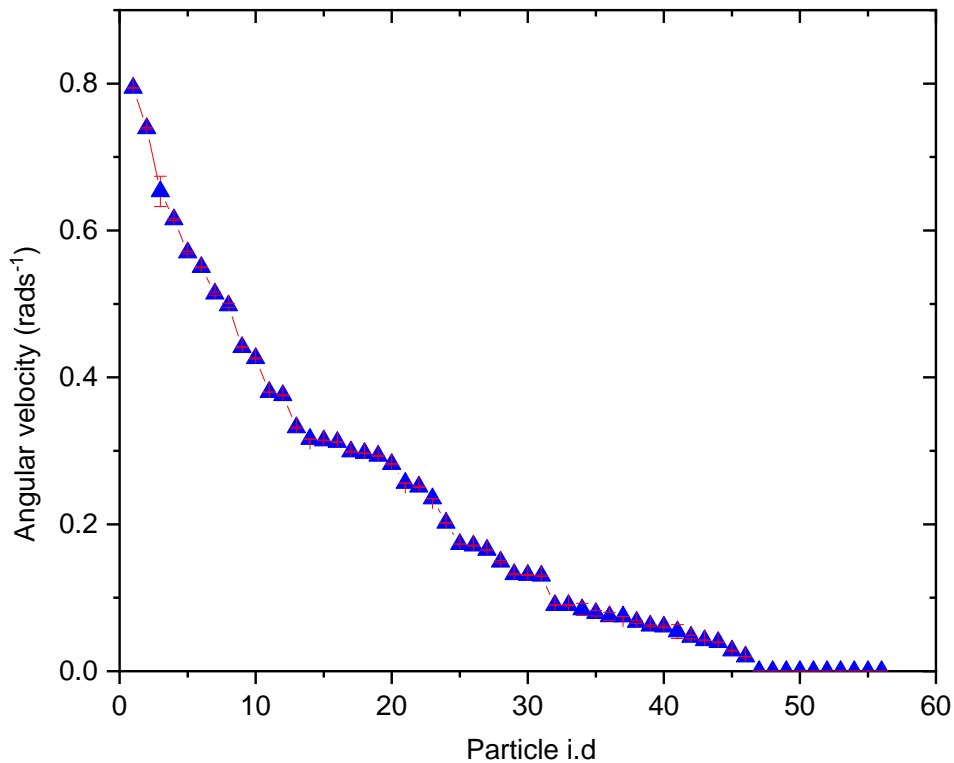


Figure 6-19: Angular velocities for a set of swimmers. Error bars (calculated by Originpro fitting software are provided for all data points but are too small to be seen in most cases.

The results of the angular velocity analysis were concordant with the 3 types of behaviour previously established and were binned every 0.05 rads^{-1} then normalised to give a distribution seen in *Figure 6-20*. Results for the distribution of angular velocities are more evenly spaced than dumping shaped swimmers with at least one swimmer for every band.

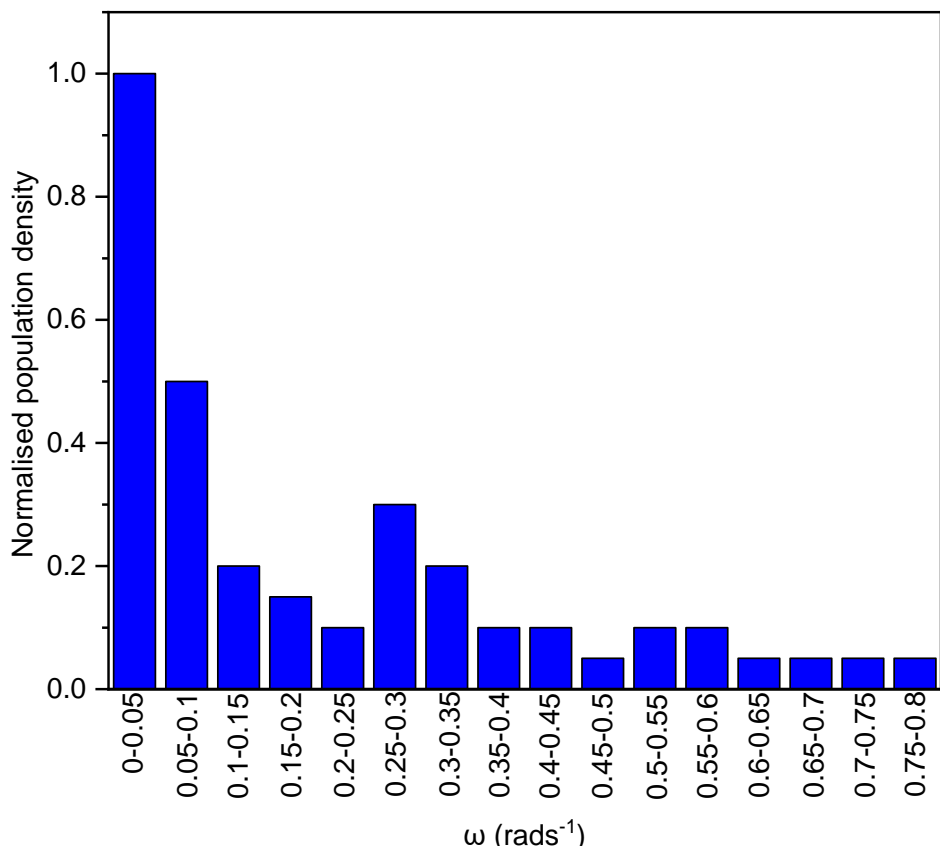


Figure 6-20: Bar chart showing the distribution of angular velocities for a set of swimmers at 0.05 rads^{-1} intervals.

There are 3 distinct bands for angular velocity (Figure 6-21) with highly rotational swimmers occurring most often. The number of swimmers with very low angular velocity is the least common and the number of swimmers (18%) correlates with the number of colloids with the cavity oriented downwards before deposition (20%). It makes sense that bowl shaped colloids coated in this way would be the most analogous to spherical Janus swimmers as the catalytic area is very similar in both shapes. For the other orientations there is no correlation which unfortunately means that the data is not sufficient to form conclusions that a certain orientation would give a discrete band of possible angular velocity.

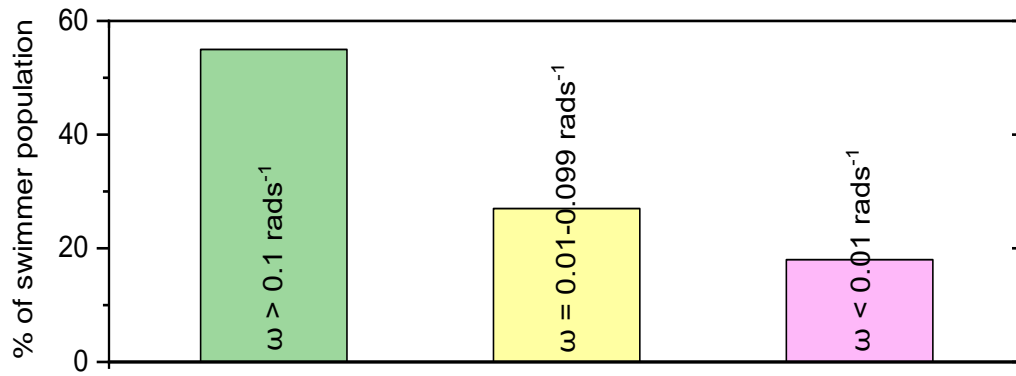


Figure 6-21: A bar chart showing angular velocities grouped as high ($>0.1 \text{ rads}^{-1}$), medium ($0.01-0.099 \text{ rads}^{-1}$) and low ($>0.01 \text{ rads}^{-1}$) for a set of swimmers.

As previously discussed in 6.3.1.3, control over the orientation before deposition would allow more rigorous testing of this link.

When the data for angular velocity and translational velocity was combined (Figure 6-22) it can be seen that the highest translational velocity was achieved by a swimmer with very low angular velocity which is consistent with ‘Dumpling’ shaped PDMS colloids. However, unlike the dumplings, there are several highly rotational swimmers that are also showing high translational velocities.

The bulk of the data displayed no obvious link between increased translational velocity and low angular velocity.

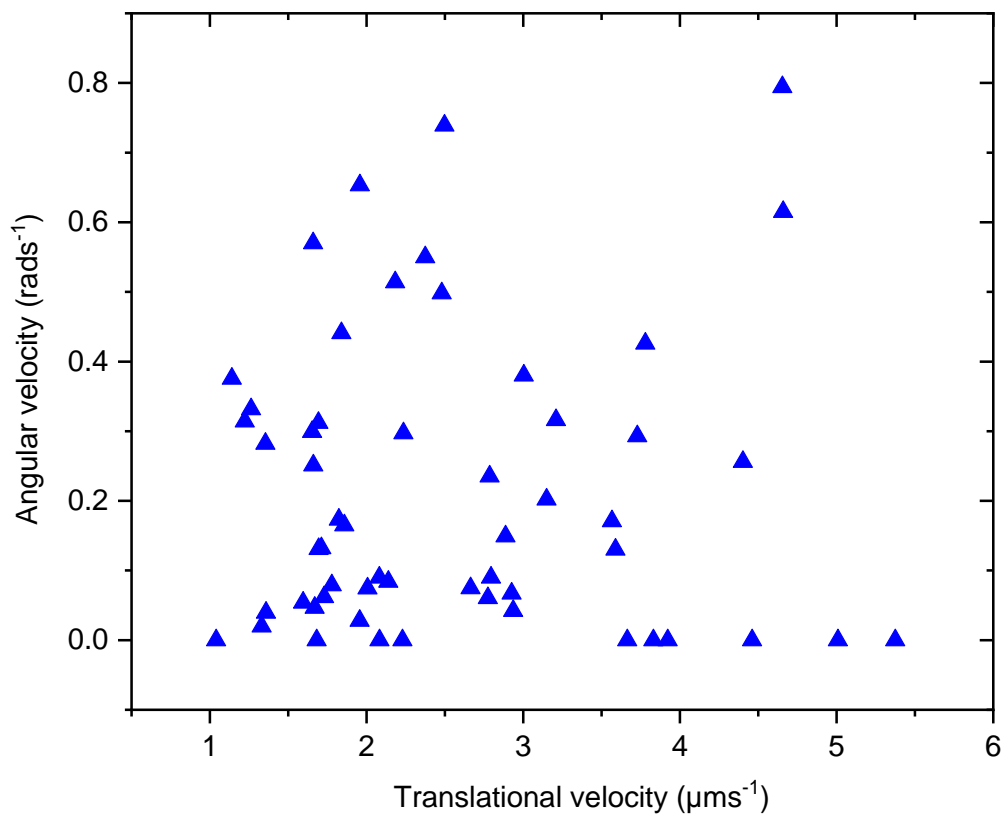


Figure 6-22: Scatter plot of translational velocity vs. angular velocity

Figure 6-23 shows that swimmers with the lowest spin on average have the highest velocity which is expected based upon qualitative analysis of the trajectories, although there is not a huge amount of variation between the other two angular velocity groups. This is in agreement with qualitative analysis of trajectories.

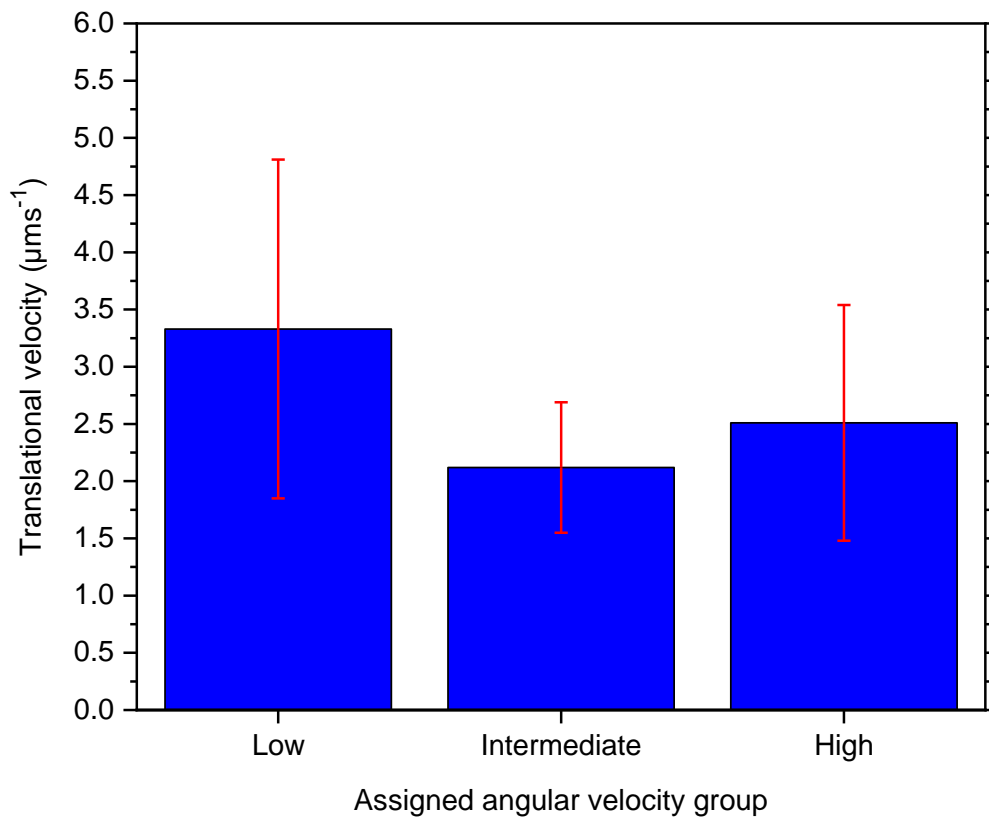


Figure 6-23: A bar chart showing the average velocity of a set of swimmers within defined bands for angular velocity.

6.4 Discussion

The results from sections 6.3.1 and 6.3.2 were compared with the angular velocity analysis for a set of 30 hemispherically coated spherical swimmers.

When the distributions of angular velocity are compared it highlights the significant effect that shape has on the range of angular velocities produced and it is clear that higher angular velocities can be introduced purely by changing the colloidal shape. All spherical swimmers populate the first 0.05 rads^{-1} band with a negligible average angular velocity of $1.98 \times 10^{-8} \pm 5.10 \times 10^{-8} \mu\text{ms}^{-1}$.

Within the bowl and dumpling shaped samples there are swimmers with negligible angular velocity, which are similar in number to the number of colloids expected to be oriented such that the resulting catalytic area after coating closely resembles a

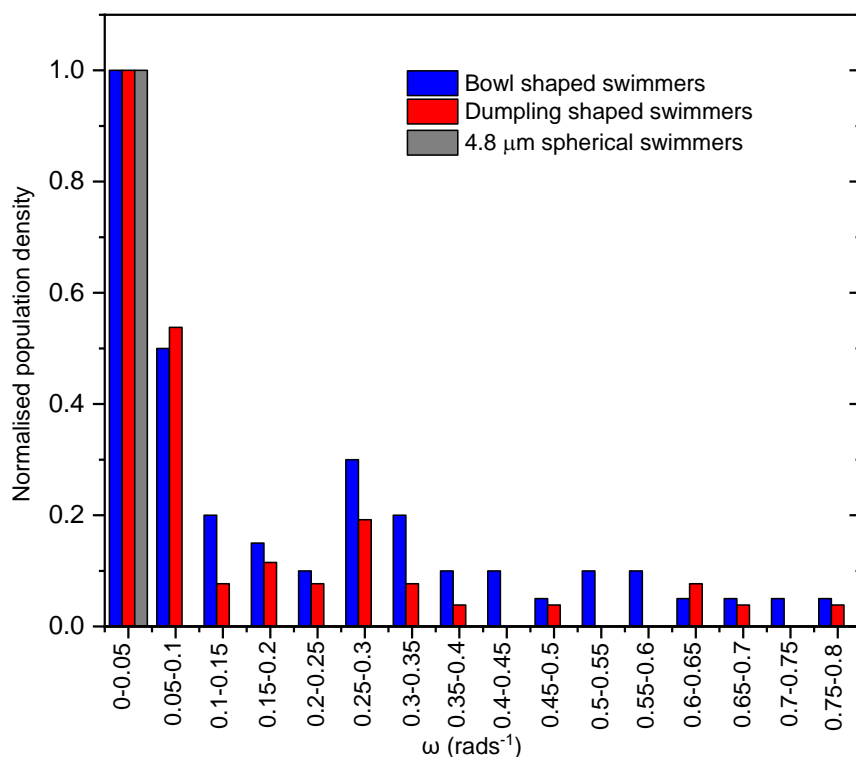


Figure 6-24: A comparison bar chart showing the distribution of angular velocities for all samples at 0.05 rads^{-1} intervals.

hemisphere. For dumpling shaped colloids, 31% of the population were oriented with a convex surface facing up and 36% of tested swimmers were found to have negligible angular velocity. For bowl shaped swimmers, 20% of the population were oriented with the cavity facing down and 18% of tested swimmers were found to have negligible angular velocity. This data is consistent with the assertion that catalytic coating areas shaped like hemispheres produce ballistic motion.

Swimmers with higher angular velocities most likely arose from colloids that were oriented on the slides in such a way that they shadow portions of their own body. For example, with bowl shaped colloids oriented on their side illustrated in *Figure 6-14b*, when coated, the concave surface is shadowed, and no platinum is deposited. This would lead to highly asymmetrical coatings that enhance rotational motion. The number of swimmers in each case that had a rotational component to their motion was again well correlated with the number of colloids in orientations that would lead to non-hemispherical coating shapes, 69% and 82% respectively. Above this rotational threshold however, the data does not indicate any correlation between specific 'non-hemispherical' orientations and how large the angular velocity is.

Based on the distinct patterns in the distribution graphs (*Figure 6-24*) it may be possible to assign a pattern as a 'fingerprint' type identifier for a given sample's expected range of angular velocities. In order to achieve this, many more shapes would need to be analysed and this is something that is under consideration for future work in the project.

As with the ellipsoids discussed in chapter 5 rotational motion of bowl and dumpling shaped swimmers could be further enhanced by glancing angle deposition.

6.5 Conclusions

The aim of producing a 'one-pot' synthesis of swimmers that had a broad range of angular velocities was achieved, with bowl shaped swimmers displaying angular velocities of up to 0.8 rads^{-1} under standard coating conditions (no glancing angle). This is significantly higher than the ellipsoids coated under standard conditions in chapter 3, where the maximum angular velocities were $\approx 0.3 \text{ rads}^{-1}$. These values for angular velocity are both consistently higher than for spherical Janus swimmers (*Figure 6-24*).

The results did not reveal any significant correlation between the increased angular velocity and the orientations on the slide during the coating process, and as such this cannot be assigned as the cause of the increase. In fact, it is more likely that the inherent asymmetry of the starting colloids caused significant enough symmetry breaking of the catalyst coating to induce these enhanced rotations. Due to the concave and convex surfaces of these colloids, depending on how they are oriented on the slide during coating, could induce a degree of self-shadowing like the ellipsoidal colloids investigated in chapter 5. This shadowing could be explored further by employing the glancing angle deposition technique that succeeded in enhancing rotation in Ellipsoidal swimmers.

This is a very straight forward process to achieve enhanced rotations in Janus swimmers, however if discreet angular velocities are desired then it would be much more appropriate to use a glancing angle e-beam evaporation synthesis.

Chapter 7:

Conclusions and Future work

7 Conclusions and Future Work

This thesis has explored the effect of making changes to the geometries of previously tested swimmers' systems on the resulting swimmer dynamics. Many of these effects were expected, such as asymmetrical catalytic patches and colloids leading to increased rotational motion and the work focused on improving ease of synthesis. The work here shows that rotational motion across a population of swimmers can be easily enhanced by using a non-rotationally symmetrical colloid. The effects are significantly improved when a glancing angle deposition is employed, without the need for a laboriously crafted colloidal crystal.

Most significantly, it was found that use of an ellipsoidal starting colloid produces a swimmer with both surface and fluid flow alignment capabilities. The swimmers generate a density driven convective flow at very low volume fractions which once established, the swimmers align in such a way that they travel across the flow field rather than being carried by it. This has been achieved with externally imposed flows with rods and spheres, but this is the first work where the flow is self-generated, and a closed system confined by the cuvette. This simplified set up would allow for use of these swimmers outside of laboratory settings.

This thesis highlights the rich effects of geometry changes on micron-scale swimmers and the general lack of experimental data for swimmers which deviate from the standard rods and spheres.

As each chapter explores differing conditions and phenomena the rest of this chapter will be broken down into respective experimental chapters.

The experimental work has been predominantly focussed on ellipsoidal micron scale Janus swimmers and their rich dynamics, especially near surface swimming and when exposed to slow shear flows in the early experimental chapters (3&4).

The later chapters (5&6) focus more on the introduction of advantageous rotations in non- symmetrical colloids of various geometries (ellipsoid, bowl, dumpling) with an emphasis on the simplicity of synthesis.

7.1 Ellipsoidal Micro-swimmers

7.1.1 Conclusions

When the basic motion of $\sim 9 \times 2 \mu\text{m}$ Janus ellipsoidal swimmers was investigated, most ellipsoids were found to sediment to the lower surface of the cuvette. Once sedimented, these ellipsoids translated at $\sim 90^\circ$ from their major axis with a steady orientation of $\sim 20^\circ$ between the cuvette surface and the ellipsoid major axis, this tilt is unexpected and warrants further investigation.

Few ellipsoids were found in the bulk fluid, those that were had no orientational alignment in either direction, and this was attributed to an increase in degrees of freedom when not bounded by the cuvette surface.

Translational velocities of ellipsoids were slower than an analogous sphere, likely due to their increased surface area, whilst angular velocity analysis revealed a broad spread of values not typically seen in spherical swimmers. The increased angular velocities were attributed to asymmetries in the catalyst coating, and this was investigated more thoroughly as the basis for chapter 5.

7.1.2 Future work

Observations of ellipsoidal swimmers were significant enough to suggest a mechanism of motion as the same as their spherical counterparts, however, the conclusions drawn around ellipsoidal swimmers are without definitive proof of the mechanism of motion at play. This would usually be achieved by directly observing the direction of motion with respect to the catalytic patch using fluorescence microscopy. Unprecedented fluorescence bleaching of ellipsoidal colloids vs. spheres made this method impossible during these experiments.

Other publications with similar results have also not achieved this yet, and as such this would be important future work to consider.

Rather than relying on the inbuilt fluorophores in the purchased colloids, fluorescence tagging of the swimmers after the electron beam coating could potentially be employed to overcome this obstacle. This would require a large supply of ellipsoidal colloids, as they are produced and cleaned in small batches and each added step to the synthesis results in more lost colloids and non-practical volume fractions of swimmers.

7.2 Flow phenomena in ellipsoidal micro-swimmers

7.2.1 Conclusions

Ellipsoidal swimmers in a confined cuvette were found to generate a density driven flow field when exposed to hydrogen peroxide fuel at low volume fractions. There

was a qualitatively observed preference for the swimmers to translate across the direction of the flow, rather than with it as expected.

Statistical assessment of this phenomena showed that ellipsoids with low angular velocity ($<0.2 \text{ rads}^{-1}$) spend the majority of their time translating in a direction approximately perpendicular to the flow direction, with their major axis showing a preference to align $\sim 38^\circ$ from the flow direction.

Control experiments of passive ellipsoidal colloids in an externally imposed flow of similar magnitude show that, in the absence of activity, there is a clear preference for the colloids to travel in the direction of the flow with their major axis aligned $\sim 25^\circ$ from the flow direction.

Ellipsoidal swimmers with higher angular velocities ($>0.2 \text{ rads}^{-1}$)-were found to have poor alignment of both the major axis orientation and travel direction with the flow. This is suspected to be caused by competing effects of driven angular rotation and flow alignment.

7.2.2 Future work

Future work for this chapter is largely theoretical, and is already in progress as part of a collaboration with Prof. Raphael Wittkowski (Institute of Theoretical Physics, University of Munster) and his research group. This collaboration has the potential for the results in this chapter to be published alongside a model which aims to improve the understanding of the flow alignment mechanism.

As the specific conditions described here, in which ellipsoidal colloids are able to align have yet to be discussed in the literature either experimentally or theoretically, this is the next major step in understanding why the alignment is seen.

Further to understanding more about why the ellipsoids align, it would be beneficial to control the angular velocity of the ellipsoidal colloids, as rotations appear to overpower the alignment effect. Consistently lower angular velocity swimmers would require control over the orientation of the ellipsoid during coating to minimise asymmetries in the catalyst coating that introduce the angular component. This will be described in further detail in section 7.3.2 but could be achieved, for example by using magnetic colloids that are then aligned at a known angle prior to coating.

7.3 Ellipsoidal micro-swimmers with enhanced rotational motion

7.3.1 Conclusions

This chapter investigated the cause of the previously seen 'high' angular velocity ellipsoidal swimmers and then exploited this cause to produce significantly enhanced rotational velocities by breaking the symmetry of the catalyst coating.

This symmetry breaking was easily achieved when compared to the synthesis of rotating spherical swimmers, which require a closely packed colloidal crystal monolayer to achieve any shadowing during coating.

The ellipsoidal colloids, when tilted during the coating process, cause shadowing along their major axis which leads to a build-up of platinum at the tip closest to the metal source.

The angular velocities achieved were comparable to their spherical counterparts. However, as the orientation of the ellipsoids on the substrate before coating was not controlled, there were still a broad range of angular velocities observed. Controlling the orientation of the long axis during coating would give narrower ranges of angular velocity for a given glancing angle.

7.3.2 Future work

7.3.2.1 Controlling the long axis orientation, α

Control over the long axis orientation, α , has the potential to impart added control over angular velocity. Use of a micro ridged surface with ‘trenches’, the appropriate width of the colloid would encourage settling into the ridges when allowed to dry naturally. *Figure 7-1* from Wilts et al.⁹² shows an example of a substrate made from epoxy that mimics the ridged surface of a petal, that could be used to align ellipsoidal colloids prior to coating. If a micro-ridged substrate were to be used, care over the material used is paramount, as the coating process involves high energy electrons and temperatures that could cause melting or burning.

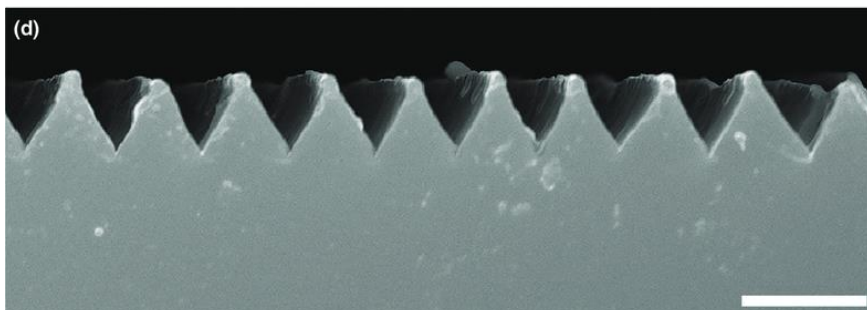


Figure 7-1: Epoxy replica of the surface of a petal. Scale bar 10 μ m from Wilts. et al.⁹²

Use of magnetic materials built into the colloids would also allow long axis alignment. The magnetic colloids could be deposited onto a glass slide as they usually are, and then aligned (before they dry) using a magnetic field.

7.3.2.2 Increasing angular velocity by varying the glancing angle, θ

The publication regarding rotating spheres found that the angular velocity could be further increased at shallower glancing angles, peaking at a 20° coating angle.

Due to time constraints caused by the pandemic, systematic testing of a wide range of glancing angles was not possible. Instead, the catalyst coatings at these further angles were predicted using ray tracing and displayed in *Figure 7-2*. In *Figure 7-2 a)-d)* it can be seen that little asymmetry is introduced before the glancing angle hits at least 60°, the experimentally tested glancing angle. After this point small changes in the glancing angle dramatically increase the asymmetry in the coating. As such, it would be useful to test shallower glancing angles (40°-10°) experimentally in future if higher angular velocities are desired.

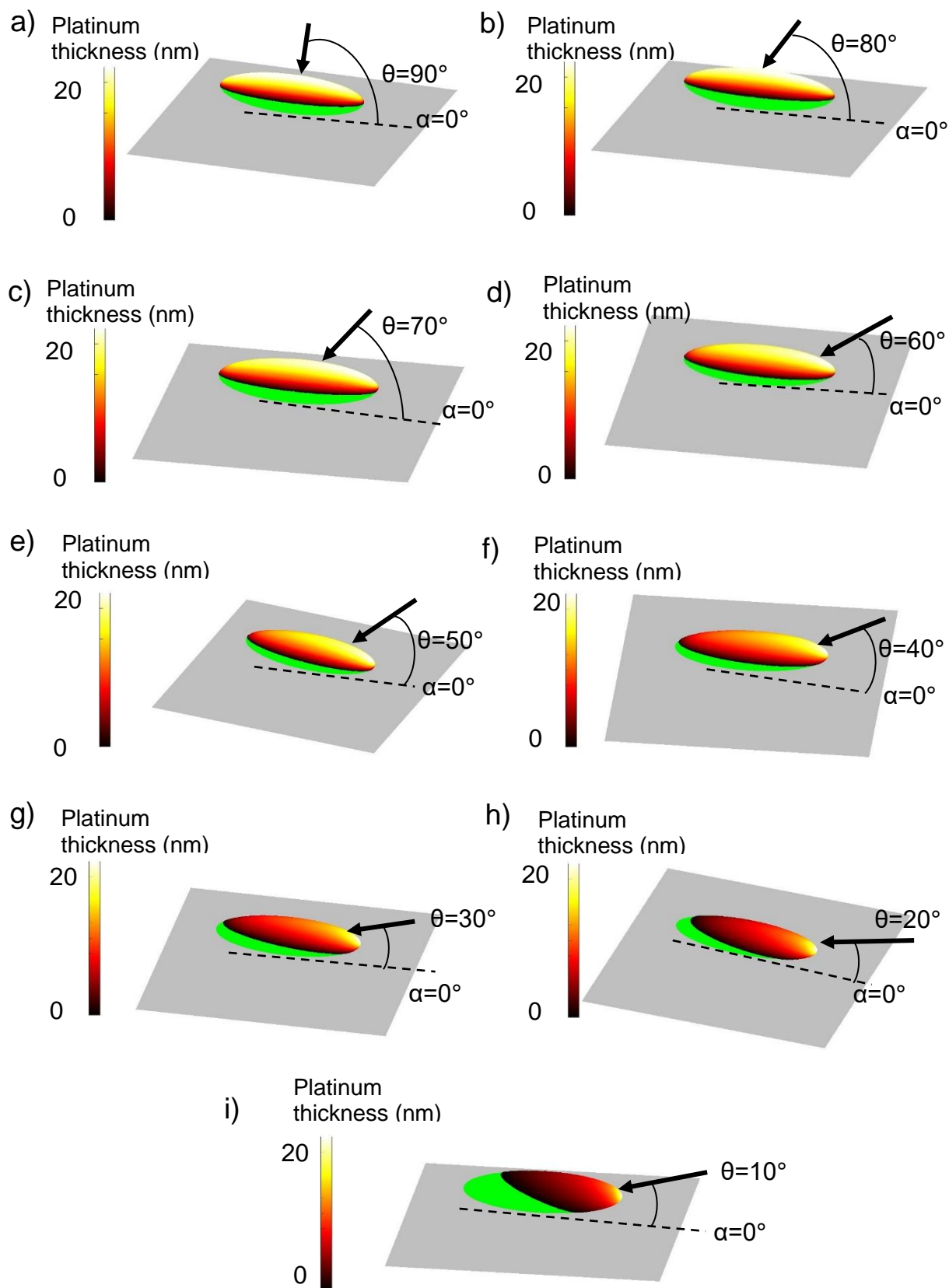


Figure 7-2: Schematic showing predictions for how the reducing glancing angle results in increased symmetry breaking in the catalyst. a) $\theta=90^\circ$, b) $\theta=80^\circ$, c) $\theta=70^\circ$, d) $\theta=60^\circ$, e) $\theta=50^\circ$, f) $\theta=40^\circ$, g) $\theta=30^\circ$, h) $\theta=20^\circ$, i) $\theta=10^\circ$.

7.4 Dumping and Bowl-shaped swimmers

7.4.1 Conclusions

The final experimental chapter (6) explored colloids with less monodisperse geometries and therefore, more available orientations before coating, as a substrate for rotational swimmers.

The dumping and bowl-shaped swimmers produced similar results to ellipsoidal swimmers in that there was a broad range of angular velocity distribution across the samples. Bowl shaped swimmers achieved significantly higher angular velocities than the fastest spinning ellipsoids coated under standard conditions. The trajectories more resembled rotational spheres than the smooth circular behaviour seen for ellipsoidal swimmers.

These colloids are more difficult to orient than ellipsoidal colloids, so where a controlled range of angular velocities are desired, ellipsoids or spheres would be a more appropriate geometry.

Where a range of angular velocities is desired in a simple 'one pot' synthesis, starting colloids of a variety of geometries are very effective. The synthesis methods for such colloids tend to be quite complicated and as such, use of diatomic frustules as a naturally occurring and very cheap substrate for active swimmers, is proposed and discussed in section 7.4.2.

7.4.2 Future work

Diatomic frustules, pictured in *Figure 7-3* from Hildebrand et al.⁹³, are the shells of dead diatomic algae. The shells are hard but porous and composed predominantly out of silica which is an ideal material for the basis of catalytic swimmers. These frustules, which come in a rich variety of geometries and sizes (2 μ m-200 μ m) are readily available and extremely cheap.

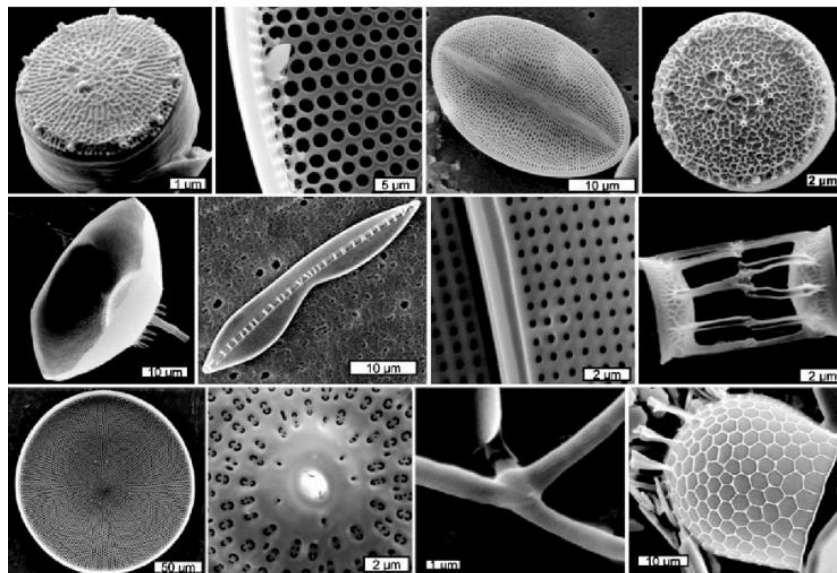


Figure 7-3: Diatomic frustules in various geometries imaged by SEM, by Hildebrand et al.⁹³

Diatoms, when coated in platinum would produce swimmers with geometries that are currently impossible to synthesise and would allow access to swimmer dynamics not yet seen in the literature. With the porous nature of the structure increasing their ability to collect, carry and deliver cargo in microfluidic applications.

This work has described in detail the effects of changing geometries of active colloids and highlighted the lack of complex shaped swimmers in the literature. The shape induced dynamics of active colloids are extensive and the enhanced potential for applications of non-spherical swimmers, such as self-induced flow alignment, would allow for uses outside of the lab.

These findings indicate that, given an unlimited budget and without time constraints, it would be prudent to experimentally test any conceivable non-rotationally symmetrically shaped swimmer to investigate their shape induced dynamics.

8 References

- 1 A. Kirvin, D. Gregory, A. Parnell, A. I. Campbell and S. Ebbens, Rotating ellipsoidal catalytic micro-swimmers via glancing angle evaporation, *Mater. Adv.*, 2021.
- 2 W. Gao, B. E. F. de Ávila, L. Zhang and J. Wang, *Adv. Drug Deliv. Rev.*, 2018, 125, 94–101.
- 3 J. R. Baylis, K. Y. T. Chan and C. J. Kastrup, Halting hemorrhage with self-propelling particles and local drug delivery, *Thromb. Res.*, 2016, **141**, S36--S39.
- 4 M. A. Jalali, A. Khoshnood and M.-R. Alam, Microswimmer-induced chaotic mixing, *J. Fluid Mech.*, 2015, **779**, 669–683.
- 5 W. Z. Teo, R. Zboril, I. Medrik and M. Pumera, Fe⁰ Nanomotors in Ton Quantities (10²⁰ Units) for Environmental Remediation, *Chem. - A Eur. J.*, 2016, **22**, 4789–4793.
- 6 J. Wu, S. Balasubramanian, D. Kagan, K. M. Manesh, S. Campuzano and J. Wang, Motion-based DNA detection using catalytic nanomotors, *Nat. Commun.*, 2010, **1**, 36.
- 7 J. Li, O. E. Shklyaev, T. Li, W. Liu, H. Shum, I. Rozen, A. C. Balazs and J. Wang, Self-Propelled Nanomotors Autonomously Seek and Repair Cracks, *Nano Lett.*, 2015, **15**, 7077–7085.
- 8 A. Einstein, *Investigations on the theory of the Brownian movement*, Dover Publications, New York, 1956.

- 9 O. Reynolds, An Experimental Investigation of the Circumstances Which Determine Whether the Motion of Water Shall Be Direct or Sinuous, and of the Law of Resistance in Parallel Channels, *Philos. Trans. R. Soc. London*, 1883, **174**, 935–982.
- 10 E. M. Purcell, Life at low Reynolds number, *Am. J. Phys.*, 1977, **45**, 3–11.
- 11 M. A. Sleight, Mechanisms of flagellar propulsion, *Protoplasma*, 1991, **164**, 45–53.
- 12 B. J. Williams, S. V Anand, J. Rajagopalan and M. T. A. Saif, A self-propelled biohybrid swimmer at low Reynolds number., *Nat. Commun.*, 2014, **5**, 3081.
- 13 C. Casagrande, P. Fabre, E. Raphaël and M. Veyssié, ‘Janus Beads’: Realization and Behaviour at Water/Oil Interfaces, *EPL (Europhysics Lett.)*, 1989, **9**, 251.
- 14 W. Gao, X. Feng, A. Pei, C. R. Kane, R. Tam, C. Hennessy and J. Wang, Bioinspired helical microswimmers based on vascular plants, *Nano Lett.*, 2014, **14**, 305–310.
- 15 M. M. Stanton, B.-W. Park, A. Miguel-Lopez, X. Ma, M. Sitti and S. Sanchez, Biohybrid Microtube Swimmers Driven by Single Captured Bacteria., *Small*, , DOI:10.1002/smll.201603679.
- 16 X. Lin, T. Si, Z. Wu and Q. He, Self-thermophoretic motion of controlled assembled micro-/nanomotors, *Phys. Chem. Chem. Phys.*, 2017, **19**, 23606–23613.
- 17 Z. Wu, T. Si, W. Gao, X. Lin, J. Wang and Q. He, Superfast Near-Infrared

- Light-Driven Polymer Multilayer Rockets, *Small*, 2016, **12**, 577–582.
- 18 T. C. Lee, M. Alarcón-Correa, C. Miksch, K. Hahn, J. G. Gibbs and P. Fischer, Self-propelling nanomotors in the presence of strong Brownian forces, *Nano Lett.*, 2014, **14**, 2407–2412.
- 19 W. F. Paxton, K. C. Kistler, C. C. Olmeda, A. Sen, S. K. St. Angelo, Y. Cao, T. E. Mallouk, P. E. Lammert and V. H. Crespi, Catalytic Nanomotors: Autonomous Movement of Striped Nanorods, *J. Am. Chem. Soc.*, 2004, **126**, 13424–13431.
- 20 G. Zhao, A. Ambrosi and M. Pumera, Self-propelled nanojets via template electrodeposition, *Nanoscale*, 2013, **5**, 1319–1324.
- 21 R. J. Archer, A. I. Campbell and S. J. Ebbens, Glancing angle metal evaporation synthesis of catalytic swimming Janus colloids with well defined angular velocity, *Soft Matter*, 2015, **11**, 6872–6880.
- 22 S. Ebbens, D. A. Gregory, G. Dunderdale, J. R. Howse, Y. Ibrahim, T. B. Liverpool and R. Golestanian, Electrokinetic effects in catalytic platinum-insulator Janus swimmers, *Epl*, , DOI:10.1209/0295-5075/106/58003.
- 23 Q. Rao, T. Si, Z. Wu, M. Xuan and Q. He, A Light-Activated Explosive Micropropeller, *Sci. Rep.*, 2017, **7**, 4621.
- 24 Y. Wang, R. M. Hernandez, D. J. Bartlett, J. M. Bingham, T. R. Kline, A. Sen and T. E. Mallouk, Bipolar electrochemical mechanism for the propulsion of catalytic nanomotors in hydrogen peroxide solutions, *Langmuir*, 2006, **22**, 10451–10456.

- 25 W. Wang, W. Duan, S. Ahmed, T. E. Mallouk and A. Sen, *Nano Today*, 2013, 8.
- 26 W. Wang, W. Duan, A. Sen and T. E. Mallouk, Catalytically powered dynamic assembly of rod-shaped nanomotors and passive tracer particles, *Proc. Natl. Acad. Sci.*, 2013, **110**, 17744–17749.
- 27 F. Wong and A. Sen, Progress toward Light-Harvesting Self-Electrophoretic Motors: Highly Efficient Bimetallic Nanomotors and Micropumps in Halogen Media, *ACS Nano*, 2016, **10**, 7172–7179.
- 28 J. Orozco, B. Jurado-Sánchez, G. Wagner, W. Gao, R. Vazquez-Duhalt, S. Sattayasamitsathit, M. Galarnyk, A. Cortés, D. Saintillan and J. Wang, Bubble-Propelled Micromotors for Enhanced Transport of Passive Tracers, *Langmuir*, 2014, **30**, 5082–5087.
- 29 W. Z. Teo, H. Wang and M. Pumera, Beyond platinum: silver-catalyst based bubble-propelled tubular micromotors, *Chem. Commun.*, 2016, **52**, 4333–4336.
- 30 D. Velegol, A. Garg, R. Guha, A. Kar and M. Kumar, Origins of concentration gradients for diffusiophoresis, *Soft Matter*, 2016, **12**, 4686–4703.
- 31 T. Hayat, A. Tanveer, H. Yasmin and F. Alsaadi, Simultaneous effects of Hall current and thermal deposition in peristaltic transport of Eyring–Powell fluid, *Int. J. Biomath.*, 2015, **08**, 1550024.
- 32 P. Geelhoed, J. Westerweel, S. Kjelstrup and D. Bedeaux, in *Encyclopedia of Microfluidics and Nanofluidics*, ed. D. Li, Springer US, Boston, MA, 2008, pp.

- 2061–2064.
- 33 S. Duhr and D. Braun, Why molecules move along a temperature gradient, *Proc. Natl. Acad. Sci.*, 2006, **103**, 19678 LP – 19682.
- 34 J. F. Robyt and B. J. White, *Biochemical Techniques: Theory and Practice*, Waveland Press, 1987.
- 35 C. GELFI, M. PEREGO, S. MORELLI, A. NICOLIN and P. G. RIGHETTI, Analysis of Antisense Oligonucleotides by Capillary Electrophoresis, Gel-Slab Electrophoresis, and HPLC: A Comparison, *Antisense Nucleic Acid Drug Dev.*, 1996, **6**, 47–53.
- 36 R. Larter and P. Ortoleva, A theoretical basis for self-electrophoresis, *J. Theor. Biol.*, 1981, **88**, 599–630.
- 37 W. F. Paxton, P. T. Baker, T. R. Kline, Y. Wang, T. E. Mallouk and A. Sen, Catalytically induced electrokinetics for motors and micropumps, *J. Am. Chem. Soc.*, 2006, **128**, 14881–14888.
- 38 J. Hopkins and J. Biol, Sa , I < , Ca , and Mg in Human Blood.
- 39 L. Restrepo-Pérez, L. Soler, C. Martínez-Cisneros, S. Sánchez and O. G. Schmidt, Biofunctionalized self-propelled micromotors as an alternative on-chip concentrating system, *Lab Chip*, 2014, **14**, 2914–2917.
- 40 W. Gao, X. Feng, A. Pei, Y. Gu, J. Li and J. Wang, Seawater-driven magnesium based Janus micromotors for environmental remediation, *Nanoscale*, 2013, **5**, 4696–4700.

- 41 M. García, J. Orozco, M. Guix, W. Gao, S. Sattayasamitsathit, A. Escarpa, A. Merkoçi and J. Wang, Micromotor-based lab-on-chip immunoassays, *Nanoscale*, 2013, **5**, 1325–1331.
- 42 D. A. Gregory, A. I. Campbell and S. J. Ebbens, Effect of Catalyst Distribution on Spherical Bubble Swimmer Trajectories, *J. Phys. Chem. C*, 2015, **119**, 15339–15348.
- 43 W. Uspal, M. Popescu, S. Dietrich and M. Tasinkevych, Active Janus colloids at chemically structured surfaces, *J. Chem. Phys.*, 2019, **150**, 204904.
- 44 B. ten Hagen, F. Kümmel, R. Wittkowski, D. Takagi, H. Löwen and C. Bechinger, Gravitaxis of asymmetric self-propelled colloidal particles, *Nat. Commun.*, 2014, **5**, 4829.
- 45 Y. Ibrahim, R. Golestanian and T. Liverpool, Shape dependent phoretic propulsion of slender active particles, *Phys. Rev. Fluids*.
- 46 W. E. Uspal, M. N. Popescu, M. Tasinkevych and S. Dietrich, Shape-dependent guidance of active Janus particles by chemically patterned surfaces, *New J. Phys.*, 2018, **20**, 015013.
- 47 O. Shemi and M. J. Solomon, Self-Propulsion and Active Motion of Janus Ellipsoids, *J. Phys. Chem. B*, 2018, **122**, 10247–10255.
- 48 S. Das, A. Garg, A. I. Campbell, J. Howse, A. Sen, D. Velegol, R. Golestanian and S. J. (orcid:0000-0002-4727-4426) Ebbens, Boundaries can steer active Janus spheres.
- 49 D. S. Lemons and A. Gythiel, Paul Langevin’s 1908 paper “On the Theory of

- Brownian Motion” [“Sur la théorie du mouvement brownien,” C. R. Acad. Sci. (Paris) **146** , 530–533 (1908)], *Am. J. Phys.*, 1997, **65**, 1079–1081.
- 50 F. Lugli, E. Brini and F. Zerbetto, Shape governs the motion of chemically propelled Janus swimmers, *J. Phys. Chem. C*, 2012, **116**, 592–598.
- 51 P. J. Hoogerbrugge and J. M. V. A. Koelman, Simulating Microscopic Hydrodynamic Phenomena with Dissipative Particle Dynamics, *Europhys. Lett.*, 1992, **19**, 155–160.
- 52 R. Golestanian, T. Liverpool and A. Ajdari, Designing phoretic micro- and nano-swimmers, *New J. Phys.*
- 53 W. E. Uspal, M. N. Popescu, M. Tasinkevych and S. Dietrich, Shape-dependent guidance of active Janus particles by chemically patterned surfaces, *New J. Phys.*, 2018, **20**, 1–19.
- 54 O. E. Shklyaev, H. Shum, V. V Yashin and A. C. Balazs, Convective Self-Sustained Motion in Mixtures of Chemically Active and Passive Particles, *Langmuir*, 2017, **33**, 7873–7880.
- 55 A. Afshar Farniya, M. J. Esplandiu and A. Bachtold, Sequential tasks performed by catalytic pumps for colloidal crystallization, *Langmuir*, 2014, **30**, 11841–11845.
- 56 S. Sengupta, D. Patra, I. Ortiz-Rivera, A. Agrawal, S. Shklyaev, K. K. Dey, U. Córdova-Figueroa, T. E. Mallouk and A. Sen, Self-powered enzyme micropumps, *Nat. Chem.*, 2014, **6**, 415–422.
- 57 J. Katuri, W. E. Uspal, J. Simmchen, A. Miguel-López and S. Sánchez, Cross-

- stream migration of active particles, *Sci. Adv.*, 2018, **4**, eaao1755.
- 58 L. Ren, D. Zhou, Z. Mao, P. Xu, T. J. Huang and T. E. Mallouk, Rheotaxis of Bimetallic Micromotors Driven by Chemical-Acoustic Hybrid Power, *ACS Nano*, 2017, **11**, 10591–10598.
- 59 W. E. Uspal, M. N. Popescu, S. Dietrich and M. Tasinkevych, Rheotaxis of spherical active particles near a planar wall, *Soft Matter*, 2015, **11**, 6613–6632.
- 60 Q. Brosseau, F. B. Usabiaga, E. Lushi, Y. Wu, L. Ristroph, J. Zhang, M. Ward and M. J. Shelley, Relating rheotaxis and hydrodynamic actuation using asymmetric gold-platinum phoretic rods, *Phys. Rev. Lett.*, 2019, **123**, 178004.
- 61 J. Palacci, S. Sacanna, A. Abramian, J. Barral, K. Hanson, A. Y. Grosberg, D. J. Pine and P. M. Chaikin, Artificial rheotaxis, *Sci. Adv.*, 2015, **1**, 1–7.
- 62 R. Baker, J. E. Kauffman, A. Laskar, O. E. Shklyaev, M. Potomkin, L. Dominguez-Rubio, H. Shum, Y. Cruz-Rivera, I. S. Aranson, A. C. Balazs and A. Sen, Fight the flow: The role of shear in artificial rheotaxis for individual and collective motion, *Nanoscale*, 2019, **11**, 10944–10951.
- 63 C. C. Ho, A. Keller, J. A. Odell and R. H. Ottewill, Preparation of monodisperse ellipsoidal polystyrene particles, *Colloid Polym. Sci.*, 1993, **271**, 469–479.
- 64 J. Zhang, B. A. Grzybowski and S. Granick, Janus Particle Synthesis, Assembly, and Application, *Langmuir*, 2017, **33**, 6964–6977.
- 65 G. Sauerbrey, Verwendung von Schwingquarzen zur Wägung dünner Schichten und zur Mikrowägung, *Zeitschrift für Phys.*, 1959, **155**, 206–222.

- 66 Q. 100-Q. C. M. T. and Calibration, 2005.
- 67 G. Mertens, J. Elsen, M. R. Veiga, J. Aguiar, A. S. Silva, F. Carvalho, A. Moropoulou, A. Bakolas, K. Bisbikou, E. S. Goins, A. Moropoulou, A. Bakolas, K. Bisbikou, A. E. Candeias, P. Nogueira, J. Mirão, A. S. Silva, R. Veiga, M. Franzini, L. Leoni, M. Lezzerini, V. S. Maria, S. Abd, E. Salam, M. A. Part, A. Methods, J. Freedland, L. B. Shotwell, D. Slaton, R. F. Egerton and J. Elsen, *Physical principles of electron microscopy*, 2006, vol. 36.
- 68 C. G. Cleaver, Scanning electron microscopy, x-ray microanalysis and analytical electron microscopy a laboratory workbook. Charles E. Lyman, Dale E. Newbury, Joseph I. Goldstein, David B. Williams, Alton D. Romig, Jr., John T. Armstron, Patrick Echlin, Charles E. Fiori, *Scanning*, 1993, **15**, 51.
- 69 E. Abbe, Beiträge zur Theorie des Mikroskops und der mikroskopischen Wahrnehmung, *Arch. für mikroskopische Anat.*, 1873, **9**, 413–468.
- 70 G. Dunderdale, S. Ebbens, P. Fairclough and J. Howse, Importance of particle tracking and calculating the mean-squared displacement in distinguishing nanopropulsion from other processes, *Langmuir*, 2012, **28**, 10997–11006.
- 71 Y. Wang, Y. Jeong, S. Jhiang, L. Yu and C.-H. Menq, Quantitative Characterization of Cell Behaviors through Cell Cycle Progression via Automated Cell Tracking, *PLoS One*, 2014, **9**, e98762.
- 72 G. Dunderdale, S. Ebbens, P. Fairclough and J. Howse, Importance of Particle Tracking and Calculating the Mean-Squared Displacement in Distinguishing Nanopropulsion from Other Processes, *Langmuir*, 2012, **28**, 10997–11006.

- 73 R. J. Archer, A. I. Campbell and S. J. Ebbens, Glancing angle metal evaporation synthesis of catalytic swimming Janus colloids with well defined angular velocity, *Soft Matter*, 2015, **11**, 6872–6880.
- 74 S. H. Koenig, Brownian motion of an ellipsoid. A correction to Perrin's results, *Biopolymers*, 1975, **14**, 2421–2423.
- 75 C. C. Miller and J. Walker, The Stokes-Einstein law for diffusion in solution, *Proc. R. Soc. London. Ser. A, Contain. Pap. a Math. Phys. Character*, 1924, **106**, 724–749.
- 76 S. Ebbens, M.-H. Tu, J. R. Howse and R. Golestanian, Size dependence of the propulsion velocity for catalytic Janus-sphere swimmers, *Phys. Rev. E. Stat. Nonlin. Soft Matter Phys.*, 2012, **85**, 20401.
- 77 D. A. Gregory and S. J. Ebbens, Symmetrical Catalytically Active Colloids Collectively Induce Convective Flow, *Langmuir*, 2018, **34**, 4307–4313.
- 78 Engineering ToolBox, (2003). Hydraulic Diameter. [online] Available at: https://www.engineeringtoolbox.com/hydraulic-equivalent-diameter-d_458.html [29/09/2020].
- 79 F. Mosetti, in *Beaches and Coastal Geology*, Springer US, Boston, MA, 1984, pp. 686–688.
- 80 D. B. Holmes and J. R. Vermeulen, Velocity profiles in ducts with rectangular cross sections, *Chem. Eng. Sci.*, 1968, **23**, 717–722.
- 81 A. I. Campbell, R. Wittkowski, B. ten Hagen, H. Löwen and S. J. Ebbens, Helical paths, gravitaxis, and separation phenomena for mass-anisotropic self-

- propelling colloids: Experiment versus theory, *J. Chem. Phys.*, 2017, **147**, 084905.
- 82 P. H. Mortensen, H. I. Andersson, J. J. J. Gillissen and B. J. Boersma, On the orientation of ellipsoidal particles in a turbulent shear flow, *Int. J. Multiph. Flow*, 2008, **34**, 678–683.
- 83 N. Sato and S. Makino, Numerical analysis of the motion of a single fiber interacting with a solid wall in a wall-bounded shear flow, *J. Nonnewton. Fluid Mech.*, 2019, **267**, 51–60.
- 84 A. Scheuer, G. Grégoire, E. Abisset-Chavanne, F. Chinesta and R. Keunings, Modelling the effect of particle inertia on the orientation kinematics of fibres and spheroids immersed in a simple shear flow, *Comput. Math. with Appl.*, 2020, **79**, 539–554.
- 85 I. Williams, S. Lee, A. Apriceno, R. P. Sear and G. Battaglia, Diffusioosmotic and convective flows induced by a nonelectrolyte concentration gradient, *Proc. Natl. Acad. Sci. - PNAS*, 2020, **117**, 25263–25271.
- 86 Y. Gu, V. Hegde and K. J. M. Bishop, Measurement and mitigation of free convection in microfluidic gradient generators, *Lab Chip*, 2018, **18**, 3371–3378.
- 87 L. Baraban, D. Makarov, R. Streubel, I. Mönch, D. Grimm, S. Sanchez and O. G. Schmidt, Catalytic Janus Motors on Microfluidic Chip: Deterministic Motion for Targeted Cargo Delivery, *ACS Nano*, 2012, **6**, 3383–3389.
- 88 T. Wu, T. Nieminen, S. Mohanty, J. Miotke, R. L. Meyer, H. Rubinsztein-Dunlop and M. W. Berns, A photon-driven micromotor can direct nerve fibre

- growth, *Nat. Photonics - NAT PHOTONICS*, 2011, **6**, 62–67.
- 89 E. Zhang, M. F. Kircher, M. Koch, L. Eliasson, S. N. Goldberg and E. Renström, Dynamic Magnetic Fields Remote-Control Apoptosis via Nanoparticle Rotation, *ACS Nano*, 2014, **8**, 3192–3201.
- 90 A. van Reenen, A. M. de Jong and M. W. J. Prins, Accelerated Particle-Based Target Capture—The Roles of Volume Transport and Near-Surface Alignment, *J. Phys. Chem. B*, 2013, **117**, 1210–1218.
- 91 S. J. Ebbens and J. R. Howse, Direct Observation of the Direction of Motion for Spherical Catalytic Swimmers, *Langmuir*, 2011, **27**, 12293–12296.
- 92 B. Wilts, P. Rudall, E. Moyroud, T. Gregory, Y. Ogawa, S. Vignolini, U. Steiner and B. Glover, Ultrastructure and optics of the prism-like petal epidermal cells of *Eschscholzia californica* (California poppy), *New Phytol.*, , DOI:10.1111/nph.15229.
- 93 M. Hildebrand, M. Doktycz and D. Allison, Application of AFM in understanding biomineral formation in diatoms, *Pflügers Arch. - Eur. J. Physiol.*, 2007, **456**, 127–137.